# Physics of Dissipative Kerr Solitons in Optical Microresonators and Application to Frequency Synthesis

Thèse N°9109

Présentée le 28 juin 2019

à la Faculté des sciences de base Laboratoire de photonique et mesures quantiques (SB/STI) Programme doctoral en photonique

pour l'obtention du grade de Docteur ès Sciences

par

#### **Erwan Guillaume Albert LUCAS**

Acceptée sur proposition du jury

Prof. C. S. Brès, présidente du jury Prof. T. Kippenberg, directeur de thèse

Prof. K. Vahala, rapporteur Dr S. Papp, rapporteur

Prof. L. Thévenaz, rapporteur



" Je levais les yeux. Contempler le ciel, qui n'est pas vivant, pour tout ce qui est vivant, c'est contempler le seul aïeul."

PASCAL QUIGNARD

À ceux qui nous ont quittés, mais qui ont tant compté, À Michael Gorodetsky, À Emmanuel Rosencher, À Victoria, Nicaise, Albert et Roland,

À ma famille, Merci de m'avoir supporté et soutenu jusqu'ici . . .

## Acknowledgements

This thesis is the fruit of four and a half years of work in the Laboratory of Photonics and Quantum Measurements and could not have been done without the help of many people.

First I want to thank my advisor Prof. Tobias Kippenberg. Without his constant insistence, immoderate enthusiasm and his help to highlight the important aspects of my results, my publication record would have looked different. Many experiments were only possible thanks to the freedom and trust he gave me, combined with the excellent infrastructure of his laboratory. Despite his tremendous schedule, he was always eager to follow and understand the latest experimental advances and difficulties.

This thesis is dedicated to Prof. Michael Gorodetsky, who sadly passed away earlier this year. I would like to acknowledge with much appreciation his scientific wisdom and guidance. He has substantially contributed to this work, provided me physical insights on the soliton physics and was never short on new smart ideas.

I wish to thank my thesis committee, Prof. Camille Brès, Prof. Kerry Vahala, Dr. Scott Papp and Prof. Luc Thévenaz for kindly agreeing to take the time to review this work.

I am particularly thankful to my direct crystalline 'comb team' colleagues. First, I would like to acknowledge the initial guidance and help of Caroline Lecaplain. I was then fortunate to benefit from John Jost's tutoring, his expertise and experimental skills, his constructive nature and his support were a great help to me at the beginning and remain so today. Wenle Weng and Romain Bouchand joined the group towards the end of my thesis. They quickly managed to give a second wind to the experiments, and I am happy to have been able to assist them.

Hairun Guo orchestrated most of the simulations presented in this work. I'll keep a vivid memory of the long discussions we had in his office in company of Maxim Karpov, whose creativity and initiative were very fruitful.

Miles Anderson has been more than just a nice office colleague, who greatly enriched my understanding of soliton dynamics. I also appreciated his cheerful character and his insatiable ability to debate on a wide range of topics and ideas. I enjoyed listening with a distracted ear, sometimes quite amused, to his long exchanges with the other office mates on cultural references and politics, which enlivened our office.

I am very grateful to Nils Engelsen, whose comments have greatly improved this thesis. His cheerfulness and sarcasms have enlightened the BM lab atmosphere over the last two years (unless that was thanks to the LEDs...). Besides work I value him as a friend and I enjoyed the occasional climbing and skiing together as well as the numerous beer tastings and diners with

his wife Deborah. He has also been the main instigator of my obscure smuggling of French chocolates into Switzerland.

During my time in the LPQM, the group has kept growing constantly. I have enjoyed to work in this international and diverse community, and to collaborate with enthusiastic and highly motivated people. This feeling is one of the main reasons I want to pursue in scientific research. My colleagues Jia-Jung Anton Clemens and Fabien deserve a special mention for regularly joining my evening sessions to the bouldering hall. Thank Connor for proofreading the first draft of this document. I would also like to thank the rest of the present LPQM team and in particular Alberto, Arslan, Guanhao, Itay, Jordan, Junqiu, Mohammad, Nathan, Philippe, and Sergey. I wish them all the best for what is to come.

I am happy to have worked with Victor Brasch. I keep an epic memory of the entire night we spent in the lab with John, trying to self-reference his comb. I am glad to occasionally meet him and Tobias Herr for scientific collaboration or for more casual occasions. I also take the opportunity to hereby forgive Martin Pfeiffer for his very German driving style on winding road of the Centovalli valley. I would also like to extend my acknowledgments to all the former lab members and in particular Nicolas Piro, Clément Javerzac-Galy, Hendrik Schütz, Ryan Schilling, Vivishek Sudhir and Dal Wilson, who instilled some amount of fun, drama, and rebellion into the lab, as well as for the many interesting scientific and non-scientific discussions.

I enjoyed teaching with Prof. Juan Mosig and Mina Bjelogrlic, and want to salute the other former LEMA members, my 'adoption lab'.

The technical support of the mechanic and electronic workshops has been vital for many aspects of this experimental work. For that, I want to thank Gilles Grandjean, Alfred Thomas, José Grandjean and their respective staff. The group's assistants Hélène Laurens, Antonella Ragnelli, Nicole Bouendin, and Kathleen Vionnet also deserve a lot of credit for swiftly solving many administrative issues.

I would like to acknowledge the financial support of the DARPA, the Air Force, the SNSF, and the ESA. I am particularly grateful to Eamonn Murphy for his benevolent attention to my work. Thanks to his international relations, I got in contact with Prof. Mauro Tonelli and hope that the collaboration we initiated will be fruitful.

Я также хотел бы поблагодарить Григория (Гришку) Лихачева, а также его коллег из Российского Квантового Центра – Николая Павлова, Андрея Волошина и Артема Шитикова, с которыми мне посчастливилось совместно работать в лаборатории во время их летних командировок в Лозанну. От души вам всем большое спасибо.

One of the perks of doing a PhD has been going to conferences, summer schools... I enjoyed traveling, get to know the community and stimulate my creativity. This lead in particular, to a collaboration with Pierre Brochard and Stéphane Schilt, from the LTF in Neuchatel. I thank them for the energy they have put into making the frequency division setup work quickly. I also met Miro Erkintalo, whom I would like to thank for his recommendation and the news & views he wrote on the multiplexing work<sup>1</sup>.

<sup>&</sup>lt;sup>1</sup>M. Erkintalo, "And then there were three", *Nature Photonics* 12.11 (2018), pp. 645–647.

But there is nothing like traveling without a home to return to. I would like to thank all my friends, who have made my life in Lausanne so pleasant. I am grateful to Johann, Nico P., Bram, Evi, Lynn, Aster, Lydia, Lise, Adam, Nevena, Harmonie & Guillaume, Nico L. and many others, for being there to share a beer, pizza, barbecue, concerts, going climbing, skiing, hiking... Many thanks to Mina and her accomplices for organizing our annual European trips. Merci à Charles, mon quasi-frère, pour son amitié fidèle depuis plus de 20 ans.

Cette thèse représente également l'achèvement de mon parcours académique et j'aimerais à cette occasion m'acquitter de la dette intellectuelle que je porte envers mes nombreux enseignants et professeurs, qui ont su insuffler et maintenir mon intérêt pour les sciences. Ma gratitude s'adresse particulièrement à Mesdames Verneuil, Casals, Malval, Bris, Maynard, et Messieurs Enjalbert, Thomas Lafforgue, Gilles De Boüard, Jean Dalibard, Fabien Bretenaker, Alain Aspect, Riad Haidar, Julien Jaeck et Emmanuel Rosencher.

Un immense merci à Nathalie pour m'avoir ouvert de nouveaux horizons et pour tous les beaux moments partagés au long de cette année et demie.

Pour finir, je souhaite remercier ma famille. Cette thèse n'a été possible que grâce à leur amour et leur soutien. Elle leur est également dédiée. Merci à Jacqueline, Victoria, Roland pour leur chaleureuse humanité et leur bienveillance constante. Merci à ma sœur Gwenaëlle pour sa gentillesse, son énergie, son enthousiasme et son imagination débordante. Merci à Alain et Marie-Thérèse d'avoir toujours été présents pour moi et de m'avoir soutenu tout en me laissant libre de mes choix.

Lausanne, June 2019

**Erwan Lucas** 

"It's hard to stay mad when there's so much beauty in the world. Sometimes I feel like I'm seeing it all at once, and it's too much, my heart fills up like a balloon that's about to burst. And then I remember to relax, and stop trying to hold on to it, and then it flows through me like rain and I can't feel anything but gratitude for every single moment of my stupid little life. You have no idea what I'm talking about, I'm sure. But don't worry, you will someday."

SCIENCE ET MÉTHODE HENRI POINCARÉ AMERICAN BEAUTY
ALAN BALL

<sup>&</sup>quot;Le savant n'étudie pas la nature parce que cela est utile; il l'étudie parce qu'il y prend plaisir et il y prend plaisir parce qu'elle est belle. Si la nature n'était pas belle, elle ne vaudrait pas la peine d'être connue, la vie ne vaudrait pas la peine d'être vécue. Je ne parle pas ici, bien entendu, de cette beauté qui frappe les sens, de la beauté des qualités et des apparences; non que j'en fasse fi, loin de là, mais elle n'a rien à faire avec la science; je veux parler de cette beauté plus intime qui vient de l'ordre harmonieux des parties, et qu'une intelligence pure peut saisir."

## **Abstract**

Optical-frequency combs, that is spectra of equidistant coherent optical lines, have revolutionized the precision measurements of time and frequency. In 2007 a new method to generate optical frequency combs was discovered. In contrast to conventional generation methods based on pulsed laser sources, these 'Kerr combs' or 'microcombs' are generated entirely via nonlinear frequency conversion in a microresonator pumped by a continuous-wave laser. More recently, the discovery of dissipative soliton formation in these cavities has enabled the generation of low-noise comb states with reproducible spectral envelopes, required in applications. Solitons are pulses of light which retain their shape as they circulate in the resonator, owing to the balance between counter-acting effects. On the one hand, the tendency of the pulse to spread due to anomalous group velocity dispersion is counteracted by the nonlinear self-phase modulation. On the other hand, the losses in the cavity are lifted by the nonlinear parametric gain provided by the driving laser. These states are robust attractors of the nonlinear cavity system under specific driving conditions.

In this thesis, the properties and dynamics of dissipative soliton states are studied experimentally in crystalline magnesium fluoride whispering gallery mode resonators. Several methods are developed to accurately determine and control the driving parameters as well as to improve the comb stability. The observations provide an accurate verification of the Lugiato-Lefever equation commonly used to describe the system. Furthermore, unexpected deviations from this canonical model are observed and accounted for with an enriched framework.

The improved fundamental understanding and control of the system is applied for the generation of an ultralow-noise microcomb driven with an ultra-stable laser. In combination with a novel transfer oscillator method, this comb is used to synthesize ultralow-noise microwaves via optical frequency division.

Lastly, a novel method for synthesizing multiple distinct frequency combs from a single resonator and with a single laser is devised. It relies on multiplexing solitons in different spatial modes of the microresonator. Up to three combs are generated simultaneously from a single device for the first time.

#### **Keywords:**

- · Optical frequency combs
- · Optical microresonators
- Nonlinear optics
- Frequency metrology

- Dissipative Kerr-cavity solitons
- Low-noise microwave synthesis
- Dual / triple-comb generation

## Résumé

Les peignes de fréquences optiques sont des sources de lumière, dont le spectre est constitué de composantes fréquentielles équidistantes et cohérentes, qui ont révolutionné les mesures précises de temps et de fréquence. En 2007, une nouvelle méthode de génération de peignes de fréquences optiques fut découverte. Contrairement aux méthodes de génération conventionnelles basées sur des sources laser pulsées, ces « peignes de Kerr » ou « micro-peignes » sont entièrement générés par conversion de fréquence non-linéaire dans un micro-résonateur pompé par un laser continu. Plus récemment, il a été découvert que des solitons dissipatifs peuvent être formés dans ces cavités. Ceux-ci permettent la génération d'états de peignes à faible bruit ayant une enveloppe spectrale régulière, ce qui constitue un prérequis nécessaire aux applications. Les solitons sont des impulsions lumineuses qui circulent dans le résonateur sans se déformer, résultant d'un équilibre dynamique entre plusieurs effets contraires. D'une part, la tendance de l'impulsion à s'élargir temporellement, en raison de la dispersion anormale de la vitesse de groupe, est contrecarrée par l'automodulation de phase associée à la non-linéarité de Kerr. D'autre part, les pertes dans la cavité sont compensées par le gain paramétrique non linéaire fourni par le laser de pompe. Ces états de soliton sont des attracteurs robustes de la cavité non-linéaire dans des conditions de pompage spécifiques.

Dans cette thèse, les propriétés et la dynamique des états de solitons dissipatifs sont étudiées expérimentalement dans des résonateurs à mode de galerie en fluorure de magnésium cristal-lin. Plusieurs méthodes sont mises au point pour déterminer et contrôler avec précision les paramètres de pompage du système ainsi que pour améliorer la stabilité du peigne formé par le soliton. Les observations fournissent une vérification de l'exactitude de l'équation de Lugiato-Lefever couramment utilisée pour décrire le système. De plus, des écarts inattendus par rapport à ce modèle canonique sont observés et pris en compte dans un formalisme enrichi.

L'amélioration de la compréhension fondamentale du système et de son contrôle sont appliqués à la génération d'un peigne à très faible produit avec un laser ultra-stable. Ce peigne est utilisé en combinaison avec une nouvelle méthode d'oscillateur de transfert pour synthétiser les micro-ondes à très faible bruit par division de fréquence optique.

De surcroît, une nouvelle méthode permettant la synthèse de plusieurs peignes de fréquences distincts, à partir d'un seul résonateur et d'un seul laser, est mise au point. Elle repose sur le multiplexage de solitons dans différents modes spatiaux du micro-résonateur. Pour la première fois, jusqu'à trois peignes de fréquences sont générés simultanément à partir d'un seul système.

#### Acknowledgements

#### Mots-clés:

- Peigne de fréquences optiques
- Micro-résonateur
- Optique non-linéaire
- Métrologie temps-fréquence
- Soliton dissipatif en cavité
- Synthèse de micro-ondes à bas bruit
- Double et triple peigne de fréquences

## List of publications

"The secret is comprised in three words — Work, Finish, Publish."

MICHAEL FARADAY

#### **Main Publications**

- J. Liu\*, E. Lucas\*, A. S. Raja\*, J. He\*, J. Riemensberger, R. N. Wang, M. Karpov, H. Guo, R. Bouchand, and T. J. Kippenberg, "Nanophotonic soliton-based microwave synthesizers" (2019), arXiv: 1901.10372.
- E. Lucas\*, P. Brochard\*, R. Bouchand, S. Schilt, T. Südmeyer, and T. J. Kippenberg, "Ultralow-Noise Photonic Microwave Synthesis using a Soliton Microcomb-based Transfer Oscillator" (2019), arXiv: 1903.01213.
- W. Weng\*, E. Lucas\*, G. Lihachev, V. E. Lobanov, H. Guo, M. L. Gorodetsky, and T. J. Kippenberg, "Spectral Purification of Microwave Signals with Disciplined Dissipative Kerr Solitons", *Physical Review Letters* 122.1 (2019), p. 13902.
- E. Lucas, G. Lihachev, R. Bouchand, N. G. Pavlov, A. S. Raja, M. Karpov, M. L. Gorodetsky, and T. J. Kippenberg, "Spatial multiplexing of soliton microcombs", *Nature Photonics* 12.11 (2018), pp. 699–705.
- V. Brasch\*, **E. Lucas**\*, J. D. Jost, M. Geiselmann, and T. J. Kippenberg, "Self-referenced photonic chip soliton Kerr frequency comb", *Light: Science & Applications* 6.1 (2017), e16202.
- H. Guo\*, M. Karpov\*, **E. Lucas**\*, A. Kordts, M. H. Pfeiffer, V. Brasch, G. Lihachev, V. E. Lobanov, M. L. Gorodetsky, and T. J. Kippenberg, "Universal dynamics and deterministic switching of dissipative Kerr solitons in optical microresonators", *Nature Physics* 13.1 (2017), pp. 94–102.

<sup>\*</sup> These authors contributed equally to this work.

- H. Guo, **E. Lucas**, M. H. P. Pfeiffer, M. Karpov, M. Anderson, J. Liu, M. Geiselmann, J. D. Jost, and T. J. Kippenberg, "Intermode Breather Solitons in Optical Microresonators", *Physical Review X* 7.4 (2017), p. 041055.
- **E. Lucas**\*, M. Karpov\*, H. Guo, M. L. Gorodetsky, and T. J. Kippenberg, "Breathing dissipative solitons in optical microresonators", *Nature Communications* 8.1 (2017), p. 736.
- E. Lucas, H. Guo, J. D. Jost, M. Karpov, and T. J. Kippenberg, "Detuning-dependent properties and dispersion-induced instabilities of temporal dissipative Kerr solitons in optical microresonators", *Physical Review A* 95.4 (2017), p. 43822.
- J. D. Jost\*, **E. Lucas**\*, T. Herr, C. Lecaplain, V. Brasch, M. H. P. Pfeiffer, and T. J. Kippenberg, "All-optical stabilization of a soliton frequency comb in a crystalline microresonator", *Optics Letters* 40.20 (2015), p. 4723.

#### **Additional contributions**

- R. Bouchand, W. Weng, **E. Lucas**, and T. Kippenberg, "Cherenkov radiation induced symmetry breaking in counter propagating dissipative Kerr solitons" (2019), pp. 1–11, arXiv: 1905.01771.
- G. Huang, E. Lucas, J. Liu, A. S. Raja, G. Lihachev, M. L. Gorodetsky, N. J. Engelsen, and T. J. Kippenberg, "Thermo-refractive noise in silicon nitride microresonators" (2019), arXiv: 1901.07112.
- A. S. Raja, J. Liu, N. Volet, R. N. Wang, J. He, **E. Lucas**, R. Bouchand, P. Morton, J. Bowers, and T. J. Kippenberg, "Packaged photonic chip-based soliton microcomb using an ultralownoise laser" (2019), pp. 3–7, arXiv: 1906.03194.
- A. S. Raja et al., "Electrically pumped photonic integrated soliton microcomb", *Nature Communications* 10.1 (2019), p. 680.
- W. Weng, R. Bouchand, E. Lucas, E. Obrzud, T. Herr, and T. Kippenberg, "Heteronuclear soliton molecules in optical microresonators" (2019), arXiv: 1901.04026.
- N. G. Pavlov, G. Lihachev, S. Koptyaev, **E. Lucas**, M. Karpov, N. M. Kondratiev, I. A. Bilenko, T. J. Kippenberg, and M. L. Gorodetsky, "Soliton dual frequency combs in crystalline microresonators", *Optics Letters* 42.3 (2017), pp. 514–517.
- M. H. P. Pfeiffer, C. Herkommer, J. Liu, H. Guo, M. Karpov, **E. Lucas**, M. Zervas, and T. J. Kippenberg, "Octave-spanning dissipative Kerr soliton frequency combs in Si<sub>3</sub>N<sub>4</sub> microresonators", *Optica* 4.7 (2017), p. 684. ✓

# **Contents**

| A  | cknov | wledge  | ments  | V   |
|----|-------|---------|--|-----|
| Al | bstra | ct (Eng | glish/Français)  | ix  |
| Li | st of | public  | ations   | xii |
| Ac | crony | /ms     |  | xix |
| In | trod  | uction  |  | 1   |
| 1  | Fun   | ıdameı  | ntal concepts of optical microresonators and soliton-based Kerr frequenc | y   |
|    | con   | ıbs     |  | 3   |
|    | 1.1   | Optic   | al frequency combs   | 3   |
|    |       | 1.1.1   | Introduction   | 3   |
|    |       | 1.1.2   | Self-referencing and stabilization of optical frequency combs            | 5   |
|    |       | 1.1.3   | Applications of frequency combs  | 6   |
|    |       | 1.1.4   | Comb generation methods  | 7   |
|    | 1.2   | Micro   | oresonator-based optical Kerr frequency combs                            | 8   |
|    |       | 1.2.1   | Fundamental concepts of nonlinear optics in waveguides                   | g   |
|    |       | 1.2.2   | Dielectric resonators  | 14  |
|    |       | 1.2.3   | Theory of microresonator-based optical frequency combs                   | 26  |
|    |       | 1.2.4   | Dissipative Kerr solitons  | 31  |
|    |       | 1.2.5   | Applications of microresonator based combs                               | 37  |
| 2  | Exp   | erime   | ntal generation, probing and characterization of solitons                | 39  |
|    | 2.1   | Exper   | rimental soliton generation  | 39  |
|    |       | 2.1.1   | Resonator fabrication  | 39  |
|    |       | 2.1.2   | Resonator characterization   | 41  |
|    |       | 2.1.3   | Basic setup for soliton generation                                       | 42  |
|    | 2.2   | Probi   | ng the soliton parameters  | 45  |
|    |       | 2.2.1   | Non destructive probing with a network analyzer                          | 45  |
|    |       | 2.2.2   | Soliton $\mathcal{S}$ -resonance   | 49  |
|    | 2.3   | Exper   | rimental scaling of the soliton properties                               | 53  |
|    |       | 2.3.1   | Network analyzer-based digital locking of the detuning                   | 53  |
|    |       | 2.3.2   | Detuning-dependent dissipative Kerr soliton duration                     | 54  |

#### **Contents**

|   |      | 2.3.3  | Detuning-dependent mode crossings and soliton recoil                                  | 57  |
|---|------|--------|---|-----|
| 3 | Soli | ton br | eathing and dynamical instabilities   | 63  |
|   | 3.1  | Detail | led analysis of the fundamental soliton instabilities                                 | 63  |
|   | 3.2  | Breatl | hing dissipative solitons   | 68  |
|   |      | 3.2.1  | Experimental identification of breathing  | 70  |
|   |      | 3.2.2  | Breathing dynamics  | 71  |
|   |      | 3.2.3  | Breathing region  | 75  |
|   |      | 3.2.4  | Real-time observation of breathers  | 75  |
|   |      | 3.2.5  | Breathers synchronizations  | 78  |
|   | 3.3  | Multi  | -soliton states switching   | 80  |
|   |      | 3.3.1  | Observation of switching between dissipative Kerr soliton states by laser             |     |
|   |      |        | backward tuning   | 80  |
|   |      | 3.3.2  | Deterministic switching of soliton states   | 81  |
|   |      | 3.3.3  | Thermally enabled transitions of soliton states                                       | 83  |
|   |      | 3.3.4  | Thermal lifting of the multi-soliton states degeneracy                                | 83  |
|   | 3.4  |        | node breathing  | 86  |
|   |      | 3.4.1  | Presentation and modeling   | 86  |
|   |      | 3.4.2  | Experimental results  | 89  |
|   |      | 3.4.3  | Mode crossing-induced multi-solitons breathing and destabilization                    | 92  |
| 4 | Mic  | rocom  | b stability and control   | 95  |
|   | 4.1  | Introd | duction   | 95  |
|   | 4.2  | Using  | the microresonator as an optical reference  | 96  |
|   |      | 4.2.1  | Improving the temperature stability   | 96  |
|   |      | 4.2.2  | Detuning stabilization using the soliton average power                                | 98  |
|   |      | 4.2.3  | Detuning stabilization via offset Pound-Drever-Hall laser locking $\ \ldots \ \ldots$ | 99  |
|   |      | 4.2.4  | Dual-mode temperature compensation technique  | 101 |
|   |      | 4.2.5  | Summary   | 103 |
|   | 4.3  | Direc  | t phase locking of the comb degrees of freedom  | 104 |
|   |      | 4.3.1  | Phase locking the pump to a reference comb  | 104 |
|   |      | 4.3.2  | Repetition rate actuation with a probe laser  | 105 |
|   |      | 4.3.3  | Stabilization results   | 107 |
|   | 4.4  | RF inj | ection-locking for repetition rate control and microwave purification                 | 110 |
|   |      | 4.4.1  | Stabilization of the repetition rate with the pump power and associated               |     |
|   |      |        | limitations   | 110 |
|   |      | 4.4.2  | Stabilization of the resonator and pump to a stable optical reference                 | 110 |
|   |      | 4.4.3  | Repetition-rate injection-locking effect and locking range scaling                    | 111 |
|   |      | 4.4.4  | Spectral purification effect  | 115 |
|   |      | 4.4.5  | Numerical modeling  | 116 |
|   |      |        | Experimental measurement of PM-to-PM transfer function                                |     |

| 5 | Ultr | alow-1   | noise soliton microcomb for microwaves generation  | 119                                    |
|---|------|--|--|--|
|   | 5.1  | Intro  | luction  | 119                                    |
|   | 5.2  | Solito   | n generation and stabilization with an ultra-low-noise pump laser $ \ldots  .$   | 120                                    |
|   |      | 5.2.1  | Soliton generation procedure   | 121                                    |
|   |      | 5.2.2  | Optical phase lock loop  | 121                                    |
|   |      | 5.2.3  | Resonator stabilization  | 122                                    |
|   | 5.3  | Solito   | n repetition rate noise minimization   | 122                                    |
|   |      | 5.3.1  | Repetition rate dependence on detuning   | 122                                    |
|   |      | 5.3.2  | Coupling adjustment and impact on the repetition rate stability $\ldots$   | 124                                    |
|   |      | 5.3.3  | Soliton repetition rate quiet point  | 125                                    |
|   |      | 5.3.4  | Residual limitations   | 126                                    |
|   | 5.4  | Ultral   | ow-noise microcomb as a broadband narrow laser reference   | 128                                    |
|   | 5.5  | Ultral   | ow-noise photonic microwave synthesis using a soliton microcomb-based  |  |
|   |      | transf   | Fer oscillator   | 130                                    |
|   |      | 5.5.1  | Principle of the transfer oscillator technique   | 131                                    |
|   |      | 5.5.2  | Implementation with an auxiliary comb  | 132                                    |
|   |      | 5.5.3  | Result   | 134                                    |
|   |      | 5.5.4  | Division chain   | 135                                    |
|   |      | 5.5.5  | Outlook  | 140                                    |
| 6 | Mul  | tiplexi  | ng solitons in a microresonator  | 143                                    |
| Ū | 6.1  | _  | luction  |  |
|   | 6.2  |  | al multiplexing with co-propagating pump fields  |  |
|   |      | -  | Principle  |  |
|   |      | 6.2.2  | Identification of soliton resonances and tuning method   |  |
|   |      | 6.2.3  | First demonstration  |  |
|   |      |  | Repetition rate difference modification  |  |
|   |      |  | Intermodulation products   |  |
|   | 6.3  | 00   | micerial definition of the first section of the fir |  |
|   | 0.0  | Spatia   | al multiplexing in the counter-propagating configuration   | 156                                    |
|   |      | _  | al multiplexing in the counter-propagating configuration   |  |
|   |      | 6.3.1  | Principle and demonstration  | 156                                    |
|   |      | 6.3.1<br>6.3.2   | Principle and demonstration  | 156<br>157                             |
|   |      | 6.3.1<br>6.3.2<br>6.3.3                                      | Principle and demonstration  | 156<br>157<br>157                      |
|   | 6.4  | 6.3.1<br>6.3.2<br>6.3.3<br>6.3.4                             | Principle and demonstration  | 156<br>157<br>157<br>159               |
|   | 6.4  | 6.3.1<br>6.3.2<br>6.3.3<br>6.3.4<br>Triple                   | Principle and demonstration  | 156<br>157<br>157<br>159<br>160        |
|   | 6.4  | 6.3.1<br>6.3.2<br>6.3.3<br>6.3.4<br>Triple<br>6.4.1          | Principle and demonstration  | 156<br>157<br>157<br>159<br>160<br>160 |
|   |      | 6.3.1<br>6.3.2<br>6.3.3<br>6.3.4<br>Triple<br>6.4.1<br>6.4.2 | Principle and demonstration  | 156<br>157<br>157<br>159<br>160<br>160 |
|   | 6.4  | 6.3.1<br>6.3.2<br>6.3.3<br>6.3.4<br>Triple<br>6.4.1<br>6.4.2 | Principle and demonstration  | 156<br>157<br>157<br>159<br>160<br>160 |

#### **Contents**

| A  | Add    | itional | experimental results and contributions   | 171 |
|----|--------|---------|--|-----|
|    | A.1    | Micro   | wave-rates solitons in integrated $\mathrm{Si}_3\mathrm{N}_4$ microresonators $\ldots\ldots\ldots$ | 171 |
|    |        | A.1.1   | Principle and sample description   | 171 |
|    |        | A.1.2   | Phase noise characterization   | 171 |
|    |        | A.1.3   | Soliton injection-locking  | 175 |
|    |        | A.1.4   | Noise transduction mechanisms  | 175 |
|    | A.2    | Self re | eferencing of an on chip comb  | 180 |
|    |        | A.2.1   | Broadband spectrum generation via soliton dispersive wave emission .                               | 180 |
|    |        | A.2.2   | 2f-3f interferometry and CEO detection   | 180 |
|    |        | A.2.3   | Experimental setup for self-referencing  | 181 |
|    |        | A.2.4   | Counting the continuous-wave pump laser frequency  | 183 |
|    | A.3    | Pulse   | d driving of a crystalline microresonator  | 185 |
| В  | Exp    | erimeı  | ntal methods   | 187 |
|    | B.1    | Laser   | phase noise characterization   | 187 |
|    | B.2    | Frequ   | ency counter benchmark for Allan deviation measurement   | 187 |
|    |        | B.2.1   | Allan variance   | 188 |
|    |        | B.2.2   | Experimental results   | 189 |
| C  | Der    | ivation | of the coupled mode equations model  | 195 |
| Bi | bliog  | graphy  |  | 222 |
| Cı | ırricı | ulum V  | <b>Titae</b>   | 227 |

## **Acronyms**

AM Amplitude Modulation
AMX Avoided Mode Crossing
AOM Acousto-Optic Modulator
ASE Amplified Spontaneous Emission

CCW Counter-Clockwise
CEO Carrier Envelope Offset
CEP Carrier-envelope Phase
CME Coupled Mode Equations
CW Continuous Wave / Clockwise
(depending on context)

**DBM** Double Balanced Mixer **DDS** Direct Digital Synthesizer **DKS** Dissipative Kerr Soliton

ECDL External Cavity Diode LaserEDFA Erbium Doped Fiber AmplifierEOM Electro-Optic ModulatorESA Electronic Spectrum Analyzer

FBG Fiber Bragg Grating
FEM Finite Element Modeling
FPC Fiber Polarization Controller
FSR Free Spectral Range
FWHM Full Width at Half Maximum
FWM Four-Wave Mixing

**GVD** Group Velocity Dispersion

**IF** Intermediate Frequency **IQ** In-phase-and-Quadrature

**LLE** Lugiato-Lefever Equation **LO** Local Oscillator

MI Modulation Instability
MLL Mode-Locked Laser

NPR Nonlinear Polarization Rotation

OAD Overlapping Allan Deviation
OBP / OBPF Optical Bandpass Filter
OFC Optical Frequency Comb
ONF Optical Notch Filter
OPLL Optical Phase Lock Loop
OSA Optical Spectrum Analyzer

PC Phase Comparator
PD Photodetector
PDH Pound-Drever-Hall
PID Proportional-Integral-Derivative
PM Phase Modulation
PSD Power Spectral Density

RBW Resolution Bandwidth
RF Radio-Frequency
RIN Relative Intensity Noise
RT Roundtrip Period

SCG Supercontinuum Generation SHG Second-Harmonic Generation SNR Signal-to-Noise Ratio SPM Self-Phase Modulation SSB Single Sideband

**TE** Transverse Electric **THG** Third Harmonic Generation **TM** Transverse Magnetic

USL Ultra-Stable Laser

#### Acronyms

**VCO** Voltage-Controlled Oscillator **VNA** Vector Network Analyzer

**WGM** Whispering Gallery Mode

**WDM** Wavelength Division Multiplexing

**XPM** Cross-Phase Modulation

## Introduction

"The wondrous pageant of a tiny world I will in due order to you unfold."

GEORGICS BOOK IV
VIRGIL

On May 20<sup>th</sup>, 2019, a redefinition of the SI base units is scheduled to come into force. At the 26<sup>th</sup> meeting of the Conférence Générale des Poids et Mesures in Versailles, the unanimous decision was taken to revise the definition of the SI in terms of a set of seven reference constants, to be known as the "defining constants of the SI" [1]. For example, the base unit of mass will no longer be defined based on a physical artifact kept in a vault near Paris, but by fixing the value of the Plank constant.

Most units of the system, will experience similar modification, with one notable exception: the base unit of time is left unchanged. This latter point hints at a peculiarity of this physical quantity. Time and frequency are indeed the quantities that can be measured with the greatest accuracy. Measuring a frequency, i.e. counting its number of cycles in a given time interval, is a digital procedure that is free of many sources of noise. Electronic meters capable of counting microwave frequencies have been available for a long time. In 1967, the Conférence Générale des Poids et Mesures thus defined the second, our time unit, as the period during which the microwave transition between two hyperfine levels of the caesium 133 atom oscillates 9 192 631 770 times.

Today, caesium microwave clocks are accurate down to the 15<sup>th</sup> digit [2]. They are able to keep time to within one second over 100 million years. Even better accuracy can be achieved with atomic clocks, which use optical transitions of atoms or ions. The 'pendulum' of these clocks thus oscillates at the frequency of light that is on the order of 10<sup>14</sup> oscillations per second. There are no detectors and electronic circuits fast enough to build an optical frequency counter. For a long time, the only way to connect microwave frequencies and optical frequencies has been via extremely complex harmonic frequency multiplication chains [3] designed to measure a single optical frequency. The long missing clockwork mechanism is now realized with femtosecond

frequency comb laser [4, 5], a simple and ultra-precise measuring tool that can consistently link and compare an optical frequency to a microwave frequency in a single step. These devices have become one of the main building blocks of optical atomic clocks and thanks to them, we may soon experience a new redefinition of the second based on optical standards [6, 7].

Invented at the end of the 90's, optical frequency combs have since then revolutionized the field of spectroscopy and paved the way for groundbreaking measurements at previously unattainable accuracy, which has been rewarded with the Nobel Prize in 2005. Today, they are used in an ever-increasing number of applications that extend far beyond their original purpose. The historical, and best established, way to generate frequency combs is through the emission of a train of optical pulses by a mode-locked laser.

This thesis implements another principle of frequency comb generation discovered in 2007. It is based on non-linear frequency conversion in optical microresonators [8] driven by a continuous-wave laser, to produce a 'Kerr' frequency comb. I joined the Laboratory of Photonics and Quantum Measurements in 2014, shortly after the first dissipative Kerr soliton generation in crystalline microresonators by Tobias Herr [9]. This achievement represented a true quantum leap for the field of microresonator-based combs, as it provided a mean of 'mode locking' these combs, that is obtain a pulsed coherent regime.

This thesis builds on this discovery and explores the properties of dissipative Kerr solitons in crystalline microcavities, both fundamentally and for the purpose of frequency comb stabilization. The fundamental concepts of microresonator-based Kerr frequency combs are presented in Chapter 1. The formalism and modeling of nonlinear optical cavities is introduced. Chapter 2 describes the experimental procedures for generating frequency combs. A new probing method is also introduced, which unveils new properties of soliton and grants a better control over the operating parameters of the system. First experimental validations of the analytic models are also performed and several deviations from the predictions are observed and explained. In Chapter 3, I explore the dynamical regimes of 'breathing' dissipative solitons and their 'switching' behavior. These periodically oscillating pulses are predicted as an intrinsic feature of the nonlinear model, that find remarkable experimental agreement. I also observed a new unexpected soliton breathing regime caused by the imperfections in the real system. Chapter 4 reviews the Kerr comb stabilization strategies that have been implemented during this work. Thermal effects were used for resonator tuning and injectionlocking of the soliton repetition rate is demonstrated and studied. The strength an weakness of each method is identified. The acquired knowledge on comb stabilization is put in practice in Chapter 5 for the development of an ultralow-noise Kerr comb that is used to generate lownoise microwaves. A careful noise analysis of the comb is performed. We also demonstrate the synthesis of ultra-stable microwaves using a transfer-oscillator method. Finally, a new method of soliton multiplexing is presented in **Chapter 6**, which allows several frequency combs with distinct properties to be generated simultaneously in a single resonator and from the same pump laser. Several pumping configurations are demonstrated and up to three combs are generated at the same time. The properties of these combs, in particular the presence of intermodulation products, are carefully studied.

# I Fundamental concepts of optical microresonators and soliton-based Kerr frequency combs

" Où l'on commence à ne pas comprendre "

LE MYSTÈRE DE LA CHAMBRE JAUNE GASTON LEROUX

#### 1.1 Optical frequency combs

#### 1.1.1 Introduction

An optical frequency comb is a light source whose spectrum consists of equidistant lines that are all mutually coherent (cf. fig. 1.1). An analogy can be made with the ticks of a ruler or the teeth of a hair comb, but in the frequency domain, as shown in fig. 1.1b. In general, each frequency component on the comb can be written in terms of the simple expression:

$$v_m = m f_{\text{rep}} + f_{\text{CEO}} \tag{1.1}$$

where  $f_{\text{rep}}$  is the spacing of the grid,  $f_{\text{CEO}}$  is an overall offset of the grid and  $m \in \mathbb{N}$  is a positive integer number.

This apparently simplistic relation hints at the fundamental reason optical frequency combs are useful: they provide a link from the optical to the radio-frequency (RF) domain. If both comb parameters ( $f_{\text{rep}}$ ,  $f_{\text{CEO}}$ ) lie in the RF domain, they can be detected, counted and referenced to primary frequency standards, such as caesium-based atomic clocks [10].

Given a laser with an unknown frequency  $v_L$ , its interference with the nearest optical frequency comb tooth creates an intensity beatnote at the frequency

$$\Delta f_L = v_L - v_{\rm m_L} = (v_L - f_{\rm CEO}) - m_L f_{\rm rep} \qquad m_L = \left\lfloor \frac{v_L - f_{\rm CEO}}{f_{\rm rep}} \right\rfloor$$
 (1.2)

## Chapter 1. Fundamental concepts of optical microresonators and soliton-based Kerr frequency combs

which an RF frequency that can be electronically counted. Thus, the knowledge of 3 RF frequencies  $f_{\text{CEO}}$ ,  $f_{\text{rep}}$ , and  $\Delta f_L$  as well as  $m_L$  allows for a very accurate and precise determination of the unknown optical frequency  $v_L$ . The optical frequency comb essentially performs a modulo operation on the optical frequencies, in the range of hundreds of terahertz, to link them back to the RF domain, where they can be processed electronically. As such, combs are also often referred to as "frequency gear-boxes" or "optical clockworks". This approach revolutionized optical frequency metrology and precision spectroscopy in the early 2000's. Combs rapidly replaced the cumbersome RF-to-optical frequency chains [3], and their inventors T. Hänsch and J. Hall were awarded the Nobel prize in Physics 2005.

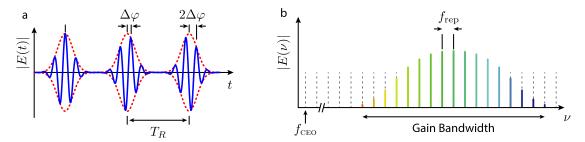


**Figure 1.1 – (a)** Pulse train generated by a mode-locked laser. The pulses are separated by the laser cavity roundtrip time  $T_R$ . The blue line indicates the electric field strength E(t) and the red line marks the pulse envelope. From one pulse to the other the electric field is phase-shifted with respect to the pulse envelope by the carrier-envelope offset phase  $\Delta \varphi$  caused by the different propagation velocities of the pulse envelope and the phase. **(b)** In the frequency domain the pulse train of a) corresponds to a frequency comb spectrum where the equidistant lines are spaced by the pulse repetition rate frequency  $f_{\text{CEO}} = \frac{1}{T_R}$ . The carrier-envelope offset frequency  $f_{\text{CEO}} = \frac{\Delta \varphi}{2\pi T_R}$ .

Optical frequency combs were first obtained from a train of ultra short pulses emitted by mode-locked lasers [4, 5, 11, 12], as shown in fig. 1.1a. A mode-locked laser (MLL) typically consists of an optical cavity containing a pumped gain medium and a saturable absorber. The broadband gain medium permits multiple longitudinal modes of the cavity to oscillate, while the saturable absorber couples them together, such that all the modes have a fixed phase relation — thereby the name mode-locked laser. In the time domain, the coherent superposition of all the in-phase modes corresponds to the formation of an optical pulse circulating in the cavity, which is amplified by the gain and shaped by the saturable absorber at every roundtrip time  $T_R$ . Dispersion management enables the formation of short pulses. The light out-coupled from the laser cavity forms a train of optical pulses that are each separated in time by  $T_R$  from the previous pulse (cf. fig. 1.1b). From one pulse to the next the electric field acquires a so-called carrier-envelope phase (CEP) slippage  $\Delta \varphi$  with respect to the pulse envelope due to the difference between the phase and group velocity in the laser cavity.

The Fourier-transform of the pulse train corresponds to a frequency comb spectrum (cf. fig. 1.1b). The pulse repetition rate  $f_{\text{rep}} = 1/T_R$  is equal to the frequency spacing of the comb lines. For typical conventional MLL,  $f_{\text{rep}}$  is on the order of few megahertz up to several

gigahertz [13–16]. The carrier-envelope phase slippage is responsible for the overall shift of the comb grid by the so-called carrier envelope offset (CEO) frequency  $f_{\rm CEO} = \frac{\Delta \phi}{2\pi T_R}$ . The bandwidth of the comb spectrum  $\Delta v$  is inversely proportional to the temporal with of the pulse intensity  $\Delta \tau$ , in virtue of the Fourier transform:  $\Delta v \Delta \tau = {\rm TBP}$  where  ${\rm TBP}$  is the time-bandwidth product, which value depends on the pulse shape and chirp.

#### 1.1.2 Self-referencing and stabilization of optical frequency combs

Detecting the two parameters of the comb is a necessary premise for any metrological application. In most cases, the repetition rate is easily measured by detecting the pulse train with a sufficiently fast photodiode. On the other hand, the measurement of the offset frequency is far less trivial and typically relies on nonlinear interferomerty [17–21]. The most common method, the f-2f self referencing, requires an octave spanning optical spectrum, that is a spectrum that spans more than a factor of two in optical frequency (i.e., covers lines n to 2n). The lower frequency components of the spectrum are sent through a nonlinear crystal for second-harmonic generation (SHG), which transfers the original comb tooth  $v_n = f_{\text{CEO}} + n f_{\text{rep}}$  to the doubled optical frequency  $2v_n$ . Mixing the frequency-doubled spectrum with the high frequency portion of the original comb on a photodiode, generates a heterdoyne beatnote between  $v_{2n}$  and  $2v_n$ , whose frequency  $2v_n - v_{2n} = f_{\text{CEO}}$  corresponds to the CEO (see fig. 1.2).

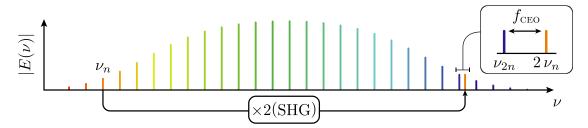


**Figure 1.2** – Schematic representation of the f-2f self-referencing principle in the spectral domain. Assuming an octave-spanning spectral bandwidth, a frequency component at the lower frequency end  $v_n$  is doubled via second harmonic generation (SHG). The doubled frequency components beat with the frequency component one octave apart  $v_{2n}$  and their beating frequency corresponds to  $2v_n - v_{2n} = f_{\text{CEO}}$ .

Typically, the optical spectrum produced by mode-locked lasers does not cover one octave, and nonlinear broadening via supercontinuum generation is usually needed to obtain octave spanning spectra [18, 19, 22–25].

Measuring both degrees of freedom provides a self-contained optical frequency reference linked to RF frequencies in an absolute way. Self-referencing allows for the full stabilization of the optical comb grid and via constant monitoring and feedback actuation on  $f_{\rm rep}$  and  $f_{\rm CEO}$ . The control mechanisms depend on the type of comb generator [4, 26, 27]. The following section highlights some applications of optical frequency combs.

#### 1.1.3 Applications of frequency combs

**Optical frequency synthesis and optical clockwork** Frequency combs provide a link from the optical to the radio-frequency (RF) domain [17–21, 28] and consequently enable unprecedentedly precise, absolute measurements of optical frequencies, which cannot be achieved using grating based spectrometers. To form an optical synthesizer, a tunable laser can be phase-locked [29, 30] to a self-referenced frequency comb. This enables optical frequency control, referenced to an RF frequency standard. Such tool is a key enabler for highly precise and accurate spectroscopy [31].

Conversely, frequency combs can serve to transfer optical references to the RF domain. Optical atomic clocks use highly stable optical transitions of cold atomic gases as frequency references [6, 32, 33], which need to be phase-coherently converted in the RF domain. Frequency combs provide the clockwork mechanism to perform this division.

**Ultrashort pulse generation** The train of short optical pulses [4, 5, 12] is useful in pump-probe spectroscopy [34], to characterize chemical reactions or energy transfers in molecules, which are happening at sub-picosecond timescales. Moreover, line-by-line phase and intensity adjustments of the comb lines enable the synthesis of complex optical waveforms[35]. The ability to control the carrier-envelope phase of femtosecond pulses also allows for the generation of ultra-intense electric fields, which can be used for high-order harmonic generation and attosecond pulse generation [36].

**Spectrometer calibration** The stable and precise line spacing of the comb may be harnessed to calibrate regular grating or Fourier-transform based spectrometers [37]. Frequency combs with a large line spacing > 10 GHz are particularly relevant here, as their individual comb teeth can be resolved by the spectrometer. One domain where high stability is particularly essential is the search for exoplanets by tracking slow Doppler shifts of emission lines induced by a planet orbiting a star [38, 39].

**Ultra-low noise microwave generation** Today, microwave signals with the lowest reported phase noise are produced by optical-frequency division using mode-locked laser frequency combs [40–43]. This techniques uses a self-referenced fs-laser comb optically-locked to an ultra-stable laser (USL) with a typical linewidth at the Hz-level [40–43]. If the comb line of index N is tightly phase-locked to the USL (after subtraction of  $f_{\rm CEO}$ ), the comb repetition rate is directly phase-stabilized to the ultra-stable frequency  $v_{\rm USL}$  by frequency division:  $f_{\rm rep} = (v_{\rm USL} - f_{\rm CEO})/N$ . Importantly, owing to the carrier frequency division from optics to microwaves, the absolute phase noise power spectral density is reduced by a factor  $N^2 \sim 10^8$ , when going from a C-band laser  $v_{\rm USL} \sim 192$  THz to a  $\sim 10$  GHz microwave signal.

**Coherent telecommunication** Wavelength division multiplexing (WDM) consists of encoding the data onto spectrally separated optical carrier tones all propagating in a single optical fiber. Current WDM networks rely on large banks of lasers to generate each individual carrier, which can be replaced by the teeth of a single frequency comb. Furthermore, a comb ensures

a fixed and stable spacing between the channels. Moreover, the optical carriers are all mutually coherent, which enables advanced digital correction schemes [44]. A comb line spacing on the order of  $\sim 50$  GHz is typically targeted to match the current modulation standards.

**Dual-comb spectroscopy** Combining two frequency combs, with slightly different repetition rate, on a photodiode generates multi-heterodyne beat-notes that map the optical spectrum into the RF domain without any moving parts [45, 46], as shown in fig. 1.3. This dual-comb technique is especially useful for spectroscopic applications and has been demonstrated to resolve both amplitude and phase of absorption profiles, in both real-time [47, 48] and mid-infrared [49] spectroscopy as well as for coherent anti-Stokes Raman spectro-imaging [50].

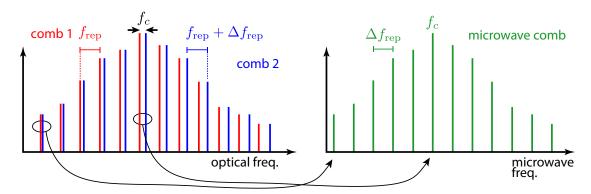


**Figure 1.3 – Dual-comb multi-heterodyne concept.** Beating two frequency combs with a small repetition rate difference  $\Delta f_{\rm rep}$  on a photodetector creates an RF comb that corresponds to the product of both combs, with a line spacing equals to  $\Delta f_{\rm rep}$ .

**Distance measurement** Optical frequency combs can also be employed for distance measurements, either using time-of-flight methods [51] leveraging the precise timing of the optical pulses, or employing dual-comb techniques to compare the optical phase of each tooth in the RF domain [52]. Ultra-rapid distance measurements can be achieved by increasing the repetition rate, at the expense of the accessible absolute measurement range [53, 54].

#### 1.1.4 Comb generation methods

This section reviews some popular and emerging technologies for optical frequency comb generation.

**Mode-locked lasers** As mentioned, the traditional implementation of optical frequency combs relies on mode locked lasers. They generally follow similar working principles, with variations in the implementations, depending on the wavelength or power.

The first demonstrations of frequency combs for metrology purposes were realized in the early 2000s, using Kerr lens mode locked titanium sapphire lasers around 860 nm [28, 55]. The diversity in this class of ultrafast *solid state lasers* have since then been greatly enriched. Most are based on a crystal gain medium doped with either transition-metal or rare earth ions [56],

## Chapter 1. Fundamental concepts of optical microresonators and soliton-based Kerr frequency combs

such as thin disk gain media, and can be mode-locked via semiconductor saturable absorber mirrors (SESAM) [57]. Such systems can provide high output power and relatively high repetition rates approaching 10 GHz. Using optically or electrically pumped semiconductor gain medium such as VECSEL provides fine tuning of the emission wavelength [58].

Mode-locked *fiber lasers*, which are robust and compact are also successful as compact low noise combs [14, 59–61]. Using nonlinear mode-locking techniques such as nonlinear (amplifying) loop mirrors (NOLM / NALM) [62], nonlinear polarization rotation (NPR) or a variety of saturable absorbers such as SESAM, they can be reliably mode locked. Fibers doped with various rare earth elements (Er, Yt, Th) can be employed for generation of pulses at different wavelengths.

**Quantum cascade laser frequency combs** This technology allows the generation of frequency combs in the mid-infrared and THz spectral regions [63], which is highly relevant for spectroscopic applications. This frequency comb generation process was only recently discovered and is based on four wave mixing and mode competition in quantum cascade lasers, which leads to a frequency modulated output instead of the emission of a pulse train [63].

**Electro-optic combs** This method consists of carving a pulse-train from a continuous wave seed laser via amplitude and phase modulation using electro-optic modulators [64]. This allows for the realization of optical frequency combs with widely tunable repetition rate which can be conveniently dialed into an RF generator. However, the technique requires non-trivial cascaded modulator geometries to realize the required modulation depth, which must then be followed by nonlinear broadening. The self-referencing of such combs has been achieved, but complex filter schemes are required to reduce the accumulated noise due to the multiplication of the original synthesizer [65, 66].

**Microresonator based optical frequency combs** This platform is the topic of this thesis and is introduced in detail in the following section. Microresonator-based frequency combs are also often referred to as *Kerr combs* or *microcombs*. Compared to the technologies described above, they represent an attracting potential for miniaturized combs [67, 68] with high repetition rates > 10 GHz. Moreover, compatibility with on-chip integration could ease mass fabrication and ultimately lead to the widespread use of this frequency comb generation technology. Nevertheless, bringing this technology to a level of maturity that allows it to be deployed in the field will require major technical developments.

#### 1.2 Microresonator-based optical Kerr frequency combs

The formation of frequency combs in microresonators is based on nonlinear frequency conversion processes mediated by the Kerr effect [8, 69]. Typically, a continuous wave (CW) input laser is converted into a series of optical lines and, when the operating conditions are adjusted properly, into an optical pulse train. The microresonator is made out of a nonlinear dielectric material and confines the light into a small volume. It also serves to resonantly enhance the

circulating power, leading to efficient nonlinear optical frequency conversion. Importantly, the microresonator is a passive optical device that performs frequency conversion and does not exhibit traditional laser gain. Instead, the Kerr effect may be described in terms of the parametric gain, which is phase and frequency selective. Although the CW laser is conveniently referred to as 'pump', it is, in our case, a constituent tooth of the final comb, which is inherently phase locked to it. It can be said that Kerr combs share more similarities with EO combs than they do with other comb architectures. This is because the nonlinear action of the system imprints a modulation onto the CW input laser in a similar fashion to the EOMs used in EO combs. In the case of Kerr combs, however, the modulation spontaneously arises from the nonlinearities of the system. This is notably different from EO combs which produce modulation via a frequency synthesizer.

In this section, the fundamental aspects of linear and nonlinear optics in waveguides are first presented. In particular, group velocity dispersion, the Kerr nonlinearity, and the nonlinear Schrödinger equation, which describes wave propagation in the nonlinear waveguide, are introduced. These basic effects are then applied to a nonlinear resonator, leading to the the mean-field model of passive Kerr cavities, described by the Lugiato-Lefever Equation (LLE). The patterned and localized structures governed by the LLE are then detailed, with emphasis on dissipative Kerr solitons.

#### 1.2.1 Fundamental concepts of nonlinear optics in waveguides

An optical waveguide is typically a dielectric structure that guides electromagnetic waves along one dimension of propagation. One commonly used example is the optical fiber, which uses total internal refraction between a core material with a higher refractive index than a surrounding cladding to guide the light. The refractive index profile and contrast (see fig. 1.4) acts as a potential well for the electromagnetic wave, which thereby remains guided and confined in the high index region.

Mathematically, the field propagating in the waveguide can be decomposed into a series of eigenmodes that remain invariant along the propagation. For a given optical frequency  $\omega/2\pi$ , assuming propagation along the z direction, the electric field of a mode can be written as:

$$E(\mathbf{r},t) = \frac{1}{2}\mathbf{u}(\mathbf{r}_{\perp})\,\mathcal{E}_0\,\mathrm{e}^{\Upsilon z - i\omega t} + \mathrm{c.c.}$$
(1.3)

where  $u(r_{\perp})$  describes the transverse spatial distribution of the electric field and obeys the Helmholtz equation for the waveguide structure ( $r_{\perp}$  is the coordinate vector in the plane transverse to the propagation direction),  $\mathcal{E}_0$  is the complex field envelope, and c.c stands for complex conjugate. The complex propagation constant  $\Upsilon$  can be separated in real and imaginary parts:

$$\Upsilon = -\frac{\alpha_{\text{loss}}}{2} + i\beta(\omega) \tag{1.4}$$

## Chapter 1. Fundamental concepts of optical microresonators and soliton-based Kerr frequency combs

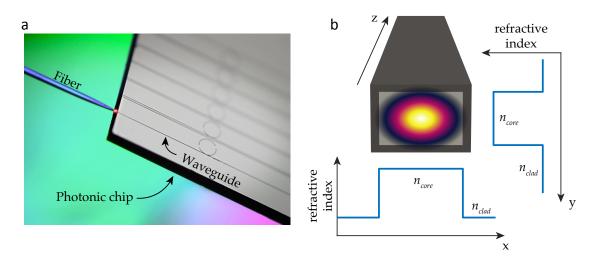


**Figure 1.4 – Optical waveguides.** (a) Picture of a photonic chip comprising  $\mathrm{Si}_3\mathrm{N}_4$  waveguides forming a bus from one chip facet to the other and a ring. The optical lensed fiber used to couple light into the chip is also a waveguide itself [Photograph credits: Victor Brasch]. (b) Illustration of a rectangular waveguide cross section with the associated refractive index profile. The gradient shading in the cross section illustrates the profile of the fundamental mode.

The different modes are typically classified into different families depending on the quantization of  $\boldsymbol{u}$ , first based on the dominant orientation of the electric or magnetic field. Because of this, modes are typically referred to as quasi-transverse electric (TE) or quasi-transverse magnetic (TM) modes. Depending on its dimensions compared to the wavelength, a waveguide may also support several spatially transverse modes for each TE/TM family.

#### Attenuation

The *attenuation constant*  $\alpha_{loss}$  describes the exponential attenuation of the optical power (proportional to  $||E||^2$  in the mode during the propagation. After a distance L in the waveguide, the remaining power is:

$$P(L) = P(0) e^{-\alpha_{\text{loss}} L}$$
 (1.5)

The losses in waveguides are typically due to either absorption or scattering. Absorption is mostly caused by material properties, depending on the electronic or vibrational resonances, as well as impurities such as OH ions in silica or transition metal atoms. Scattering arises from random variations of the waveguide's dimensions or roughness introduced during the fabrication. The resulting local fluctuations in the refractive index scatter light in non-guided modes (or can couple light into higher order spatial modes).

#### Waveguide dispersion

The quantity  $\beta(\omega)$  is referred to as the propagation constant. It can be rewritten in terms of effective refractive index

$$\beta(\omega) = \frac{\omega}{c} n_{\text{eff}}(\omega) \tag{1.6}$$

where c is the speed of light. The frequency dependence of  $n_{\rm eff}(\omega) \in [n_{\rm clad}, n_{\rm core}]$  gives rise to dispersion, which is not only due to the dielectric material that compose the waveguide, but also arises from the geometry of the waveguiding structure. Indeed, the wavelength-dependent confinement of the waveguide leads to a modification of the refractive index experienced by the mode. The latter effect can be engineered to a very fine level in the case of nano-fabricated waveguides, where nm-level dimension control can be achieved [70]. Another direct consequence of this effect is that each mode undergoes a different dispersion (modal dispersion).

At a specific frequency  $\omega_0$ , a Taylor series of  $\beta(\omega)$  provides a better intuition of the effects of dispersion:

$$\beta(\omega) = \beta_0 + \beta_1(\omega - \omega_0) + \frac{\beta_2}{2}(\omega - \omega_0)^2 + \dots \quad \text{where} \quad \beta_i = \frac{\partial^i \beta}{\partial \omega^i}\Big|_{\omega_0}$$
(1.7)

The phase velocity  $v_{\varphi} = \frac{\omega}{\beta_0} = \frac{c}{n_0}$  and group velocity  $v_g = (\beta_1)^{-1} = \frac{c}{n_g(\omega_0)}$  can differ, which typically induces the CEP slippage in mode locked lasers (equivalently, the phase index  $n_0$  and group index  $n_g(\omega_0)$  are different). The next term in the expansion  $\beta_2$  is the *group velocity dispersion* (GVD), expressed in  $s^2/m$ , which quantifies the frequency dependence of the group velocity. If  $\beta_2 < 0$ , higher frequencies travel faster than lower ones and the GVD is called *anomalous*. The opposite situation is termed *normal* GVD ( $\beta_2 > 0$ ).

#### Nonlinearities in waveguides

Nonlinear optical processes are described by the polarization P(z, t) of the optical medium in response to an optical field E(z, t)

$$\mathbf{P} = \varepsilon_0 \left( \boldsymbol{\chi}^{(1)} \, \boldsymbol{E} + \boldsymbol{\chi}^{(2)} \, \boldsymbol{E} \cdot \boldsymbol{E} + \boldsymbol{\chi}^{(3)} \, \boldsymbol{E} \cdot \boldsymbol{E} \cdot \boldsymbol{E} + \dots \right) = \varepsilon_0 \, \boldsymbol{\chi}^{(1)} \, \boldsymbol{E} + \boldsymbol{P}_{\mathrm{NL}}$$
(1.8)

where  $\varepsilon_0$  is the vacuum permittivity and  $\chi^{(k)}$  denotes the k-th order susceptibility tensor. For simplicity, we assume here that the field is linearly polarized along one direction and that the susceptibilities are scalars. The first-order susceptibility relates to the index of the material via  $n_0 = \sqrt{1 + \chi^{(1)}}$ . Next, we note that all materials used in this work exhibit inversion symmetry, such that  $\chi^{(2)}$  vanishes as well as all other even terms [71]. We therefore ignore the  $\chi^{(2)}$  term, and focus only on the term induced by the  $\chi^{(3)}$  nonlinearity:

$$\mathbf{P}_{\mathrm{NL}}(\mathbf{r},t) = \varepsilon_0 \chi^{(3)} \| \mathbf{E}(\mathbf{r},t) \|^2 \mathbf{E}(\mathbf{r},t)$$
(1.9)

where the scalar value  $\chi^{(3)}$  is assumed to be real and typically referred to as the *Kerr-nonlinearity*. As such, it describes all third order parametric frequency conversion processes in which the quantum state of the medium remains unchanged and consequently the total energy and momentum of the involved photons is conserved<sup>1</sup>.

 $<sup>^1</sup>$ A complex-valued  $\chi^{(3)}$  can describe non-parametric and inelastic processes, such as two photons absorption, or the scattering of photons with phonons, corresponding to either molecular (Raman scattering) or acoustic (Brillouin scattering) vibrations.

## Chapter 1. Fundamental concepts of optical microresonators and soliton-based Kerr frequency combs

The electric field in the nonlinear medium is described by the nonlinear wave equation, which can be derived from Maxwells equations [71]

$$\left[\nabla^2 - \frac{n_0^2}{c^2} \frac{\partial^2}{\partial t^2}\right] \boldsymbol{E}(\boldsymbol{r}, t) = -\mu_0 \frac{\partial^2 \boldsymbol{P}_{\text{NL}}}{\partial t^2}$$
(1.10)

where the nonlinear polarization acts as a source term ( $\mu_0$  here is the vacuum permeability). To illustrate the effect of the nonlinear polarization, we consider an electric field composed of three monochromatic plane waves, propagating through a nonlinear medium in the *z*-direction

$$E(z,t) = \frac{1}{2} \left( E_1 e^{i(k_1 - \omega_1 t)} + E_2 e^{i(k_2 - \omega_2 t)} + E_3 e^{i(k_3 - \omega_3 t)} + \text{c.c.} \right)$$
(1.11)

The terms in the expansion of the cubic term in the nonlinear polarization can be grouped in three physical processes:

Intensity dependent refractive index Self-phase modulation (SPM) arises from terms

$$P_{\rm NL}^{(k,k,-k)} = 3\varepsilon_0 \chi^{(3)} |E_k|^2 E_k e^{i(k_k z - \omega_k t)}$$
(1.12)

and can be thought of as an induced refractive index modification experienced by a light field due to its own intensity.

Cross-phase modulation (XPM) arises from terms

$$P_{NL}^{(k,l,-l)} = 6 \varepsilon_0 \chi^{(3)} |E_l|^2 E_k e^{i(k_k z - \omega_k t)}$$
(1.13)

It can be thought of as an index modulation induced by the intensity of a co-propagating beam. Note that no new light frequencies are generated. We are able to write an effective refractive index experienced by the light field  $E_k$  as [71]

$$n = n_0 + n_2 I_k + 2 n_2 (I_l + I_m)$$
(1.14)

where  $I_k = \frac{1}{2} n_0 \varepsilon_0 c |E_k|^2$  is the light intensity and

$$n_2 = \frac{3}{4n_0^2 \varepsilon_0 c} \chi^{(3)} \tag{1.15}$$

is the *nonlinear refractive index*, which depends on the third-order nonlinearity. From (1.14) we see that, for the same intensity, the effect of cross-phase modulation is twice as strong as the effect of self-phase modulation.

**Four-wave mixing (FWM)** is the process responsible for the frequency conversion in microcomb generation. The corresponding terms in the nonlinear polarization are

$$\begin{cases} P_{\mathrm{NL}}^{(k,l,-m)} = 6\,\varepsilon_0\chi^{(3)}E_kE_lE_m^*\,\,\mathrm{e}^{i(k_k+k_l-k_m)z}\,\,\mathrm{e}^{-i(\omega_k+\omega_l-\omega_m)t} & \text{Non-degenerate case} \\ P_{\mathrm{NL}}^{(k,k,-l)} = 3\,\varepsilon_0\chi^{(3)}E_k^2E_l^*\,\,\mathrm{e}^{i(2k_k-k_l)z}\,\,\mathrm{e}^{-i(2\omega_k-\omega_l)t} & \text{Degenerate case} \end{cases}$$

and act as a source for a new wave at frequency  $\omega_n = \omega_k + \omega_l - \omega_m$  that propagates with wave vector  $k_n = k_k + k_l - k_m$ . The different numeric pre-factors are due to the numbers of possible permutations. The degenerate case corresponds to k = l. For a maximally efficient frequency conversion process, the source and the new generated wave need to be *phase-matched* i.e.  $k_n + k_m = k_k + k_l$ . In a photon picture, FWM is the annihilation of two photons followed by the generation of one signal and idler photons with respectively higher and lower frequency than the mean frequency of the two initial photons, as illustrated in fig. 1.5. In the time domain, degenerate FWM can be interpreted as follows: the interference of the waves k and l creates a traveling index modulation at the frequency difference. In turn, this index grating phase modulates the incoming wave k and leads to the amplification of l and the creation of the new wave (k + k - l) [72–74].

**Triple component sum frequency generation** arises from terms  $\omega_k + \omega_l + \omega_m$ ,  $2\omega_k + \omega_l$  or  $\omega_k + \omega_k + \omega_k = 3\omega_k$ . During these processes, three photons are transformed into one of higher frequency, which may not be supported by a cavity resonance. Although this effect has been reported in microresonators [75, 76], they are neglected in the present study.

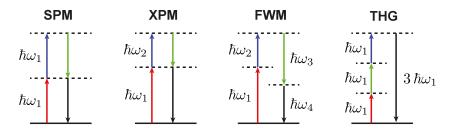


**Figure 1.5** –  $\chi^{(3)}$ -**nonlinear parametric processes**. Illustration of the annihilation (upwards pointing arrows) and creation (downward pointing arrows) of photons in the third order conservative processes. The length of the arrows corresponds to the energy of the photons SPM: Self-phase modulation, XPM: Cross-phase modulation, FWM: Four-wave mixing, THG: Third harmonic generation.

The strength of the  $\chi^{(3)}$  nonlinear effects in a waveguide is determined by its constituent materials, while the geometric confinement provides a way to enhance the intensity for a given optical power. If we assume that the influence of nonlinearities in the spatial domain, such as self-focusing, is negligible, the transverse intensity profile of the propagating mode is typically non-uniform, but preserved upon propagation. It is therefore convenient to integrate eq. (1.14) along the transverse directions in order to estimate the nonlinear phase shift caused by SPM over a distance L, for a propagating power P:

$$\delta \varphi_{\rm NL} = \gamma P L \tag{1.17}$$

where we introduced the effective nonlinear coefficient:

$$\gamma = \frac{n_2 \,\omega_0}{c \,A_{\text{eff}}} \tag{1.18}$$

## Chapter 1. Fundamental concepts of optical microresonators and soliton-based Kerr frequency combs

and the effective mode area [77]:

$$A_{\text{eff}} = \frac{\left(\iint \|\boldsymbol{E}(\boldsymbol{r},t)\|^2 \, \mathrm{d}A_{\perp}\right)^2}{\iint \|\boldsymbol{E}(\boldsymbol{r},t)\|^4 \, \mathrm{d}A_{\perp}}$$
(1.19)

where the integral is over the surface transverse to the propagation direction.

#### Pulse propagation in a nonlinear waveguide

The propagation of a pulse waveform in a mode of the waveguide can be described by separating the rapidly varying optical carrier centred at frequency  $\omega_0/2\pi$ 

$$E(\mathbf{r},t) = \frac{1}{2}\mathcal{E}(z,t) e^{-i(\beta_0 z - \omega_0 t)} \mathbf{u}(\mathbf{r}_\perp) + \text{c.c.}$$
(1.20)

where  $\mathcal{E}(z,t)$  is a 'slow' varying envelope (i.e.  $\left|\frac{\partial^2 \mathcal{E}}{\partial t^2}\right| \ll \left|\omega \frac{\partial \mathcal{E}}{\partial t}\right| \ll \left|\omega^2 \mathcal{E}\right|$ ). If both effects, dispersion and self-phase modulation, act simultaneously on a propagating pulse, the field envelope obeys [77]

$$\frac{\partial \mathcal{E}}{\partial z} + i \frac{\beta_2}{2} \frac{\partial^2 \mathcal{E}}{\partial \tau^2} = i \gamma |\mathcal{E}|^2 \mathcal{E}$$
 (1.21)

known as the *Nonlinear Schrödinger Equation* (NLSE). In the previous equation, the time coordinate t was transformed to describe the pulse evolution in a frame of reference moving with the pulse at the group velocity  $v_g$  (the so-called retarded frame), such that  $\tau = t - \beta_1 z$ .

#### 1.2.2 Dielectric resonators

An optical resonator can be formed by closing a waveguide onto itself, thus forming a closed trajectory for light. A resonance occurs when the light interferes constructively with itself after one roundtrip, i.e. when the optical path length is an integer multiple of the wavelength  $\lambda$ .

$$\beta(\omega_m) L_R = 2\pi m , \qquad m \in \mathbb{N}$$
 (1.22)

where  $L_R$  is the roundtrip length.

The simplest approach of 'looping' a waveguide on itself forms a so-called ring resonator (see fig. 1.6). However, a curved waveguide differs from a straight waveguide, as the radius of curvature modifies the optical mode profile of the waveguide, which is shifted outwards. In polar coordinates, this shift of the optical mode profile can be understood by introducing a conformal mapping [78, 79] of the Helmholtz equation that describes an equivalent straight waveguide with an effective refractive index that increases radially in the new coordinate system. In fact, the inner interface of a curved waveguide is therefore redundant and is not needed to complete the confinement. Thus, a cylindrical dielectric slab, which can be

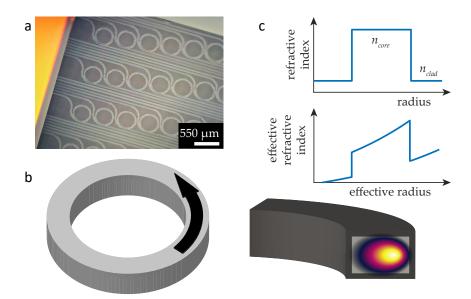


**Figure 1.6 – From a waveguide to a ring resonator.** (a) Picture of a photonic chip with patterned ring waveguides in  $\mathrm{Si_3N_4}$ . The coupling waveguides running from one chip facet to the other are also visible. (b) Schematic illustration of a waveguide ring, which forms a closed optical path. (c) Illustration of the bending effect on the optical mode of a waveguide. Radially, the index (top) is still an inverted well, but in the effective radial coordinate system (middle), the effective index is highest at the outer radial core / cladding interface. The optical mode profile (gradient shading) is thus shifted outward with respect to the core cross section (bottom).

viewed as a ring waveguide where the inner interface has been removed, still guides the light along its circumference<sup>2</sup>. In a simple geometrical picture, the light is guided via TIR at the outer interface, as illustrated in fig. 1.7. The eigenmodes of such a resonator correspond to the *whispering gallery modes* (WGM), named according to the analogous acoustic effect discovered in the dome of the St. Paul Cathedral in London. A WGM structure can thus be understood as a waveguiding structure where the radius of curvature ensures one dimension of the confinement.

#### **Coupling to WGM resonators**

Achieving the coupling of light into the whispering gallery mode resonator is the prerequisite for any practical application. Free-space excitation of dielectric micro-resonators is extremely inefficient due to the phase velocity mismatch between the air and the dielectric. An efficient excitation can be achieved using the evanescent coupling technique [80]. By bringing a phase-matched evanescent field in close proximity to a resonator, coupling can be achieved via the

$$L_{R} = \frac{V_{\text{eff}}}{A_{\text{eff}}} = \frac{\iint \|E(\mathbf{r}, t)\|^{4} dA_{\perp} \left( \iiint \|E(\mathbf{r}, t)\|^{2} dV \right)^{2}}{\iiint \|E(\mathbf{r}, t)\|^{4} dV \left( \iint \|E(\mathbf{r}, t)\|^{2} dA_{\perp} \right)^{2}}$$
(1.23)

<sup>&</sup>lt;sup>2</sup>The roundtrip length however differs from the resonator circumference and is given by

Chapter 1. Fundamental concepts of optical microresonators and soliton-based Kerr frequency combs

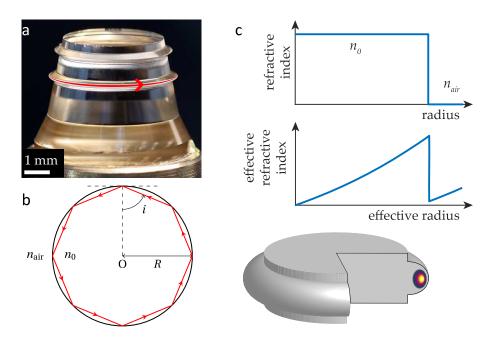


**Figure 1.7 – Whispering gallery mode resonator.** (a) Picture of a crystalline  $\mathrm{MgF}_2$  whispering gallery mode (WGM) resonator. The crystalline rod was turned and polished to feature two protrusions that support WGMs [Photograph credits: Tobias Herr]. (b) Geometrical interpretation of the WGM. The light is trapped along the circumference of the cylinder via total internal reflexion. (c) Illustration of the whispering gallery mode potential. The refractive index profile (top) has a step-like radial dependence at the transition from the dielectric  $(n_0)$  to the air  $(n_{\mathrm{air}} \sim 1)$ . However, in the modified coordinate system, the effective index features a maximum at this boundary, which explains why the light is guided radially at this interface. The bottom panel shows the typical cross section of a WGM protrusion. In the other transverse direction, the protrusion ensures the confinement of the light. The gradient shading symbolizes the optical mode profile supported in the structure.

overlap with the evanescent portion of the WGM field. Two methods are usually employed to perform evanescent coupling: prism coupling and tapered fiber coupling.

A first implementation is the prism coupling technique: an evanescent wave is produced at the total internal reflection of a beam on a prism facet. Changing the angle of incidence enables tuning of the phase matching to achieve coupling [81]. Another method, preferred in this work, uses a tapered optical fiber, obtained by drawing a single-mode optical fiber into a small filament with a diameter less than 3  $\mu$ m. The tapered region consists of the transition from the original single mode fiber (9  $\mu$ m core, 125  $\mu$ m diameter silica cladding), where light is guided by total internal reflection at the core - cladding interface, to the 3  $\mu$ m taper where light is effectively guided by reflections at the silica - air interface. This region exhibits a large evanescent field in the air, making the coupling possible. The taper diameter variation gives some freedom to achieve phase matching. Just like any coupler, this coupling method can be described in term of its coupling ratio  $\theta_{\rm ex}$  from the power in the taper to the resonator. This approach can provide efficiency up to 99.9% as the phase-matching between the two coupled

electromagnetic waves can be achieved by scanning along the taper region [82]. Furthermore, excellent coupling ideality [83] can be achieved such that the coupler transmission can be well approximated by  $(1 - \theta_{\rm ex})$ .

The fabrication of the taper takes place in the lab. A section of optical fiber is heated (with a hydrogen flame) while both ends are pulled apart simultaneously with stepper motors, which causes a reduction of the fiber diameter down to a few microns.

# Resonance lineshape

We consider the following coupling configuration, illustrated in fig. 1.8: a monochromatic external pump field  $E_{\rm in}$  (pulsation  $\omega_p$ ) is circulating in the tapered waveguide close to the resonator. The spatial overlap of the evanescent field of the waveguide and the resonator (at z=0) creates the coupling  $\theta_{\rm ex}$  between  $E_{\rm in}$  and the intracavity field E(z,t).

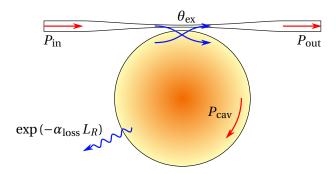


**Figure 1.8 – Coupling and loss parameters in a taper-resonator system.** The input power  $P_{\rm in}$  in the fundamental taper mode couples into the resonator with a ratio  $\theta_{\rm ex}$  which can be adjusted by changing the relative position between the taper and the resonator. Reciprocally, the intracavity power couples into the fundamental taper mode with coupling constant  $\theta_{\rm ex}$  at each roundtrip. The fraction of optical power intrinsically dissipated per roundtrip is given by  $\exp(-\alpha_{\rm loss}\,L_R)$ .

In the steady state, the intracavity light can be viewed as the coherent superposition of light from an infinite number of previous roundtrip propagations. At each roundtrip, light propagates over the roundtrip distance, with associated phase shift and intrinsic propagation loss, before reaching the coupling point. Here, a fraction  $\theta_{\rm ex}$  of the intracavity intensity will couple out of the cavity and into the waveguide, thus a fraction  $1-\theta_{\rm ex}$  stays in the resonator for the next roundtrip propagation. Simultaneously, a portion  $\theta_{\rm ex}$  of the pump intensity is coupled out of the waveguide and into the cavity. This process then repeats. In mathematical terms,

$$E = \sqrt{\theta_{\rm ex}} E_{\rm in} \sum_{n=0}^{+\infty} (g_{\rm RT})^n$$
 (1.24)

$$g_{\text{RT}} = \frac{E_{n+1}(z=0,t)}{E_n(z=L_R,t)} = \sqrt{1-\theta_{\text{ex}}} \exp\left(-\frac{\alpha_{\text{loss}}}{2}L_R\right) \exp\left(i\varphi_R\right)$$
(1.25)

where  $L_R$  is the effective cavity roundtrip length, m is the roundtrip number and  $\varphi_R = \beta(\omega_p)L_R$  is the accumulated phase shift along one roundtrip. We can express the fraction of power

transmitted from one roundtrip to the next as  $\rho = (1 - \theta_{\rm ex}) \exp{(-\alpha_{\rm loss} L_R)}$ . The geometric sum in eq. (1.24) yields:

$$\frac{E}{E_{\rm in}} = \frac{\sqrt{\theta_{\rm ex}}}{1 - \sqrt{\rho} \, e^{i\varphi_R}} \tag{1.26}$$

And thus, the circulating intracavity power follows:

$$\frac{P_{\rm circ}}{P_{\rm in}} = \left| \frac{E}{E_{\rm in}} \right|^2 = \frac{W}{1 + F \sin^2\left(\varphi_R/2\right)}, \quad \text{where} \quad W = \frac{\theta_{\rm ex}}{(1 - \sqrt{\rho})^2} \quad \text{and} \quad F = \frac{4\sqrt{\rho}}{(1 - \sqrt{\rho})^2} \quad (1.27)$$

From the above equation, three main characteristics can be highlighted. First, the function is periodic and present a resonance peak each time  $\varphi_R = 2m\pi$ ,  $m \in \mathbb{N}$ . In a first order approximation (neglecting dispersion), we can assume  $\varphi_R = \omega_p T_R = \omega_p / c n_0 L_R$ . The resonance condition can thus be re-expressed as  $\omega_m = m \Delta \omega_{\text{FSR}}$ , where the quantity

$$\Delta v_{\rm FSR} = \frac{\Delta \omega_{\rm FSR}}{2\pi} = \frac{1}{T_R} \approx \frac{1}{n_0 L_R},\tag{1.28}$$

is called the *free spectral range* (FSR) and is equal to the inverse cavity roundtrip time  $T_R$ . In a dispersion-less cavity, the resonance frequencies are therefore perfectly equidistant and spaced by the FSR.

Second, the 'sharpness' of the peaks depends on the cavity losses and is characterized via the ratio between the FSR and the full width at half maximum (FWHM) of the peaks ( $\kappa/2\pi$  in frequency):

$$\mathcal{F} \equiv \frac{\Delta \nu_{\text{FSR}}}{\kappa / 2\pi} = \frac{\Delta \omega_{\text{FSR}}}{\kappa} = \frac{\pi}{2 \arcsin(F^{-1/2})} \approx \frac{2\pi}{1 - \rho}$$
 (1.29)

known as the Finesse. The final approximation is valid for small roundtrip losses.

Finally, the intracavity intensity is greatly enhanced on resonance. The coherent buildup of the light leads to a circulating intensity enhanced by a factor W compared to the input pump intensity.

In the context of this work, we will concentrate on cavities with high finesse ( $\mathcal{F} > 1000$ ) and thus well isolated resonant peaks, such that a single resonance of the cavity can be adressed. We consider that the coupling only excites one cavity mode near  $\omega_p$  and denote  $\omega_0$  the associated resonance frequency. We introduce the normalized field amplitude A, such that  $|A|^2$  is the number of photons in the mode of interest

$$A(t) = \sqrt{\frac{n_0^2 \epsilon_0 V_{\text{eff}}}{2\hbar\omega_0}} \mathcal{E}(t)$$
 (1.30)

where the *effective mode volume*  $V_{\text{eff}} = A_{\text{eff}} L_R$  is introduced.

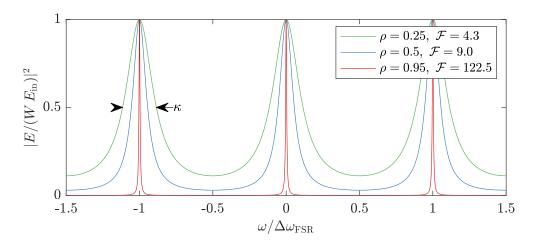


**Figure 1.9 – Normalized intracavity intensity evolution as a function of** The periodic resonance condition leads to a periodic enhancement of the intracavity intensity. Lower losses lead to sharper resonances (higher Finesse).

Following Haus *et al.* [84], the dynamics of this simplified single-mode approach can be described by a simple rate equation that describes the photons entering and exiting the cavity. If the change in amplitude experienced by the waveform as it passes the coupling segment at each roundtrip is small, we can consider the effect to be continuous, and averaged over time. The intrinsic loss of the resonator implies a decay at the rate

$$\kappa_0 = [1 - \exp(-\alpha_{\text{loss}} L_R)] / T_R \approx \alpha_{\text{loss}} L_R / T_R. \tag{1.31}$$

The coupling of the cavity also represents a loss channel for the circulating photons at a rate  $\kappa_{\rm ex} \approx \theta_{\rm ex}/T_R$ . These two quantities comprise the total energy loss rate, which as we will see below relates to the resonance FWHM as  $\kappa = \kappa_0 + \kappa_{\rm ex} = 1/t_{\rm ph}$ , where  $t_{\rm ph}$  is defined as the *photon lifetime*.

We choose a different normalization for the pump amplitude denoted  $s_{in}$ . As explained above,  $|A|^2$  is the number of photons inside the cavity and represents the energy stored in the resonator, while  $|s_{in}|^2$  represents the photon flux of the pump and relates to the incident power. The final rate equation is given by:

$$\frac{dA}{dt} = -\left(\frac{\kappa}{2} + i\delta\omega\right)A(t) + \sqrt{\kappa_{\rm ex}}\,s_{\rm in}(t) \tag{1.32}$$

The detuning term  $\delta\omega = \omega_0 - \omega_p$  was introduced here as an approximation of the complex phase boundary conditions under the assumption  $\delta\omega\,T_R\ll 2\pi$ . The factor  $\sqrt{\kappa_{\rm ex}}$  accounts for the different normalization of A and  $s_{\rm in}$ . The latter equation essentially describes the dynamics of a damped driven oscillator, as can be expected for this single mode approach. Assuming constant driving condition  $(s_{\rm in}(t)=s_{\rm in})$  we can derive the steady-state solution of

the intracavity amplitude:

$$A = \frac{\sqrt{\kappa_{\rm ex}}}{\frac{\kappa}{2} + i \delta \omega} s_{\rm in} \qquad \frac{P_{\rm cav}}{P_{\rm in}} = \frac{\mathcal{F}}{\pi} \frac{2\eta}{1 + \left(\frac{\delta \omega}{\kappa/2}\right)^2} \qquad \tan(\varphi) = -\frac{2\delta \omega}{\kappa} \qquad (1.33)$$

where we introduced the *coupling ratio*  $\eta = \kappa_{\rm ex}/\kappa$  and where  $\varphi$  is the dephasing between the intracavity field and the pump field.

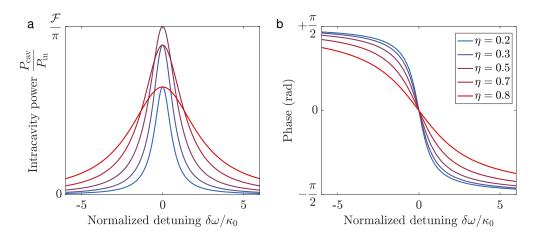


**Figure 1.10 – Intracavity field evolution over the resonance** (a) Evolution of the normalized intracavity power when the pump laser is detuned from the cavity resonance, for different coupling conditions: undercoupled (blue) critically coupled (gray) and overcoupled (red). The intrinsic linewidth  $\kappa_0$  is constant. (b) Evolution of the intracavity field phase.

Energy conservation implies that the transmitted field s<sub>out</sub> writes

$$s_{\text{out}} = s_{\text{in}} - \sqrt{\kappa_{\text{ex}}} a \tag{1.34}$$

which means that the steady state transmission can be expressed as

$$\left|\frac{s_{\text{out}}}{s_{\text{in}}}\right|^2 = 1 - \frac{\kappa_0 \kappa_{\text{ex}}}{\left(\frac{\kappa}{2}\right)^2 + \delta \omega^2} = 1 - \frac{4\eta (1 - \eta)}{1 + \left(\frac{\delta \omega}{\kappa/2}\right)^2}$$
(1.35)

The transmitted signal has a *Lorentzian* dip profile with minimal transmission on resonance, and a full width at half maximum (FWHM) linewidth given by  $\kappa$  in angular frequency ( $\kappa/2\pi$  in frequency). This lineshape can also be viewed as an second order approximation of eq. (1.27) around a single resonant peak.

Depending on the ratio  $\eta$ , three distinct regimes of coupling can be distinguished which are depicted in fig. 1.11.

**Under-coupling** ( $\eta$  < 1/2) In this regime the intrinsic cavity loss rate exceeds the coupling rate. The field leaking out of the cavity to the waveguide has a phase shift between zero

and  $\pi$  and the resonance linewidth tends towards the intrinsic losses  $\kappa_0$ . This situation is experimentally realized with a large resonator-taper gap.

**Critical coupling** ( $\eta = 1/2$ ) At this point the external coupling rate equals the intrinsic cavity loss rate. At resonance, the transmission vanishes due to the interference between the cavity leakage field and the incoming field, which exhibit equal magnitude but a relative phase shift of  $\pi$  between each other. In this situation, the intracavity power  $P_{\text{cav}}$  is maximal at resonance, as shown in fig. 1.10.

**Over-coupling**  $(\eta > 1/2)$  Here the coupling rate exceeds the intrinsic cavity loss rate. More power is coupled to the cavity then lost in it, so that the cavity leakage field (with a relative phase shift between  $\pi$  and  $2\pi$ ) dominates the waveguide field. The resonance width is dominated by  $\kappa_{\rm ex}$  and broadens for higher coupling. This situation is experimentally achieved for a small coupling gap.

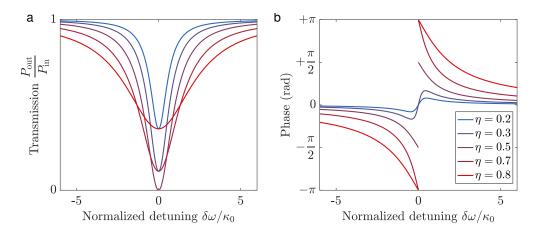


**Figure 1.11 – Cavity transmission evolution** (a) Illustration of the system transmission  $|s_{\text{out}}/s_{\text{in}}|^2$  when the pump laser is detuned from the cavity resonance, for different coupling conditions: undercoupled (blue) critically coupled (gray) and overcoupled (red). The intrinsic linewidth  $\kappa_0$  is constant. (b) Evolution of the phase  $(\varphi_{\text{out}}-\varphi_{\text{in}})$  of the cavity transmission.

Rewriting the resonator finesse in terms of rates sheds a new light on this parameter:  $\mathcal{F} = \frac{\Delta \omega_{\text{FSR}}}{\kappa} = 2\pi \frac{t_{\text{ph}}}{T_R} = 2\pi N_{\text{RT}}$ , where  $N_{\text{RT}}$  is the number of roundtrips the photons travel during their lifetime in the cavity, which illustrates how this factor is related to the cavity power enhancement factor<sup>3</sup>. The high circulating optical intensities accessible in resonators with long photon lifetimes make these devices ideally suited for nonlinear optics.

$$P_{\text{cav}} = \frac{1}{T_R} \frac{\kappa_{\text{ex}}}{(\kappa/2)^2 + \delta\omega^2} P_{\text{in}} = \frac{2}{\pi} \frac{\eta \mathcal{F}}{1 + \left(\frac{\delta\omega}{\kappa/2}\right)^2} P_{\text{in}} \xrightarrow{\kappa_{\text{ex}} = \kappa_0} \frac{\mathcal{F}}{\pi} P_{\text{in}}$$

 $<sup>^3</sup>$ The circulating power inside the cavity can be found by multiplying  $|a|^2$  by the photon energy and dividing by the roundtrip time

The *quality factor Q* is another figure of merit used to characterize the resonator

$$Q = 2\pi \frac{\text{intracavity energy}}{\text{energy lost per roundtrip}} = \frac{\omega_0}{\kappa}.$$
 (1.36)

It compares the frequency at which the system oscillates to the rate at which it dissipates its energy, or equivalently, represents the number of oscillations of the carrier wave during the photon lifetime.

# Dispersion properties of dielectric resonators

Our derivations have so far neglected the impact of dispersion on the cavity. Recall the resonance condition:

$$\beta(\omega_m) = \frac{\omega_m}{c} \, n_{\text{eff}}(\omega_m) = \frac{2\pi}{L_R} \, m \quad \text{where } m \in \mathbb{N}.$$
 (1.37)

The integer m can be interpreted as the number of wavelengths contained in the roundtrip distance and is often referred to as the azimuthal mode number. For most waveguiding structures and WGM resonators, analytical expressions for the effective refractive index are not known<sup>4</sup>. In particular, the radius of curvature of the latter structures modifies not only the mode profile, but also the dispersion [86]. The evaluation of the function  $\beta(\omega)$  is thus done numerically by solving the Helmholtz equation via finite element modeling (FEM). Note that the dispersion leads to a non-uniform spacing of the resonance spectrum. A Taylor series of the resonance frequencies around a mode of interest  $m_0$  labeled  $\omega_0$  can be written as:

$$\omega_{\mu} = \omega_0 + D_1 \mu + \frac{D_2}{2!} \mu^2 + \frac{D_3}{3!} \mu^3 + \dots \quad \text{where} \quad D_i = \frac{\partial^i \omega_{\mu}}{\partial \mu^i} \bigg|_{\mu=0}$$
 (1.38)

where  $\mu = m - m_0 \in \mathbb{Z}$  is a relative mode number counted with respect to  $\omega_0$ . The physical interpretation of the  $D_i$  coefficients and their relation to  $\beta$  and the refractive index can be obtained by deriving 1.37 with respect to  $\mu$ :

$$D_1 = \Delta \omega_{\text{FSR}} = \frac{\omega_{+1} - \omega_{-1}}{2} = \frac{2\pi}{\beta_1 L_R} = \frac{2\pi c}{n_g L_R} = \frac{2\pi}{T_R}$$
(1.39)

The parameter  $D_1$  thus describes the local cavity FSR around the frequency  $\omega_0$  and depends on the group index<sup>5</sup>  $n_g$ . The group velocity dispersion induces a quadratic walkoff of the resonances from the uniform FSR-spacing and is described by  $D_2$  according to

$$D_2 = \omega_{+1} - 2\omega_0 + \omega_{-1} = -\frac{\beta_2 D_1^2}{\beta_1}. (1.40)$$

equivalently, this factor describes by how much the local FSR is increased when going from mode  $\mu$  to  $\mu+1$ . Note that anomalous GVD corresponds to  $D_2>0$  (i.e. an increasing FSR with

<sup>&</sup>lt;sup>4</sup>An analytical approximate solution was derived in the case of a spherical resonator [85]

<sup>&</sup>lt;sup>5</sup>The group index is defined as  $n_g = c\beta_1 = n_0 + \omega_0 \left. \frac{\partial n}{\partial \omega} \right|_{\omega}$ 

frequency).

The resonance walk-off from an equidistant resonance grid spaced by  $D_1$  is an important quantity in the context of Kerr comb generation and is described using the *integrated dispersion* which, based on the above development, is given by

$$D_{\rm int}(\mu) = \omega_{\mu} - (\omega_0 + \mu D_1) = \frac{D_2}{2} \mu^2 + \frac{D_3}{6} \mu^3 + \dots$$
 (1.41)

and accounts for all the higher order dispersion.

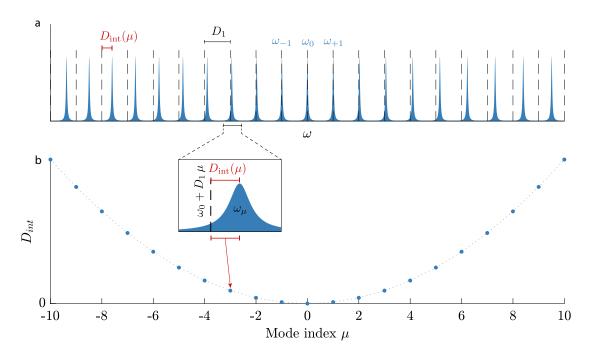


**Figure 1.12 – Schematic illustration of resonator dispersion.** (a) The resonances (in blue) are not aligned on the equidistant frequency grid spaced by  $D_1$  aligned with the central resonance  $\omega_0$  (dashed lines). An increasing mismatch is accumulated with increasing distance to the central line due to the quadratic dispersion. (b) Representation of the dispersion induced frequency mismatch as  $D_{\rm int}$ . The relation can be approximated as parabola around the central mode due to the GVD. The case represented here corresponds to anomalous GVD, which bends  $D_{\rm int}$  upward.

# Spatial modes of WGM resonator

Just like waveguides, resonators can support modes with different transverse intensity profiles, depending on their dimensions and design. The latter is especially true for WGM resonators that typically feature rather large dimensions. For a given geometry, the modes can be identified via numerical solving of the Helmholtz equation via FEM simulations, as shown in fig. 1.13. Such analysis also enables the determination of the effective index and effective mode volume of each of the modes.

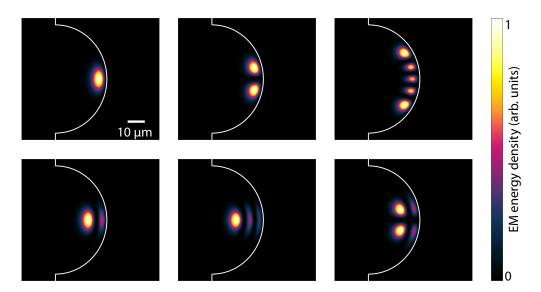


**Figure 1.13 – Spatial mode profiles** of various transverse modes in the cross-section of a typical crystalline WGM protrusion, as depicted in fig. 1.7. The modes are typically classified in families depending on their polarization and on the number of maxima in the radial and polar directions. The simulations were performed using the software Comsol.

# **Modal crossing**

The unequal dispersion experienced by two mode families typically implies that their respective FSR is different. Considering only two mode families (labeled *A*, *B*), the FSR mismatch implies that their resonances will crossover at a certain frequency. In a perfect resonator, eigenmodes with different azimuthal mode number are orthogonal, such that two resonances can coincide and remain unaffected. However, any defect (e.g. imperfect rotation symmetry or scattering points) in the microresonator geometry can induce coupling of the two mode families.

Modal coupling causes two branches of hybrid modes to form as shown in fig. 1.14. The frequencies of the hybrid modes in the upper (+) and lower (-) branches are given by [87]

$$\omega_{\mu}^{(\pm)} = \frac{\omega_{\mu}^{A} + \omega_{\mu}^{B}}{2} \pm \sqrt{G^{2} + \left(\frac{\omega_{\mu}^{A} - \omega_{\mu}^{B}}{2}\right)^{2}}$$
(1.42)

where  $\omega_{\mu}^{A,B}$  are the resonances of unperturbed mode families and G is the coupling rate induced from the perturbation. The typical profile near the point where the  $(\pm)$  branches meet is referred to as level repulsion or *avoided mode crossing* (AMX). At the crossover point, the solutions are the symmetric and antisymmetric combinations of the two families. Further from this point the solutions acquire the spatial profile of the family whose frequency is the closest. Note that the deviation of these two branches near the crossover point leads to a strong modification of the local dispersion. The (+) branch experiences a stronger anomalous GVD, while the (-) branch bends toward normal GVD.

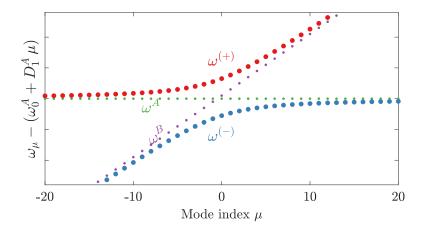


**Figure 1.14 – Avoided mode crossing.** Illustration of the impact of modal crossing on the mode families resonances and on dispersion. The resonances are plotted in the frame of the mode family *A*. Dispersion is neglected here.

#### Thermal effect

When a high power pump laser is coupled and tuned into a resonance, a small fraction of the intracavity energy is absorbed and heats up the cavity. This temperature increase changes the roundtrip length and the refractive index, described respectively by the coefficient of thermal expansion  $\alpha_L = \frac{1}{L} \frac{\partial L}{\partial \theta}$  and the thermo-optic coefficient  $\alpha_n = \frac{1}{n} \frac{\partial n}{\partial \theta}$ , where  $\theta$  is the temperature. Assuming  $\alpha_L > 0$  and  $\alpha_n > 0$  means that these effects lead to a decreasing resonance frequency (and resonator FSR) as the intracavity power  $P_{\text{cav}}$  increases:

$$\widetilde{\omega}_0 = \omega_0 \left( 1 - (\alpha_L + \alpha_n) \, \Delta \theta(P_{\text{cav}}) \right) \tag{1.43}$$

where  $\widetilde{\omega}_0$  is the thermally-shifted resonance frequency,  $\omega_0$  is the "cold" resonance and  $\Delta\theta(P_{\text{cav}})$  the associated temperature increase of the mode volume.

A thermal feedback is thereby established [88], which enables the passive locking of a microresonator resonance to the pump laser. For an adiabatic tuning of the laser into the resonance from higher to lower frequency (blue to red detuned), a self-locking effect occurs: power is coupled into the resonator, and the resonance frequency shifts and follows the laser frequency. This frequency drag distorts the Lorentzian profile of the cold cavity mode, which becomes triangular ("thermal triangle") as shown in fig. 1.15. Tuning into resonance from the red detuned side (i.e. increasing the pump laser frequency) is however unstable as a positive feedback loop is established. Besides the thermal effects, an additional resonance shift arises from the Kerrnonlinearity of the system (SPM), as will be described in section 1.2.3. Finally, for situations in which the coefficients  $\alpha_n$  and  $\alpha_L$  have opposite signs, the thermal effects are typically unstable and lead to oscillation in the described mechanism [89].

Compared to the femtosecond timescales of the Kerr nonlinear processes, thermal effects have vastly slower response times, as they rely on changing the temperature across the mode area and volume via heat diffusion. In theoretical descriptions, thermal resonance shifts can

therefore usually be ignored. However, these effects are important in experiments when trying to generate and stabilize microcombs.

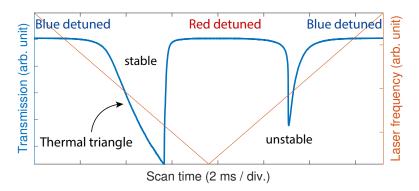


**Figure 1.15** – Thermal bistability observed in a MgF<sub>2</sub> resonator, when scanning a laser from the blue to red detuned side and reversely.

# 1.2.3 Theory of microresonator-based optical frequency combs

The general framework to describe microresonator-based optical frequency combs formation is essentially based on (Kerr)-nonlinear optics in a cavity. This section builds upon the concepts already discussed regarding nonlinearities in waveguides, and extends this discussion to the specific case of cavities.

# Nonlinear resonator modeling and dynamics of Kerr comb formation

Various models exist to describe Kerr frequency comb generation [90]. They mainly differ in the level of approximations made to describe the field in the resonant cavity and on the time of frequency domain perspective they adopt. Over the years, they have also been enriched to include a number of effects such as high order dispersion, Raman scattering and multi-photon absorption. The three most relevant models are based on the Ikeda map, a set of coupled mode equations (CME), and the Lugiato-Lefever equation (LLE).

**Ikeda Map** This model describes the field evolution in the cavity roundtrip by roundtrip, similar to the approach used in eq. (1.24). The roundtrip propagation is described via the NLSE and the final boundary conditions and coupling are applied at the transition from roundtrip n to roundtrip n+1 [91]

$$\mathcal{E}_{n+1}(0,\tau) = \sqrt{\theta_{\rm ex}} \mathcal{E}_{\rm in} + \sqrt{1 - \theta_{\rm ex}} \,\mathrm{e}^{i\varphi_0} \,\mathcal{E}_n(L_R,\tau) \tag{1.44}$$

$$\frac{\partial}{\partial z}\mathcal{E}_{n}(z,\tau) = \left(-\frac{\alpha_{\text{loss}}}{2} - i\frac{\beta_{2}}{2}\frac{\partial^{2}}{\partial \tau^{2}} + i\gamma \left|\mathcal{E}_{n}(z,\tau)\right|^{2}\right)\mathcal{E}_{n}(z,\tau)$$
(1.45)

where the phase factor is  $\varphi_0 = \beta(\omega_0 - \delta\omega) L_R - 2\pi \mu$ ,  $\mu \in \mathbb{Z}$  and we introduced the detuning  $\delta\omega = \omega_p - \omega_0$ . Note here that the NLSE was modified to account for the losses. This lumped model makes the least amount of assumptions on the field propagation and can include complex and discrete intracavity elements if necessary. However, the method requires a

simulation step that is shorter than the roundtrip time, and is thus computationally intensive. This problem is particularly acute for high finesse cavities, as the photon lifetime, which dictates dynamical timescale is much longer than the roundtrip time.

**Lugiato-Lefever mean field model** The mean-field model [92] was introduced to solve the aforementioned problem. It assumes that the field is slowly varying over the duration of a roundtrip, such that the spatial dependence in z can be dropped and the integration becomes trivial. This approximation is valid in the case of a high finesse cavity, small detuning (relative to the FSR), and dispersion and nonlinear lengths much longer than the cavity length. A new 'slow' time quantity t can be introduced, such that  $\mathcal{E}(t=nT_R,\tau)=\mathcal{E}_n(z=L_R,\tau)$ , and assuming that this variable is continuous, we can effectively write  $T_R\frac{\partial}{\partial t}=L_R\frac{\partial}{\partial z}$ . The 'short' time  $\tau$  can also be normalized by the roundtrip time to  $\phi=\frac{2\pi\tau}{T_R}=D_1\tau$ , which represents the angular location of the envelope-function around the resonator (in a frame rotating at the group velocity). Normalizing the field according to eq. (1.30), such that  $|A|^2$  is the intracavity photon number yields the single governing equation

$$\frac{\partial A}{\partial t} = \left( -\left( \frac{\kappa}{2} + i\delta\omega \right) + i\frac{D_2}{2} \frac{\partial^2}{\partial \phi^2} + ig_0 |A|^2 \right) A + \sqrt{\kappa_{\text{ex}}} \, s_{\text{in}}$$
 (1.46)

where the per photon Kerr shift (in rad/s) was introduced

$$g_0 = \frac{\gamma L_R}{T_R} \frac{\hbar \omega_0}{T_R} = \frac{\hbar \omega_0^2 c \, n_2}{n_g^2 V_{\text{eff}}} \tag{1.47}$$

Note that the detuning  $\delta \omega = \omega_0 - \omega_p$  is taken to be positive for a red-detuned pump laser, i.e.,  $\omega_p < \omega_0$ . The transmitted field after the cavity can be calculated using eq. (1.34).

Equation (1.46) is better known as the *Lugiato-Lefever equation* (LLE) [93], which was originally derived to describe the transverse spatial fields patterns in two-dimensional cavities (diffraction balanced by nonlinear self-focusing). This one-dimensional version where the role of diffraction is replaced by chromatic dispersion can be understood as a damped-driven version of the nonlinear Schrödinger equation [94]. Note that the higher order dispersion can be accounted for in the LLE, replacing  $iD_2\frac{\partial^2}{\partial\phi^2} \rightarrow i\sum_{k\geq 2}\left(i\frac{\partial}{\partial\phi}\right)$ . In the time domain, higher order dispersion thus takes a rather complex expression. Finally, by introducing the following normalization factors (assuming the dispersion is anomalous)

$$T = \frac{\kappa}{2}t \qquad \Theta = \sqrt{\frac{\kappa}{2D_2}}\phi \qquad d_l = \frac{2}{\kappa} \frac{D_l}{l!} \left(\frac{\kappa}{2D_2}\right)^{l/2}, \ l \ge 2$$
 (1.48)

$$\zeta_0 = \frac{2\delta\omega}{\kappa}$$
 $\psi = \sqrt{\frac{2g_0}{\kappa}} A$ 
 $f = \sqrt{\frac{8\eta g_0}{\kappa^2}} s_{\text{in}} = \sqrt{\frac{P_{\text{in}}}{P_{\text{thres}}}}$ 
(1.49)

the LLE can be written in a dimensionless form

$$\frac{\partial \psi}{\partial T} = -(1 + i\zeta_0) \psi + \frac{i}{2} \frac{\partial^2 \psi}{\partial \Theta^2} + i|\psi|^2 \psi + f \tag{1.50}$$

which is useful for identifying the fundamental parameters of this equation. Namely, if the resonator dispersion, linewidth and nonlinearity are given, then only two parameter define the operating conditions: the pump power f and detuning  $\zeta_0$ .

**Coupled mode equations** Transforming the LLE to the frequency domain also brings many insights into the dynamics of nonlinear interactions in cavities. The angular coordinate  $\phi$  and the relative mode number  $\mu$  are linked via the decomposition of the cavity field in a Fourier series (in the frame rotating at  $D_1$ )

$$A(\phi, t) = \sum_{\mu \in \mathbb{Z}} \tilde{A}_{\mu}(t) e^{-i\mu\phi} e^{i[\omega_{\mu} - (\omega_{p} + \mu D_{1}\mu)]t}$$

$$(1.51)$$

which we will also denote  $\tilde{A}_{\mu} = \mathcal{F}_{\mathcal{T}}[A]_{\mu}$  in the following equations. Applying this transform to the LLE and projecting onto the mode  $\mu$  yields an infinite system of equations, which details the dynamics of each mode

$$\frac{\partial \tilde{A}_{\mu}}{\partial t} = -\left(\frac{\kappa}{2} + i\delta\omega_{\mu}\right)\tilde{A}_{\mu} + ig_{0}\sum_{\mu' \leq \mu''}\left(2 - \delta_{\mu',\mu''}\right)\tilde{A}_{\mu'}\tilde{A}_{\mu''}\tilde{A}_{\mu''+\mu''-\mu}^{*} + \delta_{\mu,0}\sqrt{\kappa_{\text{ex}}}s_{\text{in}}$$
(1.52)

where  $\delta\omega_{\mu}=(\omega_{\mu}-\omega_{p}-\mu D_{1})=\delta\omega+D_{\rm int}(\mu)$  and  $\delta_{\mu,0}$  is the Kronecker delta. In the spectral domain, the nonlinear term thus assumes a more complex form, which accounts for the nonlinear coupling between the cavity modes via self / cross phase modulation and four wave mixing. This model of nonlinear *coupled modes equations* (CME) was the first developed to describe Kerr frequency comb formation in microresonators [95]. Its main drawback is the inefficient computation of the nonlinear coupling term, which scales with the cube of the number of modes considered. On the other hand, a complex dispersion profile can be easily computed.

**Simulating the dynamics of Kerr combs** Given the relative complexity of the nonlinear partial differential equation, analytical solutions are in general not known. A numerical simulation is thus generally needed to simulate the evolution of the cavity field described by the LLE, which can be done efficiently using the split-step Fourier method, often used in nonlinear fiber optics [77, 96]. We illustrate here its basic principle. It consists of separating the right hand side of the LLE between a linear and nonlinear operator:

$$\frac{\partial \psi}{\partial T} = (\hat{D} + \hat{N}) \psi(T, \Theta), \quad \text{where} \begin{cases} \hat{D} = -(1 + i\zeta_0) + i \sum_{k \ge 2} d_k \left( i \frac{\partial}{\partial \Theta} \right)^k \\ \hat{N} = i |\psi|^2 \psi + \frac{f}{\psi} \end{cases}$$
(1.53)

The principle of the split step Fourier method is to simulate the propagation from instant t to t+h, by splitting the propagation in two independent steps, one of length h where only the nonlinear operator  $\hat{N}$  is applied while  $\hat{D}=0$  and a second step h of pure linear propagation.

In that case, the integration of the equation is trivial and we get

$$\psi(T+h,\Theta) \approx \exp\left(h\hat{D}\right) \underbrace{\exp\left(h\hat{N}\right) \psi(T,\Theta)}_{=\Psi(T,\Theta)} \tag{1.54}$$

As highlighted in the previous paragraphs, the main difficulty in the mean field model in the time domain is to efficiently compute the dispersion term. Instead, it is advantageous to evaluate it in the frequency domain

$$\exp(h\hat{D})\Psi(T,\Theta) = \mathcal{F}_{\mathcal{T}}^{-1} \left\{ \exp(h\hat{D}_{\mu})\mathcal{F}_{\mathcal{T}}[\Psi(T,\Theta)]_{\mu} \right\}, \tag{1.55}$$

where 
$$\hat{D}_{\mu} = -(1 + i\zeta_0) + i\sum_{k \ge 2} d_k \mu^k$$
 (1.56)

and take advantage of the efficient computation of the FFT algorithm. The simulation code used in the present work was mainly developed by Hairun Guo and Miles Anderson.

## Continuous wave solution, Kerr tilt and bistability

Now that we have introduced the main concepts to describe the effect of the Kerr nonlinearity in cavities, we can start to investigate its effect in the simplest case of a continuous-wave in the cavity, or equivalently, the case of a single cavity mode subjected to SPM. The 'flat' homogeneous solution condition implies  $\frac{\partial \psi_0}{\partial \Theta} = 0$  and, assuming a steady state solution  $(\frac{\partial \psi_0}{\partial T} = 0)$ , the LLE simplifies to

$$-(1+i\zeta_0)\psi_0+i|\psi_0|^2\psi_0+f=0 \quad \Leftrightarrow \quad \psi_0=\frac{f}{1+i\left(\zeta_0-|\psi_0|^2\right)} \tag{1.57}$$

and in energy we can recognize a typical Lorentzian profile,

$$\left|\frac{\psi_0}{f}\right|^2 = \frac{1}{1 + (\zeta_0 - |\psi_0|^2)^2}$$
 
$$\tan(\varphi) = |\psi_0|^2 - \zeta_0$$
 (1.58)

but in which the detuning effectively depends on the cavity power  $\zeta_{\rm eff} = \zeta_0 + |\psi_0|^2$ , which creates a 'tilt' of the resonance along the line  $\zeta_0 = |\psi_0|^2$ , as shown in fig. 1.16. The effective zero detuning is thus reached for  $\zeta_0 = f^2$ . Furthermore, the response becomes multivalued over a detuning range that increases with the pump power  $\zeta_0 \in \left[\zeta_1, \zeta_1\right]$ , where  $\zeta_1 \approx 3(f^2/4)^{1/3}$  and  $\zeta_1 \approx f^2$  [92, 97, 98]. In fact the cavity field can only be bi-stable as the intermediate solution between the upper and lower branches is always unstable and switched either to the upper or lower branch. Importantly, in the bistable region, the lower branch is effectively red-detuned, while the upper branch remains effectively blue-detuned up to the effective zero detuning point. The minimum pump power required to achieved bistability is  $f_{\rm bistab}^2 = 8\sqrt{3}/9 \approx 1.54$ , and the corresponding critical bistable detuning  $\zeta_{\rm bistab} = \sqrt{3}$ . This bistable region is fundamental in this work as it is the region where solitons can form in the cavity as shown in section 1.2.4.

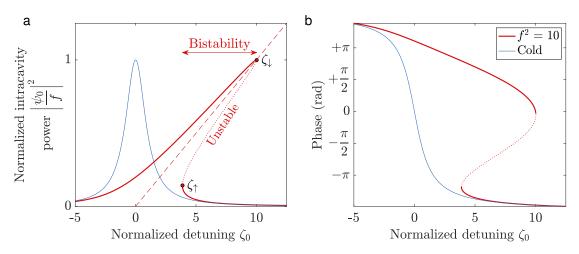


**Figure 1.16 – Resonance Kerr tilt.** (a) Resonance tilt of the CW solution for a normalized pump power  $f^2=10$ , due to the Kerr effect (self-phase modulation). The dashed line shows the relation  $\zeta_0=|\psi_0|^2$  along which the Lorentian is tilted. In a region of red-detuning  $\zeta_0\in[\zeta_\uparrow,f^2]$  a bistability appears. At the point  $\zeta_\uparrow$ , the lower branch loses stability and cavity field up-switches to the upper branch. Conversely, at  $\zeta_\downarrow\approx f^2$  (effective zero detuning), the cavity field drops on the lower branch. (b) Associated intracavity phase evolution.

# Modulation instability

The homogeneous CW region exhibits *modulation instability* (MI), when the intracavity energy is beyond the threshold  $|\psi_0|^2 > 1$  [92, 97, 98], which is fulfilled for a detuning

$$\zeta_0 > \zeta_0^{\text{(MI)}} = 1 - \sqrt{f^2 - 1}$$
 (1.59)

The minimum input pump power required to reach MI is thus

$$f_{\text{thres}}^2 = 1 \quad \Leftrightarrow \quad P_{\text{thres}} = \frac{\kappa^2}{8g_0\eta} = \frac{n_g^2}{8\omega_0c} \frac{V_{\text{eff}}}{n_2} \frac{\kappa^2}{\eta}$$
 (1.60)

The threshold power notably depends on the cavity properties such as the effective mode volume  $V_{\text{eff}}$  and nonlinear refractive index  $n_2$ . Note also, the quadratic influence of the cavity linewidth on the threshold power, meaning that a small resonator with highly nonlinear material and high quality factor greatly reduces the threshold of nonlinear parametric effects.

Modulation instability means that the CW solution in the cavity becomes unstable and any small power fluctuation will be amplified at an exponential rate. In the frequency domain, this can be understood as the formation and growth of sidebands around the pump carrier due to degenerate four wave mixing. These sidebands appear at the frequency (or equivalently mode number) where the nonlinear parametric gain, which forms two symmetric lobes around the central pump, surpasses the cavity losses and is dictated by the phase matching condition set

via dispersion and pump power, according to [99]

$$\mu_{\text{MI}} = \sqrt{\frac{\kappa}{D_2}} \left( 1 + \sqrt{f^2 - 1} \right)^{1/2} = \sqrt{\frac{\kappa}{D_2} \left( 1 + \sqrt{\frac{P_{\text{in}}}{P_{\text{thres}}} - 1} \right)}$$
(1.61)

which at threshold gives  $\mu_{\rm thres} = \sqrt{\kappa/D_2}$ . The first pair of sidebands corresponds to the formation of a sinusoidal modulation in the cavity and the mode number  $\mu_{\rm MI}$  defines the number of oscillations along the roundtrip. However, the growth of these first sidebands further seeds an additional set of *primary sidebands* are equally spaced in frequency, corresponding to an initial frequency comb spectrum with a spacing  $\mu_{\rm MI}$  that is typically a multiple of the resonator FSR. In the time domain, this corresponds to the formation of a periodic pattern that fills the cavity with  $\mu_{\rm MI}$  repetitions. For low pump powers and detunings, these patterns are stable i.e. invariant along the slow time axis, and correspond to *Turing patterns* (or Turing rolls) and is a state of stable MI, also known as hyperparametric oscillations (as depicted in fig. 1.19).

Increasing the intracavity power leads to destabilization of the Turing pattern. First, this happens via period doubling of the pattern in the cavity, which oscillates along the slow time axis. In the frequency domain, this corresponds to the appearance of secondary sidebands and subcombs around each primary sideband [99]. As the power is increased further, the intracavity pattern become chaotic in both time and space. The comb spectrum becomes more dense as the subcombs merge together, with a very low coherence due to the fluctuations of the waveform. Such comb states are termed unstable or chaotic MI (see fig. 1.19).

Historically, the first Kerr microcombs [8, 99–102] were generated from such MI combs. For most applications however, MI combs are typically not suitable as they feature either few and widely spaced lines, or chaotic dynamics with low coherence, high amplitude and phase noise [76, 99, 103], which posed serious doubts in the early 2010s regarding the potential of such frequency combs [76, 99, 104, 105].

# 1.2.4 Dissipative Kerr solitons

The dissipative Kerr soliton (DKS) constitutes another possible state of the nonlinear cavity field, and is the central focus of the present study. DKSs are localized pulses of light that circulate in the driven cavity and maintain their shape thanks to a double balance.

On the one hand, chromatic dispersion is balanced by nonlinearity. As such, they are also termed *temporal* cavity solitons [9, 106] in contrast to their *spatial* two-dimensional analog subjected to diffraction [107]. On the other hand, they are of dissipative nature, as they also result from the balance of the cavity losses with the parametric gain offered by the external continuous-wave pump. The DKS properties are thus uniquely defined to realize this double balancing act [108]. Furthermore, they constitute robust attractors of the dynamical system in the bistable region and can be viewed as 'modes' of the nonlinear system [109]. An excitation of the intracavity field beyond a certain threshold converges to a soliton solution [110].

Furthermore, DKSs are discrete localized patterns. A single and stable pulse can exist in the cavity, and as such, the resulting microcomb has well defined narrow lines and a repetition rate corresponding to the cavity FSR. First discovered in fiber loop cavities [106] and in microresonators shortly after [9], this soliton 'mode-locking' of Kerr combs offered a second breath to the field. Interestingly, the fiber and microresonator communities have emerged independently and each had established its own formalism (LLE in fiber cavities [92] and CME in microresonators [95]). The equivalence between the two was demonstrated [90, 96] and the formalism is now unified.

The analytical soliton solution to the LLE is not known. However, an approximate ansatz in the form of the fundamental soliton solution of the NLSE (no drive nor damping), having a secant hyperbolic profile plus a continuous wave background provides a good approximation, especially for the large detuning limit [94]. It is stationary and thus does not depends on the slow time coordinate. It is given by:

$$\psi_{\text{sol}}(\Theta) \approx \psi_0 + B \operatorname{sech}(B\Theta) e^{i\varphi_s}$$
 (1.62)

where  $\psi_0$  is the lower branch homogeneous solution defined in eq. (1.57). The pulse amplitude and duration are linked via the parameter B, while  $\varphi_s$  is the phase shift of the soliton with respect to the pump drive. Inserting this ansatz into the LLE and performing a perturbative Lagrangian treatment [111] yields

$$B = \sqrt{2\zeta_0} \tag{1.63}$$

$$\cos\left(\varphi_{s}\right) = \frac{\sqrt{8\zeta_{0}}}{\pi f} \tag{1.64}$$

The condition  $|\cos(\varphi_s)| < 1$  imposes a limit on the maximum detuning up to which the soliton can be sustained as

$$\zeta_{\text{max}} = \frac{\pi^2 f^2}{8}.\tag{1.65}$$

On the other hand, the lowest detuning for soliton formation is the start of the bistable region  $\zeta_{\uparrow}$ . The detuning interval  $[\zeta_{\uparrow}, \zeta_{max}]$  is often referred to as 'soliton existence range' for a given constant input power.

In physical units, the temporal profile of the soliton follows

$$A(t,\tau) = \sqrt{\frac{2\delta\omega}{g_0}} \operatorname{sech}\left(\frac{\tau}{\Delta\tau_s}\right) \tag{1.66}$$

$$\Delta \tau_s = \frac{1}{D_1} \sqrt{\frac{D_2}{2\delta\omega}} = \sqrt{\frac{c|\beta_2|}{2n_g\delta\omega}} \tag{1.67}$$

It is interesting to note that the DKS duration is determined by only three frequencies, namely the cavity FSR  $D_1$ , the GVD parameter  $D_2$  and the detuning  $\delta \omega$ . Importantly, minimizing the

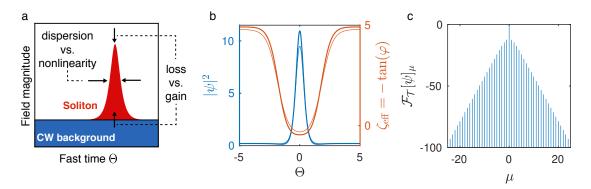


**Figure 1.17 – Single dissipative Kerr soliton.** (a) Illustration of the double balance that sets the soliton properties. On the one hand, the dispersion is compensated by the nonlinearity such that the soliton does not spread. On the other the cavity losses are lifted by the parametric gain brought by the pump (the soliton 'feeds' from the CW background locally beneath it). (b) Example of soliton solution simulated in the case  $f^2 = 5$ ,  $\zeta_0 = 5$  showing the normalized intensity in blue and the estimated effective detuning in red. The thick curves correspond to the simulation result, while the thin lines correspond to the analytical ansatz eq. (1.62). The instantaneous detuning shows that the soliton is still blue detuned, while the background is red-detuned. (c) Spectrum corresponding to (b).

absolute GVD  $|\beta_2|$  and maximizing the detuning leads to shorter and more intense pulses (neglecting the influence of the background). For a given input pump power, the shortest achievable pulse duration is reached for  $\zeta_0 = \zeta_{max}$ 

$$\Delta \tau_s^{\min} = \frac{2}{\pi D_1 f} \sqrt{\frac{2D_2}{\kappa}} = \frac{2}{\sqrt{\pi}} \sqrt{\frac{|\beta_2|}{\gamma \mathcal{F} P_{\text{in}}}}$$
(1.68)

The soliton spectrum follows

$$\tilde{\psi}_{\mu} = \sqrt{\frac{D_2}{2\kappa}} \operatorname{sech}\left(\frac{D_1 \mu}{\Delta \omega_s}\right) \tag{1.69}$$

$$\Delta\omega_s = \frac{2}{\pi} \frac{1}{\Delta\tau_s} \tag{1.70}$$

The power per mode (ignoring the background) follows a squared hyperbolic secant shape:

$$P(\mu) = \frac{\hbar\omega_0}{T_R} \frac{D_2}{4g_0} \operatorname{sech}^2\left(\frac{D_1\mu}{\Delta\omega_s}\right) = \frac{\left|\beta_2\right|D_1^2}{\gamma} \operatorname{sech}^2\left(\frac{D_1\mu}{\Delta\omega_s}\right)$$
(1.71)

It is interesting to note that the maximum power per line is fixed by the cavity properties and is independent of the driving strength and detuning. The increase of the soliton peak power with detuning is solely due to the increase of the total number of comb lines. Note that the values of  $\Delta\omega_s$  and  $\Delta t_s$  need to be multiplied by  $2 \operatorname{acosh}(\sqrt{2}) = 1.763$  to yield the FWHM of the sech<sup>2</sup> power spectral envelope and pulse intensity. For time and frequency units, the FWHM time bandwidth product of the sech<sup>2</sup> thus corresponds to  $\Delta \tau_{s^2} \Delta v_{s^2} = \left[\frac{2}{\pi} \operatorname{acosh}(\sqrt{2})\right]^2 \approx 0.3148$ .

Chapter 1. Fundamental concepts of optical microresonators and soliton-based Kerr frequency combs

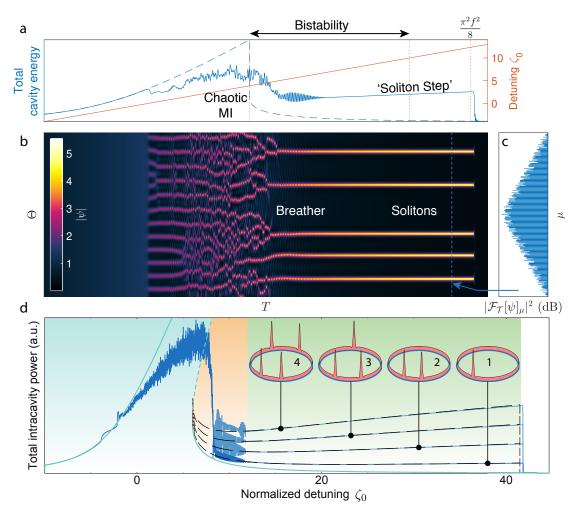


Figure 1.18 - Spontaneous DKS generation via laser tuning (a) Evolution of the total intracavity energy (blue) upon sweeping the detuning from blue-detuned pump to red-detuned (red curve) for  $f^2 = 10$ . The initial CW solution becomes unstable and leads to MI. Upon entering into the bistable region, the chaotic modulation converges into a series of solitons, to form a characteristic 'soliton step'. Of note, it can be seen that solitons persist beyond the CW bistability. The dashed line shows the evolution of the homogeneous background (on the lower branch). (b) Corresponding spatio-temporal evolution, showing the extended pattern formation (Turing patterns, chaotic MI) and their convergence to solitons in the bistable region. 5 solitons are obtained in this example, but the final number of solitons is stochastic as it depends on the evolution in the chaotic region. (c) The spectrum corresponding to the final multi-soliton state. The presence of multiple solitons is revealed by the structured interference pattern in the spectrum. (d) Examples of multiple realization of laser tuning for soliton generation, for  $f^2 = 35$ . The number of soliton in the final state varies from one to four. An example of resulting intracavity waveform if shown for illustration. The black dashed lines correspond to the theoretical expression of the total soliton power os eq. (1.74). The shaded areas are mark the regions of MI (blue), breathing solitons (orange) and stable DKS (green).

The soliton solution is sub-critical [98], meaning that it does not appear spontaneously from small perturbations of the red-detuned background, but needs an excitation mechanism. In fiber cavities, addressing pulses as well as phase or amplitude pulses have been employed [106, 110, 112] to trigger the formation of solitons. In microresonators, one of the simplest and most employed techniques is called 'soft excitation' via laser tuning [9]. Here, the pump laser is scanned from blue- to red-detuned, thereby exciting MI patterns (eventually chaotic). Upon entering the bistable region, only the most intense MI pulses will then converge to a soliton state, as shown in fig. 1.18. This spontaneous soliton formation was experimentally imaged in a fiber cavity [113] and in a microresonator [114]. This formation method is advantageous as requires no complex elements such as a modulator or a pulsed laser. However, the resulting state usually contains multiple solitons with a stochastic number and separation, due to the previous chaotic modulation. A way to gradually erase solitons and preserve a single one is presented in section 3.3. Finally, at low detuning and high pump power, solitons naturally destabilize and start to oscillate. This instability is called *breathing* and will be investigated in section 3.2.

The fact that solitons exist in the bistable cavity region can be qualitatively understood as follows: although the pump laser is off-resonance and detuned by  $\delta\omega$ , the Kerr nonlinearity locally shifts the resonance, such that the pump is locally efficiently coupled in and 'feeds' the soliton. In a microresonator, the intracavity field is enhanced when the light is on-resonance with the resonator mode. The nonlinear and detuned cavity thus enhances the on-resonance solitary waves, while damping any other waves that cannot achieve a sufficient Kerr shift, to the lower CW branch. In fact, the local detuning of the soliton can be inferred from the phase shift using the relation between phase and detuning in a cavity  $\zeta_{\rm eff} = -\tan{(\varphi_s)}$ . A soliton can also be viewed as corresponding to a single period of the upper branch Turing pattern that connects to the lower branch homogeneous solution via a so-called heteroclinic connection [115, 116]. In the absence of higher order dispersion or mode coupling [117], multiple solitons can thus coexist in the cavity without interacting, assuming that their separation is larger than the periodicity of the underlying MI pattern (or equivalently larger than one soliton width), as predicted using eq. (1.61). The maximum number of solitons can therefore be roughly estimated via  $N_{\rm max} \approx \sqrt{\kappa/D_2}$ .

The coexistence of N solitons in the cavity at various positions  $\phi_i$  can be simply expressed as

$$\psi^{(N)}(t,\phi) = \psi_0 + \sqrt{2\zeta_0} e^{i\varphi_s} \sum_{k=1}^N \operatorname{sech}\left(\sqrt{\frac{\kappa\zeta_0}{D_2}} (\phi - \phi_k)\right)$$
(1.72)

thus, the corresponding power spectrum follows

$$S^{(N)}(\mu) = S^{(1)}(\mu) \left[ N + 2 \sum_{j \neq l} \cos((\phi_j - \phi_l) \mu) \right]. \tag{1.73}$$

where  $S(\mu) = \left| \mathcal{F}_{\mathcal{T}} [\psi]_{\mu} \right|^2$  and  $S^{(1)}(\mu)$  is the power spectral envelope of a single soliton. The spectrum of a multi-soliton state thus corresponds to the sech<sup>2</sup> spectral envelope of a single

soliton, modulated by an interference pattern that depends on the solitons relative distances.

The total normalized energy in the multi-soliton state can be retrieved by integrating the waveform, which can be approximated by [9]

$$\overline{\left|\psi^{(N)}\right|^{2}} \approx \frac{f^{2}}{\zeta_{0}^{2}} + N\frac{2}{\pi}\sqrt{\frac{D_{2}}{\kappa}\zeta_{0}}.$$
 (1.74)

This formula shows that multi-soliton states are degenerate in pump and detuning and explains the 'soliton staircase' as depicted in fig. 1.18d.

# Regimes of Kerr combs: attractor chart

The various states of the LLE introduced in this section can be summarized on an 'attractor map' that summarize which type of comb state can be achieved, depending on the pumping parameters  $(\zeta_0, f^2)$ . One such map is presented in fig. 1.19.

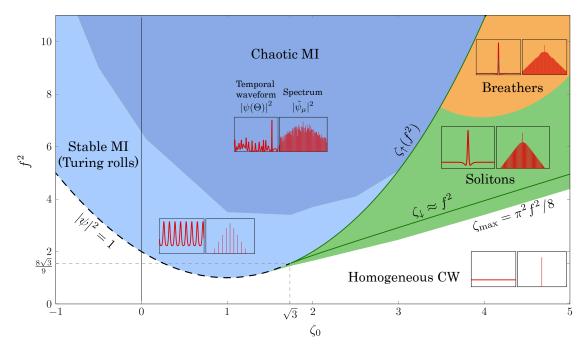


**Figure 1.19 – Attractor map of the LLE in the anomalous GVD case.** This stability diagram illustrates the various solutions of the Lugiato-Lefever equation as function of the driving power and detuning parameters  $(f^2,\zeta_0)$ . The lines present the few analytical boundaries for MI threshold (dashed black) as well as the region of bistability  $([\zeta_1,\zeta_1]$  in dark green). The shaded regions were estimated through simulations and are approximate. They delimit the existence pure CW solution (white), Turing patterns (light blue), chaotic MI (dark blue), stable solitons (green) and breathing solitons (orange). Further charting of the soliton instabilities is presented in fig. 3.1. Adapted from ref. [98].

# 1.2.5 Applications of microresonator based combs

The salient feature of microcombs is their natively much wider mode-spacing, compared to conventional mode-locked laser combs, which is simply related to the physical dimensions of the cavity. While mode-locked lasers with repetition rates up to  $\sim 10$  GHz have been achieved [118, 119], the cavity length needs to accommodate the gain medium and the saturable absorber. Kerr combs suffer no such limitations and repetition rates up to 1 THz have been demonstrated [70, 120].

Wide comb line spacing can prove essential in several applications [69, 121] including high-capacity telecommunications [122], line-by-line pulse shaping and optical waveform synthesis [35, 123, 124], astronomical spectrometer calibration [125, 126], and low phase noise microwave generation [127], where Kerr combs have been employed in proof-of-concept experiments. The small footprint and potential ease of integration for these combs [67, 68] also opens a number of prospects for miniature optical clocks [128–130], chip-scale dual-comb spectrometers [131], and coherent LIDAR [53, 132]. In these applications, the *single soliton* states, is of particular utility as it features a spectrally-smooth sech<sup>2</sup> envelope.

Finally, generating Kerr combs does not require the broad spectral gain required by mode-locked laser. This could allow for the generation of combs at new operating wavelengths not attainable so far. Because Kerr comb generation relies on low-optical-loss dielectric materials with anomalous GVD (which can be adjusted via the choice of microresonator material and geometry) and only necessitates a CW pump laser, they allow comb generation toward the visible range [133, 134] and in the mid-infrared [135–137]. The use of modal coupling, and complex resonator geometries can allow advanced dispersion engineering to reach new spectral coverage [138–140].

# 2 Experimental generation, probing and characterization of solitons

"Witness me!"

MAD MAX: FURY ROAD
GEORGE MILLER

The following chapter details the basic steps for the generation and control of dissipative solitons, allowing to test the theoretical scaling laws. The probing method also unveiled a peculiar resonance feature of the soliton that is also investigated in this chapter.

# 2.1 Experimental soliton generation

This first section briefly reviews the basic experimental steps for comb generation.

## 2.1.1 Resonator fabrication

Two types of microresonator platforms have been employed in this work and are described below.

# Magnesium fluoride whispering gallery mode resonators

Most of the work in this thesis was realized using whispering gallery mode resonators made from crystalline fluorides [141]. These resonators feature record-high quality-factors exceeding  $10^{11}$  [142, 143]. In this work crystalline magnesium fluoride MgF $_2$  microresonators are used [135, 144, 145]. This slightly birefringent material was selected as it exhibits anomalous material GVD in the telecom band. The weak confinement offered by the WGM potential and protrusion means that the geometric dispersion plays a relatively weak role and the resonator dispersion is overall dominated by the material. Furthermore, the thermal coefficients  $\alpha_L$  and  $\alpha_n$  are both positive in this material, which allows stable thermal locking. Resonators are manufactured from cylindrical blanks with millimeter-scale dimensions (typically UV windows).

The axially-symmetric protrusion required to support whispering gallery modes is defined using diamond turning followed by hand polishing on an air bearing spindle lathe, to achieve a smooth surface and very low scattering<sup>1</sup>. With this process, the original monocrystalline structure and composition is preserved, ensuring a low material loss. However, the mechanical fabrication and polishing only allows for the realization of relatively large protrusions with dimensions of several tens of microns, leading to a loose confinement of light (i.e. large modearea  $A_{\rm eff}$ ). Moreover, MgF<sub>2</sub> has a rather low nonlinear index  $n_2 = 0.9 \times 10^{-20}$  m<sup>2</sup>/W, leading overall to a low nonlinear coefficient  $\gamma \sim 10^{-4}$  W<sup>-1</sup>m<sup>-1</sup> for this type of resonator structures. Nonetheless, the ultra-high quality factors achieved in these resonators ( $Q > 10^9$ ) still allow for efficient frequency conversion with sub-mW threshold pump powers. The relatively large protrusions are also highly multimode and avoided modal crossings are common in crystalline microresonators. Table 2.1 details the properties of the resonator mainly used in this work.

| Parameter   | Value  |  |
|---|--|--|
| FSR $(D_1/2\pi)$  | 14.09 GHz  |  |
| GVD $(\beta_2)$   | $-7.2 \text{ fs}^2/\text{mm}$                    |  |
| $D_2/2\pi$  | 1.962 kHz  |  |
| $\kappa_0$  | 80 kHz   |  |
| $\eta$  | 0 - 0.92   |  |
| $n_0$   | 1.37(o), 1.38(e)                                 |  |
| $\alpha_n = \frac{1}{n} \frac{\mathrm{d}n}{\mathrm{d}\theta}$ | $0.09(o), 0.03(e) \times 10^{-6} \text{ K}^{-1}$ |  |

| Parameter   | Value   |  |  |
|---|---|--|--|
| $n_2$   | $0.9 \times 10^{-20} \text{ m}^2/\text{W}$        |  |  |
|   | $150  \mu m^2$                                    |  |  |
| $V_{ m eff}$  | $2.3 \times 10^{-12} \text{ m}^3$                 |  |  |
| γ   | $2.4 \times 10^{-4} \text{ m}^{-1} \text{W}^{-1}$ |  |  |
| $g_0/2\pi$  | $1.5 \times 10^{-5} \text{ Hz}$                   |  |  |
| $P_{\rm thres} \ (\eta = 0.5)$                                | $\sim 530~\mu W$                                  |  |  |
| $\alpha_L = \frac{1}{L} \frac{\mathrm{d}L}{\mathrm{d}\theta}$ | $\sim 11 \times 10^{-6} \text{ K}^{-1}$           |  |  |

**Table 2.1 – Properties of the MgF<sub>2</sub> resonator mainly used in this work.** The properties are selected at a wavelength of 1553 nm. o: ordinary axis; e: extraordinary axis.

## Silicon-nitride waveguide resonators

Silicon nitride based waveguides have recently become one of the most investigated integrated photonics platform for nonlinear optics [146]. They are fabricated using nanofabrication techniques in a CMOS-compatible fabrication process to define  $\mathrm{Si_3N_4}$  waveguides embedded into silica ( $\mathrm{SiO_2}$ ). Two fabrication methods were developed, either using a substractive [146] or a damascene approach [147]. The lithographic and etching control allows for precise and reproducible resonator designs and thereby geometric dispersion engineering [148]. The high index contrast provides a sub-wavelength confinement of light and thus a much larger nonlinear coefficient compared to crystals. Constant progress in the fabrication methods [149, 150] have led to large improvements of the quality factor, with an approach informed by characterization of scattering and absorption losses [151]. As part of this thesis, the work carried out with this platform is presented in appendices A.1 and A.2.

<sup>&</sup>lt;sup>1</sup>The fabrication of the microresoantors used in this work was carried out by the former lab member Tobias Herr, as well as in the group of Michael Gorodetsky by Grigory Lihachev and Nikolay Pavlov.

<sup>&</sup>lt;sup>2</sup>The integrated resonators used in this work were fabricated by Victor Brasch, Martin Pfeiffer and Junqiu Liu.

#### 2.1.2 Resonator characterization

## **Quality factor control**

After fabrication, the linewidth  $\kappa/2\pi$  of the resonances needs to be measured accurately to determine the optical quality factor of the resonators. They are characterized either via a comb-assisted broadband spectroscopy [152, 153] or, if the resonances are too narrow, by scanning a low noise laser across a single resonance, with phase-modulated sidebands for frequency calibration [154]. Low power must be used to avoid nonlinearities and thermal skewness of the resonance profile. In the case of crystalline resonators, if the quality factor is not satisfactory, additional polishing and cleaning can be performed.

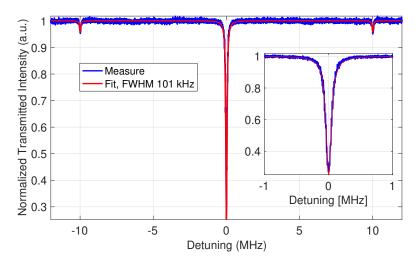


**Figure 2.1 – Quality factor measurement of a crystalline resonator.** The blue trace is the recorded transmission trace. The two smaller replicas of the resonance are separated from the main resonance by a distance corresponding to the modulation frequency (here: 10 MHz) and provide the frequency calibration to determine the FWHM of the resonance (here  $\kappa/2\pi = 101 \, \text{kHz}$ ). The red line shows a triple-Lorentzian fit used for frequency calibration.

## Resonator mode structure and dispersion measurement

The mode structure of a resonator refers to the ensemble of its mode families and their respective dispersion. It requires the precise knowledge of the resonance frequencies over a large bandwidth. Using the previously mentioned spectroscopy method, the relative frequency spacing between each resonance can be determined. Knowing the major radius of the resonator allows the estimation of an approximate FSR  $\Delta v_{FSR}^{\rm estim}$ , that can be refined to match the FSR of a particular mode family. The resonance walk-off from this estimated FSR spacing provides a way to estimate the integrated dispersion and FSR of each mode families as well as identify the presence of modal crossings.

#### Nonlinear threshold measurement

The measurement of the minimum pump power  $P_{\rm thres}$  for the generation of the first MI sidebands is useful to get an estimate of the nonlinear coefficient  $g_0$  according to eq. (1.60). This estimate can be verified with the analytical expression in eq. (1.47), using the nonlinearity of the material and an estimation of the mode volume based on FEM simulations.

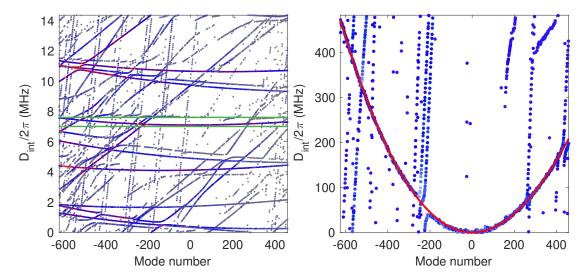


**Figure 2.2 – Dispersion measurement of a MgF**<sub>2</sub> **resonator.** (a) In this 2-dimensional representation of the mode structure, mode families are represented by their resonance frequencies forming lines. Different FSRs correspond to different (linear) slopes. The graph is obtained for  $\Delta v_{\rm FSR}^{\rm estim} = 14.352$  GHz. Dispersion causes the lines to bend. An upward curvature corresponds to anomalous dispersion. The different FSR of the mode families leads to avoided crossings. (b) Dispersion for the mode family within the green rectangle in (a). A quadratic fit provides an estimate of the GVD  $D_2/2\pi = 2.16$  kHz, which corresponds to  $\beta_2 \approx 7.6$  fs<sup>2</sup>/mm and is very close to the material GVD of MgF<sub>2</sub>.

## 2.1.3 Basic setup for soliton generation

# **Setup description**

A generic setup for frequency comb generation is presented in fig. 2.3. The main components of are the pump laser, the microresonator and coupling stages, and the electronics for monitoring the generated light. The pump laser is a tunable near-infrared CW laser source around 1550 nm wavelength. Both a fiber laser (Koheras Adjustik) and an external cavity diode laser (ECDL, Toptica CTL1550) were used in this work. The laser power is then typically amplified with an erbium-doped fiber amplifier (EDFA) to a power ranging from  $\sim 10$  mW to a few hundreds of mW. The EDFA amplified spontaneous emission (ASE) is rejected a narrowband band-pass filter at the laser wavelength.

Another central element of this setup is the fiber – resonator coupling. For  ${\rm MgF}_2$  WGM resonators, a tapered optical fiber is used to achieve evanescent coupling. The resonator or taper is mounted on a nanopositioner to adjust the relative distance between the two and thereby tune the coupling rate and optimize coupling to a targeted mode family. The coupling to chip-integrated resonator is predefined in the design by setting the gap distance of the coupling bus waveguide. The fiber-to-chip in and out coupling is achieved using lensed fibers. The coupling to a specific mode family is also optimized by adjusting the polarization of the pump, using a fiber polarization controller (PC).

After the resonator, a fraction of the light is sent to an optical spectrum analyzer (OSA) to

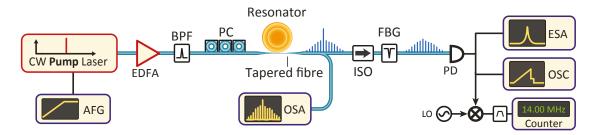


**Figure 2.3 – Generic setup for Kerr frequency comb generation.** The description is provided in the main text. The blue links symbolize optical fiber connections. The black lines symbolize electrical cables. EDFA: erbium-doped fiber amplifier; BPF: band-pass filter; PC: fiber polarization controller; OSA: optical spectrum analyzer; ISO: isolator; FBG: fiber Bragg grating; PD: photodetector; ESA: electronic spectrum analyzer; OSC: oscilloscope; LO: local oscillator; AFG: arbitrary function generator.

monitor the generated comb state. The remaining fraction is filtered with a narrowband notch filter to reject the dominating pump light. This is realized with a tunable fiber Bragg grating (FBG) in combination with an isolator which dissipates the reflected pump light. This filtered optical signal is sent to a fast photodetector (PD) to monitor the 'generated' light signal near DC (i.e. the total power generated nonlinearly in the resonator), as well as to detect the RF beatnote between neighboring comb lines. The detected RF beatnote is monitored on an electronic spectrum analyzer (ESA) and on a frequency counter after down-conversion realized by mixing the signal with an RF local oscillator (LO).

# Soliton generation via 'forward' laser tuning

As described in section 1.2.4, DKS generation can be achieved by tuning the laser from blue to effective red detuning [9], which we refer to as 'forward' tuning. An arbitrary function generator is used for tuning the frequency of the CW pump, either using the piezoelectric actuator or the laser current in the case of the ECDL. The result of such a scan is displayed in fig. 2.4a and features the characteristic modulation instability 'triangle' that corresponds to an effective blue detuning, followed by a sharp drop in the generated power upon entering in the bistable region, which coincides with the start of the soliton existence range (also named 'soliton step'). In experiments, this large power drop is problematic and prevents adiabatic tuning of the laser to reach the DKS state. Indeed, if the cavity has the time to thermalize with the large MI optical power, the large power drop when entering the DKS state will induce a large temperature shift and thus a change of the detuning via the thermo-optical effect described in section 1.2.2. This detuning shift can be much larger than the soliton step and therefore, the solitons cannot be stably accessed. In order to stably access the soliton step, the tuning across the resonance must be faster or on the order of the thermal response time of the microresonator. This issue of thermal stability is addressed in details in refs [9, 155]. Luckily, the thermal response of crystalline resonators is relatively slow ( $\sim 10-100$  Hz), and any laser actuator is fast enough to reach the DKS state. In integrated devices with a much smaller mode volume, the challenge is much more significant and a number of solutions have been proposed to overcome it [155–158].

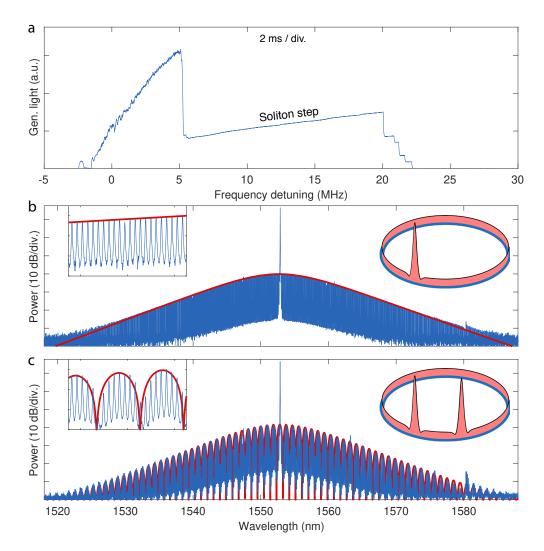


**Figure 2.4 – Soliton comb generation and spectrum (a)** Evolution of the generated comb light when scanning a 200 mW pump laser over a high Q resonance in a MgF<sub>2</sub> resonator (FSR 14 GHz). The effectively blue detuned region follows a triangular shape as the MI gets more powerful and chaotic with smaller effective detuning. In the bistable region, the MI converges to discrete solitons that amount to a lower total power. Increasing the detuning leads to a characteristic 'soliton step'. The detuning was calibrated with phase modulated sidebands. The scanning rate is approximately 2.5 GHz/s. (b) Optical spectrum of a single soliton state comb revealing the characteristic sech<sup>2</sup> spectral envelope. The line spacing is 14 GHz and can be resolved on the optical spectrum analyzer (left inset). The fit of the spectral envelope (red line) yields a 3 dB bandwidth of 11 nm (1.4 THz) corresponding to an intracavity pulse duration of 225 fs (the intracavity field envelope is represented in the right inset, the duration is not to scale). (c) Spectral characteristics of a multi-soliton state with 2 solitons. The structured spectrum is caused by soliton interference according to eq. (1.73). A fit of the interference pattern (red line) allows the estimation of the inter-soliton separation (shown in the right inset, the separation distance is to scale).

After reaching the DKS state, the comb state is generally comprised of multiple solitons that 'condensed' from the chaotic MI pattern evolution. The number of solitons and their relative separation is stochastic, but it was observed that larger pump powers help reaching a smaller number of solitons. This behavior can be understood in light of the more detailed dynamics of the system presented in section 3.3. The 'length' of the soliton step depends also on the pump power and it can be observed in fig. 2.4a that several solitons decay when approaching the end of the soliton step, revealing a stair-like pattern in the generated light trace. This destabilization of soliton is most certainly due to avoided mode crossings [117], as explained later section 3.4.3.

After stably tuning into the soliton step, the optical spectrum can be measured. A single soliton state can be reached with low probability via this direct tuning. The associated spectrum exhibits a typical sech<sup>2</sup> profile as shown in fig. 2.4b. However, most of time, tuning in a soliton step results in a multisoliton state, as shown in fig. 2.4c for a state containing two solitons. According to eq. (1.73), the relative delay between the solitons leads to a spectral interference pattern, that get increasingly complicated with greater number of solitons.

# **2.2** Probing the soliton parameters<sup>3</sup>

# 2.2.1 Non destructive probing with a network analyzer

The driven nonlinear resonator system described by the LLE is mainly determined by two key parameters: the pump power and the effective laser-resonance frequency detuning. While the former is fairly straightforward to measure e.g., by using a powermeter just ahead of the tapered fiber, the latter is more challenging to access but yet is the most critical as it determines both the amplitude and the DKS pulse duration, according to eq. (1.67). This effective detuning is defined as  $\delta \omega = \widetilde{\omega}_0 - \omega_p$ , where  $\omega_p$  is the pump laser frequency and  $\widetilde{\omega}_0$  indicates the frequency of the *thermally shifted* cavity resonance. Indeed, in experiments the pump frequency can be precisely controlled, but the resonance is thermally shifted from the initial cold cavity resonance frequency  $\omega_0$ , due to the amount of light dissipated in the cavity as well as drifts of the lab environment, making it a priori not possible to evaluate the effective detuning. On the other hand, the absolute detuning  $\delta \omega_{abs} = \omega_0 - \omega_p$  is the position of the pump frequency relative to the fixed cold cavity resonance and can be readily measured.

We developed a probing scheme that allows tracking of the effective detuning in a DKS state and permits the determination of the number N of DKSs in the cavity. It is based on the measurement of the transfer function between modulation of the pump optical phase and the resulting amplitude modulation of the cavity transmission. This transfer function is acquired using a network analyzer.

The experimental setup and measurement concept are shown in fig. 2.5. Using an electrooptic modulator, the pump laser is phase-modulated with a frequency-swept signal generated

<sup>&</sup>lt;sup>3</sup>The results of this section are partially adapted from the publication: H. Guo et al., "Universal dynamics and deterministic switching of dissipative Kerr solitons in optical microresonators", *Nature Physics* 13.1 (Jan. 2017), pp. 94–102.

by a vector network analyzer (VNA). After the cavity, a portion of the transmitted light, or a fraction of the pump light reflected off the fiber Bragg grating is detected on a photodiode. The cavity induces a quadrature rotation on one of the sideband resulting in an amplitude modulation in the cavity transmission, which is detected and subsequently demodulated via the RF-homodyne detection inside the VNA.

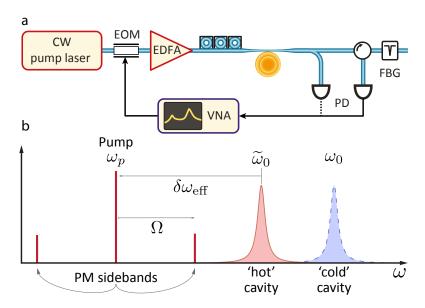


**Figure 2.5 – VNA cavity probing concept.** (a) Experimental setup. The intensity modulation after the cavity can be measured either directly on the full cavity transmission or on the rejected pump power, using a circulator (and attenuator not shown). EOM: electro-optic modulator; EDFA: erbium-doped fiber amplifier; FBG: fiber Bragg grating; PD: photodiode; VNA: vector network analyzer. (b) Schematic representation of the pump laser and cavity detuning in the soliton state. The cold cavity is the intrinsic resonance condition  $\omega_0$  with no light in the cavity. When the cavity contains some optical energy (e.g. a soliton), the amount of power dissipated thermally-shifts the resonance condition to a lower frequency  $\widetilde{\omega}_0$ . The effective detuning of the laser to this shifted resonance determines the soliton properties.

## Probing of a linear cavity

Let us first consider this measurement in the context of a linear cavity. The pump laser is detuned by  $\delta\omega$  and phase modulated with a deviation  $\epsilon$  at a frequency  $\Omega$ . Assuming  $\epsilon\ll 1$ , only first-order sidebands can be considered around the pump

$$s_{\rm in} = s_0 \, \mathrm{e}^{i \left( \delta \omega t + \epsilon \cos(\Omega t) \right)} \approx s_0 \, \mathrm{e}^{i \delta \omega t} \left[ 1 + \frac{i \, \epsilon}{2} \left( \mathrm{e}^{i \Omega t} + \mathrm{e}^{-i \Omega t} \right) \right]$$
 (2.1)

Inserting this triplet of sidebands into eq. (1.33) and extracting the magnitude of the modulation at  $\Omega$  of the intensity transmitted through the cavity (i.e.  $|s_{\text{out}}|^2$  in eq. (1.34)) yields the

following expected response from the VNA;

$$\mathcal{R}(\Omega) = \frac{8\epsilon \eta \delta \omega \Omega}{1 + \left(\frac{\delta \omega}{\kappa/2}\right)^2} \sqrt{\frac{(1 - \eta)^2 + (\Omega/\kappa)^2}{\left(\delta \omega^2 + (\kappa/2)^2\right)^2 + 2\Omega^2(\kappa/2 - \delta\omega)(\kappa/2 + \delta\omega) + \Omega^4}}$$
(2.2)

This response is plotted in fig. 2.6, for different detuning values and cavity coupling strength  $\eta$  (the phase is also plotted although not analytically derived here). If the detuning is significantly larger than the cavity linewidth, this transfer function exhibits a Lorentzian-like profile that originates from the cavity resonance. The peak of this resonance coincides to  $\delta \omega$  with a very good approximation, thus offering a way to track this quantity while the laser remains detuned. Note that this response cannot distinguish between red or blue detuning (positive or negative  $\delta$ ) due to the symmetrical probing by the sidebands around the laser. Finally, this response also allows the evaluation of the cavity linewidth and coupling as shown in fig. 2.6c.

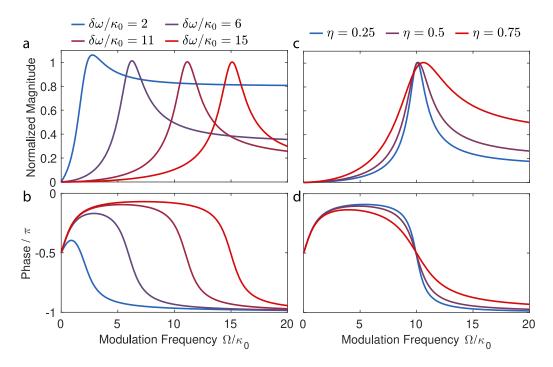


**Figure 2.6 – Linear cavity probing.** Evolution of the analytic VNA response with various parameters. The modulation is normalized to the instrinsic cavity linewidth. **(a)** Plot of the response magnitude  $\mathcal{R}$  in eq. (2.2) for four detuning values. The coupling is assumed to be critical ( $\eta = 1/2$ ). **(b)** Phase of the response associated with (a). **(c)** Evolution of the magnitude  $\mathcal{R}$  for different coupling strength. The detuning is fixed at  $\delta\omega = 10\,\kappa_0$ . **(d)** Phase of the response associated to (c).

# Probing a nonlinear cavity

We applied the VNA probing experimentally to both  ${\rm MgF_2}$  and  ${\rm Si_3N_4}$  resonator during various comb generation stages, as shown in fig. 2.7a-d and the same behavior was observed (account-

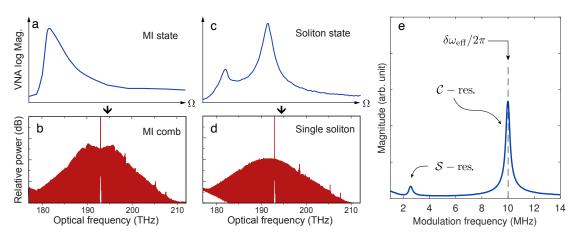


**Figure 2.7 – Comb states and VNA probing**: **(a)** VNA response of a cavity supporting a chaotic MI comb (the magnitude is shown in dB). **(b)** MI comb state corresponding to the measurement showed in (a) (Measurement made in  $\mathrm{Si_3N_4}$  resonator). **(c)** VNA response of a cavity supporting a single DKS. The response features a characteristic double resonance. **(d)** Corresponding single DKS state optical comb spectrum. **(e)** VNA response measured in a MgF $_2$  resonator supporting a single DKS state. The double resonance is well resolved (the magnitude scale is linear here). The  $\mathcal C$ -resonance corresponds to the red-detuned cavity and its position indicates the effective pump detuning. The  $\mathcal S$ -resonance is associated with the presence of a single DKS in the cavity.

ing for the difference in quality factor). First, when the pump frequency is tuned out of the DKS or MI range (no comb formation), the transfer function behaves as in the linear cavity case, featuring a single Lorentzian-like resonance according to eq. (2.2). For a comb state in the chaotic MI regime, the transfer function shows an asymmetric profile with a peak positioned at a small detuning. This peak remains fixed when tuning the laser back an forth over a small range, indicating the thermal and Kerr locking of the cavity resonance to the pump frequency. Finally, when the pump laser is tuned into the soliton existence range (i.e. in the effective red-detuned background regime), the transfer function exhibits an unexpected *double-resonance* feature, as shown in fig. 2.7. We applied the modulation probing scheme to both  $Si_3N_4$  and  $MgF_2$  microresonators and observed the double-resonance transfer function in both platforms when a DKS state is obtained.

In qualitative physical terms, the double-resonance feature may be interpreted as the result of the fundamental cavity bistability in the presence of a soliton. In the DKS state, the intracavity field consists simultaneously of a weak CW background and intense solitary pulses. The CW background represents the lower branch of the cavity field solution, which sees the laser as effectively red-detuned. On the other hand, the soliton pulse with its high peak intensity induces a local shift of the cavity resonance, such that the soliton is effectively slightly blue detuned. This process allows the pump laser being coupled into the resonance, such that the soliton experiences gain. The net result appears as a double-resonance feature, with one soliton induced ' $\mathcal{S}$ -resonance' and a second ' $\mathcal{C}$ -resonance' related to the linear cavity, marked in fig. 2.7e. The 3-dB-width of the resonances is the same and corresponds to the cold optical

resonance width.

First, the C-resonance peak (frequency) indicates the effective detuning between the pump and the cavity background. In normalized units [159],

$$\Omega_C^2 = 1 + (\zeta_0 - |\psi_0|^2)(\zeta_0 - 3|\psi_0|^2) \approx \zeta_0$$
(2.3)

where  $\Omega_{\mathcal{C}}$  is expressed in units of the cavity's half width at half maximum ( $\kappa/2$ ). The approximation is valid for a large detuning  $\zeta_0 \gg 1$ , such that the background is weak and the associated Kerr shift can be neglected. This measurement thereby allows the access to the *thermally-shifted* cavity detuning.

Importantly, the probing technique allows for tracking the effective detuning  $2\pi\,\delta_{\rm eff}=\delta\omega=\kappa\zeta_0/2$ , which is a key parameter in soliton generation experiments. In a DKS state, thermal drifts of the cavity resonance originating from various external sources may cause variations of  $\delta_{\rm eff}$ . Using the measured transfer function, the effective detuning can be monitored and adjusted (e.g. by tuning the pump frequency) in order to maintain the effective detuning within the soliton existence range. In practice, feedback-locking of  $\delta_{\rm eff}$  is also possible, which allows for long-term operation of soliton state in a microresonator, as demonstrated in section 2.3.1.

The second S-resonance is investigated in more details in the following section.

## **2.2.2** Soliton S-resonance

The presence of the  $\mathcal{S}$ -resonance in the transfer function, is uniquely due to the presence of a soliton and is rich in information about the microresonator system. Furthermore, it constitutes a useful criterion for the identification of a soliton state in Kerr combs [70], which is sometimes non-trivial when many solitons exist in the cavity [160]. In fact, transfer function measurements of this type were also applied in mode locked laser systems but no soliton feature was captured [161–163]. We note that the cavity transfer function between a weak pump modulation and the modulation on the comb power in the soliton state was earlier numerically investigated in [164]. While two peaks of the transfer function were also numerically observed in this work, they were attributed conceptually to Feshbach and relaxation oscillations in the presence of third order dispersion.

## **Simulations**

The  $\mathcal{S}$ -resonance feature and scaling can be verified and studied from simulations. The response can be efficiently simulated by computing the field evolution following an impulse on the pump laser phase, as shown in fig. 2.9 and taking the Fourier transform of the total cavity energy (or of the transmitted intensity). Simulations also help to artificially track the evolution of the field at specific points of the cavity and look at the corresponding response. A clear difference is observed if the solution is composed only of the homogeneous background, where only one peak appears, while the double resonance feature is observed when solitons are present in the cavity. The  $\mathcal{S}$ -resonance feature is also solely induced by the soliton. Indeed,

computing the response on the background fraction of the soliton (i.e. away from the soliton pulse) yields a single  $\mathcal{C}$ -resonance, while the response at the soliton peak displays the double resonance as shown in fig. 2.9h. Furthermore, the soliton phase seems to be the parameter that preferentially oscillate at the  $\mathcal{S}$ -resonance frequency  $\Omega_{\mathcal{S}}$ .

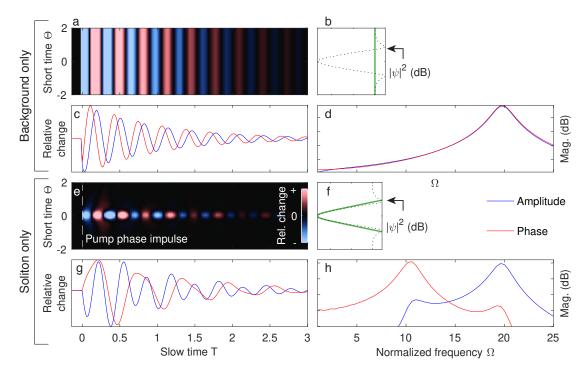
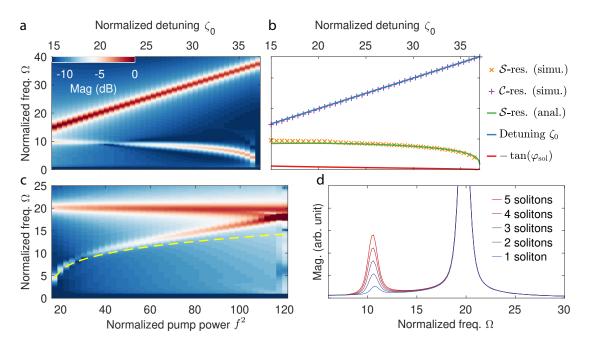


Figure 2.8 - Simulation of the solitonic resonance feature. Response of the background and soliton solution pulse to an impulse of the pump phase. The driving parameters are  $\zeta_0 = 20$ and  $f^2 = 40$ . (a) Relative evolution of the homogeneous background solution amplitude  $|\psi_0|$   $(\Theta, T)$  after the pump phase impulse. The steady state solution was subtracted to show the deviations from it (blue means lower relative amplitude, red means higher). (b) Spatial profile of the steady state background (green) compared to the complete soliton solution  $|\psi_{sol}|$  (black dotted line) The inset is plotted in decibel. (c) Amplitude (blue) and phase (red) relative evolution of the homogeneous solution after the pump phase impulse at T=0. (d) Fourier transform of the signals in panel (c). Both feature only a single peak (C-resonance) at the detuning value  $\Omega_{\mathcal{C}} \approx \zeta_0$ . (e) Relative evolution of the solitonic pulse amplitude only (i.e. after complex background subtraction  $|\psi_{sol} - \psi_0|$ ). (f) Spatial profile of the soliton component (green) compared to the complete soliton solution  $|\psi_{sol}|$  (black dotted line). The inset is plotted in decibel. (g) Evolution of the amplitude (blue) and phase (red) taken at the peak of the soliton pulse, following the pump phase impulse at T = 0. The phase evolves at a noticeably slower rate than the soliton amplitude or the background field. (h) Fourier transform of the signals in panel (g). The double resonance feature is observed on both signals. The S-resonance is dominant in the soliton phase response.

While simulations confirm the soliton-related nature of the S-resonance feature, it is hard to intuitively explain its physical origin. As mentioned in the previous section, a the double resonance feature can be thought of as the result of the cavity bistability in the soliton state.



**Figure 2.9 – Simulated scaling of the** S-resonance and comparison to the analytic estimate (a) Evolution of the cavity response with the detuning, simulated for a single soliton and  $f^2 = 30$ . (b) Comparison of the simulated C, S-resonance peak positions in (a) with respectively the detuning  $\zeta_0$  and the analytical approximation of  $\Omega_S$  in eq. (2.4). (c) Simulated evolution of the response with the driving strength  $f^2$  for a single soliton and a fixed detuning  $\zeta_0 = 20$ . The dashed yellow line corresponds to the analytical expression eq. (2.4). For small C-S resonances separation, the approximation fails. (d) Evolution of the response with the number of solitons in the cavity. The S-resonance amplitude scales linearly with the number of solitons.

However, it is important to note that the S-resonance frequency  $\Omega_S$  does *not* correspond to the effective soliton detuning.

## **Analytical approximation**

An analytical approximation of the  $\mathcal{S}$ -resonance frequency  $\Omega_{\mathcal{S}}$  was derived in the supplementary information of ref [159] by Prof. M. Gorodetsky. It corresponds to the response of the soliton phase to the pump phase modulation in the LLE and predicts a normalized  $\mathcal{S}$ -resonance frequency following

$$\Omega_{\mathcal{S}}^2 = \pi f \sin(\varphi_0) \sqrt{2\zeta_0} \qquad \cos(\varphi_0) = \frac{\sqrt{8\zeta_0}}{\pi f}. \tag{2.4}$$

Note that this model is a rough approximation as the soliton effectively interacts with the cavity background and not directly with the pump. Nonetheless, this model provides useful insights on the  $\mathcal{S}$ -resonance origin, which can be viewed rather as a natural 'mode of oscillation' of the soliton. It may correspond to the rate at which the soliton exchanges energy with the background. We may hypothesize that the  $\mathcal{S}$ -resonance corresponds to the stability of the heteroclinic connections that link the soliton to the background [115]. This interpretation

is further motivated by the relation established between the S-resonance and the breathing dynamics of solitons, detailed in section 3.2.

Several characteristics of the S-resonance can be highlighted from eq. (2.4) and tested through numerical simulations. First, the S-resonance weakly depends on the detuning and appears practically at a fixed frequency for a given pumping strength, as shown in fig. 2.9a,b. It also systematically appears at a smaller frequency than the detuning peak  $\Omega_C$ . Figure 2.9c reveals that the frequency  $\Omega_S$  increases with the pump strength  $f^2$ , in accordance with the analytical model. Note however that the approximation loses validity when  $\Omega_S$  gets on the order of the detuning, which is the case when the detuning is small or the pump power is strong. This parameter region corresponds to the breathing regime, where DKSs lose stability, and is hard to describe analytically and intuitively.

Finally, the magnitude of the S-resonance peak linearly depends on the soliton number N, as the response signal is enhanced by the higher comb power generated with a larger number of solitons (or in other words, the solitons contribute individually to the response if they are not too close).

# **Experimental verification**

The scaling of the double resonance feature was investigated experimentally in the  ${\rm MgF}_2$  resonator. The results are displayed in fig. 2.10.

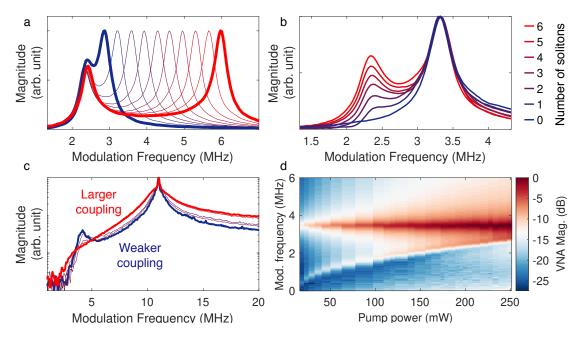


**Figure 2.10 – Experimental verification of the double resonance scaling.** Evolution of the double resonance feature as a function of various system parameter: **(a)** Detuning, **(b)** Number of solitons, **(c)** Resonator coupling, **(d)** Pump power.

First, a measurement for a constant power ( $P_{\rm in} \approx 200$  mW,  $f^2 \sim 377$ ) validates that the S-resonance is practically fixed, when the detuning is changed. A more extensive measurement

of the dependence over a larger detuning span is also reported in the next section (fig. 2.13) and confirms the behavior of the  $\mathcal{S}$ -resonance with detuning, although some soliton perturbations induce some deviations. The scaling with the number of DKSs also follows the predicted linear scaling of the amplitude of the resonance. The evolution of the  $\Omega_{\mathcal{S}}$  with the power for a fixed detuning also closely follows the expected behavior as shown in fig. 2.10d. Finally, the effect of changing the coupling rate to the resonator was explored by changing the taper position. Increasing the coupling rate increases the resonance linewidth accordingly, but also modifies the overall scaling os the frequencies and in particular of the pumping term. Eventually, strongly overcoupling of the resonator has the same effect as lowering the effective pump power and the  $\mathcal{S}$ -resonance shifts toward lower frequencies.

# 2.3 Experimental scaling of the soliton properties<sup>4</sup>

# 2.3.1 Network analyzer-based digital locking of the detuning

In order to study the soliton properties as a function of the effective detuning, this parameter must be measured, stabilized, and tuned in a controlled way. In this context the measurement of the  $\mathcal{C}$ -resonance frequency in the VNA response provides a way to readout and therefore stabilize the effective pump detuning  $\delta \omega \gg \kappa$  as explained in section 2.2.1.

We implemented a digital feedback-stabilization of the effective detuning, as shown in Fig. 2.11a. The response of the system is measured with the VNA (sweep time  $\sim$  100 ms) and recorded with a computer. The detuning value is identified by detecting the  $\mathcal C$ -resonance frequency with a peak detection algorithm, and a digital PID algorithm determines the required feedback to apply to the pump laser frequency to stabilize the detuning to a given value. The overall feedback is slow ( $\sim$  10 Hz) but sufficient to compensate the thermal drift, which is the main source of variations.

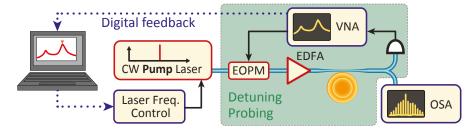


**Figure 2.11 – Kerr comb probing and digital stabilization.** Experimental setup: Vector Network Analyzer (VNA), Electro-Optic Phase Modulator (EOPM), Erbium Doped Fiber Amplifier (EDFA), Optical Spectrum Analyzer (OSA)

This method was first applied for the measurement of the soliton existence range in the crystalline MgF<sub>2</sub> microresonator ( $P_{\rm in} \approx 215$  mW, intrinsic linewidth  $\kappa_0/2\pi \approx 100$  kHz,  $\eta \approx 0.44$ ).

<sup>&</sup>lt;sup>4</sup>The results of this section are partially adapted from the publication: E. Lucas et al., "Detuning-dependent properties and dispersion-induced instabilities of temporal dissipative Kerr solitons in optical microresonators", *Physical Review A* 95.4 (Apr. 2017), p. 43822. ☑

The laser was red-detuned until the collapse of the soliton. We measured it to extend from  $\delta \omega_{\rm min}/2\pi \sim 2$  MHz to  $\delta \omega_{\rm max}/2\pi \sim 30$  MHz, which corresponds to a normalized laser-cavity detuning of  $\zeta_{\rm max} = 2\delta \omega_{\rm max}/\kappa \sim 320$  times half the resonance linewidth. This is enabled by the strong pumping of the resonator, that is  $f^2 \sim 445$  times above the parametric threshold. Note that the measured maximum detuning value is lower than the theoretical prediction of  $\zeta_{\rm max}^{\rm theo} \approx 549$  according to eq. (1.65), which is probably due to the imperfect determination of the cavity linewidth and to the impact of modal crossing that destabilize the DKS [117, 166].

The feedback also enabled the long-term stabilization of a single soliton at a fixed effective detuning over 15 h as presented on fig. 2.12. Over this period, the laser frequency was adjusted by more than 350 MHz, which represents over ten times the existence range of the soliton. The active compensation maintained the effective detuning fixed at 10 MHz and stabilized the comb bandwidth (fig. 2.12c,e). However, the parameters of the resulting frequency comb are not stabilized, since the cavity FSR drifts thermally and so does the pulse repetition rate. To highlight the effect of the stabilization, the lock was disabled on purpose after  $\sim$  15 h and the thermal drifts caused the comb properties to shift until the soliton state decayed after 17 min.

# 2.3.2 Detuning-dependent dissipative Kerr soliton duration

The feedback stabilization of the detuning clears a way to carry out a controlled experimental study of the effect of the detuning on the properties of a single soliton in the crystalline  ${\rm MgF}_2$  resonator, and perform a careful comparison of the measurements to theoretical predictions.

In particular, validating the scaling of the soliton duration  $\Delta \tau_s$  (or equivalently the comb bandwidth) according to the approximate solution eq. (1.67) is very relevant. For instance, this relation was employed in several recent works on DKSs (as in ref [167]), where it was used to swap  $\delta \omega$  dependencies with  $\Delta \tau_s$ , which could be inferred from the comb optical spectrum. A direct experimental verification of this approximation would consolidate the validity of such approach.

In order to study the dependence of the soliton on the effective detuning, this parameter was swept by changing the set-point of the digital lock on the computer. Figure 2.13a shows a sweep of the effective detuning from 6 to 28 MHz, in 50 steps. At each step, once the detuning was stabilized, an optical spectrum was acquired (OSA scan time  $\sim$  30 s) and the comb average power (after suppressing the pump with a narrow-band fiber Bragg grating) was measured with a photodiode, before moving to the next detuning value. At the same time, the comb repetition rate  $\omega_r$  was measured with a frequency counter after photo-detection and downmixing. The overall measurement duration was  $\sim$  30 min and the active detuning stabilization is required to counteract the environmental drift over that time.

Each optical spectrum was fitted with a sech<sup>2</sup> envelope:

$$A \operatorname{sech}^{2}\left(\frac{\mu\omega_{r} - \Omega}{B}\right),\tag{2.5}$$

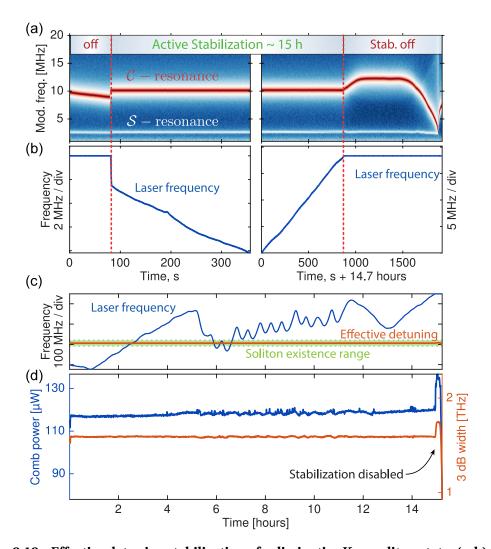


**Figure 2.12 – Effective detuning stabilization of a dissipative Kerr soliton state. (a-b)** Closein view of the lock enabling and disabling. The colormaps in **(a)** show the concatenated set of acquired VNA traces used to determine the detuning. The plots in **(b)** trace the pump frequency. If the lock is enabled, the laser is tuned to keep the effective detuning at a fixed value. When the lock is disabled, the laser frequency is fixed, but the soliton is lost after 17 min. **(c-d)** Stabilization and continuous soliton measurement over 15 h. **(c)** The blue line indicates the evolution of the pump laser frequency when tracking the microresonator resonance, which is measured by counting the heterodyne beat of the pump with an ultra-stable laser. The temperature drifts of the microresonator cavity are the main source of variations and the slow oscillations are caused by the air conditioning. The red line indicates the stabilized effective detuning (at 10 MHz) that remains within the soliton existence range. **(d)** The comb power and the 3 dB bandwidth (obtained by fitting the optical spectra) are stabilized when the laser compensates the drifts.

where  $\mu$  is the relative mode number,  $\omega_r$  the repetition rate of the comb,  $B = 2/(\pi \Delta \tau_s)$  the bandwidth, A the power of the central comb line and  $\Omega$  the spectral shift of the sech<sup>2</sup> centroid from the pump.

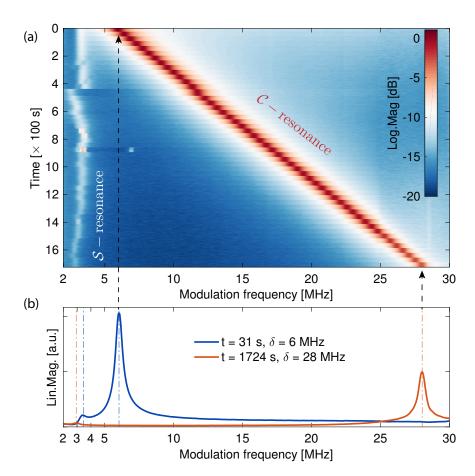
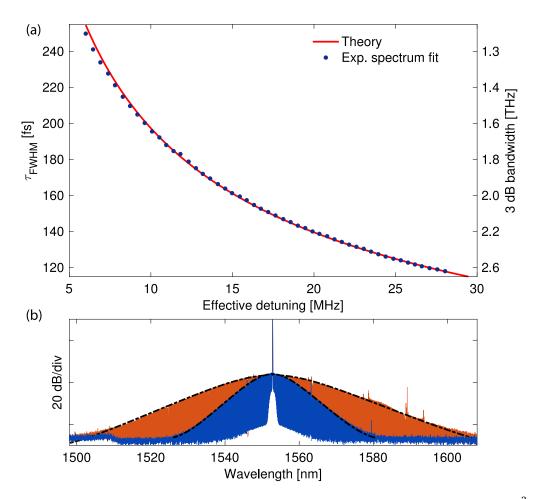


Figure 2.13 – Tuning of the effective detuning and evolution of the soliton duration. (a) Map showing the evolution of the modulation response (log scale) as the effective detuning is swept. The detuning is stabilized at each step. (b) The observed VNA traces at the extrema of the effective detuning  $(\delta\omega)$ .

The presented method enables a precise comparison between the measured comb properties and the theoretical predictions. The dispersion parameters of the resonator were measured experimentally via frequency comb assisted scanning laser spectroscopy [152, 166] and shown in fig. 2.16d. (the corresponding dispersion parameters are  $D_1/2\pi=14.094$  GHz,  $D_2/2\pi=1.96$  kHz,  $D_3/2\pi=-1.39$  Hz). The soliton spectral bandwidth (and deduced pulse duration) obtained experimentally is compared with the approximate expression eq. (1.67), using the measured dispersion and detuning parameters (fig. 2.14a). We observe an excellent agreement of the two curves (normalized RMS deviation of 0.8 %) supporting the validity of the approximation. The results also show that the soliton duration can be tuned by more than a factor of 2 by changing the detuning.



**Figure 2.14** – (a) The measured soliton full width at half maximum (derived from a sech<sup>2</sup> fit) is plotted versus the detuning (blue dots) with comparison to the expression in Eq. (1.67) (red line). (b) Corresponding spectra at the limits of the sweep. As expected, the comb bandwidth increases with larger effective detuning. The black lines mark a sech<sup>2</sup> fit of the combs.

#### 2.3.3 Detuning-dependent mode crossings and soliton recoil

The relation between average power of the comb and detuning is obtained by integrating eq. (1.71):

$$\overline{P} = \frac{2\eta A_{\text{eff}} n_0 \kappa}{n_2 \omega_0 D_1} \sqrt{2D_2 \delta \omega} = \frac{\kappa_{\text{ex}} \hbar \omega_0}{\pi g_0} \sqrt{2D_2 \delta \omega}.$$
(2.6)

The evolution of the measured comb power, shown in fig. 2.15a, follows the trend of the previous equation, but significant discrepancies are observed at several detuning values, such as at  $\delta\omega/2\pi=12$  MHz, where a large spike in the comb power is measured. Integrating the fit expression (2.5) reveals that the power in the soliton is reduced at these points (blue dots in fig. 2.15a). The corresponding spectrum exhibits specific comb lines that are strongly enhanced (fig. 2.15b).

This effect is typically caused by avoided mode crossings (AMX), that cause a local disruption in

the resonator dispersion, leading to a modification of the phase matching condition between the pump to a sideband mode. This is associated with an enhancement or suppression of the comb generation at the crossing position [117, 166, 168]. The excess power in certain lines (spikes) makes the frequency comb asymmetric, which induces a recoil – i.e. a shift in the soliton center frequency with respect to the pump – in the opposite direction, in order to keep the spectral center of mass invariant [169, 170]. This phenomenon is similar to the emission of dispersive waves [171] in the cavity, but that occurs over a very limited number of modes or even a single comb mode. An analytic model of the phase matching condition and power variation of such single-mode dispersive waves has been proposed in ref. [172]. In the time domain, the spike beats with the pump laser, leading to an oscillating intracavity background. The soliton(s) are then trapped on this oscillating pattern, creating a bound state [173].

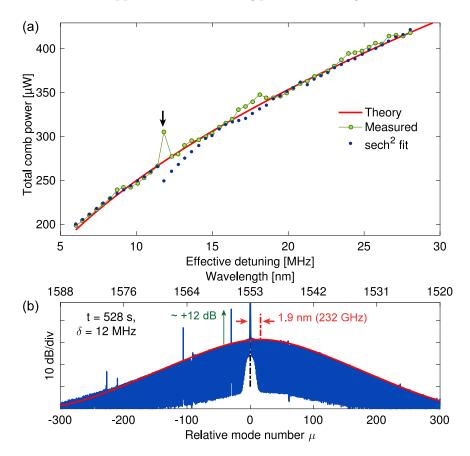


**Figure 2.15 – Evolution of the soliton power. (a)** Evolution of the measured comb power with the effective detuning (green dots), compared to Eq. (2.6), and the estimated power in the soliton component (blue dots, derived from the sech<sup>2</sup> fit). **(b)** Comb spectrum corresponding to the arrow in **a**. The black dashed line marks the pump position ( $\mu$  = 0). Two strong avoided mode crossing are visible at  $\mu$  = -31 and  $\mu$  = -106, and induce a shift of the sech<sup>2</sup> centroid from the pump toward shorter wavelength, marked by the red arrows.

The evolution of the mode crossing features with the laser detuning is further investigated in fig. 2.16. Interestingly, the measured dispersion of the mode family supporting the soliton

does not exhibit strong disruptions (see fig. 2.16d), instead we observe weak periodic crossings with a mode family having a different FSR.

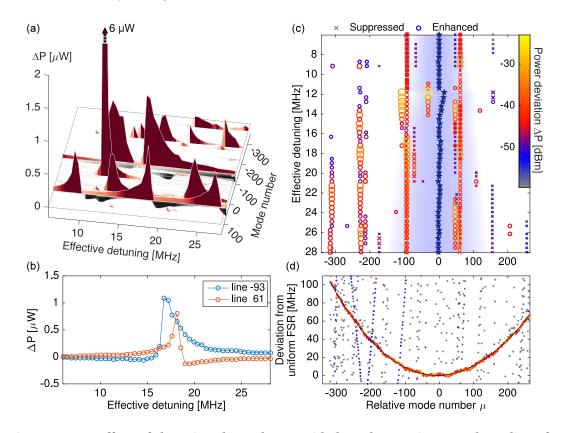


Figure 2.16 – Effect of detuning dependent avoided mode crossings on the soliton frequency comb. (a) Map of  $\Delta P$  indicating the spurs and dips in the spectrum after subtracting the fitted sech² soliton envelope. (b) Section of the  $\Delta P$  map showing the evolution of the power deviation for the comb line +61 and -93 (relative to the pump) (c) Representation of the peaks in the  $\Delta P$  map, in logarithmic units, showing the evolution of the intensity spurs caused by avoided mode crossings. The lines higher than the sech² envelope (enhanced) are marked with a dot, the lines lower (suppressed) with a cross. The blue stars mark the comb centroid Ω. The shaded blue region indicates the comb 3 dB width. When lines are strongly enhanced, the comb centroid shift away from them.(d) Measured frequency dispersion of the mode family supporting the soliton. A quadratic fit yields  $D_1/2\pi = 14.0938$  GHz and  $D_2/2\pi = 1.96$  kHz. Multiple mode families with a different FSR exist in the resonator and cross the family of interest, inducing small periodic disruptions on the dispersion.

We detect the mode crossing features in the comb spectrum by first subtracting the sech<sup>2</sup> fit, to estimate the power deviation  $\Delta P$  of each comb line (see fig. 2.16a). The power deviation of the concerned comb lines evolves with the detuning, abruptly transitioning to being enhanced or suppressed over a small range of detuning, as illustrated in fig. 2.16b. Such evolution is in agreement with the model of ref. [172]. The deviations in the residual  $\Delta P$  are detected, and plotted on fig. 2.16c. We observe here that the spectral location of the mode crossing features in the comb spectrum is fixed and match those of the modal deviations in the measured

dispersion. We also note that strongly enhanced comb lines lead to a recoil of the soliton centroid that shifts away from these lines. To further check the appearance of avoided mode crossings induced recoil, we estimate the expected soliton recoil  $\tilde{\Omega}$  based on the conservation of the spectral center of mass:

$$\int_{-\infty}^{+\infty} \mu A \, \mathrm{sech}^2 \left( \frac{\mu \omega_r - \tilde{\Omega}}{B} \right) d\mu + \sum_{\mu} \mu \Delta P = 0 \quad \Leftrightarrow \quad \tilde{\Omega} = -\frac{\omega_r^2}{2AB} \sum_{\mu} \mu \Delta P,$$

This estimate is plotted in fig. 2.17a, together with the fitted parameter  $\Omega$  in eq. (2.5), and an overall agreement is found between these two values. It is interesting to note that the soliton experiences a spectral recoil toward higher optical frequencies, which is opposite to the so far reported frequency shifts observed in microresonators in amorphous  ${\rm SiO_2}$  or  ${\rm Si_3N_4}$ . Indeed, in these platforms, the Raman self frequency shift dominates and systemically shifts the frequency comb center toward lower frequencies, which can compensate the recoil induced by a dispersive wave [174, 175]. In crystalline MgF $_2$  platforms, the Raman gain is spectrally narrow [176] and such effects are negligible.

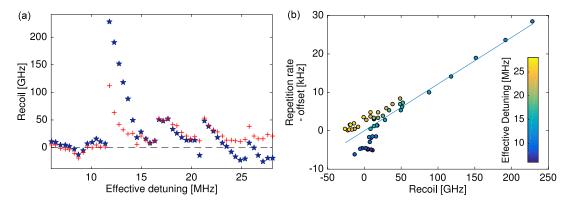


**Figure 2.17 – Avoided mode crossings and recoil effect on the soliton.** (a) Evolution of the soliton recoil. The blue stars result from the fit of the optical spectrum, while the red crosses mark the estimated recoil using (2.3.3). (b) The repetition rate frequency is strongly correlated with the recoil. This enables the determination of the dispersion parameter as given by the slope  $(D_2/D_1)$ . The offset on the repetition rate is 14.094005 GHz.

The recoil on the soliton implies a change in the soliton's group velocity and thus a modification of the comb repetition rate, according to  $\omega_r = D_1 + \Omega \, D_2 / D_1$  [177], similar to the Gordon–Haus effect in mode-locked lasers [178, 179]. This is verified in Figure 2.16f, where the change in the repetition rate frequency is plotted as a function of the measured recoil and fitted with a linear model. The intercept matches the free spectral range  $D_1/2\pi$  and the slope yields  $D_2/2\pi = 1.72 \pm 0.48$  kHz, which overlaps with the measured dispersion. The spread of the datapoints at small recoil values could originate from the thermal drift during the measurement.

Overall, we observed that the excitation of avoided mode crossing are detrimental for the stability of the soliton Kerr comb, and cause an enhanced sensitivity of the soliton repetition rate to pump laser frequency fluctuations. At certain detuning points, the excitation of mode

crossings causes abrupt changes in the comb repetition rate, resulting from the induced recoil, in agreement with simulations performed in ref. [180]. The present method enables the identification of detuning regions that minimize the impact of avoided mode crossings, which is further investigated in section 5.3. We also observed that the excitation of the strong avoided mode crossing at  $\delta\omega/2\pi=12$  MHz ( $t\sim450$  s) is correlated with a sudden shift of the  $\mathcal{S}$ -resonance toward lower frequency (see VNA map fig. 2.14a). This is not yet understood and needs further investigation.

These observations of a detuning dependent repetition rate have important repercussions for low phase noise microwave generation, as they may enhance the transduction of pump laser frequency noise onto noise in the soliton pulse repetition rate. This aspect is further studied in section 5.3.3.

AMX can also degrade the stability of the soliton and induce breathing in a region where solitons are expected to be stable. At other detuning values  $\delta\omega/2\pi=15.5$ , 15.9, 17.2 MHz ( $t\sim750$ , 780, 880 s), the  $\mathcal{S}$ -resonance peak appears greatly enhanced. This is concomitant with the appearance of sidebands around the repetition rate of the comb and of an amplitude modulation of the soliton pulse train at a frequency of  $\sim3.5$  MHz. These observations suggest that the soliton is breathing, meaning its amplitude and width oscillate in time, with a frequency typically much smaller than the repetition rate [181–184]. Such instabilities are predicted in the LLE, but are unexpected for the large detuning values explored here and are further studied in section 3.4.

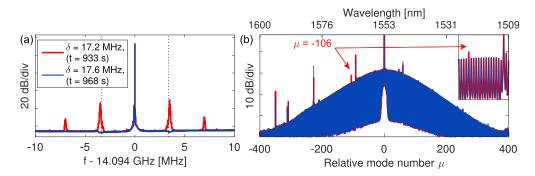
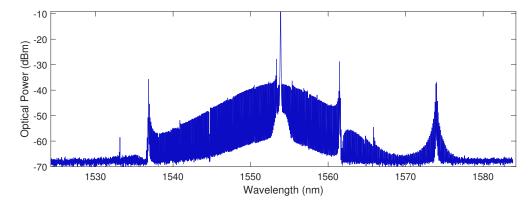


Figure 2.18 – Avoided mode crossing induced soliton breathing (a) RF spectrum of the repetition rate for two adjacent detuning steps  $\delta\omega/2\pi=17.2$  and 17.6 MHz (resolution bandwidth 1 kHz). In the first case, modulations sidebands appear on the repetition beatnote, with a frequency of  $\sim 3.5$  MHz, closely matching the  $\mathcal{S}$ -resonance frequency measured on the VNA (indicated by the dashed lines). This is typically indicative of a soliton breathing. (b) Corresponding optical spectrum comparison. The red (blue) trace corresponds to the soliton breathing (stable). The breathing seems to correlate with the excitation of the mode  $\mu=-106$ .

Nevertheless, it is interesting to point out that our observations highlight the surprising robustness of the dissipative soliton, which is sustained in the cavity in spite of all the reported perturbations. In particular, the relation eq. (1.67) linking the detuning and soliton duration is surprisingly well preserved although the studied microresonator exhibits non-negligible

deviations in its mode spectrum in the form of avoided mode crossings. To further illustrate this point, we show in fig. 2.19 the optical spectrum of a soliton heavily perturbed by modal crossings (obtained in another microresonator). It is almost surprising that soliton can be formed even if the dispersion is strongly altered.



**Figure 2.19 – Soliton heavily perturbed by mode crossings.** Note that the perturbations are in good agreement with the model developed in ref. [166].

Our method provides a way to experimentally explore the existence range of the soliton and identify optimal sets of operating parameters that favor a stable operation of the optical frequency comb. Moreover, we reveal how these crossings induce deviations in the relation between comb power and detuning, which can be a limitation for stabilization techniques based on the comb power alone [167, 185]. The presented method also enables the long-term operation of soliton-based combs with stabilized bandwidth and power. The stabilization could alternatively be achieved by direct actuation on the microresonator [186–188], to tune the free spectral range and stabilize the cavity resonance on a stable pump laser. The fine control of the two driving parameters of the nonlinear system (detuning and pump power) also enable the controlled access to various soliton regimes predicted by theory [189], and that are explored in the next chapter.

# 3 Soliton breathing and dynamical instabilities

"The world is a dynamic mess of jiggling things if you look at it right. [...] It's lucky that we have such a large scale view of everything, that we could see them as things, without having to worry about all these little atoms all the time."

FUN TO IMAGINE RICHARD FEYNMAN

In this chapter, the dynamical behaviors of solitons are characterized. We begin by presenting the bifurcation chart that maps the various solitons fundamental instabilities predicted by the LLE model. These theoretical and numerical predictions are then tested experimentally where several novel features are discovered. A type of soliton instability that leads to the decay of solitons is also discovered and found to have practical applications to reduce the number of DKS in microresonators (i.e. from N to N-1), opening a path to access the single soliton state. Finally, the impact of modal interactions (such as avoided mode crossings) on the stability of solitons is investigated.

# 3.1 Detailed analysis of the fundamental soliton instabilities

As mentioned in section 1.2.4, the solitons are not stable for all values of detuning and driving strength. Similar phenomenon were first analyzed in plasma physics [190, 191]. These early studies demonstrated that stable soliton attractors exist within a certain range of effective detuning in the red-detuned regime that destabilize to time-periodic solitons (i.e. breathers) and chaotic states are possible [94]. Extensive numerical analysis and charting of the parameter space of the LLE [94, 98, 115, 189] revealed that the breathing region is located close to the low-detuning boundary of the soliton existence range. In the attractor chart in fig. 1.19, an instability zone was already introduced, where solitons develop a breathing instability and oscillate. This attractor map is further developed in fig. 3.1, which was adapted from ref. [189].

In particular, the focus is placed on the lower detuning end of the soliton existence ( $\zeta_{\downarrow}$ ) and higher driving powers are explored (up to  $f^2 = 100$ ). It reveals that solitons can exhibit a rich panel of instabilities that develop from a Hopf bifurcation [189] of a stable DKS. Beyond the Hopf threshold (for lower detuning or higher power), the attractor chart can be sub-divided in several regions (I, II, III, IV) depending on the type of predicted spatio-temporal instabilities.

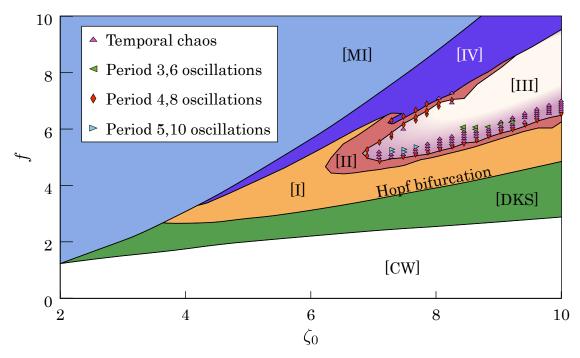


**Figure 3.1 – Attractor chart of the various dynamical instabilities of DKS predicted by the LLE.** The shaded regions classify the various solutions of the LLE and their stability. [CW] Monostable homogeneous lower branch solution [DKS] Stable DKS existence [I] Breathing DKS (fundamental periodicity) [II] Period 2 breathing and higher periodicity (dots and shaded area) [III] Transient temporal chaos [IV] Spatiotemporal chaos [MI] Modulation instability. Adapted from ref. [189].

## **Breathing soliton**

In the region I, DKSs become unstable and develop an oscillating profile, which is known as breathing [181, 182, 184, 189]. Mathematically, the transition from stationary to breathing DKS results from a Hopf bifurcation that arises above a certain pump power level [189] (boundary between green and yellow areas in fig. 3.1). When the driving parameters cross this boundary, the stable equilibrium point of the DKS develops into a limit cycle shown fig. 3.2a.

The simulated temporal evolution of the amplitude profile of a breathing soliton is displayed in fig. 3.2c, showing that the soliton width and amplitude oscillate, such that the DKS compresses and stretches periodically. The spectral envelope also reflects this effect (fig. 3.2d). Breathers are also known to radiate weakly-decaying dispersive waves on the CW background [192] that induce sidebands on the optical spectrum. No analytical ansatz for a breathing DKS exist to date, but they were shown to relate to the Kuznetsov-Ma types of breathers in the context of

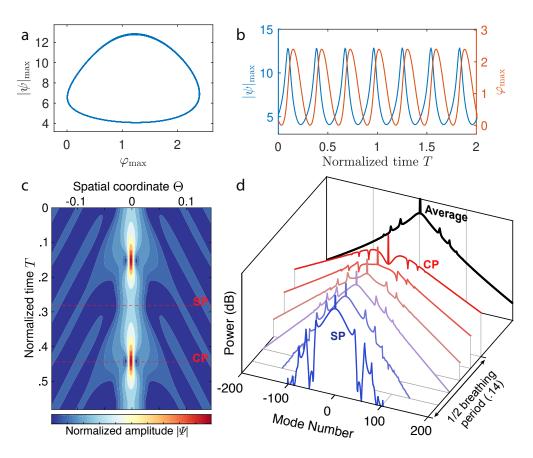


**Figure 3.2 – Breathing DKS simulations.** The simulations were carried out at  $f^2 = 465$  and  $\zeta_0 = 27$ . (a) Limit cycle orbital of the breathing DKS in the phase space  $(\varphi_{\text{max}}, |\psi|_{\text{max}})$  corresponding to the phase and amplitude of the field at the peak of the DKS. (b) Corresponding time traces for the center amplitude and phase over the slow time. (c) Temporal evolution of a breathing dissipative soliton over one breathing period illustrating the periodic compression (CP) and stretching (SP), both indicated by a red dashed line and the emission of waves in the background. (d) Corresponding optical spectrum of the intracavity pattern over half a period, showing the evolution between the maximal stretching and compression instants (S and CP). On average, over one period, the spectrum features a triangular shape (in log scale). The emitted waves are causing the sidebands in the spectrum.

the NLSE [193, 194]. The breathing instability may be interpreted as a destabilization of the DKS caused by several factors occurring at low detuning. On the one hand, the solitons get longer and its peak amplitude is reduced. On the other hand, as the resonance is closer, the background level increases and becomes more unstable to modulations, which explains why the weak dispersive waves can be emitted. Overall, the contrast of the soliton with respect to the background is reduced, which destabilizes the soliton and enhances the energy exchange with the homogeneous solution. We can therefore expect a relation between the breathing dynamics and the  $\mathcal{S}$ -resonance, which will be confirmed experimentally in the next section. Another interpretation may be related to the loss of stability of the heteroclinic connections that link the soliton to the background [115].

A simulated chart of the breathing frequency is shown in fig. 3.3. The general trend of the numerical simulations shows how the breathing period and amplitude tend to increase with higher pump and lower detuning after passing the Hopf bifurcation, meaning that the limit cycle orbit opens and is covered over a longer time. The basin of attraction of the soliton becomes more shallow, permitting wider excursions in the phase space.

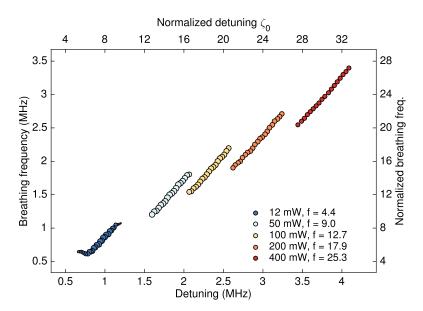


Figure 3.3 – Simulated evolution of the breathing frequency  $f_b$  as a function of the detuning and pump power. The breathing frequency is normalized to the half width at half maximum of the cavity  $(2f_b/\kappa)$ . In these simulations, we assumed realistic conditions for the crystalline MgF<sub>2</sub> resonator.

#### Higher order periodicity and temporal chaos

Reducing the detuning or increasing the pump power beyond the Hopf bifurcation leads to a further widening of the limit cycle and complex destabilization of the soliton with transition to higher breathing periodicity, starting with period doubling in regions II and period quadrupling or higher periods in the gradient shading of region III. This is reflected in the limit cycle that tends to develop loops, as shown in fig. 3.4. Eventually, the breathing turns chaotic also in region III, but returns to a regular periodicity in very localized parameter regions, such as the period tripling shown in fig. 3.4d. This type of branching to higher periodicity as a function of the systems parameters is typical of dynamical systems leading to chaos, such as the canonical example of the logistic map.

#### Transient chaos and decay

The increasing breathing depth naturally leads the DKS amplitude to approach the homogeneous background. In region III, the excursions in phase space are very large and approach the saddle node bifuraction separating the chaotic breathing orbit and the basin of attraction of the homogeneous solution. While the excursions remain below this separation, the soliton

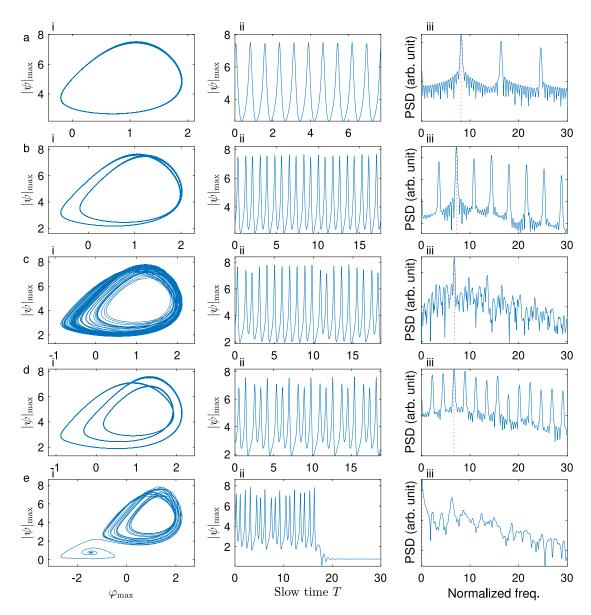


**Figure 3.4 – Higher breathing periodicity and route to chaos.** Evolution of the limit cycle for  $f^2 = 36$  and decreasing values of detuning. The panels i show the limit cycle of the soliton peak in the phase and amplitude phase space. The panels ii show the temporal evolution of the peak amplitude. The panels iii show the spectrum associated with ii. (a) Period 1 breathing at  $\zeta_0 = 10$ . (b) Period doubling,  $\zeta_0 = 9.2$ . Subharmonic peaks appear in the spectrum (c) Temporal chaos,  $\zeta_0 = 8.8$ . The spectrum loses coherence (d) Period tripling,  $\zeta_0 = 8.6$ . Note the peculiar subhamonic distribution. (e) Transient chaos and soliton decay,  $\zeta_0 = 8.2$ .

is pulled back into the cycle. However, the slightest perturbation can lead to the soliton exiting the limit cycle and collapsing to the homogeneous solution. An example of such event is shown in fig. 3.4.

#### Spatiotemporal chaos

In region IV, the breathing solitons regain stability. However, in this area, the amplitude of the emitted waves become large enough to spontaneously converge to cavity solitons solutions. This phenomenon is essentially a reverse of the collapse process described above and seeds the formation of new DKS on either side of the original breather. These new solitons follow the limit cycle and thereby excite new DKS in a chain-reaction type of excitation. Eventually the entire cavity is filled with soliton and the system loses symmetry and effectively become spatially and temporally chaotic, similarly to MI, although these effects happen in the bistable cavity region. This instability was investigated by M. Anderson in fiver cavities [195] and will not be explored here.

# 3.2 Breathing dissipative solitons<sup>1</sup>

The first experimental demonstration of breathing dissipative solitons was realized in fiber cavities by Leo et al. [189]. However, the experimental observation of breathers in optical microresonators has posed a significant challenge due to the non-trivial soliton generation process [9, 148], the thermal nonlinearity that may impact the effective laser detuning [88, 159] and high repetition rates (> 10 GHz) that make direct time-resolved observations difficult. Nevertheless, microresonators remain an attractive platform to study breathers, as their very high finesse allows easy access to strong driving regimes where the complex instabilities are predicted to occur. Furthermore, the ability to generate a single soliton in the cavity combined with the fact that the timescale of the instabilities scales with the relatively long photon lifetime, suggests that the soliton dynamics can still be captured with a sampling rate much smaller than the inverse soliton roundtrip. The first observation of breathers in microresonators was reported by Bao et al. [184], evidencing the link with the Fermi-Pasta-Ulam recurrence. Other attempts at characterizing breather dynamics [182] have since been realized. In this section, a comprehensive analysis of breathing dissipative solitons in microresonators is presented. First, a deterministic route to access and characterize breathing solitons is established. Second, using the VNA probing method, the operating conditions are directly measured, allowing a detailed exploration and mapping of the breathers' existence range, revealing the relation between breathing frequency and the driving laser parameters. Finally, time-resolved observations of the intracavity pattern evolution are performed. This enables the behavior of individual soliton pulses to be tracked, even with several solitons in the cavity, revealing non-stationary breathing dynamics as well as evidence of breather synchronization. These findings not only carry importance from an application perspective, but also contribute more broadly to the fundamental understanding of dissipative soliton physics.

<sup>&</sup>lt;sup>1</sup>The results of this section are partially adapted from the publication: E. Lucas et al., "Breathing dissipative solitons in optical microresonators", *Nature Communications* 8.1 (2017), p. 736. ☑

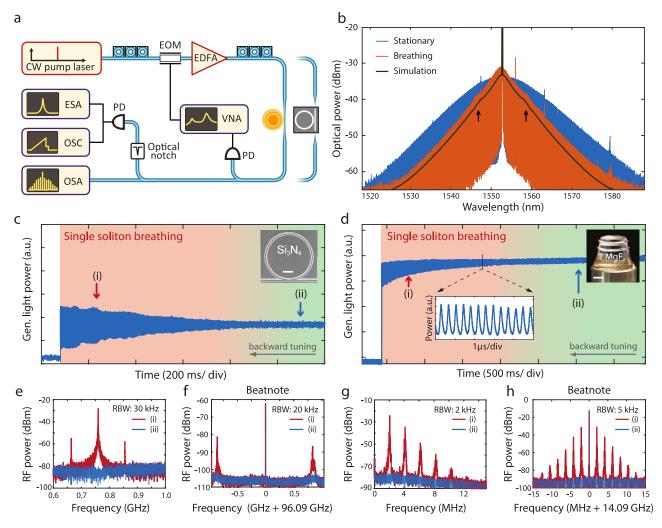


Figure 3.5 – Experimental observation of breathing solitons in Si<sub>3</sub>N<sub>4</sub> and MgF<sub>2</sub> platforms (a) A similar experimental setup is used for both platforms: A tunable continuous wave laser is used as a pump source. EDFA, erbium-doped fiber amplifier; EOM, electro-optical phase modulator; OSA, optical spectrum analyzer; PD, photodiode; OSC, oscilloscope; ESA, electronic spectrum analyzer; VNA, vector network analyser. (b) Experimental optical spectra of a stationary (blue) and breathing soliton states (red), in the 14 GHz FSR MgF<sub>2</sub> crystalline resonator. The effective detuning  $\delta$  is varied by 0.5 MHz between the two states. The simulated optical spectrum averaged over one breathing period (black line) was offset by 3 dB for better visibility. The arrows mark the positions of weak sidebands visible in both the simulated and measured spectra. (c) Generated-light power evolution for a single soliton state in the 100 GHz Si<sub>3</sub>N<sub>4</sub> microresonator as the pump is tuned backward, showing the transition from stationary state (green shading) to breathing (red shading) and final decay. The inset shows an SEM image of the microresonator used (the scale bar corresponds to 100  $\mu$ m). (d) In the MgF<sub>2</sub> crystalline resonator (see inset, the scale bar corresponds to 2 mm), the comb light evolution features a similar behaviour as in (d), when tuning backward. The inset shows the oscillations of the generated comb power, resolved with a fast photodiode and high sampling rate. (e, f) RF spectra of the generated light for a breathing (point (i) in (c, d), red trace) and stationary (point (ii) in (c, d), blue trace) soliton state respectively in the Si<sub>3</sub>N<sub>4</sub> and MgF<sub>2</sub> resonators. In (f), the 0.4 GHz span is centred at 0.8 GHz, close to the fundamental breathing frequency. The resolution bandwidth (RBW) is indicated. (g, h) Repetition rate beatnote for a breathing (i, red) and stationary (ii, blue) soliton state in the Si<sub>3</sub>N<sub>4</sub> and MgF<sub>2</sub> resonators.

#### 3.2.1 Experimental identification of breathing

We applied the so-called *backward tuning method* in order to deterministically access the breathing regime of a single soliton in a microresonator. The principle is straightforward: starting from a stable DKS state, the detuning is gradually decreased until the Hopf bifurcation is crossed. Importantly, the breathing dynamics can be unambiguously characterized only in the single soliton state, where interactions among different solitons (in a multiple soliton state) are avoided.

We experimentally verified our approach in the  ${\rm MgF_2}$  resonator as well as in the  ${\rm Si_3N_4}$  platform. Despite significant differences in the resonators properties<sup>2</sup>, both systems behave qualitatively similar when approaching and entering the breathing regime. Figure 3.5c,d show the experimental evolution of the generated light power of a single soliton in  ${\rm Si_3N_4}$  and  ${\rm MgF_2}$  optical resonators when the backward tuning is applied. The signal is obtained by detecting the out-coupled light, after attenuation of the strong pump laser with a narrow fiber Bragg grating notch filter. In both cases the system evolved from a stationary DKS on the right of each trace, to a breathing DKS, and finally switched to a homogeneous background, without a soliton. In both platforms, reaching the breathing regime coincides with a progressively increased amplitude noise of the generated light power. A detailed measurement (with an increased sampling rate) reveals that the power is oscillating, as shown in the inset of fig. 3.5d.

The oscillatory nature of the out-coupled pulse train in the breathing state can also be characterized by measuring its radio frequency (RF) spectrum on an electronic spectrum analyzer (ESA). Figure 3.5e,g show the RF spectra of the generated light for stationary and breathing DKS in both optical resonator platforms, at the points marked in fig. 3.5c,d. The stationary soliton state (blue traces) corresponds to a low-noise state of the system, while the breathing state exhibits sharp tones indicating the fundamental breathing frequency and its harmonics (red traces). For our systems, the breathing frequencies were in the range of 0.5-1 GHz for the  $\mathrm{Si_3N_4}$  microresonator (free spectral range (FSR)  $\sim 100$  GHz) and 1-4 MHz for the MgF<sub>2</sub> platform (FSR  $\sim 14$  GHz). The breather regime can also be evidenced when measuring the repetition rate beatnote on the ESA. The oscillating pulse dynamics give rise to additional sidebands around the repetition rate, spaced by the breathing frequency (see fig. 3.5f,h which compare stationary and breathing states in both platforms).

Another characteristic signature of the breathing state is observed in the optical spectrum. Figure 3.5b shows the measured spectra of both stationary and breathing single soliton based frequency combs, in a  ${\rm MgF}_2$  resonator. In the stationary state, the spectrum has a squared hyperbolic secant envelope corresponding to the stationary soliton solution, while in the breathing state, the spectrum features a triangular envelope (on a logarithmic scale), resulting from the averaging of the oscillating comb bandwidth, by the optical spectrum analyzer (see fig. 3.2d). The simulated spectrum (averaged over one breathing period) reproduces well the triangular feature. The weak sidebands on the optical spectrum are also captured on both the measured spectrum and averaged simulated spectrum (marked by arrows in 3.5b).

 $<sup>^{2}</sup>$ The Si $_{3}$ N $_{4}$  integrated microring resonators has a FSR of  $\sim$  100 GHz and Q-factors  $\sim$  10 $^{6}$  (linewidth  $\frac{\kappa}{2\pi}=150-200$  MHz). The resonators dispersion parameters are  $\frac{D_{2}}{2\pi}=2$  MHz,  $\frac{D_{3}}{2\pi}=\mathcal{O}(1$  kHz). The wavelength of the CW pump laser in experiments was set at 1553 nm, and the pump power varied from 1 to 4 W.

## 3.2.2 Breathing dynamics

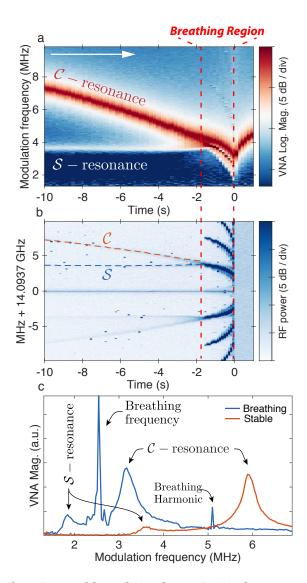
Having established a deterministic access to breathers, we next characterised the breathing dynamics. We use the VNA probing method to determine the effective laser detuning of the driven nonlinear system (see section 2.2.1).

Figure 3.6 shows the evolution of a single soliton in the  ${\rm MgF}_2$  resonator while tuning backward from the stationary state (pump power of 200 mW). During the scan, the transfer function of the system is monitored simultaneously with the comb repetition rate beatnote and total comb power. As the laser detuning is reduced, the  ${\cal C}$ -resonance consequently shifts to lower frequencies (fig. 3.6a). Interestingly, both  ${\cal C}$ - and  ${\cal S}$ -resonances are also observed in the comb beatnote measurement, appearing as features on the background noise of the electronic spectrum analyzer (dashed lines in fig. 3.6b). We ascribe this effect to the transduction of laser input noise via the response of the system (i.e. incoherent response which is identical to the probed coherent response).

Importantly, the transition from stationary to breathing soliton occurs when the  $\mathcal{C}$ - and  $\mathcal{S}$ -resonances separation is on the order of the linewidth ( $\kappa/2\pi$ ), for a detuning  $\delta=\delta\omega/2\pi\sim4$  MHz. Afterwards, in the breathing region, strong sidebands at the soliton breathing frequency and its harmonics emerge around the beatnote. The sidebands move progressively closer to the beatnote, revealing that the breathing frequency decreases for smaller detuning. In the breathing state, the transfer function (blue curve in Figure 3.6c) features a strong sharp peak at the breathing frequency that appears in between the  $\mathcal C$  and  $\mathcal S$ -resonances. From this response, the breathing frequency and the effective laser detuning can thus be measured with a good precision. Notably, the  $\mathcal S$ -resonance behavior is greatly modified in the breathing domain as it shifts together with the breathing frequency and detuning. We also observed that the transition into the breather regime is reversible by tuning the laser forward (back into the stationary state).

Figures 3.7a–d show the detailed breathing dynamics within the breathing region. In particular, the comb power is measured in two ways. First, the global evolution is monitored continuously on a DC coupled photodiode with a slow sampling of ~ 100 kSa/s (fig. 3.7a). Since the breathing oscillations are faster than this sampling rate, they appear as increased amplitude noise, which can be quantified with the relative standard deviation  $\tilde{\sigma}_{\tau}(t) = \sigma_{\tau}(t)/\mu_{\tau}(t)$ , where  $\sigma_{\tau}$  and  $\mu_{\tau}$  are the local standard deviation and mean power level over  $\tau = 1000$  samples. Second, the fast dynamics of the intracavity soliton are also recorded on a real-time oscilloscope with 120 GSa/s, but in short sequences spread over the scan. This allows the observation of the pulsed nature of the intracavity pattern (see below). The breathing oscillations in each sequence are then recovered by detecting the envelope of the resolved pulse train and down sampled (fig. 3.7c). Ultimately, the breathing dynamics could be resolved with a slower oscilloscope.

The breathing starts with a weak oscillation of the soliton pulse train power (stage i,  $\delta \sim 4$  MHz). This corresponds to a single pair of weak sidebands on the comb beatnote. For smaller detuning the breathing becomes stronger, so that the first sidebands (fundamental breathing



**Figure 3.6 – Backward tuning and breathing dynamics in the MgF**<sub>2</sub> **resonator** (a) Map of concatenated vector network analyser (VNA) traces showing the evolution of the modulation response (log scale) from stationary soliton on the right of the time axis to breathing and decay on the left (the time origin t=0 s, is set at the soliton decay). As the laser is tuned towards shorter wavelength, the effective detuning ( $\mathcal{C}$ -resonance) is reduced. The breathing starts typically when the separation of the  $\mathcal{C}$ - and  $\mathcal{S}$ -resonances is on the order of the resonator linewidth. (b) Corresponding spectrum of the comb repetition rate heterodyne beatnote. The modulation response measured on the VNA is also visible in the noise of the RF beatnote spectrum (the dotted lines correspond to the  $\mathcal{C}$ - and  $\mathcal{S}$ - frequencies determined on the VNA). The breathing is indicated by the formation of sidebands around the repetition rate beat. As the detuning is reduced, the breathing frequency decreases until the soliton is lost. (c) Recorded modulation response in the state of a breathing and stationary soliton (linear scale).

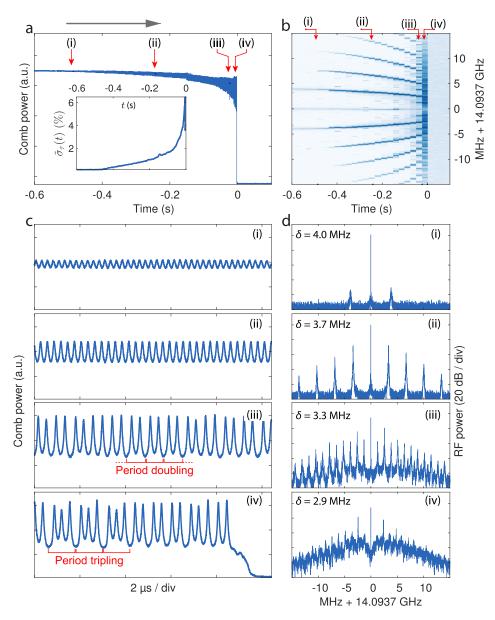
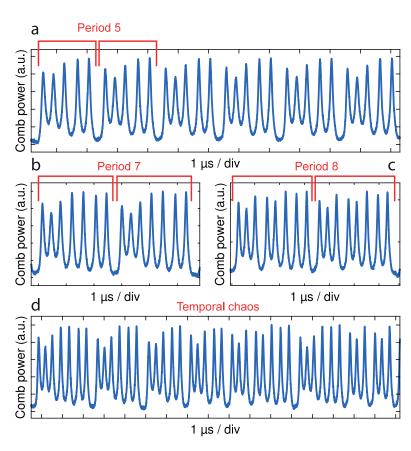


Figure 3.7 – Evolution of the breathing dynamics of a single soliton in backward tuning in the  $\mathrm{MgF}_2$  resonator (a) Generated comb light evolution within the breathing region. The inset shows the evolution of the relative standard deviation of the main trace. (b) Zoom-in spectrogram of the corresponding repetition rate beat evolution. (c) Recording of generated light power oscillations at the points (i)-(iv) highlighted in (d,e). (d) Repetition rate beat spectra in the various breathing stages (i)-(iv) highlighted in (d,e) (resolution bandwidth 2 kHz).

frequency) increase, and breathing harmonics emerge (stage ii) as the breathing pattern is not sinusoidal. At  $\delta \sim 3.3$  MHz (stage iii) the system exhibits a period doubling, which corresponds to the appearance of sub-sidebands with frequency half of the initial breathing frequency. At last, the breathing turns into strong and irregular oscillations (stage iv,  $\delta \sim 2.9$  MHz), exhibiting sporadic transitions to tripling. This coincides with a large increase in the noise pedestal around the beatnote, although the fundamental breathing frequency remains distinguishable. Finally, the soliton decays quickly thereafter. Other sections of the same trace are presented in fig. 3.8, revealing further transitions to period 5, 7 and 8 oscillations within a very irregular breathing state. Such transitions to higher periodicity, temporal chaos, as well as the soliton collapse very closely match the predicted evolution from numerical studies.



**Figure 3.8** – **Experimental observation of high periodicity breathing and temporal chaos.** The periodicity is assessed when the pattern is repeated at least twice. **(a)** Period 5 oscillations **(b)** Period 7 oscillations **(c)** Period 8 oscillations **(d)** Irregular breathing, no clear periodicity can be determined.

The combined effect of increased modulation depth and reduced breathing frequency is reminiscent of a typical characteristic of complex dynamical systems approaching critical transitions [196, 197]. In the present case, the critical event consists in the loss of the single soliton, either via collapse into the continuous background as observed in this work (switching), or via spatiotemporal instabilities [195]. When approaching a tipping point, early warning signals in

the form of a variance increase and a critical slowing down have been reported in a wide variety of systems, ranging from lasers near threshold to entire ecosystems and the climate [198–200].

We next study the breathing frequency as a function of laser detuning for a single soliton state in the  $\mathrm{MgF}_2$  resonator. The backward tuning over the breathing region was repeated for different pump power levels, and the breathing frequency was measured as a function of effective laser detuning (fig. 3.9a) using the transfer function of the system. The detuning dependence is close to linear:  $f_b \approx 1.23 \, \delta + f_b^0$ , where  $f_b$  is the breathing frequency and  $\delta$  indicates the effective laser detuning. The offset  $f_b^0$  is observed to decrease with the pump power. We performed numerical simulations based on the LLE and obtained an excellent quantitative agreement, with almost identical results (fig. 3.9a).

Note that the relation we measured is of opposite sign to a trend reported by Yu *et al.* [182], where the breathing frequency was shown to increase for reduced detuning. However, the dominant evolution of the breathing frequency matches with our observations. In ref. [182], the detuning was not accessed directly, and the measurements carried with multiple solitons in the cavity, making the validation difficult.

#### 3.2.3 Breathing region

We experimentally studied and mapped the stability chart of DKS solitons in the two-parameter space (pump power  $P_{\rm in}$  and effective detuning  $\delta$ ) of the CW-pumped microresonator system [98, 106, 201].

As noted earlier, the breathing emerges when the  $\mathcal{C}$ -resonance is tuned close to the  $\mathcal{S}$ -resonance, and their separation is on the order of the resonator linewidth. Therefore the  $\mathcal{S}$ -resonance frequency provides an estimate for the detuning value of the upper boundary of the breathing region (Hopf bifurcation). Experimentally, we monitor the  $\mathcal{S}$ -resonance frequency as the pump power is raised, while stabilizing the laser detuning ( $\mathcal{C}$ -resonance frequency) to a constant value in the stationary soliton state [165]. Figure 3.9b reports the evolution of the  $\mathcal{S}$ -resonance frequency with the pump power for the MgF $_2$  resonator, whose smaller linewidth produces narrower resonance peaks in the transfer function that are easily resolved. The obtained relation fits to a parabolic dependence and matches the Hopf boundary retrieved from simulations with a frequency offset that does not exceed twice the linewidth, showing that the breathing region can be identified even from the stationary state.

#### 3.2.4 Real-time observation of breathers

The soliton dynamics in the microresonator is studied further in the time domain by measuring the 14 GHz soliton pulse train coupled out of the  ${\rm MgF}_2$  resonator. The generated light is amplified and detected on a fast photodiode (70 GHz bandwidth) connected to a real-time oscilloscope with 45 GHz analog bandwidth (sampling rate 120 GSa/s). We note that so far, the real time sampling of successive solitons in microresonators had not been attained

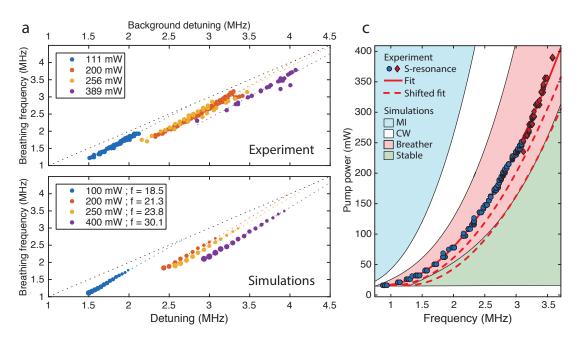
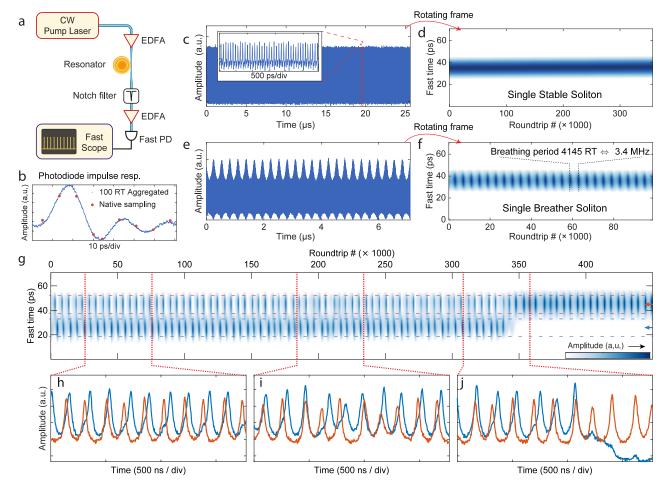


Figure 3.9 – Breathing dynamics and dependence on the parameters of the system (a) Top: Experimental determination of the breathing frequency evolution with the detuning for different pump powers, retrieved by the modulation response measurement. Bottom: Simulated evolution of the breathing frequency. (b) Dependence of the  $\mathcal S$ -resonance on the pump power, measured for a stationary soliton. This resonance provides an estimate of the detuning point at which the breathing starts. The measurements were carried with the detuning stabilized to  $\delta = 3.5$  MHz for P < 300 mW (blue dots) and  $\delta = 7$  MHz P > 300 mW (red marks). The evolution fits to a parabolic dependence. The regions were retrieved with a polynomial fitting of the boundaries from a simulated stability chart. The Hopf boundary obtained from the simulations is contained within a  $[+1,+2] \kappa/2\pi$  margin (dashed lines) to the measured  $\mathcal S$  frequency, which is in agreement with the experimental observations reported in fig. 3.6a.

due to the required high sampling bandwidth. The present configuration allows for the measurement of  $\sim 9$  samples per roundtrip and enables a coarse localization of the soliton pulse within one roundtrip as shown in Figure 3.10b,c. Since we observe that the soliton breathing dynamics evolve over a large number of roundtrips (> 1000), we aggregate together the samples contained in segments of 100 roundtrips, to achieve an effectively larger sampling rate. This produces smoother traces, revealing the impulse response of the acquisition system (matching with the photodiode response), where the instantaneous soliton peak amplitude can be reliably retrieved (fig. 3.10b). Longer traces (fig. 3.10c,e) that measure the evolution over a large number of roundtrips are divided in 100-roundtrips segments, which are aggregated and stacked. This facilitates the visualization of a spatiotemporal evolution of the cavity content over a large number of roundtrips.

The measurement procedure was first benchmarked in the single soliton state. At a pump power of 230 mW and for the effective laser detuning  $\sim 10$  MHz, the soliton is stationary as expected, with a constant amplitude (fig. 3.10d). For a smaller detuning  $\sim 3.5$  MHz, the



**Figure 3.10 – Direct observation of the spatiotemporal dynamics (a)** Experimental setup. Erbium doped fiber amplifier (EDFA); Photodiode (PD). **(b)** Photodiode response. The red dots mark the original sampling over a single roundtrip period (RT). With 9 points per period, the pulse amplitude cannot be accurately resolved. This problem is solved by aggregating 100 roundtrips to increase the effective sampling rate and retrieve the impulse response to a single soliton. **(c)** Single soliton pulse train, containing  $3.5 \times 10^5$  roundtrips. The inset shown a short section of the trace, where individual pulses can be coarsely located. **(d)**. Dividing the trace into groups of 100 aggregated roundtrips, and stacking reveals the spatiotemporal evolution of the soliton. The soliton position and amplitude is fixed as the soliton is stable. In this map, the colourmap is set to remove the ripples of the photodiode response. **(e)** Single breathing soliton pulse train. **(f)** Applying the same procedure as in (d) reveals the oscillating pulse amplitude while its position remains stable. **(g)** Spatiotemporal evolution of a breathing two-soliton state undergoing a transition to a breathing single-soliton state (switching). The panels h-j show the evolution of the amplitude of each soliton. **(h)** Traces showing a  $\pi/2$  phase difference between the breathing oscillations of the solitons. **(i)** Unstable breathing, after which the quadrature relation is restored. **(j)** Collapse of one soliton, while the other survives and remains in the breathing region.

soliton is breathing and the time trace reveals the oscillatory envelope of the soliton amplitude (fig. 3.10e). In the spatiotemporal frame, this leaves a dotted pattern at the breathing period (fig. 3.10f), where the blue shading indicates the soliton amplitude. The breathing frequency is  $\sim 3.4$  MHz corresponding to 4145 roundtrips.

### 3.2.5 Breathers synchronizations

The fast recording on the real-time oscilloscope also enables us to delineate the breathing dynamics of individual pulses in a multiple soliton state. Figure 3.10g shows the evolution of a breathing two-soliton state during a backward tuning around  $\delta \sim 2.1$  MHz. The state experiences a switching [159] where one soliton decays and the other survives. This kind of dynamics is investigated in depth in section 3.3. Furthermore, in this small detuning condition, the breathing is typically irregular and might be locally identified as period doubling or tripling, as reflected on the traces (fig. 3.10g-j). The measurement reveals that the two solitons breathe overall at the same frequency but are not in phase. In the present case, there seems to exist a preferred phase relation of  $\sim \pi/2$ . Even if the breathing is irregular and the phase relation can be locally altered as shown in fig. 3.10i, the relative phases seem to quickly recover this relation. A longer section of the spatiotemporal evolution of fig. 3.10g can be visualized in the video linked in the supplementary information of ref. [183]. Such behavior has been predicted by Turaev et al. [192], showing that the longer interaction length of breathing solitons can lead them to form bound states with a specific inter-distance and breathing phase relation. A quadrature breathing should correspond to a comparatively large soliton separation, which matches with the above case as the pulses are separated by more than the photodiode response time. However, we could not derive a clear correlation between the soliton separation and the relative breathing phase.

We have recorded the spatiotemporal evolution of several dual breathers realizations and analyzed the relative breathing phase (fig. 3.11). The detuning is overall larger than the case shown in fig. 3.10g, so that the breathing is more regular. The breathing synchronization is assessed in the following way: a cut of the spatiotemporal map is extracted along the peak corresponding to the position each soliton. The two resulting time series are band-pass filtered to keep only the fundamental breathing harmonic and the analytical signal of each filtered trace is computed via Hilbert transform. The relative phase is detected by taking the argument of the quotient between the two analytical signals.

Typical breathing behavior are displayed in fig. 3.11a,b,c, showing out of phase, in phase and quadrature breathing. Besides these three cases, other phenomenon were observed punctually such as synchronization with a phase multiple of  $\pi/4$ , of incomplete synchronization at the onset of breathing as shown in fig. 3.11d. The spatiotemporal evolution of fig. 3.11d can be visualized in animated format in the supplements of ref. [183]

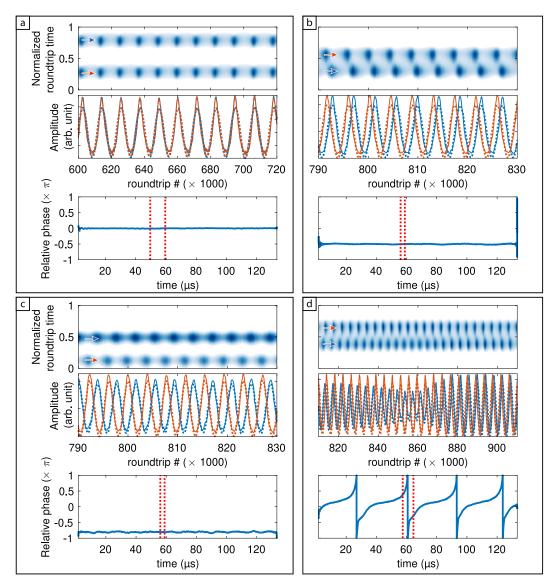


**Figure 3.11 – Relative breathing phase of two solitons.** Four realizations are presented (a,b,c,d). For each, the top panel exposes the spatiotemporal map of a fraction of the trace. The blue and red curves of the middle panel display the evolution of the amplitude of each soliton. The plain (dashed) lines show the raw (filtered) signals. The bottom panel shows the evolution of the relative breathing phase across the entire trace. The dashed red interval marks the section of the trace displayed in the middle and top panels. Upon various two breathing soliton state realizations, the relative breathing phase is observed to vary. **(a)** Out-of-phase breathing. **(b)** In-phase breathing. **(c)** Quadrature breathing. **(d)** At the breathing onset, the phase continuously accumulates but the breathing tends to synchronize when close to in phase.

# 3.3 Multi-soliton states switching<sup>3</sup>

This section, describes and studies a method allowing the number of DKSs in a microresonator to be reduced (i.e. from N to N-1), and thereby the reliable access to the single soliton state. It relies on the fine interplay between the transient chaotic state of breathing solitons and the thermal nonlinearity of the resonator that lifts the states degeneracy.

# 3.3.1 Observation of switching between dissipative Kerr soliton states by laser backward tuning

For most applications of Kerr combs, it is desirable to operate in the single soliton regime, which features a smooth spectral envelope. However, most common soliton generation procedure such as 'forward' laser tuning as described in section 2.1.3, are typically stochastic and thus cannot control the number of solitons formed in the resonator. Moreover, from a pure LLE perspective where solitons do not interact, the states containing multiple solitons are degenerate in the parameter space, which a priori forbids the transition between states containing different number of solitons via a manipulation of the pumping parameters. Some studies observed the pairwise interactions of solitons when the pump was tuned [113, 114], but no control was achieved.

Remarkably, we observed that after a multi-soliton state generation in the  $\operatorname{MgF}_2$  resonator, via forward tuning, reversing the tuning direction to perform a slow 'backward' tuning triggers the successive extinction of intracavity solitons (soliton switching) down to the single soliton state  $(N \to N-1 \to \ldots \to 1)$ . Figure 3.12a shows the evolution of the generated comb light in a  $\operatorname{MgF}_2$  microresonator, where switching from a state with six solitons to the single soliton is performed. Strikingly, the generated comb light reveals a *regular staircase* pattern with equal step height. The exact soliton number in each step can be precisely inferred from the step height. Each transition between multiple-soliton states occurs with the extinction of *one* soliton at a time, which is confirmed by looking at the inferference pattern on the comb spectrum (cf. panels in fig. 3.12c–h). The feature is almost identical over multiple experimental runs (using the same tuning speed and pump power) *regardless* of the initial soliton number N. Note that the phenomenon was successfully observed for a strong driving of the microresonator with a pump power of  $P_{\rm in} \sim 200$  mW.

In the experiments, the backward tuning process must be adiabatic to induce the successive reduction of the soliton number: the thermal equilibrium is required at each multiple-soliton state. This prerequisite is satisfied by choosing a tuning speed much slower than the thermal relaxation rate that depends on the effective mode volume and the thermal diffusivity of a microresonator [202]. For the  $MgF_2$  microresonator used here the backward tuning speed is chosen to be  $\sim 300$  kHz/s, while the forward tuning speed is  $\sim 2.5$  GHz/s. In this way all soliton

<sup>&</sup>lt;sup>3</sup>The results of this section are partially adapted from the publication: H. Guo et al., "Universal dynamics and deterministic switching of dissipative Kerr solitons in optical microresonators", *Nature Physics* 13.1 (Jan. 2017), pp. 94–102.

Solitons generation (b) Switching Gen. light power (arb. unit) Backward Tuning Relative Laser Freq. 30 20 10 N=6 0 5 0 5 180 200 10 15 20 40 60 80 100 120 140 160 Time (ms) Time (s) N=6 N=5 (c) (d) N=4 (e) Power 20 dB/div (h) (f) N=3 N=2 (g) N=1

states ( $\leq N$ ) are accessible. The backward tuning was also studied in  $\mathrm{Si_3N_4}$  microresonators, where the deterministic soliton switching to the single soliton state was also observed [159].

**Figure 3.12 – Experimental evidence of soliton switching via backward tuning (a)** Evolution of the generated comb light in blue (cavity transmission where the pump light is rejected) when generating the multi-soliton state via rapid forward tuning. The relative laser frequency is shown in red and was measured by counting the beatnote against an ulstrastable laser. The reference frequency is taken relative to the cold cavity position. (b) Evolution of the generated comb light during the slow backward tuning of the laser. The red line shows the relative laser frequency. (c-h) Frequency comb optical spectra measured during the backward tuning (the red dots in (a) mark the end of the OSA scan). As the number N of DKS is decreased, the spectral interference pattern is modified, until the single soliton state is reached revealing a sech<sup>2</sup> profile.

Center wavelength 1553.0 nm, Span 50 nm

#### 3.3.2 Deterministic switching of soliton states

We further investigate the transitions of soliton states by applying the VNA probing technique simultaneously. A multiple-soliton state with N=6 solitons was generated, the slow backward laser tuning subsequently applied. The results are displayed in fig. 3.13.

The experiments reveal a relationship between the evolution of the transfer function and the soliton switching. As expected, the backward tuning leads to the reduction of the detuning and the C-resonance is slowly moving toward the S-resonance. When both peaks merge, the switching is triggered, which results in a drop in the comb power as one soliton is lost. The

conclusions of section 3.2, indicate that the switching  $(N \to N-1)$  therefore repetitively occurs in a breathing region, where the  $\mathcal{C}$ - and  $\mathcal{S}$ -resonances merge. During the backward tuning, the switching can therefore be predicted by monitoring the  $\mathcal{C}$ - and  $\mathcal{S}$ -resonances separation in the VNA response, which provides a convenient tool to control the soliton states and induce switching on demand.

After the switching, the  $\mathcal{C}$ -resonance abruptly separates from the  $\mathcal{S}$ -resonance, meaning that the effective detuning in increased, although the laser frequency is not tuned. Simultaneously, while still being Kerr locked, the  $\mathcal{S}$ -resonance magnitude is reduced to a lower level than the previous state, since the number of solitons is reduced by one. In the absence of solitons (N=0), the  $\mathcal{S}$ -resonance is absent in the transfer function

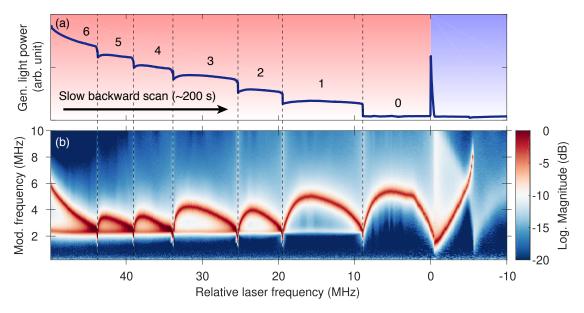


**Figure 3.13 – Deterministic switching of soliton states.** (a) Evolution of the generated comb light obtained from the  $\mathrm{MgF}_2$  microresonator when the pump is tuned backwards from a multiple-soliton state with N=6 (effectively red-detuned) to the effectively blue-detuned regime. (b) Concatenated VNA traces corresponding to the evolution depicted in (a). The evolution is plotted as a function of the laser frequency relative of the cold cavity frequency.

The switching in the breathing region was further investigated by performing a real-time imaging of a switching event, using the method exposed in section 3.2.4. The result was already exposed in fig. 3.10g. It reveals that the switching occurs when two solitons are strongly breathing. This type of event thus occurs for high pump power and strong breathing, which tends to indicate that it is triggered by the transient chaotic effect described in section 3.1. The decay of soliton is therefor triggered by minor fluctuations in this very unstable regime. Nonetheless, it remains surprising that not all the DKSs in a state are lost altogether in this region. A spontaneous thermal feedback mechanism is in fact at the core of the successive switching ability, which is described in the following section.

## 3.3.3 Thermally enabled transitions of soliton states

We attribute the successive soliton switching in backward tuning to the thermal nonlinearity of optical microresonators. Due to material absorption, the intracavity energy thermally shifts the cavity resonance via thermal expansion and thermal change of the refractive index. The 'hot' cavity resonance is therefore  $\widetilde{\omega}_0 = \omega_0 - \Delta \omega_\theta$ , where  $\Delta \omega_\theta$  is the thermally induced resonance shift which. In the soliton state and assuming thermal equilibrium, it is approximately proportional to the energy of the intracavity field:

$$\Delta\omega_{\theta}(N) = \omega_{0} (\alpha_{L} + \alpha_{n}) \Delta\theta(N) \propto E_{C} + N \cdot E_{S}$$
(3.1)

where  $E_C$  is the energy of the background component,  $E_S$  is the energy of one soliton and N the number of solitons. Thus, the effective detuning can be expressed as

$$\delta\omega = \omega_0 - \omega_p - \Delta\omega_\theta = \delta\omega_{abs} - \Delta\omega_\theta \tag{3.2}$$

where  $\delta \omega_{abs} = \omega_0 - \omega_p$  indicates the absolute detuning, i.e., the laser frequency relative to the cold cavity.

Each time a soliton is lost, through the process of transient chaos, the thermal shift  $\Delta\omega_{\theta}$  is reduced and thus the effective detuning is increased, bringing the new multi-soliton state back into the stable existence range. Therefore, this reopens the possibility of tuning the laser further backwards (reducing  $\delta\omega$ ), to induce a new switching and finally deterministically reach the single-soliton state.

This thermal model describes well the curved shape of the steps in the switching 'staircase' of the  $\mathrm{MgF}_2$  resonator (see fig. 3.15), compared to the straight and abrupt steps that were observed in the  $\mathrm{Si}_3\mathrm{N}_4$  microresonator [159]. The larger effective mode volume and physical size of the  $\mathrm{MgF}_2$  resonator as well the thermal coefficients of the material imply a longer thermal relaxation time. The slow thermal recoil of the resonance leads to curved trajectories, as the thermal drift dominates just after the switching but as the resonator thermalizes, the laser backward tuning reverses the effective tuning direction.

## 3.3.4 Thermal lifting of the multi-soliton states degeneracy

We performed numerical simulations<sup>4</sup> based on the LLE with the additional thermal relaxation equation included. The detuning term was modified to  $\delta\omega \to \delta\omega_{abs} - \Delta\omega_{\theta}$  and the dynamics of the latter is defined by the following equation

$$\frac{\partial \Delta \omega_{\theta}}{\partial T} = \frac{1}{\tau_{\theta}} \left( g_0 \frac{n_{2\theta}}{n_2} |A|^2 - \Delta \omega_{\theta} \right) \tag{3.3}$$

Here  $\tau_{\theta}$  is the thermal relaxation time and  $n_{2\theta}$  is the coefficient of thermal nonlinearity (which depends on the absorption among other things). Backward scan simulations were

 $<sup>^4</sup>$ The numerical simulations were performed by Hairun Guo, more detail can be found in ref. [159]

carried out with a slow detuning variation to provide thermal equilibrium. If the scan rate was sufficiently small, gradual decrease of soliton numbers on one per step was observed. Figure 3.14 shows an example of simulation with the thermal effects, using typical parameters of  ${\rm Si_3N_4}$  microresonator. Forward and backward tuning stages are indicated with blue and red lines correspondingly. The consecutive switchings are well reproduced, as reflected by the stair-like trace of the intracavity power. This brings an additional verification that the deterministic soliton switching is enabled by the thermal nonlinearity of the microresonator. We also observed that the breathing regime is characterized by oscillations in the intracavity power and occurs in the vicinity of the switching points in each step (see inset in fig. 3.14). We observed that at larger scan rates the switching occur faster and several solitons can be erased at each step, instead of a single one. This was also observed experimentally, where faster scanning rates reduce the controllability of the switching and typically lead to the loss of many if not all solitons.

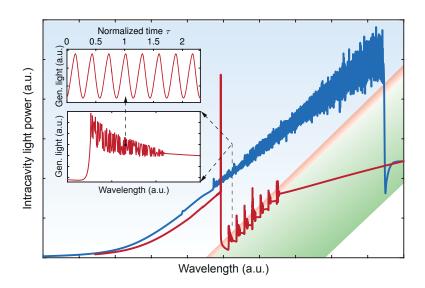


**Figure 3.14 – Simulated backward switching procedure** Simulation of the intracavity energy  $|\psi|^2$ , illustrating the backward tuning method. The generation of a stable multiple soliton state is achieved by forward tuning of the pump laser (blue curve). The backward tuning is applied next (red curve) in order to reach the low-detuning boundary of the soliton existence range where the breathing regime (increased noise) and switching effect (step features) occur, allowing the transition to the single-soliton state. The blue shading corresponds to the region where modulation instability occurs, the green marks stationary solitons existence and the red area indicates breathing. The lower inset details the single soliton breathing and switching during the backward tuning. The upper inset shows the oscillations of the power for a fixed laser frequency in the single breathing soliton state.

It was found in simulations at fixed pump power and thermal parameters, that the frequency spacing between the transitions (step width) were fixed and did not vary for different rounds of simulations. We also checked that in the absence of the thermal effects the soliton states are degenerate. Assuming the thermal equilibrium situation, we found that thermal effects

can be well accounted for via a simple affine transform of the pure Kerr simulation results in the space  $(\zeta_0, |\psi|^2)$ , by performing the change of coordinate

$$\zeta_0 \to \zeta_{abs} + (n_{2T}/n_2) |\psi|^2$$
. (3.4)

In fig. 3.15a, this transform was applied to the analytical expression of the energy in multisoliton states eq. (1.74) with different number N of DKS (black dashed lines). They reveal a displacement of the soliton existence range between different soliton states as a consequence of the thermal nonlinearity. When the thermal effects in the simulations are disabled, the soliton steps are well aligned and the soliton existence ranges are again degenerate with respect to the soliton number (N), as shown in fig. 3.15d. No successive soliton switching is therefore observed in the backward tuning.

The soliton switching in both  $\mathrm{Si_3N_4}$  and crystalline  $\mathrm{MgF_2}$  resonator, and our simulations reveals that backward tuning represents a universal approach to the generation of a single soliton state in microresonators, provided that the thermal locking can be achieved and the pump power is strong enough to access the transient chaotic region.

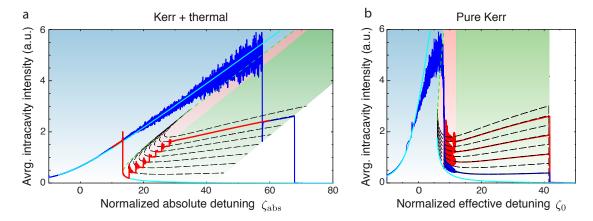


**Figure 3.15 – Numerical simulation showing the thermal lifting of the multi-soliton states degeneracy**. Numerical simulations (normalized units) and analytical solutions of the backward tuning in  $\mathrm{Si_3N_4}$ . In (a), the thermal effects are included, while they are disabled in (b). Blue lines indicate the initial excitation of a multiple-soliton state in the forward tuning. Red lines indicate the backward tuning. Light blue lines indicate the tilted resonance profile of the homogeneous solution. Dashed green lines indicate the unstable branch. The red area indicate the breathing region. The green area indicates the formation of stable solitons. The dashed lines show analytical description of soliton steps, with analytical solution of soliton states in the system according to eq. (1.74).

# 3.4 Intermode breathing<sup>5</sup>

In this section, a novel type of breathing mechanism is characterized. It is triggered by avoided mode crossings (abbreviated as AMX hereafter) and occur within a laser detuning range where conventionally stationary (i.e. stable) DKS are expected from the pure LLE model. As such, this new breathing soliton is referred to as inter-mode breather soliton and forms a new class of nonlinear instabilities.

# 3.4.1 Presentation and modeling

AMX are ubiquitous phenomena in multi-mode microresonators. Most microresonator platforms today are multi-mode either due to fabrication limitations (as in the crystalline platform) or on grounds to engineer the waveguide dispersion (in  $\mathrm{Si_3N_4}$  photonic chips). Therefore, they are prone to having inter-mode coupling, as described in section 1.2.2. It has been shown that AMXs can prevent soliton formation [166] or, if sufficiently weak and rare, produce local alterations of the dispersion that lead to the formation of dispersive waves, which induce a soliton spectral recoil of DKS as exposed in section 2.3.3. They are shown here to lead to the destabilization and breathing of DKSs. The breathing phenomenon was experimentally demonstrated in our two microresonator platforms and the results in  $\mathrm{MgF_2}$  are shown here.

A theoretical description the dynamics was derived by my colleague Hairun Guo [203] and is summarized here. It is based on a pair of coupled LLE (equivalently two sets of coupled mode equations) describing the field in each mode and adding a linear (e.g. via scattering) and nonlinear coupling (via cross phase modulation) between the two mode families. In a weak-coupling limit, one can assume that the DKS remain supported in a primary mode family (" $\mathcal{P}$ ") which is linearly coupled to a second crossing mode family (" $\mathcal{C}$ "). The integrated dispersion of the primary soliton-supporting mode family is depicted in fig. 3.16a and is defined as

$$D_{\text{int}}^{(\mathcal{P})}(\mu) = \omega_{\mu}^{(\mathcal{P})} - \omega_0^{(\mathcal{P})} - \mu \cdot D_1^{(\mathcal{P})}$$
(3.5)

where  $\omega_{\mu}^{(\mathcal{P})}$  indicates the resonance frequency over the relative mode index  $\mu$ , Relative to the frequency grid spaced by  $D_1^{(\mathcal{P})}$ , the crossing mode family has its resonance frequencies given by

$$\Delta(\mu) = \omega_0^{(C)} - \omega_0^{(P)} + \mu(D_1^{(C)} - D_1^{(P)}). \tag{3.6}$$

An AMX therefore occurs around the mode satisfying  $D_{\mathrm{int}}^{(\mathcal{P})}(\mu) \approx D_{\mathrm{int}}^{(\mathcal{C})}(\mu) + \Delta(\mu)$ , and we denote G the linear coupling between the primary and the crossing mode families. In most cases,  $\Delta \gg D_{\mathrm{int}}^{(\mathcal{C})}$ , and the crossing mode family appears almost as a slope in the frame at  $D_1^{(\mathcal{P})}$  and the condition simplifies to  $D_{\mathrm{int}}^{(\mathcal{P})} \approx \Delta$ .

Moreover, a soliton-based frequency comb is dispersionless as it consists in equally spaced teeth, such that it appears as a straight line in fig. 3.16. The soliton repetition rate can differ

<sup>&</sup>lt;sup>5</sup>The results of this section are partially adapted from the publication: H. Guo et al., "Intermode Breather Solitons in Optical Microresonators", *Physical Review X* 7.4 (Dec. 2017), p. 041055. ☑

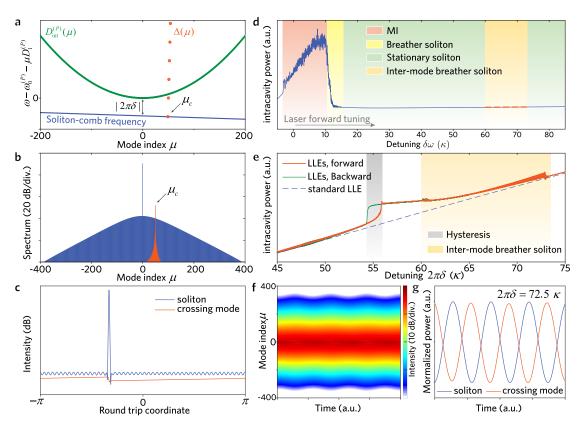


Figure 3.16 - Numerical simulation of an inter-mode breather soliton in a Kerr microresonator. (a) Integrated dispersion of a (primary) soliton-supporting mode family (green dots) in which the parabolic profile indicates the anomalous dispersion in this mode family. In the same frame, the crossing mode family shows a sloped profile corresponding to  $\Delta(\mu)$ (red dots). Once the soliton-based frequency comb is formed with a detuning  $(\delta)$ , the solitoncomb frequency is nearly constant  $(-2\pi\delta)$  (blue line), implying equal distance between the comb teeth. The slight slope corresponds to a change in the FSR (compared to  $D_1^{(P)}/2\pi$ ) as a result of the soliton central frequency shift caused either by a dispersive wave induced soliton spectral recoil or by the Raman self-frequency shift. Thus, the phase matching between the soliton and the wave in the crossing mode ( $\mu_c$ ) is  $\Delta(\mu_c) + 2\pi\delta \approx 0$ . (b) Simulated single-solitonbased frequency comb in the primary mode family (blue lines) and a narrow-band waveform in the crossing mode family (orange lines). (c) Intracavity field patterns in both mode families. (d) Intracavity power trace over the laser detuning, based on a standard LLE model in the absence of inter-mode interactions (blue line). Three stages, modulation instability (MI) regime (red area), breather soliton (yellow area) and stationary soliton (green area), are marked as typical transitions of frequency comb states in the generation process. The inter-mode breather soliton exists in the region where stationary DKS would be expected (orange area). (e) DKS in the presence of inter-mode interactions (based on the coupled LLEs model) show a different behavior, including a hysteretic power transition (gray area) and an oscillatory behaviour (orange area). (f) Spectral envelope evolution of a single inter-mode breather soliton. (g) Outof-phase oscillations in the energy of the soliton and the crossing mode waveform.

from  $D_1^{(\mathcal{P})}$  such that this line can be tilted. Therefore, at a given detuning  $\delta\omega$ , the soliton can get phase-matched to a crossing mode  $\mu_c$  given by:  $2\pi\delta\omega + \Delta(\mu_c) = 0$ .

In a frame that is co-traveling with the waveform in the primary mode family (free spectral range  $D_1^{(\mathcal{P})}/2\pi$ ) centered at the pump frequency  $(\omega_p)$ , the two sets of coupled mode equations are written as:

$$\frac{\partial \tilde{A}_{\mu}^{(\mathcal{P})}(t)}{\partial t} = \left[ -\frac{\kappa^{(\mathcal{P})}}{2} + i \left( \delta \omega + D_{\text{int}}^{(\mathcal{P})}(\mu) \right) \right] \tilde{A}_{\mu}^{(\mathcal{P})} - i G \tilde{A}_{\mu}^{(\mathcal{C})} + \delta_{\mu,0} \sqrt{\kappa_{\text{ex}}} s_{\text{in}} 
- i g^{(\mathcal{P})} \mathcal{F}_{T} \left[ \left| A^{(\mathcal{P})} \right|^{2} A^{(\mathcal{P})} \right]_{\mu} - i g^{(\mathcal{C}-\mathcal{P})} \mathcal{F}_{T} \left[ 2 \left| A^{(\mathcal{P})} \right|^{2} A^{(\mathcal{P})} \right]_{\mu}$$
(3.7)

$$\frac{\partial \tilde{A}_{\mu}^{(C)}(t)}{\partial t} = \left[ -\frac{\kappa^{(C)}}{2} + i \left( \delta \omega + D_{\text{int}}^{(C)}(\mu) + \Delta(\mu) \right) \right] \tilde{A}_{\mu}^{(C)} - i G \tilde{A}_{\mu}^{(P)} 
- i g^{(C)} \mathcal{F}_{T} \left[ \left| A^{(C)} \right|^{2} A^{(C)} \right]_{\mu} - i g^{(C-P)} \mathcal{F}_{T} \left[ 2 \left| A^{(P)} \right|^{2} A^{(C)} \right]_{\mu}$$
(3.8)

where  $\kappa^{(\mathcal{P})}$  and  $\kappa^{(\mathcal{C})}$  indicate the cavity decay rates,  $g^{(\mathcal{P},\mathcal{C})}$  is the single photon Kerr frequency shift of each respective family. The single photon Kerr frequency shift through cross-phase modulation is given by  $g^{(\mathcal{C}-P)} \propto 1/V_{\mathrm{eff}}^{(\mathcal{C}-P)}$ , depends on the effective nonlinear mode volume overlap. Note that if the nonlinearity of the mode family  $\mathcal{C}$  is neglected as well as the XPM, the model can be simplified to a single modified LLE equation with a complex response term added, as exposed in the supplement of ref. [203].

Figure 3.16 shows a simulation based on the CME of a single-soliton-based frequency comb in the presence of inter-mode interactions. The soliton comb envelope in the primary mode family remains overall a sech<sup>2</sup>-profile. In the crossing mode family a narrow-band spectral waveform is generated in the mode  $\mu_c$  is phase-matched to the cavity soliton. It produces a single enhanced tooth of the overall soliton comb spectrum (fig. 3.16b). This enhanced comb tooth then behaves similarly to a dispersive wave [172], which causes a temporal oscillation in the intracavity field pattern (fig. 3.16c), and induces a soliton recoil such that the comb envelope is shifted in a spectral direction opposite to that of the dispersive wave. The spatial pattern in the crossing mode family is almost homogeneous but features a power step induced by the soliton via the cross-phase modulation (fig. 3.16c).

When tuning  $\delta\omega$ , the intracavity energy undergoes an abrupt transition mainly caused by the formation of the power-enhanced wave localized in the mode  $\mu_c$  of the crossing mode family (Fig. 3.16e). Comparing traces in both forward (increased detuning) and backward (decreased detuning) scans of the detuning, a hysteretic behavior on the soliton power is revealed, which is in agreement with the analytical model proposed in ref. [172]: it is a result of the single-mode dispersive wave induced soliton spectral recoil that leads to a modification of the phase matching criterion and entails a power bistability with respect to the detuning.

Interestingly, in close vicinity to the hysteresis, we discover the inter-mode breathing dynamics as indicated by oscillations and increased amplitude jitter in the energy trace (Fig. 3.16e).

A periodic spectral modulation is observed in the simulation (Fig. 3.16f), which reveals an oscillation of the soliton pulse duration – an characteristic feature of breathing solitons. Moreover, a closer analysis reveals that energy is periodically exchanged between the soliton and the waveform in the crossing mode family, where *out-of-phase* power oscillations are observed (Fig. 3.16g).

#### 3.4.2 Experimental results

The novel inter-mode breather solitons were experimentally obtained in the  ${\rm MgF}_2$  crystalline microresonator and confirmed in chip-scale  ${\rm Si}_3{\rm N}_4$  microresonators.

The experimental study focuses on the soliton dynamics when the effective detuning is well within the stationary soliton existence range such that the  $\mathcal{C}$ - and  $\mathcal{S}$ -resonances are far separated. While sweeping the laser frequency, such that the effective detuning is continuously changed but remains within the soliton existence range, we observed the appearance of a breathing feature (Fig. 3.17b,c) in the form of sidebands on the RF beatnote of the comb with a fundamental breathing frequency of  $\sim$  3 MHz. Concomitantly, in the system's response, a strong-amplitude tone appears at the same frequency and close to the  $\mathcal{S}$ -resonance. These breathing characteristics emerged only in a narrow detuning range around  $\delta \sim$  12.8 MHz. We noted that the breathing frequency slightly changes with the detuning, and was increasing with the detuning in the presented case (Fig. 3.17c). The predicted abrupt power transition was also observed but the hysteretic behavior could not be resolved<sup>6</sup>

Furthermore, the energy exchange regime in the inter-mode breather soliton was experimentally validated (see Fig. 3.18), by comparing the power in the phase matched mode and the power of the soliton. Using a waveshaper (operational wavelength 1527 – 1600 nm, see sketch in Fig. 3.18a), the power-enhanced modes  $\mu_c = 47$  and  $\mu_c = -89$  were selectively filtered (Fig. 3.18b). Their oscillatory power evolution (due to the inter-mode breathing) were compared to that of a portion of the single-soliton-based frequency comb obtained through a 0.8 nm band-pass filter. In this way, we observed that the power in the mode  $\mu_c = 47$  showed an *out-of-phase* oscillation with respect to the soliton power, while the power in the mode  $\mu_c = -89$  oscillates *in-phase* (see Fig. 3.18c). These observations are in excellent agreement with our simulations (Fig. 3.16g), implying that the wave mainly localized in the mode  $\mu_c = 47$  of the crossing mode family is actively interacting with the soliton in the primary mode family, and is causing the breathing through energy exchange. In contrast, power-enhanced waves that are oscillating in-phase do not lead to breathing dynamics.

 $<sup>^6</sup>$ The hysteresis was nonetheless resolved in the  $\mathrm{Si_3N_4}$  resonator [203].

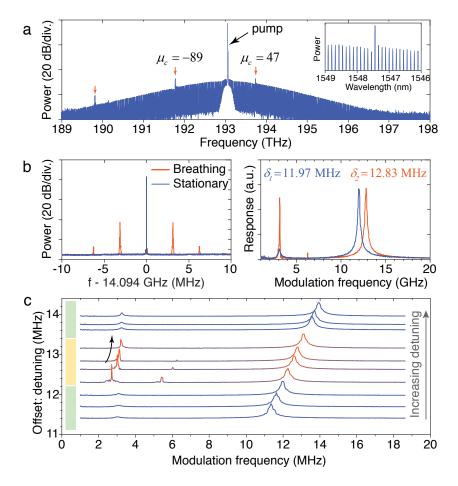


**Figure 3.17 – Observation of an inter-mode breather soliton (a)** Experimentally generated single-soliton-based frequency comb exhibiting spikes (i.e. enhanced power in comb teeth) from inter-mode interactions. Inset: zoomed-in spectrum around the mode  $\mu_c$  = 47. **(b)** Beatnote measurements (left) and VNA measurements (right) for both the stationary soliton state and the inter-mode breathing state. **(c)** Evolution of the response when increasing the laser detuning. The soliton features breathing in the detuning range 12.3 – 13.2 MHz where a strong frequency tone (and harmonics) is observed close to the  $\mathcal{S}$ -resonance. The colorbar marks the region of breathing which is within the stationary soliton existence range. The curved arrow marks the shift of the breathing frequency with an increase of the detuning.

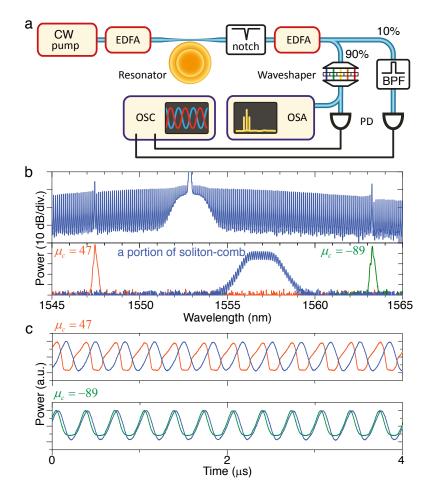


**Figure 3.18 – Observation of periodic energy exchange in an inter-mode breather soliton state (a)** Schematic of the experimental setup. EDFA: erbium-doped fiber amplifier; BPF: bandpass filter; PD: photo-detector; OSC: oscilloscope; OSA: optical spectral analyzer. **(b)** Generated single-soliton-based frequency comb in the MgF<sub>2</sub> microresonator (upper) and filtered components (lower) by using a waveshaper and by a bandpass filter. **(c)** Recorded evolution of the power in a single filtered comb mode,  $\mu_c = 47$  (red) and  $\mu_c = -89$  (green) compared to a "regular" filtered portion of the soliton spectrum (blue line). The power in  $\mu_c = 47$  shows an out-of-phase oscillation to the soliton (upper), while the power in  $\mu_c = -89$  shows an in-phase oscillation (lower).

#### 3.4.3 Mode crossing-induced multi-solitons breathing and destabilization

We further experimentally confirmed that inter-mode interactions can induce soliton decay as well as soliton switching. The abrupt power transition as well as the breathing within the stationary soliton existence range can perturb states with multiple DKSs, leading to a decrease in the number of solitons inside the resonator (i.e. soliton switching). This can first be observed by sweeping the pump forward across the resonance and observe the distribution of the steps that characterize the soliton states<sup>7</sup>. The multi-soliton states are more sensitive to AMX-induced dispersive wave excitation, which can lead to the decay of several solitons in the cavity. In that case, the multi-soliton states can be detuned over an effective existence range that is smaller than predicted by the LLE. This phenomenon was explored numerically by Zhou *et al.* [117].

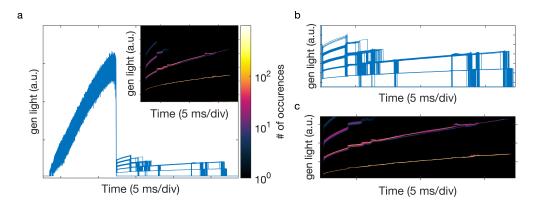


**Figure 3.19 – Multi-soliton states destabilization triggered by AMX.** (a) A forward scan over a resonance was repeated more than 1500 times and the generated light power of  $\sim$  600 realizations is shown. Multi-soliton states are stochastically created for each scan realization and random switching can occur between then when the detuning is increased. The inset shows The inset shows a color-coded histogram of the recorded soliton steps (for the full dataset), revealing that lower soliton numbers is more likely and that multi-soliton states are less likely to be sustained at large detuning. (b) Focus on the transitions between the states, which occur at similar detuning position. (c) Histogram focused on the single and two soliton steps, showing small power deviations associated with AMX excitation. They coincide with the states transitions.

We have also seen that the relative position of the solitons can be changed as the detuning is tuned across the phase matching point of certain AMX dispersive waves<sup>8</sup>. This is characterized by a modification of the spectral interference pattern of the multi-soliton state and is accompanied by slow and weak oscillations in the comb power and repetition rate beatnote, as shown in fig. 3.20. The frequency of these oscillations is smaller than the regular breathing solitons or AMX breathers frequency. We measured it to be around 1.5 MHz, while the  $\mathcal{S}$ -resonance is typically between 3 and 5 MHz. A strong hysteresis of the AMX dispersive wave power was also observed in the spectrum, when changing the detuning back and forth around this breathing point.

<sup>&</sup>lt;sup>7</sup>Similar observations are reported in the SI of ref. [9]

 $<sup>^8\</sup>mbox{A}$  similar effect is reported by Victor Brasch in his thesis

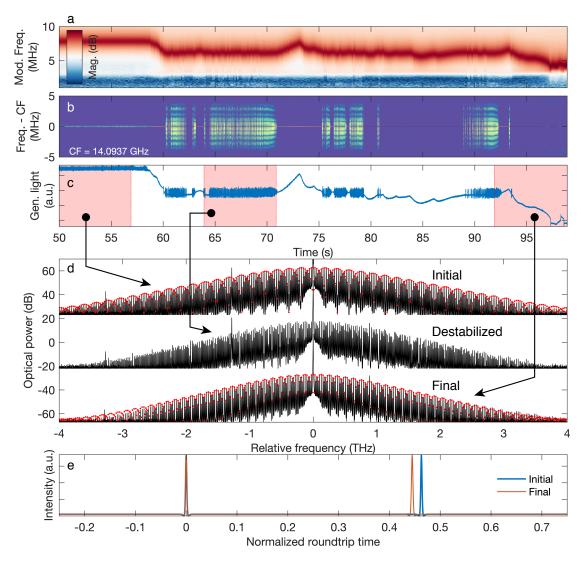


**Figure 3.20 – Two solitons showing interactions triggered by AMX.** Evolution of the state as the detuning is tuned across the region of destabilization. (a) Evolution of the VNA response. Note that the  $\mathcal{S}$ -resonance around 3 MHz is not perturbed as in regular breathers. (b) Spectrogram of the repetition rate. When the detuning reaches  $\sim 6.1$  MHz, sidebands appear on the beatnote. Note that the frequency of these sidebands is difference than the  $\mathcal{S}$ -resonance. (c) Evolution of the generated comb light power. In this breathing region, the trace displays added noise. The red shaded area show the acquisition time of the spectra below. (d) Three optical spectral acquired for a detuning above (top, labeled initial), within (middle) and below (bottom, labeled final) the destabilization region. The red dots correspond to a fit of the spectral envelope. In the destabilized state, the spectral interference pattern is smeared, indicating an evolution of the solitons' relative position, such that the initial and final state have different relative positions. (e) Reconstructed intracavity waveform based on the fit of the spectral pattern in (d). The initial and final state correspond to different soliton relative separation.

## 4 Microcomb stability and control

"You can't always get what you want You can't always get what you want You can't always get what you want But if you try sometimes you might find You get what you need"

LET IT BLEED
THE ROLLING STONES

#### 4.1 Introduction

This chapter reviews the microcomb stabilization strategies that have been attempted during this work. The aim is to reduce the frequency excursions of the comb's two degrees of freedom: the pump frequency  $f_{\rm p}$  and the line spacing  $f_{\rm rep}$ .

We must distinguish between two forms of instability when seeking to improve comb stability. On one hand we seek to reduce the *frequency instability* of the comb parameters. Just like in the case of a quartz oscillator, the goal here is to reduce the impact of the environmental factors on the comb, such that its characteristic frequencies do not change over time. The first sections of the chapter describe how the microresonator can be used as an optical reference and how thermal stability improvements lead to reduced instability. With a more stable system, it is possible to study the dynamics with a better precision and to average quantities over a longer period of time. This will prove crucial in the next chapter, where low phase noise measurements are performed with cross correlations, which require stable operation for several hours.

On the other hand, the traditional understanding of frequency comb stabilization refers to the *phase locking* of the two degrees of freedom to some reference oscillator. The goal in this case is

to reduce the frequency excursions relative to the reference oscillator. In these configurations, the microresonator is no longer setting the rhythm, but must be stabilized to the reference oscillator. The typical example is optical frequency synthesis, where  $f_{\rm rep}$  and  $f_{\rm CEO}$  are stabilized to some reference RF oscillators, allowing a direct link from RF to optics. However, a number of other configurations are used, such as the stabilization of two individual tooth of the comb to two optical references [129], or the stabilization of one teeth in the optical domain combined with the stabilization of  $f_{\rm rep}$  to an RF oscillator. The latter situation is interesting in the case of crystalline resonator-based combs as the pump line is directly controlled and the repetition rate quantity is directly measurable. These phase locking configurations are typically done via feedback control, which require a way to measure a quantity, compare it to the reference and finally actuate on the system to keep the quantity close to the target value. The goal of this chapter is not to provide a thorough quantitative comparison of the locking techniques, but instead provide an exposition of the stabilization schemes and comb actuation strategies that were tested in the framework of this thesis (presented in fig. 4.1), and to provide a more qualitative assessment of the pro and cons of each method.

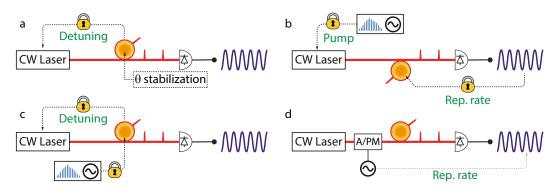


**Figure 4.1 – Overview of the tested stabilization schemes (a)** Using the microcavity as an optical reference. The pump laser is stabilized to the microresonator resonance via a detuning lock. Good thermal stability of the resonator is necessary. **(b)** Direct stabilization of the comb parameters (pump frequency and repetition rate) to a self referenced fiber-based comb. **(c)** Indirect stabilization of the pump frequency. The pump laser is stabilized to the microresonator, the resonator is then tuned to keep the pump frequency locked to a self-referenced fiber comb. **(d)** RF injection-locking of the repetition rate via electro-optic modulation.

#### 4.2 Using the microresonator as an optical reference

#### 4.2.1 Improving the temperature stability

According to the LLE model, the comb repetition rate is primarily defined by the microresonator FSR  $D_1/2\pi$ . Therefore, improving the FSR stability should stabilize the repetition rate at the same time. Furthermore, this would lead to a more stable resonance frequency, which we can use to stabilize the pump laser, for example by using digital detuning locking with a VNA (introduced in section 2.3.1). The FSR is determined by the optical roundtrip

length of the light, which depends on the major radius of the resonator and on the refractive index. Both of these quantities are sensitive to the temperature via the thermal expansion and thermorefractive effects (see section 1.2.2). Better FSR stability can thus be achieved via improved thermal stability, which is mostly dictated by the experimental setup.



Figure 4.2 – New setup design contained in an enclosure for acoustic and thermal isolation (a) Rendering of the designed setup. The whole coupling setup, including imaging microscope, is contained in an acoustic enclosure. (b) Photo of the assembled setup.

The coupling setup I inherited dated from the early ages of Kerr comb generation [8] and lacked mechanical and thermal stability<sup>1</sup>. A heater and temperature sensor had been implemented but were not employed, such that the resonator was subject to the temperature variations of the lab. The measurement presented in section 2.3.1 with the VNA digital lock were carried out in these conditions, and the corresponding repetition rate Allan deviation is shown in fig. 4.3. The implementation of a temperature controller to stabilize the crystalline resonator holder helped to maintain a much more precise operating point for the soliton comb, thereby reducing drastically the frequency instability, as shown in section 2.3.1 (the same VNA stabilization was used).

In order to improve the long-term stability of the microcomb repetition rate, I designed and assembled a new coupling setup. The resonator holder is made in copper and includes a heater and a temperature sensor for temperature stabilization. To decrease the sensitivity to vibrations, the coupling section is mounted on an actively isolated breadboard, and placed

 $<sup>^{1}</sup>$ The tapered fiber holder was not secured to the nano-positioner and the box protecting the coupling section was held together with scotch tape.

inside an acoustic enclosure. This also greatly improves the thermal stability of the crystalline resonator. Temperature measurements were performed in the air surrounding the crystal and in the laboratory. While in the former coupling box, the lab temperature variations were transmitted within 5 to 10 minutes to the coupling box, the new isolation showed a time constant of 5 hours and much reduced temperature deviations. This way, the passive long-term stability of the systems was greatly enhanced. New measurements with the VNA stabilization method showed a tenfold improvement of the stability at 1000 s. However our instability remains one order of magnitude higher than the state of the art stability reported with thermal stabilization [127].

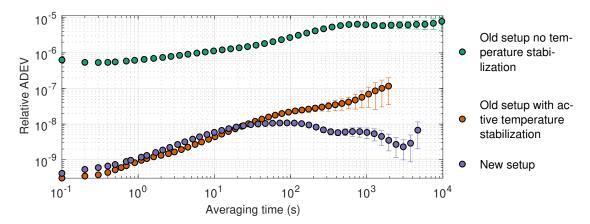


**Figure 4.3 – Repetition rate stability achieved in the different setups.** Allan deviation of the repetition rate obtained in the different setup configurations. In all cases, the detuning was stabilized via the VNA digital lock described in section 2.3.1.

#### 4.2.2 Detuning stabilization using the soliton average power

Although the digital feedback stabilization of the detuning with the VNA provides a way to quickly prototype the detuning stabilization strategy, and is quite robust to perturbations, it also suffers from several drawbacks. It requires expensive equipment to operate and has a very limited feedback bandwidth ( $\sim 10~{\rm Hz}$ ). Alternative methods have been explored in order to perform a faster and more inexpensive stabilization of the detuning.

One approached described in ref. [167, 185] utilizes indirect stabilization of the detuning. It uses the theoretical dependence of the average soliton comb power on the detuning  $P_{\rm sol} \propto \sqrt{\delta \omega}$  (according to eq. (1.74)). The stabilization scheme is thereby greatly simplified, as it only requires the comb power to be measured on a photodiode, compared with a setpoint and the feedback can be applied on the pump laser frequency (e.g. by actuation on the piezo actuator or on the current). The approach is fully analog and permits much faster actuation.

This scheme was tested in our experiment, using a fiber laser as the pump. The result is shown in fig. 4.9. The interest of the faster actuation is obvious on the short timescales as the fractional instability is below  $10^{-10}$  between 10 ms and 100 ms.

However, this technique suffers from several potential limitations. First, it is based on the detection of the intensity after the coupling section. Therefore, any drift of the coupling that may occur over time will change the out-coupled comb power and thus the detuning setpoint [167]. The laser relative intensity noise will also be detected and fed back onto the laser frequency, which can broaden the laser linewidth. Finally, as observed in fig. 2.15, the presence of the AMX-induced dispersive wave can lead to deviations from the theoretical relation eq. (1.74) and thus lead to an inaccurate or unstable locking.

#### 4.2.3 Detuning stabilization via offset Pound-Drever-Hall laser locking

The Pound-Drever-Hall (PHD) technique [204] provides a way to stabilize a laser frequency to an optical cavity. The principle is similar to the VNA method but modulating the pump phase at a single frequency and demodulating in a single quadrature. The pump light is phase-modulated at a frequency  $\Omega_{mod}$ , which creates two sidebands. After the cavity, the carrier and sidebands phasors have incurred different rotation, which creates a beatnote signal at  $\Omega_{mod}$  on a photodiode [205]. This signal is mixed down to baseband with the same local oscillator used for the modulation (with some phase shift). After low-pass filtering, the resulting PDH signal is of dispersive nature (see fig. 4.4) and gives a measure of how far the laser carrier is off resonance with the cavity and may be used as feedback for active stabilization. This technique appears particularly attractive in combination with the crystalline microcavity. The high-quality factor can be leveraged to directly narrow the linewidth of a pump diode laser, while generating a DKS at the same time.

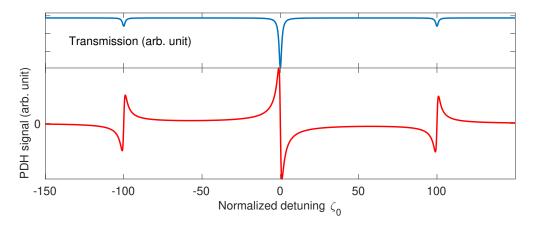
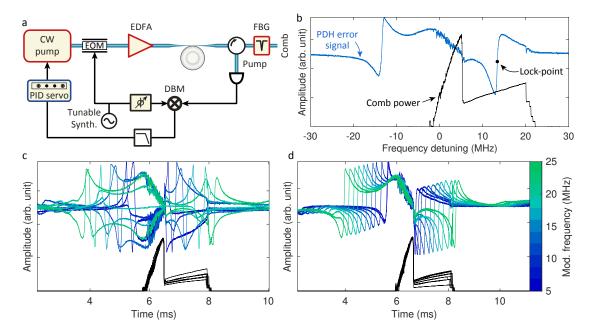


Figure 4.4 – Simulated PDH readout signal. The modulation frequency is set at  $\Omega_{\rm mod} = 100 \, \kappa/2$ . The top panel shows the microresonator transmission, the bottom panel shows the PDH signal for a demodulation in quadrature  $\phi = \pi/2$ .

The experimental setup for the PDH error signal generation and laser locking is shown in fig. 4.5a. The PDH error signal is obtained by phase-modulating the pump laser (at a frequency in the range of 5-25 MHz) before coupling to the cavity, using an electro-optic modulator (EOM, iXblue MPX-LN-0.1). The modulated signal is detected after the resonator (on the filtered residual pump) and demodulated to DC using the same phase-shifted RF signal. After

demodulation, the baseband signal is low-pass-filtered and sent to a PID servo-controller (Toptica FALC). The feedback is implemented on the laser frequency (ECDL, Toptica CTL1550) with a branch to the laser piezoelectric transducer and a fast actuation to the diode laser current.



**Figure 4.5 – Measurement and stabilization of the detuning via offset Pound-Drever-Hall locking (a)** Experimental setup for offset-PDH laser stabilization. **(b)** Evolution of the generated comb light (black) and of the PDH error signal (blue) when scanning the laser across the resonance (blue to red). The modulation frequency is set to 13.4 MHz and the lockpoint corresponds to the point when the higher frequency sideband in on resonance. **(c)** If the delay between the modulation and demodulation path is not compensated for, the demodulation angle changes and the dispersive feature of the error signal is lost when the synthesizer frequency is changed. **(d)** When the delay is balanced, the detuning lock-point can be set arbitrary in the soliton step by changing the synthesizer frequency.

When a soliton is generated in the cavity, the laser is effectively detuned from the resonance, such that the PDH locking is done on one of the sidebands instead of on-resonance, as shown in fig. 4.5b, thus the term offset-PDH technique [206]. However, with this scheme the insensitivity of the PDH signal to the laser intensity noise is lost. The soliton generation and locking procedure works as follow: first the laser tuning method is applied to generate the DKS state. The laser is tuned close to the dispersive feature of the sideband and the PID controller is activated.

The dispersive signal appears for a quadrature demodulation and an RF phase shift must be added between the modulation and demodulation path to compensate for the unequal delay between these two arms [205]. If the phase is unbalanced, changing the PDH frequency results in the distortion of the error signal (fig. 4.5c). In practice, a dual-channel arbitrary waveform

generator is used and the relative phase between the channels is adapted as a function of the modulation frequency. In this way, after calibration of the phase, the PDH frequency can be tuned and error signal remains dispersive (fig. 4.5d).

Using this method, the detuning directly corresponds to the PDH local oscillator frequency and can be precisely set and maintained. It is based on a modulation method at high frequency and thus more immune to low frequency technical noise. Second, as the cavity has a high Q factor, locking the laser reduce its linewidth and improve the noise performance, as shown in fig. 4.6. Similar results have been achieved using optical self injection locking [207]. Finally, as a fraction of the excess pump light rejected by the FBG filter is used to derive the signal, no comb power is lost.

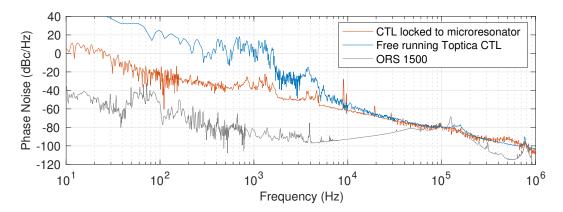


**Figure 4.6 – Impact of the offset-PDH lock on the pump laser noise.** Comparison of the absolute pump laser phase noise (Toptica CTL) in the free running case (blue) and when offset-locked to the microresonator (while a DKS is circulating in the cavity) in red. The phase noise was measured by beating with an optical reference which phase noise is shown in gray.

In terms of stability, this method provides the best short term stability in the low  $10^{-11}$  at 100 ms (fig. 4.9). On the long timescales, the thermal drift of the setup dominates, but interestingly, beyond 100 s, it seem to perform marginally better than the previous method of locking the soliton power. The offset PDH method is indeed much more insensitive to a change in coupling.

#### 4.2.4 Dual-mode temperature compensation technique

We saw already that the suppression of technical temperature variations is a precondition for achieving a good resonator stability. Shielding the mode volume from the temperature instabilities of the environment provided an appreciable reduction of the frequency instability but requires careful and complex setup design. Furthermore, the stability of the resonator is eventually limited by the resolution of the temperature controller used to thermally stabilized the microcavity. A more accurate and precise temperature measurement of the optical mode volume, would allow a finer compensation of its fluctuations and thus a better stability.

It is known that due to the birefringence of  ${\rm MgF}_2$ , orthogonally polarized modes exhibit a differential frequency shift upon a temperature change [208]. Monitoring the frequency offset between two such modes allows for a very precise measurement and stabilization of the temperature of the optical mode volume [209–211]. Our goal is to implement this method with a soliton in the microresonator.

After soliton generation and detuning stabilization based on the offset-PDH technique, we need to locate a mode with orthogonal polarization. To this end, the pump polarization is initially slightly misaligned with respect to the mode supporting the soliton, such that a small fraction of the pump can couple to orthogonal modes. Using a VNA combined on the same EOM used for the PDH modulation (see fig. 4.7), we performed modulation spectroscopy.

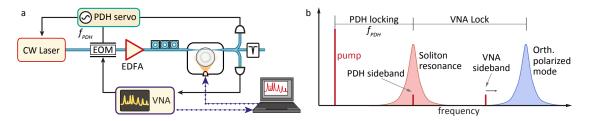


**Figure 4.7 – Stabilization of the resonator via dual mode stabilization.** (a) Experimental setup. A soliton is generated first and the detuning locked via the offset PDH technique. The VNA probes the resonances within 4 GHz of the pump laser. Once an orthogonally-polarized mode is identified, the VNA tracks its position and actuates on the resonator illumination for fine temperature stabilization. (b) Principle of dual mode stabilization. The spacing between the soliton-supporting resonance and the orthogonally-polarized mode is kept constant with the VNA-based thermal feedback.

The VNA frequency was swept in the range 400~MHz - 4~GHz to locate other modes of the resonator. The temperature was slowly tuned using a lamp shining through a microscope on the resonator, and the soliton repetition rate frequency variation as well as the modes position on the VNA were monitored at the same time. The results are shown in fig. 4.8. We observe that the frequency variations of a mode located 760 MHz away from the pump, replicate the repetition rate variations with a correlation factor of  $\sim -800$ .

This precise sensing of the temperature allows a feedback control to be implemented. As a proof of concept of temperature stabilization, we implemented a digital feedback with the VNA, which required minimal modification of the setup. The network analyzed is used to monitor the orthogonal mode centered at 762 MHz, a fit is performed and a feedback is applied on the LED illuminating the resonator, as shown in fig. 4.7. This scheme keeps the long-term stability below  $10^{-9}$  up to  $1000 \, \text{s}$  (see fig. 4.9). Better performance could be achieved with faster feedback, such as a probing the mode frequency with a PDH technique, and faster actuation using for instance the pump power.

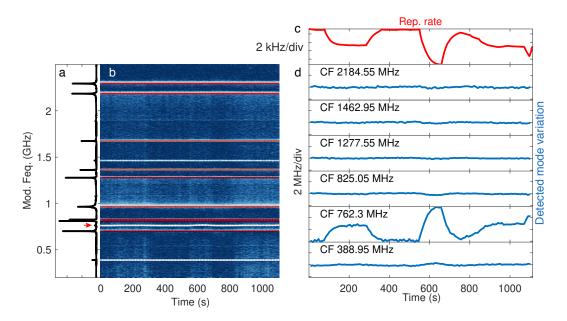


**Figure 4.8 – Dual mode temperature sensing: mode identification (a)** Recorded modes on the VNA sweep (the range 400 MHz – 2.5 GHz is shown). The red arrow points at the mode of interest. **(b)** Map showing the evolution of the VNA trace as a function of time. The dots correspond to the detected resonances. **(c)** Evolution of the repetition rate. The lamp was used to thermally change  $f_{\text{rep}}$ . **(d)** Corresponding evolution of a subset of the mode frequencies recorded on the VNA. Only the mode centered at 762 MHz reproduces the repetition rate variation (with opposite sign).

#### **4.2.5** Summary

Figure 4.9 summarizes and compares the resonator stabilization attempts made in this section in the form of the repetition rate relative overlapping Allan deviation obtained in each scenarios. Substantial progress was achieved, and there is room for improvement as most of the results shown here are proof of concepts.

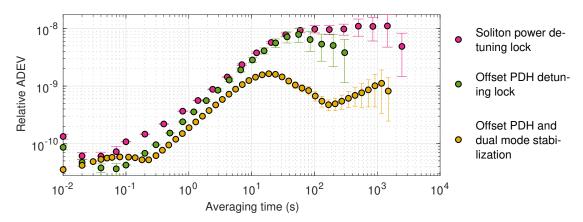


**Figure 4.9 – Allan deviation comparison, when using the microresonator as the optical reference**. The repetition rate stability achieved with the various resonator stabilization and detuning strategies is plotted. All results were obtained in the 'new' setup described in fig. 4.2.

#### 4.3 Direct phase locking of the comb degrees of freedom<sup>2</sup>

In this section, the stabilization of the two degrees of freedom of the comb is realized. The repetition rate  $f_{\rm rep}$  is stabilized to an RF clock using a thermo-optical tuning method, while the pump frequency  $f_{\rm p}$  is locked to a tooth of a self-referenced fiber comb (referenced to the same clock oscillator). Stabilizing these two parameters, grants the full stabilization of the comb grid and thus of  $f_{\rm ceo}$  indirectly. Similar to ref. [212], where an MI comb was used, the comb parameters are directly measured and stabilized, disregarding the detuning parameter.

The principle of the stabilization scheme for  $f_{\rm rep}$  and  $f_{\rm p}$  is presented in fig. 4.10.  $f_{\rm p}$  is stabilized by offset-locking the pump laser to an external reference [212]. Actuating on  $f_{\rm rep}$  is done via a second "probe" laser. By adjusting the detuning of the probe laser, the power coupled into the microresonator is changed, thereby affecting  $f_{\rm rep}$  (see fig. 4.10). In other work, auxiliary modes have been used to monitor the resonator temperature and thus the repetition rate [209] and to compensate for thermal nonlinear effects [213]. The relevant stages of the experimental setup for the stabilization of the soliton frequency comb are presented in fig. 4.11.

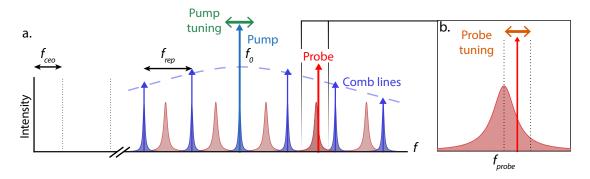


**Figure 4.10 – Actuation scheme (a)** Schematic of the concept used to stabilize the repetition rate. The CW pump laser (blue) is tuned into resonance of the high Q modes that produces the soliton frequency comb producing mode (blue). Tuning the pump frequency changes  $f_p$ . The auxiliary lower-Q spatial mode family of the cavity is shown in red. The probe laser is tuned to the high frequency side of one of the resonances. **(b)** A zoom in of the relevant auxiliary mode. Tuning the probe laser in the resonance changes the power coupled in and thus the FSR for both modes and changes  $f_{\text{rep}}$ .

To form the OFC, continuous wave laser light from a 1553 nm fiber laser (pump laser) with 240 mW is coupled evanescently into the resonator

#### 4.3.1 Phase locking the pump to a reference comb

The locking setup for  $f_p$  is shown in the green panel of fig. 4.11a. A portion of the pump light is heterodyned with light from a reference comb consisting of a commercial self-referenced and

<sup>&</sup>lt;sup>2</sup>The results of this section are partially adapted from the publication: J. D. Jost et al., "All-optical stabilization of a soliton frequency comb in a crystalline microresonator", *Optics Letters* 40.20 (Oct. 2015), p. 4723.

stabilized fiber based optical frequency comb with a repetition rate of  $\sim 250~\mathrm{MHz}$ , which is referenced to a master oscillator (commercial atomic clock). An optical band-pass filter (OBP) is used to filter the portion of the fiber comb spectrum near the pump, preventing saturation of the photodetector (PD). The heterodyning produces multiple beat signals between the pump laser and the fiber frequency comb, which represent the frequency offset of the pump with the adjacent comb lines. One of the beat signals is electronically mixed down to 20 MHz with a local oscillator phase locked to the master oscillator. A portion of the signal is sent to a frequency counter. The rest is sent to a digital phase comparator (PC) with a 20 MHz reference, which outputs an error signal to a proportional and integral (PI) servo controller (servo 1). This provides feedback to change the frequency of the pump fiber laser via an internal piezoelectric actuator.

#### 4.3.2 Repetition rate actuation with a probe laser

Controlling the repetition rate is possible through a variety of means: changing the pump power [212], actuating on a piezo electric crystal that is in contact with the resonator [188], or heating or cooling the whole system [214].

The stabilization setup for  $f_{\rm rep}$  is shown in the orange box in fig. 4.11a. To control  $f_{\rm rep}$ , the additional probe fiber laser at  $\sim$  1552.1 nm with a power of  $\sim$  2 mW, is coupled and locked to a resonance of another mode family with lower Q. By changing the lock point in this resonance, more or less optical power is coupled into the resonance. Due to absorption losses in the cavity this heats the resonator, changing the overall size and refractive index and thus the repetition rate without loss of the soliton state. The Kerr effect also changes the index of refraction on fast time scales. However, the magnitude of this is negligible compared to the thermo-refractive index change.

The probe laser is coupled into the same tapered optical fiber as the pump laser, and its frequency is tuned into a different spatial optical mode resonance of the microresonator. A portion of the light coming from the resonator is sent to the probe locking setup depicted in the blue box in fig. 4.11a. An OBP filter passes primarily the transmitted probe light to a photodetector. The probe laser's frequency is then locked to the high frequency side of the cavity resonance, where thermal locking is supported. To suppress nonlinearities, lower powers and a lower Q mode are used. It was not necessary to determine the exact mode of the cavity, because many different modes showed control over  $f_{\rm rep}$ . A PI servo controller with an adjustable set point (servo 2) controls the lock point of the probe laser on the side of the cavity resonance. The servo controller feeds back to a piezoelectric actuator on the probe fiber laser, adjusting the laser's frequency. To fix  $f_{rep}$  an additional control signal is needed, which is derived from the repetition rate heterodyne signal described above. This signal is mixed down from 14.094 GHz to 20 MHz using a local oscillator referenced to the master oscillator. The signal is filtered with an electronic bandpass filter and a portion is sent to a. The rest is sent to a digital PC with the 20 MHz signal from the master oscillator where any phase error produces an error signal for a PI servo controller (servo 3). The correction signal from the

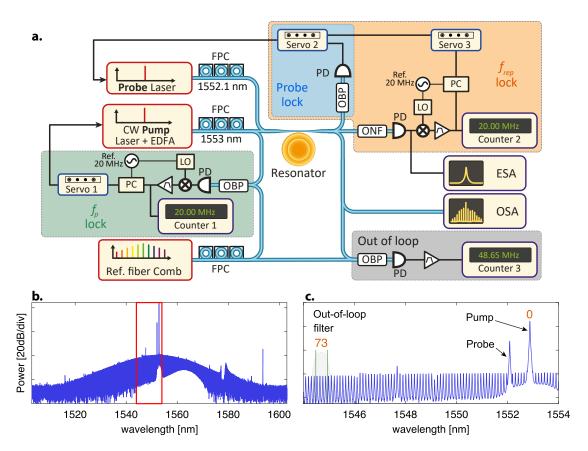


**Figure 4.11 – All optical stabilization of a soliton frequency comb.** (a) Experimental setup for generating and stabilizing the soliton frequency comb. The details are provided in the text. The components are: continuous wave (CW) pump and probe lasers, erbium doped fiber amplifier (EDFA), fiber polarization controller (FPC), optical bandpass filter (OBP), optical notch filter (ONF), optical spectrum analyzer (OSA), photodetector (PD), local oscillator (LO), phase comparator (PC), electrical spectrum analyzer (ESA) (b) The generated optical spectrum as measured on the OSA. (c) A zoom in of the optical spectrum. The pump laser and the probe laser's position is shown. Due to the limited resolution of the OSA the probe appears merged with the 7th comb line. The position of the out-of-loop optical filter, covering several comb lines of both frequency combs, is shown overlaid on the spectrum. It is centered ~ 73 comb lines away from the pump laser (0th comb line).

output of servo 3 is input to the servo 2, which maintains the probe laser's lock on the probe resonance, adjusting the lock point detuning of the probe laser to maintain the repetition rate phase lock. The time constants of the systems were not directly measured but rather the appropriate proportional and integral time constants were experimentally determined. It should be noted a sub 1 s integral time constant was used for the  $f_{\rm rep}$  servo controller due to the observed slow response of the system, indicating that thermal effects appear to dominate the response. To verify the stabilization is not injecting significant noise an independent out-of-loop measurement is performed by heterodyning a portion of the generated soliton comb with the reference fiber based comb (gray box in fig. 4.11). An OBP filter is used to select a

portion of both frequency combs centered at 1544.6 nm. Due to the  $\sim$  50 GHz bandwidth width of the filter multiple heterodyne beat signals are observed. Using a tunable electronic filter, one signal  $f_{\rm ol}$  is selected and sent to a frequency counter.

#### 4.3.3 Stabilization results

We analyze the stability of the full system by performing Allan deviation measurements on  $f_{\rm rep}$ ,  $f_{\rm p}$ , and  $f_{\rm ol}$  on both a single and multiple soliton states. The heterodyne beat frequencies are measured on Hewlett Packard 53131A high resolution counters and the overlapping Allan deviation (OAD) is processed from the recorded frequency series. For the single soliton state shown in fig. 4.11b counting data was taken for 3086 s at 100 ms gate time, yielding the OAD plot in fig. 4.12. At 100 ms the absolute fluctuations of the 14.094 GHz rep rate beat are  $\sigma_{\rm A,rep}$  = 4.98 Hz corresponding to a fractional deviation of 3.5 × 10<sup>-10</sup>. The absolute frequency fluctuations of  $f_p$  at 100 ms are  $\sigma_{A,p} = 8.9 \times 10^{-1}$  Hz. Only the absolute fluctuations of  $f_p$ can be measured since the exact value of  $f_p$  is not known in this experiment. For out-ofloop measurement the beat frequency was 70.3 MHz and the absolute fluctuations at 100 ms were found to be  $\sigma_{A,ol}$  = 283 Hz. The bump in  $\sigma_{A,rep}$  and  $\sigma_{A,ol}$  is probably a result of the slow thermal response of the system. Performing a fit to the slopes, using the data for times  $\geq$  1s to make sure the system was stabilized, we find that  $f_{rep}$ ,  $f_p$  and  $f_{ol}$  average down like  $au_{rep}^{-0.53}$ ,  $au_o^{-0.48}$  and  $au_{ol}^{-0.53}$ . We observe here a dependence of  $\sim au^{-0.5}$  while for a phase locked system the expected dependence is rather  $\sim au^{-1}$  [215]. This observation is related to the properties of the Hewlett Packard 53131A counters used. They are a Λ-type counter because they perform a weighted average of the frequency over the gate time to enhance the resolution. As a result, the computed deviation differs from the true OAD but still measures the stability of the system [216]. Also, this counter cannot be read without dead time between consecutive measurements. This creates a bias [217] in the processed OAD for the phase-locked system and leads to a  $au^{-0.5}$  dependence in the presence of white phase noise. More detail about the counter limitations can be found in appendix B.

In our case the fluctuations decrease for longer gate time showing that the stability of the master oscillator is transferred to the soliton frequency comb. The out-of-loop measurement is approximately a factor  $\sim 72$  higher than  $\sigma_{\rm A,rep}$  for times  $\geq 1{\rm s}$ . The out-of-loop OBP filter is centered approximately  $n_{\rm ol}\sim 73$  comb lines away from the central pump line. We can write  $f_{\rm ol}^k=\Delta n_{\rm ol}\times f_{\rm rep}^k+f_{\rm p}^k$  with k being the measurement number and where  $\Delta n_{\rm ol}$  is the mode number relative to the central comb line. and thus  $\sigma_{\rm A,ol}^2=\sigma_{\rm A,p}^2+\Delta n_{\rm ol}^2\sigma_{\rm A,rep}^2+\Delta n_{\rm ol}^2\left(f_{\rm rep}^{k+1}-f_{\rm rep}^k\right)(f_{\rm p}^{k+1}-f_{\rm p}^k)$  and since  $\sigma_{\rm A,p}\ll\sigma_{\rm A,rep}$  for  $\tau\geq 1$  s we expect  $\sigma_{\rm A,ol}\approx\Delta n_{\rm ol}\,\sigma_{\rm A,rep}$  which in good agreement with the observed offset.

We also demonstrate full stabilization of multi-soliton states. The desired state is created using the same tuning technique [9] as for the single soliton. The spectrum for the created state is shown in fig. 4.13. Having multiple solitons alters the microresonator optical spectrum as a result of interference between the different frequency components. The time domain pattern of the intracavity amplitude can be reconstructed by fitting an analytical expression to the

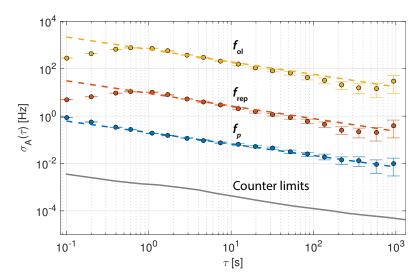
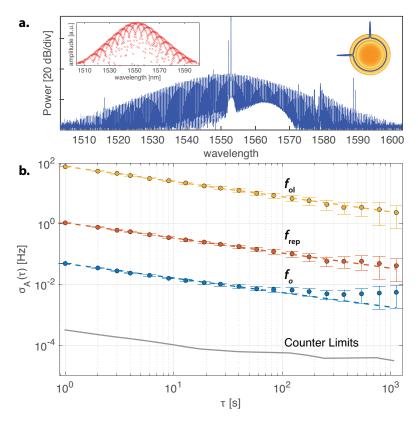


Figure 4.12 – Overlapping Allan deviation for a stabilized single soliton state. Counting data with 100 ms gate time was taken for 3086 s. The resulting OAD is shown by the traces for the pump frequency (blue), repetition rate (red), and the independent out-of-loop measurement (yellow). The error bars are one standard deviation. The dashed lines are a linear fit for the data  $\geq$ 1 s. The gray trace shows the result of counting the 20 MHz master oscillator used in the experiment.

optical spectrum [148]. The left inset in fig. 4.13 shows only the peak amplitudes for clarity. It is estimated that the state in fig. 4.13 is a two soliton state spaced apart by  $\sim 90^\circ$  in the microresonator. The same stabilization was applied as for the single soliton with  $\sim 3000$  s of counting data taken at 1 s gate times and the OAD was calculated for  $f_{\rm rep}$ ,  $f_{\rm p}$ , and  $f_{\rm ol}$ , shown in fig. 4.13b. At 1 s, the absolute fluctuations of rep rate beat is  $\sigma_{\rm A,rep}=1.1$  Hz corresponding to a fractional deviation of  $7.8\times 10^{-11}$ . The absolute frequency fluctuations of  $f_{\rm p}$  at 1 s are  $\sigma_{\rm A,p}=5\times 10^{-2}$  Hz. For the  $f_{\rm ol}$  the beat frequency was 48.7 MHz and the absolute fluctuations at 1 s were found to be  $\sigma_{\rm A,ol}=79.5$  Hz. This is a factor of  $\sim 72.6$  higher than fluctuation seen in  $f_{\rm rep}$ , which again agrees well with the out-of-loop filter position. The bump in  $\sigma_{\rm A,rep}$  and  $\sigma_{\rm A,ol}$  is absent here as the gate time was taken to be 1 s. Fitting the data gives the slopes  $\tau_{\rm rep}^{-0.50}$ ,  $\tau_{\rm o}^{-0.48}$  and  $\tau_{\rm ol}^{-0.50}$ . This data has a lower initial OAD. The servo parameters were changed between the single and multi-soliton case, which potentially explains the difference.

The out-of-loop OAD is a measure of the stability of the optical system, including the noise in  $f_{\rm rep}$  and  $f_{\rm ceo}$  and depends on which comb line is used in the measurement. In the case of the single soliton and multi-soliton the measured relative stability at the 73rd mode from the pump at 1s is  $3 \times 10^{-12}$  and  $4 \times 10^{-13}$ . These values are not state of the art, in comparison with other systems, where the servo bandwidths available are different.

The OAD data shows the system can stabilized, typically during a few thousand seconds. However, this direct comb stabilization scheme is fairly difficult to activate and operate stably beyond this duration. We believe this is due to the lack of control over the pump-cavity detuning, which plays a key role in the soliton regime unlike the MI regime [76, 212]. In the



**Figure 4.13 – Multi-soliton spectrum and overlapping Allan deviation. (a)** A measurement of the optical spectrum from the OSA of the stabilized two soliton state (blue). The peaks of the spectrum are detected and fitted with a theoretical expression [148] (left inset). This yields the duration, the number and relative position of the solitons in the cavity (see the inset in the upper right). **(b)** Counting data at a 1 s gate time was taken for 3000 s. The resulting OAD is shown by the traces for the pump frequency (blue), repetition rate (red), and the independent out-of-loop measurement (yellow). The error bars are one standard deviation. The dashed lines are a linear fit to the data. The gray trace shows the result of counting the 20 MHz master oscillator used in the experiment.

next section, we will explore how to overcome these shortcomings and take the detuning into account.

# 4.4 RF injection-locking for repetition rate control and microwave purification<sup>3</sup>

One difficulty of the previous microcomb stabilization is that the actuators have an influence on both degrees of freedom. For instance changing  $f_{\rm p}$  can also affect  $f_{\rm rep}$  via the coupling with the detuning [165, 174, 219]. On the other hand, tuning the resonator FSR also changes the resonance and thus the detuning.

In the soliton regime, it appears that controlling the detuning is pretty much essential. However, stabilizing the detuning monopolizes one actuator of the system, such as the pump laser frequency control. One solution was found by Stone  $et\ al.\ [219]$ , which involves making the detuning setpoint tunable. This work, identifies a detuning operating point in a SiO $_2$  resonator, at which the actuation on the repetition rate and on the pump laser can be made independent.

An alternative approach is developed here. The detuning is kept at a fixed point and a modulation technique disciplines the solitons repetition rate via injection-locking.

### **4.4.1** Stabilization of the repetition rate with the pump power and associated limitations

We investigate first the situation where the pump laser is locked to the microresonator with the offset-PDH technique and the repetition rate is stabilized to an RF oscillator by thermal actuation on the microresonator. The configuration is shown in fig. 4.14a. The thermal actuation on the cavity is achieved by active control of the pump power with an acousto-optic modulator (AOM) coupled to the  $0^{th}$  order.

The Allan deviation plotted in fig. 4.14b reveals the main drawback of this scheme. As expected, the repetition rate is phase locked to the reference on timescales beyond 1 s, but the pump power is not stable. Indeed, the repetition rate can differ from the cavity FSR and thus repetition stability does not imply FSR stability (and thus resonance stability). Using this approach, we have used the two possible actuators at our disposal and only stabilized one parameter.

Nonetheless, this scheme can be relevant for schemes where the optical stability of the comb is not a priority.

#### 4.4.2 Stabilization of the resonator and pump to a stable optical reference

The stabilization of the resonator to the optical reference appears to be a more promising approach (see fig. 4.15a). In this scheme, the pump laser is still PDH-stabilized to the microresonator. The frequency of the laser is then compared with a tooth of a stabilized fiber-laser-based comb, and the frequency difference is stabilized at 20 MHz through a thermal actuation of the resonator via pump power modulation.

<sup>&</sup>lt;sup>3</sup>The results of this section are partially adapted from the publication: W. Weng et al., "Spectral Purification of Microwave Signals with Disciplined Dissipative Kerr Solitons", *Physical Review Letters* 122.1 (Jan. 2019), p. 13902. 🗹

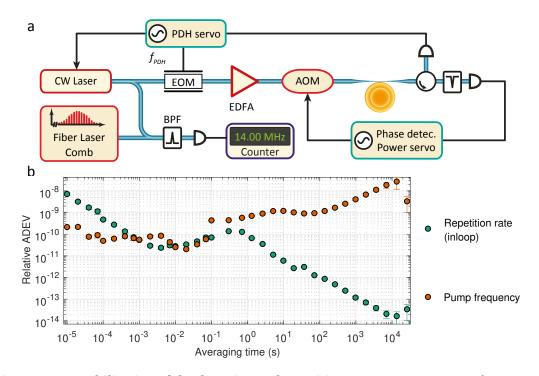


**Figure 4.14 – Stabilization of the detuning and repetition rate. (a)** Experimental setup and stabilization scheme. The detuning is locked with the offset-PDH technique and the repetition rate is stabilized via a phase lock loop to a reference clock. The pump frequency is monitored by counting its beatnote with a self-referenced fiber comb. All devices are referenced to the same clock signal. **(b)** Overlapping Allan deviation of the repetition rate and pump frequency. While the repetition rate is phase locked to the reference on timescales beyond 1 s, the pump laser is not stabilized.

As illustrated in fig. 4.15a-c, this "pre-stabilization" scheme stabilizes both the pump laser frequency and the pump-cavity detuning. As a result, the stability of  $f_{\rm rep}$  is improved by up to 2 orders of magnitude at time scales > 10 s (see fig. 4.17c). This allowed the time-consuming measurement of phase noise via cross correlation shown in fig. 4.19 to be carried out properly. One should note that the fiber-laser-based comb can be replaced with a laser stabilized by a reference cavity [220] or an atomic vapor cell [221], and that with improved thermal isolation [127] or self-referenced stabilization [211] the entire setup can be more compact.

#### 4.4.3 Repetition-rate injection-locking effect and locking range scaling

The full phase stabilization of the repetition rate is realized using an injection-locking technique that was previously used to stabilize modulation-instability (MI) combs [129, 222]. Injection locking of the soliton repetition rate is implemented by applying amplitude modulation (AM) or phase modulation (PM) on the pump laser, at a frequency close to the FSR. Intuitive illustrations of how the injection locking works are presented in fig. 4.16. From a frequency domain perspective, the modulation frequency defines  $f_{\rm rep}$  through parametric four-wave-mixing. In the time domain, a modulated CW field creates an intracavity potential gradient

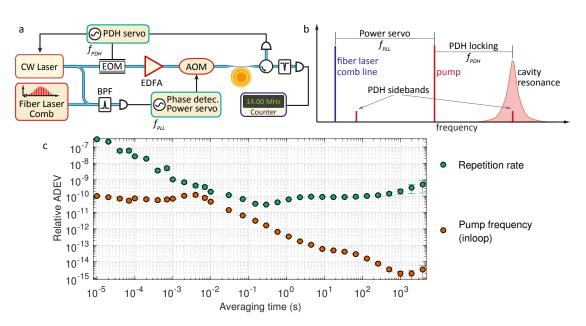


**Figure 4.15 – Stabilization of the resonator to a self-referenced fiber comb (a)** Experimental scheme. The detuning is locked with the offset-PDH technique and the pump frequency is stabilized via a phase lock loop to a tooth of the self-referenced fiber comb. The repetition rate is monitored with a frequency counter. All devices are referenced to the same clock signal. **(b)** Stabilization scheme. The laser is locked to the resonance. In turn, the resonance is tuned thermally via the pump power to lock the laser frequency to the tooth of the fiber-based comb. **(c)** Overlapping Allan deviation of the repetition rate and pump frequency. The pump is phase locked to the reference comb. The microcomb repetition rate instability is largely reduced but not phase locked.

that traps the solitons and disciplines  $f_{\rm rep}$  correspondingly. This mechanism not only relies on linear cavity filtering, but exploits further the dynamics of DKSs, and allows a substantial rejection of the phase noise of an external microwave drive.

The experimental setup is shown in fig. 4.17a. The "pre-stabilization" method described in section 4.4.2 is applied and a high bandwidth modulator is added before the optical amplifier. Pump power modulation (AM) was performed using a Mach-Zehnder modulator and phase modulation (PM) with an EOM. In this proof-of-principle experiment we use a synthesizer to drive the AM/PM modulator but the input microwave signal could be derived from a frequency-multiplied clock oscillator or a voltage-controlled oscillator (VCO).

#### Locking range measurement with amplitude modulation

The modulation frequency  $f_{\rm mod}$  is swept around the free-running  $f_{\rm rep}$  ( $\sim$  14.09 GHz) and we observe that  $f_{\rm rep}$  is injection-locked by the input microwave signal. fig. 4.18c shows the evolution of the microwave spectrum of the DKS as we slowly swept the AM  $f_{\rm mod}$ . When the difference between  $f_{\rm mod}$  and the free-running  $f_{\rm rep}$  is larger than  $\sim$  400 Hz, multiple spectral components including  $f_{\rm mod}$  (the strongest),  $f_{\rm rep}$  (the second strongest) and multiple harmonics are observed in the spectra, indicating an absence of injection locking. As  $f_{\rm mod}$  is approaching the free-running  $f_{\rm rep}$ , the spectrum displays the typical frequency-pulling effect as  $f_{\rm rep}$ 

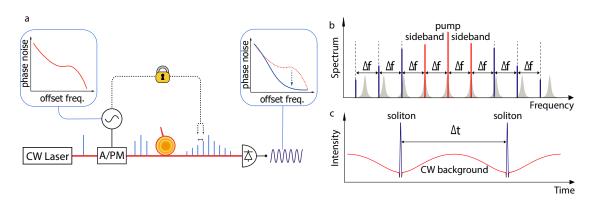


**Figure 4.16 – Concept of injection-locking of a soliton microcomb.** (a) An electronic microwave oscillator (Rohde&Schwarz SMB100A) is used to modulate the pump laser, leading to the injection locking of the soliton microcomb repetition rate. The soliton repetition rate is disciplined to the RF source on the long term, but exhibits a reduced phase noise level due to the nonlinear soliton dynamics, leading to noise reduction of the microwave signal for Fourier frequencies far away from the carrier. (b) In the frequency domain, the modulation frequency sets the microcomb repetition rate  $f_{\rm rep}$ . (c) In the time domain, the modulated CW field traps the solitons, thus locking  $f_{\rm rep}$  of the soliton train.

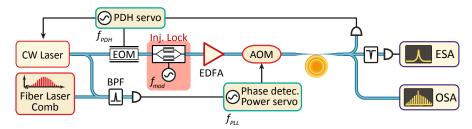


**Figure 4.17 – Experimental setup for injection locking.** The optical "pre-stabilization" method in applied to stabilize the laser frequency. A Mach-Zhender modulator or an electro-optic modulator are used to respectively perform the AM or PM.

is pulled towards  $f_{\rm mod}$  [223]. When the difference between  $f_{\rm mod}$  and free-running  $f_{\rm rep}$  is less than ~ 300 Hz all the spectral components merge into one, indicating that the  $f_{\rm rep}$  is synchronized to  $f_{\rm mod}$ , i.e. the soliton stream is locked to the external drive. We measured the frequency instabilities of the injected-locked  $f_{\rm rep}$  against  $f_{\rm mod}$ , which is also presented in eq. (4.2)b. The Allan deviation shows that at time scales of > 0.1 s the relative fluctuations of  $f_{\rm rep}$  have been suppressed significantly by more than 4 orders of magnitude at averaging time of 1000 s, indicating that the disciplined DKS tightly follows the injected microwave frequency.

We acquire the locking range from the evolution of the RF spectrum, and repeat the measurement with varied modulation strength. As shown in fig. 4.18e, with the normalized amplitude of the modulation sideband below 0.07, the locking range rises monotonically with almost perfect linearity as the modulation strength increases. With stronger modulation the slope of the locking range scaling increases, which is attributed to the appearance of higher-order modulation sidebands that increase the gradient of the potential and trap the solitons more effectively [110, 224–226]. For the same reason, we observe that the locking range increases by nearly a

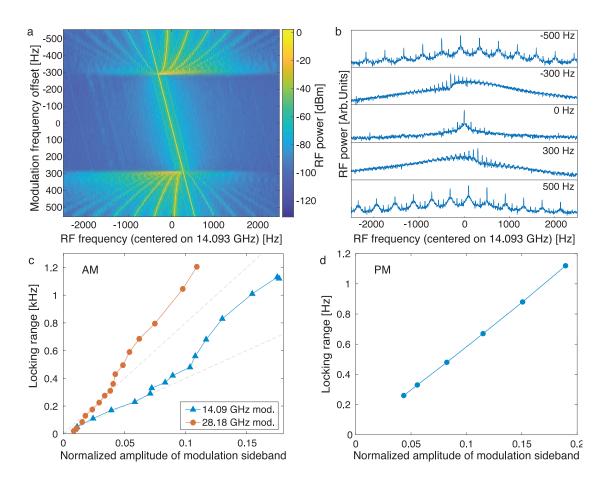


**Figure 4.18 – Injection locking effect and scaling.** (a) Evolution of the spectrum around 14.09 GHz. (b) Snapshots with different  $f_{\rm mod}$  detuned from free-running  $f_{\rm rep}$  (indicated in the upper-right corners) showing the typical states of unlocked (–500 Hz and 500 Hz), quasi-locked (-300 Hz and 300 Hz) and injection-locked (0 Hz). (c) Scaling of the locking range with the AM strength, for modulation frequencies around  $f_{\rm rep}$  (blue circles) and  $2 \times f_{\rm rep}$  (red circles) respectively. (d) Scaling of the locking range with the PM index.

factor of 2 when we measure the locking range with  $f_{\text{mod}}$  around 2 ×  $f_{\text{rep}}$  (~ 28.18 GHz).

#### Locking range measurement with phase modulation

We also measured the locking ranges with a PM scheme and with varied PM strength, which is presented in fig. 4.18. We note that the locking range can be influenced by mode coupling between different mode families, and that the resulting effect on the locking range can vary with temperature and fiber-resonator coupling condition. However, the results show a similar linear dependence of the locking range on the modulation strength with relatively small PM strength.

#### 4.4.4 Spectral purification effect

To characterize the spectral purity at  $f_{\rm rep}$ , the out-coupled soliton stream is filtered by fiber Bragg grating filters (FBG) to suppress the pump light and then amplified by an EDFA and subsequently attenuated to  $\sim 5$  mW before being registered by a fast photodetector. We use a phase noise analyzer to measure the phase noise of the 14.09 GHz signal output by the photodetector. Figure 4.19 presents the single-sideband (SSB) phase noise level when PM injection locking was performed. One should note that very similar results were also observed with AM injection locking. At low offset frequencies between  $1-100\,{\rm Hz}$  the injection-locked DKS shows an improved noise level, which matches the phase noise level of the injected microwave tone, in agreement with the Allan deviation. This result shows that the soliton stream is strictly disciplined by the potential trap at low frequency ranges.

Remarkably, at offset above 100 Hz the spectrum of the injection-locked  $f_{\rm rep}$  mostly maintains the intrinsic high quality, which is several orders of magnitude lower than the input microwave in terms of phase noise level. We note that this purifying effect cannot be explained by the cavity filtering since the frequency range where the purification is observed is  $\sim$  3 orders of magnitude lower than the loaded cavity resonance bandwidth ( $\sim$  150 kHz). At offset frequencies above 30 kHz a reduction of the input microwave phase noise level by 30 dB is achieved, showing the exceptional spectral purifying ability of the disciplined DKS. This slow actuation bandwidth on the soliton offers the possibility to discipline the comb repetition rate on long time scale using for example simple multiplied clock oscillators, while preserving a remarkable purity on the microwave signal.

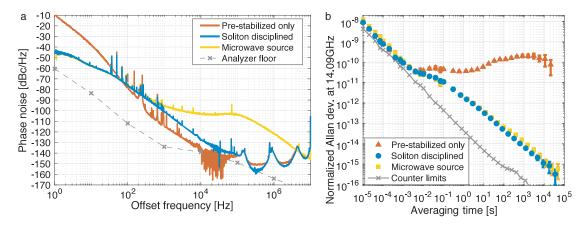


Figure 4.19 – Impact of the injection on the repetition rate noise and stability (a) Phase noise spectra of the soliton repetition rate with and without PM injection locking. The phase noise of the input microwave signal is also presented, showing that the injection locking reduces the noise level by nearly 40 dB for offsets at 100 kHz. The crosses and the dashed line show the noise floor of the phase noise analyzer. (b) Allan deviations of  $f_{\text{rep}}$  when the Kerr comb is pre-stabilized and DKS-disciplined respectively. We counted  $f_{\text{rep}}$  with a Π-type frequency counter that is referenced to the same frequency source (relative frequency instability  $< 1 \times 10^{-12}$  at 1 s averaging time) to which  $f_{\text{mod}}$  is referenced

#### 4.4.5 Numerical modeling

In order to study the mechanism of the observed spectral purification, we performed simulations of PM-to-PM transfer function based on the Lugiato-Lefever equation (LLE) [93]. The model is similar to the one described in eq. (3.7), which is expressed as:

$$\frac{\partial \tilde{A}_{\mu}(t)}{\partial t} = \left[ -\frac{\kappa}{2} + i \left( \delta \omega + D_{\text{int}}(\mu) \right) \right] \tilde{A}_{\mu} - i g_0 \mathcal{F}_T \left[ |A|^2 A \right]_{\mu} + \sqrt{\kappa_{\text{ex}}} \, s_{\text{in}} \left( \delta_{\mu,0} + i \frac{\epsilon}{2} e^{\pm i \Delta \Omega t} \delta_{\mu,\pm 1} \right)$$
(4.1)

We include third order dispersion in  $D_{\rm int}(\mu)$  to allow some drift of the soliton. A pair of PM sidebands are included in the last term of the equation, where  $\epsilon$  indicates the amplitude of the modulation sidebands, and  $\Delta\Omega = \omega_{\rm in} - D_1$  is the angular frequency difference between and the input microwave signal  $\omega_{\rm in}$  and the cavity FSR.

Adapting the technique used in [164], we introduce phase modulation on the microwave signal  $\epsilon(t) = \epsilon \, \mathrm{e}^{i \, \varrho \cos(\vartheta t)}$  with phase deviation of  $\varrho = 0.1$  radian and varied modulation frequencies  $\vartheta/2\pi$  from 200 Hz to 1 MHz. The phases of the purified microwave signal can be derived from the comb spectra with

$$\Psi(t) = \operatorname{Arg} \left[ e^{i\omega_{\text{in}}t} \sum_{\mu} \tilde{A}_{\mu} \tilde{A}_{\mu-1}^{\dagger} \right]$$
(4.2)

We use pump power of 200 mW and  $\epsilon=0.32$  for the numerical simulation. The results are presented in fig. 4.20. The simulated transfer function follows a typical first-order lowpass filtering effect, showing a magnitude that is close to unity at low frequency (200 Hz). For higher offset frequencies the magnitude decreases with a slope of -20 dB/decade, reaching a minimum of  $\sim -63$  dB around 500 kHz, thus revealing a significant phase noise suppression in the soliton state.

#### 4.4.6 Experimental measurement of PM-to-PM transfer function

To verify the simulated PM-to-PM noise transfer function, we implement PM on the input microwave signals via the synthesizer that is used to drive the optical phase modulator. The PM amplitude is set to be 0.1 radian, 1 radian and 2 radian respectively. After the soliton repetition rate is injection locked, the PM on the microwave signals is activated, and the in-phase-and-quadrature (IQ) demodulation function of the spectrum analyzer is utilized to measure the phase and amplitude responses of the microwave signals generated by the fast photodetector which detects the DKS repetition rate. The demodulation frequency on the analyzer is set equal to the synthesizer frequency and both devices are referenced to a common clock oscillator. In fig. 4.20a-b we plot the measured IQ phasors in the complex plane at 4 different PM frequencies, when the PM phase deviation is 0.1 rad and 2 rad. We note that the approach can also be used to measure the PM-to-AM noise transfer function. As the PM frequency on the input microwave signal increases, the phase deviation of the purified signal decreases. To quantify this effect, the phase deviation is extracted from the IQ

#### 4.4. RF injection-locking for repetition rate control and microwave purification

measurement and the transfer function is obtained as  $20\log_{10}\left(\frac{\Delta\phi^{(\text{measured})}(\omega)}{\Delta\phi^{(\text{in})}(\omega)}\right)$ . Eventually, the response amplitude is below the instrumental noise floor of the phase noise analyzer, which is evidently displayed as the flat floor on the transfer function at high frequencies. To increase the dynamical range of the measurement, the measurement is repeated with larger phase deviations (1 radian and 2 radians) on the modulation (see fig. 4.20b). We see that at very high PM frequency (1 MHz) the response is limited to the same instrumental noise floor. However, because of the larger input phase deviation, the noise floor level of the transfer function decreases, as shown by Fig. 5 in the main text.

The experimentally measured transfer functions are plotted in the same fig. 4.20c. From the comparison we see that at low frequencies the experimental results and the simulation are in satisfactory agreement and validate the first-order lowpass filtering effect. However, at frequencies above  $\sim 100\,\mathrm{kHz}$  the experimental curves show flat floors, which are attributed to the detection noise floor introduced by the analyzer we use to perform the measurement. This instrumental noise floor is confirmed by increasing the modulation strength, which improves the dynamic range of our measurement.

The nonlinear cavity in the soliton state acts as a passive spectral purifier that can improve the performance of an external off-the-shelf electronic oscillators. It allows the filtering of the injected microwave phase noise with a very small bandwidth, especially considering the high carrier frequencies.

As depicted in fig. 4.16, the disciplined-DKS-based microwave purifier is thus a  $f_{\text{rep}}$ -stabilized frequency comb and a spectrally pure microwave generator in a single device. It could also facilitate the application of microcombs to coherently averaged dual-comb spectroscopy [46] and coherent optical telecommunication [122].

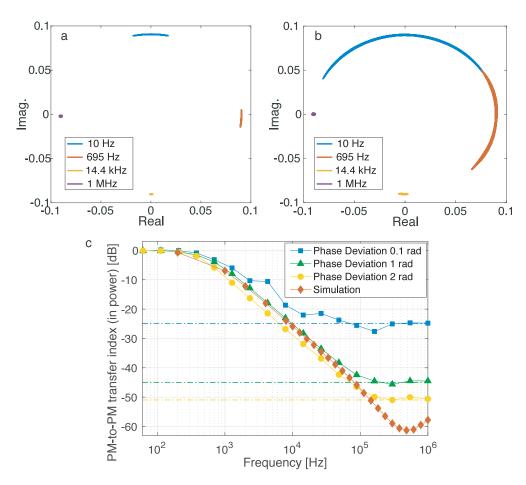


**Figure 4.20 – Transfer function between the input microwave phase and the repetition rate phase (PM-to-PM). (a-b)** The amplitude and the phase responses to the injected PM on the input microwave signal can be derived from the data in complex plane. The 4 sets of data are corresponding to 4 different PM frequencies that are indicated in the figure. The phase deviation of the PM on the input microwave signal is set to be 0.1 rad in (a) and 2 rad in (b). **(c)** Measured and simulated PM-to-PM noise transfer function between the injected microwave signal to  $f_{\text{rep}}$  of the DKS stream. The flat floors of the experimental data at frequencies above 100 kHz are due to the noise floor of the phase noise analyzer used for the IQ measurement, which are indicated by the dash-dot lines.

# 5 Ultralow-noise soliton microcomb for microwaves generation

"Whoever wants music instead of noise [...] finds no home in this trivial world of ours."

DER STEPPENWOLF HERMANN HESSE

#### 5.1 Introduction

Optical frequency combs (OFC) featuring ultra-narrow optical lines are useful in a number of applications [121], such as ultra-precise optical frequency measurements, or comparison of state-of-the-art optical clocks [227]. They can also be used to transfer the high stability of optical signals into the microwave domain [40, 41]. These applications typically require the stabilization of the comb against an ultra-stable optical reference like a narrow-linewidth, cavity-stabilized CW laser [220]. A faithful transfer of the linewidth and phase noise of the optical reference source to each tooth in the comb is thus desired, to obtain sub-hertz linewidths on the comb teeth.

Considering the case of soliton microcombs, their lines follow

$$v_{\mu} = f_{\rm p} + \mu f_{\rm rep} , \quad \mu \in \mathbb{Z}. \tag{5.1}$$

where  $f_p$  is the pump laser frequency and  $f_{rep}$  is the comb repetition rate. The generation of an ultralow-noise microcomb thus requires an ultra-stable laser (USL) as a pump. In addition, the soliton repetition rate noise must be minimized.

This chapter explains the different steps followed in the development of such microcomb. A USL source was installed in the lab (see fig. 5.1) and used as the optical frequency reference for the microcomb pump. The DKS generation procedure and stabilization was adapted based on

method exposed in chapter 4. This stabilization enabled the study of the soliton repetition rate properties with an unprecedented level of precision. This allowed the effective minimization of the comb repetition rate noise.

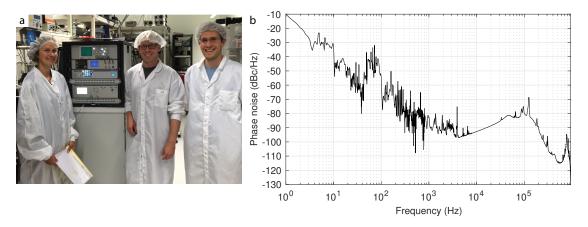


**Figure 5.1 – Ultra-stable laser.** (a) Installation of the ultra-stable laser ORS 1500 in the lab, with the assistance of Dr. Katja Beha and Dr. John D. Jost. (b) Optical phase noise of the laser measured in ref. [228].

The resulting low-noise comb was used for the characterization of the linewidth of several low-noise continous-wave lasers in our lab and for the generation of ultralow-noise microwaves.

## 5.2 Soliton generation and stabilization with an ultra-low-noise pump laser

The principle of operation of the microcomb pumped with the USL is shown in fig. 5.2. In this stabilization scheme, the pump laser is directly phase locked to the USL to allow a tight locking and a faithful replication of the USL stability. The microresonator is then stabilized to the pump (and thereby to the USL) via a PDH offset lock.

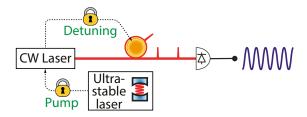


**Figure 5.2 – Stabilization scheme of the microcomb to the ultra-stable laser.** The pump laser is tightly phase locked to the ultra-stable laser and the microresonator is stabilized to the pump via an offset-PDH stabilization.

#### 5.2.1 Soliton generation procedure

The soliton generation with the laser scan method requires rapid tunability of either the pump laser or the resonator. An ultra-stable laser (USL) locked to a high-finesse reference cavity is typically not tunable and the crystalline resonator used here cannot be tuned fast enough to overcome thermal effects [88]. We circumvent this problem by implementing an optical phase lock loop (OPLL) to stabilize the frequency offset between the pump external-cavity diode laser (ECDL, Toptica CTL1550) and the reference USL (Menlo Systems ORS1500) operating at 1553 nm. The soliton state is generated by rapid tuning of the ECDL via current tuning. After soliton generation, the OPLL is activated with a frequency offset set such as to preserve the soliton. Resonators with improved tuning capabilities could remove the need for an OPLL altogether.

#### 5.2.2 Optical phase lock loop

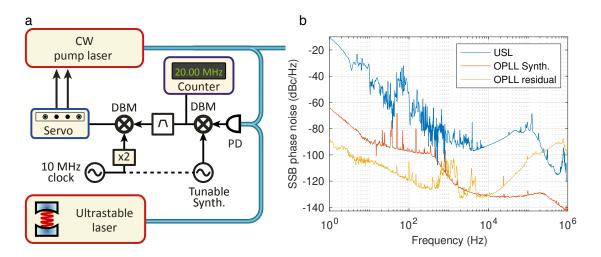


**Figure 5.3 – Optical phase lock loop (a)** Detailed experimental setup. PD, photodiode; DBM double balanced mixer;  $\times 2$ , frequency doubler. **(b)** Comparison between the USL phase noise and the residual phase noise contribution of the OPLL components. The red line shows the phase noise of the 1.7 GHz synthesizer and the yellow line the phase noise of the 20 MHz IF signal, indicating a feedback bandwidth in the range of  $\sim 500$  kHz. The overall added noise is negligible compared to the USL.

The schematic of the OPLL is presented in fig. 5.3a. The beatnote between the two lasers is photo-detected at a frequency of 1.7 GHz, and down-mixed to an intermediate frequency (IF) of 20 MHz using a frequency synthesizer. After soliton generation, the synthesizer frequency is set precisely using a frequency counter, in order to preserve the pump laser within the soliton existence range upon lock activation. The IF signal is band-pass filtered and compared to a 20 MHz RF signal derived from a 10 MHz common clock, using a double-balanced mixer (DBM). The resulting error signal passes through a proportional–integral–derivative controller

(PID, Toptica MFALC) which implements a slow feedback to the laser piezoelectric transducer and a fast feedback to the diode laser current allowing a  $\sim 500$  kHz actuation bandwidth (see fig. 5.3b). The residual noise of the OPLL and the phase noise of the synthesizer are negligible compared to the USL noise, indicating a good transfer of the USL purity to the pump laser (see fig. 5.3b).

#### 5.2.3 Resonator stabilization

Even if the pump laser is locked to a referenced comb, the thermal drift of the resonator induces detuning drifts which can lead to degraded noise performance and even loss of the soliton. Therefore, following soliton generation and OPLL activation, an offset PDH lock actively stabilizes the detuning (fig. 5.4b).

The PDH servo acts thermally on the resonator, to maintain a fixed pump-resonator detuning. The feedback is implemented to the pump laser power (using a  $0^{th}$  order AOM) and a slower actuation on a LED (Thorlabs MCWHL5 with a typical power of 800 mW) shining on the resonator through a microscope also used for imaging. With this double actuation, the pump power can be kept to a determined setpoint. The residual noise of the PDH error signal indicates an actuation bandwidth of  $\sim 100$  Hz, limited by the thermal response of the resonator (fig. 5.4d).

Owing to this overall scheme, the resonator is stabilized to the USL, which improves the stability of the system, as shown in fig. 5.4c. The comb could be maintained for more than a week without intervention.

#### 5.3 Soliton repetition rate noise minimization

#### 5.3.1 Repetition rate dependence on detuning

From a pure LLE perspective, the soliton should circulate at a rate  $D_1/2\pi$  corresponding to the cavity FSR. However, this quantity is subject to thermal drifts, which lead to repetition rate modifications.

Moreover, in real cavities the presence of the Raman effect [174, 175] and AMX can lead to repetition rate alterations [172, 177], that are detuning-dependent. The laser-resonator detuning  $2\pi \, \delta = \delta \omega = \omega_0 - \omega_p$  thus has a major impact on the noise and stability of Kerr frequency combs. The modification of the repetition rate frequency occurs mainly through the Raman self-frequency shift [174, 175]  $\Omega_{Raman}(\delta)$ , and the soliton recoil  $\Omega_{recoil}$  corresponding to dispersive wave emission [165, 172]. Indeed, these two effects lead to an overall shift of the spectral center of the soliton (i.e., the soliton spectral maximum relative to the pump frequency)  $\Omega = \Omega_{Raman} + \Omega_{recoil}$ , which induces in turn a change in the group velocity experienced by the pulse and therefore of the repetition rate according to [229]

$$\omega_{\text{rep}} = D_1 + \frac{D_2}{D_1} \Omega(\delta \omega) \tag{5.2}$$

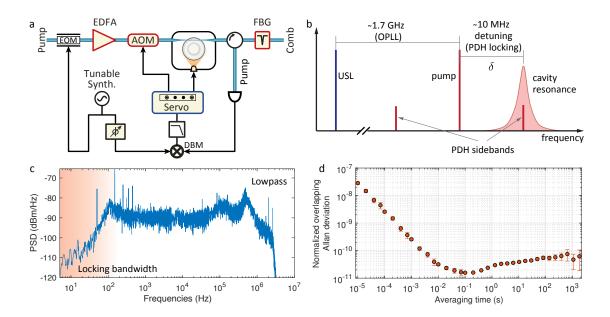


**Figure 5.4 – Pound-Drever-Hall detuning stabilization (a)** Detailed experimental setup. EOM, electro-optic modulator; EDFA, erbium-doped fiber amplifier; AOM, acousto-optic modulator; FBG, fiber Bragg grating. **(b)** Scheme of the principle of the stabilization. The pump laser is phase-locked to the USL. The cavity resonance detuning is then locked to the pump laser via PDH stabilization using feedback to the pump laser power (and radiative heating of the resonator). **(d)** Power spectral density (PSD) of the residual PDH error signal, when the detuning lock is active. **(c)** Repetition rate stability of the microcomb obtained when the pump laser is phase locked to the USL and the resonator stabilized to the USL.

where  $\omega_{\rm rep}=2\pi\,f_{\rm rep}$ ,  $D_1/2\pi=14.09$  GHz is the resonator free spectral range (FSR) and  $D_2/2\pi=1.96$  kHz is the group velocity dispersion (GVD) parameter at the pump frequency. We can rewrite this equation in terms of the fluctuations of the pump frequency  $\Delta\omega_{\rm p}$  and of the FSR fluctuations  $\Delta D_1$ 

$$\Delta\omega_{\rm rep} = \Delta D_1 + \frac{\partial\Omega}{\partial\delta\omega} \left(\Delta\omega_0 - \Delta\omega_{\rm p}\right) = \left(1 + N\frac{\partial\Omega}{\partial\delta\omega}\right) \Delta D_1 - \frac{\partial\Omega}{\partial\delta\omega} \Delta\omega_{\rm p} \tag{5.3}$$

where N is the absolute mode index of the pumped resonance. Thus, residual laser-resonator detuning noise can degrade the spectral purity of the repetition rate [219]. If we assume that the laser frequency and the cavity fluctuations are independent, it appears that the laser frequency noise is directly imprinted on the repetition rate, with a conversion coefficient equal to the local slope of the recoil with respect to detuning.

A solution to this problem was already identified by Yi *et al.* [172], who proposed to compensate the Raman-induced soliton-self-frequency shift with the dispersive-wave recoil to reduce the slope at a particular point. A similar concept is explored here to minimize the repetition rate noise of the crystalline  $MgF_2$  microresonator-based comb. Importantly, in  $MgF_2$ , the Raman self frequency shift can be neglected, due to the very narrow gain bandwidth, and the soliton

shift is dominated by the soliton recoil  $\Omega \approx \Omega_{recoil}$ .

Beyond these effects, the third order dispersion also leads to a modification of the soliton velocity with detuning, and any asymmetries in the mode spectrum of the microresonator can lead to coupling the optical fluctuations of the pump to the repetition rate [230]. A careful characterization of the relation  $f_{\rm rep}(\delta)$  is thus needed to determine an optimum operating point.

#### 5.3.2 Coupling adjustment and impact on the repetition rate stability

We measured the variation in repetition rate of the soliton comb as a function of detuning in two coupling conditions (weaker and larger coupling).

The detuning was modified by stepping the PDH modulation frequency (and by carefully balancing the demodulation phase as explained in section 4.2.3). For each modification of this frequency, the frequency of the synthesizer in the OPLL is adjusted accordingly to keep the frequency offset between the USL and the microresonator resonance constant (see fig. 5.4b).

The evanescent coupling to the resonance is achieved via a tapered optical fiber which is operated in contact with the resonator to dampen its vibrations. The coupling rate was modified by changing the position of the tapered fiber along the resonator. The lower coupling case, corresponds approximately to the critical coupling, with a loaded linewidth of  $\sim$  200 kHz. Careful adjustment of the fiber position is required to maximize the coupling rate (as much as allowed by the targeted laser detuning) and increase the out-coupled comb power. The loaded resonance linewidth in the larger coupling case is estimated at  $\sim$  2.4 MHz. For each coupling situation, the detuning was scanned forward and backward and at each detuning point, the optical spectrum was acquired and the repetition rate frequency  $f_{\rm rep}$  was counted. The results are displayed in fig. 5.5.

The weaker coupling of the resonator allows for a relatively wide detuning range to be accessed (5 to 25 MHz, see fig. 5.5b). Over this span, the repetition rate changes in total by 22 kHz, but not linearly. The non-monotonic evolution of  $f_{\rm rep}(\delta)$  is caused by the soliton recoil induced by dispersive waves through avoided mode crossings [165, 172, 177]. The soliton shift  $\Omega/2\pi$  is extracted by fitting the optical spectrum with a sech² function and the associated repetition rate variation can be estimated using eq. (5.2). Interestingly, after subtracting this contribution, the residual shift of the repetition rate follows a linear trend with a slope of  $\sim -1$  kHz/MHz. This significant variation is independent from any recoil-associated effect and could originate from more complex forms of avoided modal crossings, or third order dispersion, although we observed that the value of this slope changes with the coupling as detailed below.

Increasing the coupling rate of the resonator (see fig. 5.5d) shrinks the accessible detuning range (5.5 to 10 MHz), and radically changes the dependence of  $f_{\rm rep}$  with  $\delta$ . The overall variation is reduced to  $\sim 1.4$  kHz, and is dominated by solitonic recoil. Once this contribution is subtracted, the residual slope is on the order of  $\sim -160$  Hz/MHz, which is very close to the value expected from the non linear self-steepening effect [231].

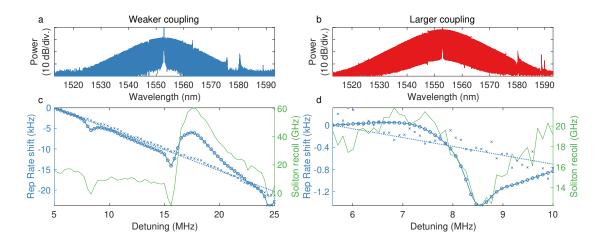


**Figure 5.5 – Optimization of**  $f_{rep}$  **phase noise (a)** Soliton spectrum for the lower coupling case (Detuning 10 MHz). **(b)** Evolution of the repetition rate (blue, solid) and of the soliton recoil  $(\Omega/2\pi)$  retrieved by fitting the optical spectrum (green), in the lower coupling case. The blue crosses and dashed line show the residual repetition rate change after subtraction of the recoil induced shift (using eq. (5.2)). **(c)** Soliton spectrum for the larger coupling case (Detuning 10 MHz). **(d)** Evolution of the repetition rate (blue, solid) and of the soliton recoil  $(\Omega/2\pi)$  retrieved by fitting the optical spectrum (green), in the larger coupling case. The blue dashed line shows the residual repetition rate change after subtraction of the recoil induced shift (using eq. (5.2)).

#### 5.3.3 Soliton repetition rate quiet point

More notably, under this larger coupling condition, the relation  $f_{rep}(\delta)$  exhibits a stationary point around  $\delta = 7$  MHz, where the coupling of pump-laser frequency noise into the soliton repetition rate is expected to be minimal since  $\partial f_{\text{rep}}/\partial \delta \approx 0$ . To verify this prediction, the phase noise of the detected soliton pulse train was measured at different detuning points. The pump laser was phase-modulated by a low frequency tone at 9 kHz to provide a reference point. Furthermore, instead of phase-locking the pump laser to the USL, the PDH feedback was applied to the pump laser current in these measurements, and the resonator was slowly stabilized to the USL via power and thermal feedback. The larger laser noise obtained in this case helps visualizing its impact on the repetition rate frequency and could be calibrated via a heterodyne measurement with the USL. The results are displayed in fig. 5.6. At the operating point 2, where the slope of  $f_{rep}(\delta)$  is maximum, the noise of  $f_{rep}$  follows the same features as the laser noise. Rescaling the laser noise to match the 9 kHz modulation peaks indicates that the optical noise is reduced by 56 dB. Conversely the point labeled 1, where the slope of  $f_{\rm rep}(\delta)$ is minimum, corresponds to the lowest optical-to-RF noise transduction (dip in fig. 5.6a), with a conversion coefficient below -100 dB. As expected, this point yields the lowest achieved phase noise, and it appears that the laser phase noise is no longer the overall limiting factor of the Kerr comb repetition rate noise.

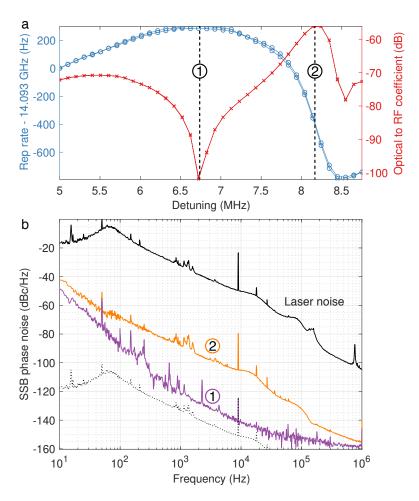


**Figure 5.6 – 'Quiet' operating point (a)** Evolution of the repetition rate with the detuning (blue) and associated optical phase modulation to RF phase modulation conversion coefficient calibrated with the 9 kHz phase modulation tone on the laser (red). **(b)** Phase noise spectra of the soliton repetition rate at the two operating points highlighted in (a). The solid black line shows the laser noise (PDH-stabilized to the microcavity). The dashed black line shows the noise of the laser scaled by -100 dB to match the 9 kHz phase calibration tone.

# 5.3.4 Residual limitations

#### Pump relative intensity noise

In a nonlinear resonator, the free spectral range  $D_1/2\pi$  depends on the circulating optical power. Therefore, the relative intensity noise (RIN) of the pump laser (power  $P_{\rm in}$ ) eventually induces timing jitter of the repetition rate, according to eq. (5.2). Assuming a laser on resonance, the self phase modulation induced shift follows [232]:

$$\frac{\delta D_1(\omega)}{2\pi} = \underbrace{\left(\frac{D_1}{2\pi} \frac{4\eta \, c \, n_2}{\kappa \, V_{\text{eff}} n_0^2}\right)}_{\delta P_{\text{in}}(\omega)} \delta P_{\text{in}}(\omega) \tag{5.4}$$

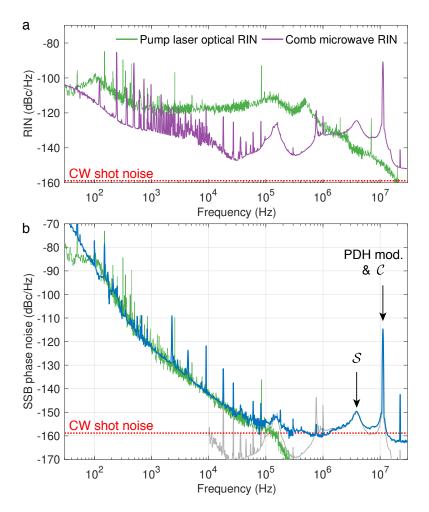


**Figure 5.7 – Pump laser RIN and estimated limitation on the phase noise (a)** Optical RIN of the pump laser (green) and microwave amplitude noise of the soliton repetition rate (purple). **(b)** Phase noise spectrum of the repetition rate at the 'quiet' point (blue) and estimated limitation from the pump laser RIN (green). The grey curve corresponds to the estimated AM to PM conversion in the photodiode (microwave amplitude noise scaled by –25 dB).

where  $\kappa/2\pi \approx 1.35$  MHz is the cavity energy decay rate,  $\eta = \kappa_{\rm ex}/\kappa \approx 0.94$  is the coupling impedance of the resonator ( $\kappa_{\rm ex}$  is the coupling rate),  $V_{\rm eff} \approx 2.32 \times 10^{-12}$  m<sup>3</sup> is the mode volume,  $n_2 = 9 \times 10^{-21}$  m<sup>2</sup>/W is the (Kerr) nonlinear index and  $n_0 = 1.37$  is the refractive index. These values yield a conversion coefficient  $\alpha \approx 3.8$  kHz/W. We measured the relative intensity noise  $S_{\rm RIN}(f)$  of the pump laser (fig. 5.7a) and the associated induced phase noise was estimated using:

$$S_{D_1/2\pi}^{\phi}(f) = \left(\frac{\alpha}{f}P_{\rm in}\right)^2 S_{\rm RIN}(f) \tag{5.5}$$

for the measured input pump power of  $P_{\rm in} \approx 212$  mW. The results are displayed in fig. 5.7b. The estimated level matches remarkably the repetition rate phase noise at offsets between

500 Hz and 100 kHz (blue and green curves in fig. 5.7b), suggesting that the pump laser RIN is limiting the performance in this range.

#### Thermal drift

At lower frequencies (50 – 500 Hz), the thermal fluctuations and drift of the resonator, which are beyond the power stabilization bandwidth, are the limiting factor [127, 233].

### **Technical noise contributions**

At higher offset frequencies, two noise bumps appear related to the characteristic double resonant response ( $\mathcal{S}$  and  $\mathcal{C}$ ) of the resonator in the soliton regime [159]. In these resonant features, the transduction of the pump laser noise is enhanced [219]. Beyond 100 kHz offset, the contributions of various factors are more difficult to identify. We observed nonetheless a correlation between the microwave RIN (fig. 5.7a) and the phase noise, which suggests that amplitude to phase noise conversion is occurring in the photodiode [234], with a conversion factor of  $\sim -25$  dB (grey curve in fig. 5.7b), which is in agreement with reported values for similar photodiodes [235]. We report here the microwave amplitude noise, as our measurement device offered a better sensitivity in this configuration, but our observations showed that this amplitude noise matches well the optical RIN (measured at DC with a diplexer).

#### Shot noise floor

Finally, the continuous-wave shot-noise floor is expected to be at  $-159~\mathrm{dBc/Hz}$  (photocurrent of 6.85 mA, microwave power of  $-3.8~\mathrm{dBm}$ ). However, we noticed that the phase noise floor of our measurement stands 4.1 dB below this value (at frequency offsets above 20 MHz), while the amplitude noise floor is 6.3 dB above. This imbalance between amplitude and phase needs further investigation and could be related to shot noise correlations in the detection of optical pulses [236–238].

# 5.4 Ultralow-noise microcomb as a broadband narrow laser reference

The optimized ultralow-noise soliton microcomb was employed to estimate the linewidth of some low-noise lasers in our laboratory. Although they operate within the C band, these lasers could not be tuned close enough to the USL to obtain a detectable beatnote. The comb was used to bridge the gap between the USL and these laser and perform a comparison (see Figure 5.8a).

First, a low-noise CW fiber laser (NKT Adjustik E15) at  $\sim 1554.5$  nm was characterized. Figure 5.8c shows that this laser is 15 comb lines away from the USL pump laser. We first estimated the limits of our system by comparing the phase noise of the USL, of the soliton repetition rate (accounting for the multiplication by 15 of the fluctuations) and of the beatnote between the fiber laser and the nearest comb line, shown in fig. 5.8. This measurement reveals

<sup>&</sup>lt;sup>1</sup>These measurements were realized with R. Bouchand and A.S. Raja.

that the main limitation of the comb between 30 kHz and 1 MHz arises from a servo bump of the USL. Between 1 MHz and 10 MHz, the  $\mathcal{S}$ - and  $\mathcal{C}$ -resonance of the repetition rate appear to be limiting. Nevertheless, the comb is not limiting the measurement at low offset frequency, which is the most important factor in our measurement. The fitting of the laser - comb beatnote with a Voigt profile provided a laser linewidth estimate of  $\sim 1.7$  kHz, which agrees with the specifications of the laser.

A second compact low-noise DFB laser operating at  $\sim$  1550 nm was also characterized. This wavelength corresponds is located 16 lines away from the USL. The beatnote fitting showed the relatively higher noise of this laser compare to the fiber one (estimated linewidth  $\sim$  33 kHz).

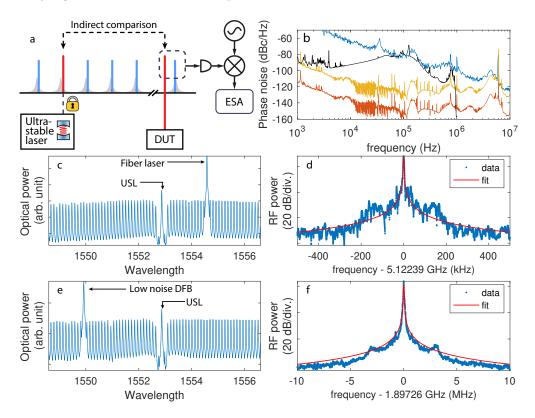


**Figure 5.8 – Laser linewidth testing with the ultralow-noise microcomb.** (a) Principle of operation. The microcomb is used to transfer the USL stability of its pump to other region of the C-band to compare with other lasers in the lab. (b) Evaluation of the limitation of the method in the case of the low-noise fiber laser. The phase noise of the USL is plotted in black, the comb repetition rate is plotted in red. The yellow line accounts for the multiplicative effect of the repetition rate noise for the comparison 15 lines away from the pump (factor  $20\log(15) \approx 23.5 \text{ dB}$  added). The blue line shows the measured noise of the laser beating with the comb line. (c) Optical spectrum of the comparison between the comb and the low-noise fiber laser. (d) Measured beatnote between the comb and the fiber laser. A Voigt fit (red) was perform, yielding a Lorentzian width of  $\sim 220 \text{ Hz}$  and a Gaussian width of  $\sim 1.7 \text{ kHz}$ . (e) Optical spectrum of the comparison between the comb and the low-noise DFB laser. (e) Measured beatnote between the comb and the DFB laser. The Voigt fit (red) yields a Lorentzian width of  $\sim 3.5 \text{ kHz}$  and a Gaussian width of  $\sim 33 \text{ kHz}$ 

# 5.5 Ultralow-noise photonic microwave synthesis using a soliton microcomb-based transfer oscillator<sup>2</sup>

The synthesis of microwave signals via photonic systems, such as dual frequency lasers [240], optoelectronic oscillators [241], Brillouin oscillators [242], or electro-optical dividers [243], hold promise for their ability to synthesize low-noise or widely tunable microwave signals with compact form factor. In particular, microcomb-based microwave oscillators hold great promise of providing a robust, portable and power-efficient way to synthesize pure microwave tones [127]. In contrast to microresonator-based approaches of generating microwave signals using Brillouin lasers, the frequency of the generated signal is mainly determined by the cavity free spectral range (FSR), rather than the host material property of the resonator, thus offering flexibility over the microwave center frequency.

Today, microwave signals with the lowest reported phase noise [41] are produced by *optical-frequency division* using mode-locked laser frequency combs. This technique makes use of a self-referenced fs-laser comb optically-locked to an USL with a typical linewidth at the Hz-level [40–43]. If the comb line of index N is tightly phase-locked to the USL (after CEO subtraction), the comb repetition rate  $f_{\rm rep}$  is directly phase-stabilized to the ultra-stable frequency  $v_{\rm USL}$  by frequency division:  $f_{\rm rep} = (v_{\rm USL} - f_{\rm CEO})/N$ . Importantly, owing to the carrier frequency division from optics to microwaves, the absolute phase noise power spectral density is reduced by a factor  $N^2 \sim 10^8$ .

This method has been mostly implemented using fiber-based fs-lasers with repetition rates of a few hundred megahertz. A fast actuator (e.g., an intra-cavity electro-optic modulator [244]) is required to achieve a tight optical lock of the comb tooth to the optical reference and perform the frequency division over a wide bandwidth. Moreover, a high harmonic of the comb repetition rate must be used to synthesise a microwave signal beyond 10 GHz. Consequently, repetition rate multipliers are typically employed to reduce the impact of shot-noise in the photodetection of the pulse train, such as optical filtering cavities [245] or fiber interleavers [246], which increases the system complexity. Therefore, the use of frequency combs directly operating at ~ 10 GHz repetition rates would be highly beneficial, but their optical lock and self-referencing are challenging.

In this context, soliton-based microcombs appear as natural candidates, as they produce comb spectra with multi-GHz line spacing [9, 148, 167, 187] and the comb is inherently perfectly phase-locked to the pump laser. Direct soliton generation from an ultra-stable pump laser thus holds high potential for compact and powerful optical-to-microwave dividers. Although self-referenced optical microcombs and clocks have been demonstrated [247–249], optical frequency division for low-noise microwave generation using such devices has not been demonstrated so far, mainly due to the complex crosstalk occurring between their two degrees of freedom [219, 248] and the limited performance of the available actuators [187, 188].

<sup>&</sup>lt;sup>2</sup>The results of this section are partially adapted from the publication: E. Lucas et al., "Ultralow-Noise Photonic Microwave Synthesis using a Soliton Microcomb-based Transfer Oscillator" (2019), arXiv: 1903.01213. □

# 5.5.1 Principle of the transfer oscillator technique

Here, we demonstrate the generation of an ultralow-noise microwave signal using a microcomb-based transfer oscillator method to realise optical-to-microwave frequency division. The transfer oscillator method [250, 251] bypasses the need for tight optical phase-locking of the frequency comb to the optical reference. Instead, it relies on an adequate manipulation and combination of signals to cancel the comb phase noise and to provide a broadband electronic division of the USL frequency to the microwave domain. The frequency division by a large factor N is performed electronically, thus removing the need for high locking bandwidth actuators. In this work, the USL is used to pump the microresonator and inherently constitutes a tooth of the resulting frequency comb. We show how to extend the transfer oscillator technique to exploit this salient feature of microcombs (or equivalently of electro-optic combs [65]).

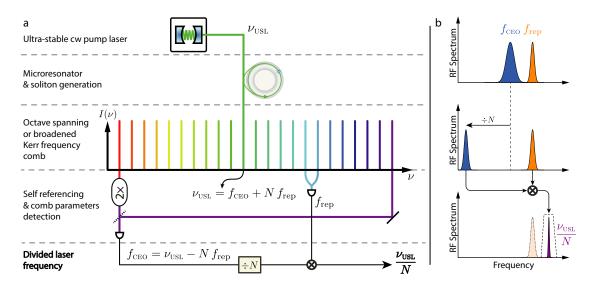


Figure 5.9 – Principle of operation of the Kerr comb-based transfer oscillator for optical-to-microwave frequency division. (a) Schematic illustration of the transfer oscillator technique applied to a Kerr comb (or electro-optic combs equivalently). (b) Schematic representation of the signal evolution along the electronic division chain leading to the low-noise output signal. The two comb parameters  $f_{\text{CEO}}$  and  $f_{\text{rep}}$  are detected. Both parameters can be free-running and fluctuate. The carrier envelope offset (CEO) frequency is electronically divided by a large number N that corresponds to the tooth number of the ultra-stable pump  $v_{\text{USL}}$ . After this step, the frequency fluctuations of the divided CEO  $f_{\text{CEO}}/N = f_{\text{rep}} + v_{\text{USL}}/N$  are dominated by the repetition rate fluctuations. These are removed by mixing  $f_{\text{CEO}}/N$  with  $f_{\text{rep}}$  to obtain the division result  $v_{\text{USL}}/N$ . A narrow-band filtering is used to reject spurs.

The working principle of our method is illustrated in fig. 5.9. A microresonator pumped by a sub-Hz-linewidth USL at frequency  $v_{\rm USL}$  generates a soliton-Kerr comb with a GHz-range repetition rate  $f_{\rm rep}$  that is set by the resonator free spectral range (FSR). The reference laser is part of the frequency comb (line N) such that its frequency can be written as  $v_{\rm USL} = f_{\rm CEO} + Nf_{\rm rep}$ . The detection of the CEO frequency (for example via f-2f interferometry [17, 18] or

with an auxiliary self-referenced comb as in the present work) is followed by electronic division by means of a combination of frequency pre-scalers and direct digital synthesizers (DDS). The final step consists of mixing the divided CEO signal with the repetition rate, which yields

$$f_{\text{signal}} = \frac{f_{\text{CEO}}}{N} + f_{\text{rep}} = \frac{v_{\text{USL}}}{N}$$
 (5.6)

Importantly, this process can be carried out with a free-running Kerr comb and obviates the need for a high-bandwidth optical lock.

# 5.5.2 Implementation with an auxiliary comb

The soliton-Kerr comb is generated in the same way as described in section 5.2. The detuning setpoint was carefully optimized in order to minimize the noise of the Kerr comb repetition rate  $f_{\text{rep}}$  (see section 5.3).

The used crystalline MgF $_2$  microcomb features a relatively narrow spectrum that prevents direct detection of its CEO frequency (fig. 5.10c). The self-referencing of Kerr combs remains highly demanding due to the high repetition rate, low optical power, and fairly long pulse duration (225 fs here) resulting in a low peak intensity which makes spectral broadening for f-2f interferometry challenging [248, 252]. Therefore, in this first proof of concept we implemented an indirect detection scheme using an auxiliary self-referenced fiber-laser frequency comb [253] with a repetition rate  $f_{\rm rep}^{\rm aux}=251.7$  MHz. The relative CEO frequency  $\Delta f_{\rm CEO}$  between the two combs can be retrieved from their beatnote, as shown in fig. 5.10b, provided that their repetition rates are harmonically phase-locked, i.e.,  $f_{\rm rep}^{\rm K}=Mf_{\rm rep}^{\rm aux}$  (superscripts 'K' and 'aux' refer to the Kerr and auxiliary comb, respectively). In this case, the repetition rate noise contributions compensate each other in the beat signal between the two combs, which thus only contains the relative noise between the two CEO frequencies  $\Delta f_{\rm CEO}$  (see fig. 5.10b). The Kerr comb CEO frequency is obtained by subtracting the CEO frequency of the auxiliary comb  $f_{\rm CEO}^{\rm aux}$  detected with an f-2f interferometer (see fig. 5.10a) and corresponds to  $f_{\rm CEO}^{\rm ceo}=\Delta f_{\rm CEO}^{\rm ceo}=v_{\rm pump}-Nf_{\rm rep}^{\rm K}$ .

The mutual phase-locking of the comb repetition rates is achieved via injection locking [218] (blue box in fig. 5.10a). The harmonic M=56 of the repetition rate of the auxiliary comb (at 14.093 GHz) is detected, filtered and amplified to  $\sim 19$  dBm, in order to drive an EOM that phase-modulates the pump light (phase deviation of  $\sim 1.4$  rad). This frequency is very close (within  $\gtrsim 2$  kHz) to the native Kerr line spacing, which gets injection-locked to this drive signal. Therefore, both repetition rates are strongly correlated over a bandwidth of  $\sim 2$  kHz.

The Kerr comb CEO signal, indirectly obtained as previously described, is detected at low frequency (MHz-range) and filtered to match the bandwidth of the injection locking of the repetition rates (not represented in fig. 5.10a, the full detail is provided in section 5.5.4). After up-mixing to 15 GHz, it is frequency-divided by a large pre-determined factor  $N \approx 13,698$  and is subtracted to the separately-detected repetition rate  $f_{\rm rep}^{\rm K}$  to obtain the frequency-divided signal

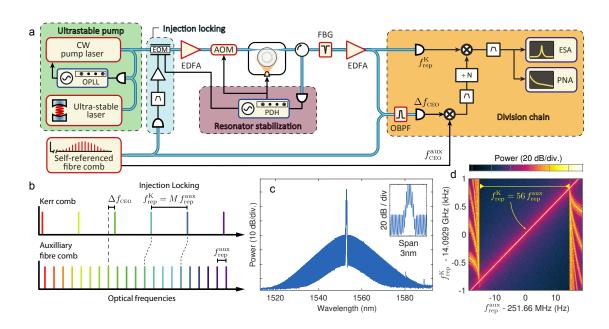


Figure 5.10 – Simplified experimental setup and principle of operation with the auxiliary comb (a) Setup for Kerr comb-based optical frequency division. The details of the division chain are given in section 5.5.4. EDFA, Er-doped fiber amplifier; AOM, Acousto-optic modulator; EOM, Electro-optic modulator; FBG, Fiber Bragg grating for pump rejection; OBPF, Optical band-pass filter; OPLL, Optical phase lock loop; PDH, Pound-Drever-Hall lock; DDS, Direct digital synthesizer; PNA, Phase noise analyzer; ESA, Electrical spectrum analyzer. The pump power after the EOM is  $\sim$  10 mW and is amplified to  $\sim$  250 mW with an EDFA. The power level after the AOM (see fig. 5.10a) is set to  $\sim$  210 mW. (b) The harmonic relation of the repetition rate of both combs is ensured via injection locking for M=56. The heterodyne beat between the two combs thus yields the difference of their carrier-envelope offset frequency ( $\Delta f_{\rm CEO}$ ). (c) Optical spectrum of the soliton-based Kerr comb. The inset shows the phase modulated sidebands around the pump laser tone which enforce the injection-locking. (d) Radio-frequency (RF) spectrogram showing the injection-locking effect between the Kerr comb repetition rate  $f_{\rm rep}^{\rm K}$  and the 56th harmonic of the auxiliary comb repetition rate  $f_{\rm rep}^{\rm aux}$ , obtained by changing the frequency of  $f_{\rm rep}^{\rm aux}$  (harmonic power  $\sim$  11 dBm applied to the EOM).

of the ultra-stable pump laser:  $v_{\text{pump}}/N = f_{\text{CEO}}^{\text{K}}/N + f_{\text{rep}}^{\text{K}}$  (orange box in fig. 5.10a). The overall division of the Kerr comb CEO signal by the factor N is realized with a frequency pre-scaler followed by two parallel DDS, which offers improved filtering capabilities in the electronic division [251]. This second stage division with the DDS allows for a precise non-integer frequency division factor and leads to a clean single-tone output signal corresponding to the frequency-divided USL (see fig. 5.11d). The overall division factor N was straightforwardly determined experimentally, without prior knowledge of the optical frequency of the ultra-stable pump laser, by measuring the frequency change of the generated microwave signal corresponding to a small variation (140 Hz) of the Kerr comb repetition rate for different programmed division factors N (see fig. 5.11b). This simple measurement also provides an accurate determination of an optical comb line index N and can be useful for absolute optical

frequency measurements.

#### **5.5.3** Result

The phase noise of the generated ultralow-noise  $14.09~\mathrm{GHz}$  signal was measured with a cross-correlator phase noise analyser (fig. 5.11a). It reaches  $-110~\mathrm{dBc/Hz}$  at  $200~\mathrm{Hz}$  Fourier frequency,  $15~\mathrm{dB}$  below the lowest phase noise microresonator-based photonics oscillator [127] at  $10~\mathrm{GHz}$ . The phase noise is below  $-135~\mathrm{dBc/Hz}$  at  $10~\mathrm{kHz}$  and  $-150~\mathrm{dBc/Hz}$  at around  $1~\mathrm{MHz}$ , showing that the intrinsic good short-term purity of the soliton Kerr comb is preserved. The calculated shot-noise predicts a noise floor at  $-152~\mathrm{dBc/Hz}$  (thermal noise floor  $\sim -170~\mathrm{dBc/Hz}$ ). At  $1~\mathrm{Hz}$  offset, the measurement is limited by the instrumental noise floor even with  $3000~\mathrm{cross}$  correlations. Nevertheless, the transfer oscillator offers an improvement by at least  $40~\mathrm{dB}$  compared to the direct detection of the Kerr comb repetition rate (despite the resonator being stabilised to the USL), showing its ability to cancel the residual thermal drifts of the Kerr cavity.

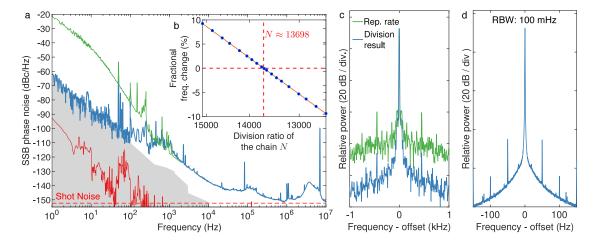


**Figure 5.11 – Experimental result of the signal generated by optical-to-microwave division** (a) Absolute single-sideband (SSB) phase noise of the 14.09 GHz signal generated by optical-to-microwave division of the USL via the Kerr comb transfer oscillator (blue) and obtained directly from the Kerr comb repetition rate (green) for comparison. The sensitivity limit of the phase noise analyzer (Rohde & Schwarz FSWP, 3000 cross correlations applied at 1 Hz) is indicated by the grey shaded area. The red line is the limit inferred from the optical phase noise, assuming an ideal noiseless division. (b) Precise determination of the optimal division factor *N* corresponding to the zero crossing of the linear fit (solid line) of the measured relative frequency change of the generated RF signal for a small variation of the repetition rate (dots). (c) Comparison between the RF spectra of the Kerr comb repetition rate and the optical-to-microwave frequency division result. The resolution bandwidth (RBW) is 5 Hz. (d) RF spectrum of the frequency-divided output signal, the RBW is 100 mHz. The data was acquired with the IQ demodulation mode of the spectrum analyzer.

In this first proof-of-principle demonstration, we achieved the lowest phase noise microwaves generated with an optical microresonator, with a measured single-sideband phase noise of

-110 dBc/Hz at 200 Hz offset from the 14.09 GHz carrier, which is 15 dB below the lowest phase noise microresonator-based photonic oscillator reported so far [127] or any other microresonator-based approach [128, 172, 242, 243]. This demonstrates the benefit of this method in microwave photonics and enlarges its previously reported implementation with low repetition rate mode-locked lasers.

#### 5.5.4 Division chain

The transfer oscillator approach is implemented in this work with a 2-DDS scheme as introduced by Brochard and co-authors [251] to perform electronic division with a finely adjustable ratio. This implementation also enables the generation of a low-noise single-tone RF output signal by efficiently filtering out other spurious peaks that would occur with a single DDS. The practical realization of this scheme with the Kerr comb is depicted in fig. 5.12.

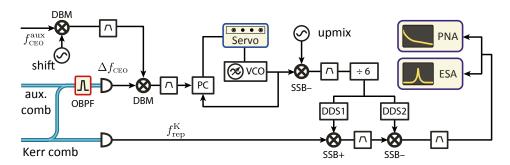


Figure 5.12 – Frequency chain for the transfer oscillator division Implementation of the optical-to-microwave frequency division using the 2-DDS transfer oscillator scheme. The  $f_{\rm rep}$  component of the Kerr comb detected with a fast photodiode (lower path) is mixed with the CEO signal frequency-divided by a factor N (upper path). The division from 15 GHz to 1.095 MHz is realized by a frequency pre-scaler (÷6) followed by two DDS in parallel that output signals at 100 MHz and 101.095 MHz, respectively, from the 2.5 GHz input clock signal. The CEO frequency of the Kerr comb is indirectly obtained from the subtraction of the frequency-shifted auxiliary self-referenced comb CEO  $f_{\rm CEO}^{\rm aux}$  with the optical beat-note from the two combs ( $\Delta f_{\rm CEO}$ ), due to the fact that the phase noise of the repetition rate of the two combs is correlated by an injection locking scheme. DBM, double-balanced mixer; VCO, voltage-controlled oscillator; PC, digital phase comparator; SSB(+/-), single sideband mixer (sum/difference frequency); DDS, direct digital synthesizer; PNA, phase noise analyzer; ESA, electrical spectrum analyzer.

An auxiliary optical frequency comb (Menlo Systems FC1500) is used here to detect the CEO frequency of the Kerr-comb  $f_{\text{CEO}}^{\text{K}}$ , as the used crystalline microcomb features a relatively narrow spectrum that prevents a direct detection of its CEO frequency. After comb generation and residual pump rejection with a fiber Bragg grating, the comb power of  $\sim 1$  mW is amplified to  $\gtrsim 5$  mW. The largest part of this power (90%) is sent onto a high power handling photodiode (Discovery Semiconductors DSC40, generating a photocurrent of 5.12 mA and a microwave power of  $\sim -7.4$  dBm), while the remaining fraction is used for the intercomb beatnote

detection. The shot noise level is estimated for a CW laser detection, based on the photocurrent and microwave power. An optical beat-note between the two combs is first detected with a photodiode (NewFocus model 1811) at a frequency of a few tens of MHz. This low-frequency beat signal corresponds to the frequency difference between one mode of each comb, i.e.,

$$f_{\text{beat}} = N(f_{\text{rep}}^{\text{K}} - 56 f_{\text{rep}}^{\text{aux}}) + (f_{\text{CEO}}^{\text{K}} - f_{\text{CEO}}^{\text{aux}})$$
 (5.7)

where the superscripts 'K' and 'aux' refer to the Kerr and auxiliary comb, respectively, and the 56<sup>th</sup> harmonic of the 251.6 MHz repetition rate of the auxiliary comb is in close vicinity to the fundamental repetition rate of the Kerr comb.

To suppress the relative phase noise between the repetition rate of the two combs in this beat signal, we imprint the  $f_{\rm rep}$  noise of the auxiliary comb to the Kerr comb by injection locking. This is realized by detecting and band-pass filtering the 56<sup>th</sup> harmonic of  $f_{\rm rep}^{\rm aux}$  (auxiliary comb) at 14.09 GHz and using this signal, after amplification to  $\sim$  19 dBm, to drive an EOM (iXblue MPZ-LN-10) to create a set of sidebands around the ultra-stable pump laser of the microresonator, which injection-lock the adjacent optical modes of the resonator. This strongly correlates the noise of the repetition rate of the two combs, but only within the bandwidth of the injection locking that is in the kHz range, as shown in fig. 5.13.

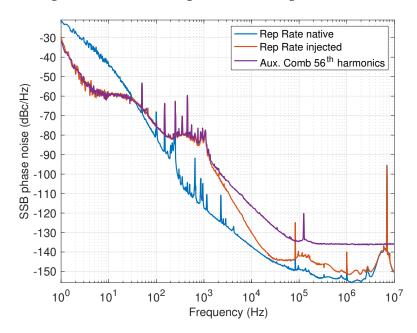


**Figure 5.13 – Injection locking of the repetition rate** Comparison between the phase noise of the Kerr comb repetition rate when it is native (blue) and injection locked (orange) by the 56<sup>th</sup> harmonic of the auxiliary comb repetition rate (purple).

The beat signal between the two combs is mixed in a double balanced mixer (DBM) with the CEO signal of the auxiliary comb (detected using a standard f-2f interferometer) in order to remove this contribution. Prior to the mixing, the CEO signal of the auxiliary comb, which is stabilized at 20 MHz, is frequency-up-shifted using a low-noise synthesizer. This

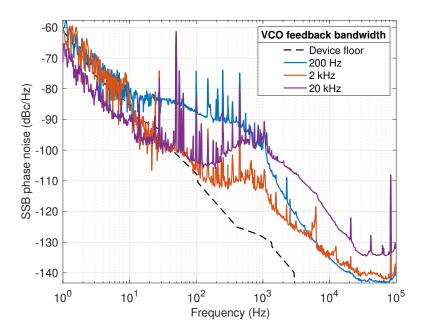


**Figure 5.14 – Tracking oscillator effect.** Influence of the bandwidth of the tracking oscillator used to filter the Kerr comb  $f_{\text{CEO}}$  on the final generated RF signal. The lowest phase noise of the final RF signal is obtained for a locking bandwidth of the VCO of  $\sim 2$  kHz (orange curve), similar to the bandwidth of the injection locking process used to correlate the noise of the repetition rate of the two combs. A lower ( $\sim 200$  Hz, blue curve) or higher ( $\sim 20$  kHz, purple curve) bandwidth results in a higher noise of the generated RF signal.

adds some flexibility to the experimental scheme by providing a straightforward means to electrically tune  $f_{\text{CEO}}^{\text{aux}}$  without changing it optically (which would also change the optical beatnote frequency by  $\Delta f_{\text{CEO}}$ ) and without frequency noise degradation, as the measured phase noise of the intermediate synthesizer is comparatively negligible. This helps to quickly change the effective sign of  $f_{\text{CEO}}^{\text{aux}}$ , without changing any RF component, in order to properly remove its contribution when mixing with  $\Delta f_{\text{CEO}}$  in the DBM. Furthermore, this flexibility enables us to finely adjust the output signal containing the effective Kerr comb CEO in order to match the frequency of a tracking oscillator around 40 MHz. This tracking oscillator consists in a narrow-band low-noise voltage-controlled oscillator (VCO) which is phase-locked to the signal. Fine adjustment of the VCO locking bandwidth enables us to filter the noise of  $f_{CEO}^{K}$  in order to counteract the influence of the finite injection locking bandwidth where the relation  $f_{\rm rep}^{\rm K}=56f_{\rm rep}^{\rm aux}$  is ensured. Hence, the contribution of the residual relative phase noise between the two combs in the generated ultralow-noise RF signal is minimized for a VCO locking bandwidth of ~ 2 kHz, which matches the injection locking bandwidth. Lower (~ 200 Hz) or higher (~ 20 kHz) feedback bandwidths lead to an increased noise in the final signal at low or high Fourier frequencies respectively (fig. 5.14) as a result of the imperfect noise compensation of the auxiliary comb. Furthermore, as an RF signal with a sufficient signal-to-noise ratio (SNR) of more than 30 dB is needed for proper and stable operation of the subsequent frequency divider, this tracking oscillator helps improve the signal quality, so that even a fairly low SNR of the signal at the output of the DBM allows us to use the transfer oscillator method.

The signal after the tracking oscillator is up-converted to 15 GHz using a synthesizer with an absolute phase noise lower than the USL (see fig. 5.15), so that its noise has a negligible contribution in the final signal. This frequency shift is necessary to perform the subsequent frequency division by a large number of around 13,698. Eventually, this synthesizer could be replaced by the repetition rate of the Kerr-comb to alleviate any of the associated limitation. This was not implemented here due to the lack of appropriate filters. The frequency division from 15 GHz to 1.095 MHz is realized by a frequency pre-scaler (÷6, RF Bay FPS-6-15) followed by two DDS (AD9915 evaluation board) in parallel that respectively output signals at 100 MHz and 101.095 MHz from their 2.5 GHz input clock signal. These two signals are subsequently mixed with the repetition rate of the Kerr comb separately detected using a fast photodiode (Discovery Semiconductors DSC40) and filtered to select the proper component that corresponds to  $f_{\rm RF} = f_{\rm rep}^{\rm K} + f_{\rm CEO}^{\rm K}/N = v_{\rm USL}/N$ . The sequential mixing followed by filtering after each DDS allows for the efficient rejection of the spurious peaks occurring at harmonics of the DDS signals, thanks to their relatively high frequency spacing (100 MHz-range). The generated ultralownoise RF signal is characterized using a phase noise analyzer (PNA, model FSWP26 from Rohde-Schwarz) and an electrical spectrum analyzer (ESA, model FSW43 from Rohde-Schwarz).

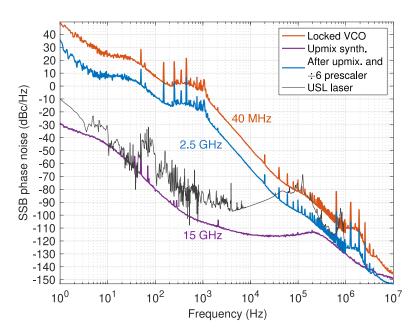


**Figure 5.15 – Upmixing and prescaler division.** Evolution of the signal phase noise during the upmixing and prescaler division of the filtered Kerr comb CEO. The carrier frequencies are indicated on the plot. The noise of the upmixing synthesizer (purple curve) is smaller than the USL noise (black), such that it does not limit the final division result. Upmixing with the comb repetition rate would avoid this potential limitation.

The effect of the frequency division performed with the 2-DDS scheme is illustrated in fig. 5.16. The frequency difference of the two signals at 100 MHz and 101.095 MHz, respectively, gives a signal at 1.095 MHz which correspond to  $f_{\text{CEO}}^{\text{K}}/N$  and is strongly correlated with  $f_{\text{rep}}^{\text{K}}$  at 14.09 GHz. Mixing these two signal results in the generation of a very low-noise RF signal

which demonstrates a high rejection of the Kerr comb phase noise.

Finally, the noise compensation in the transfer oscillator method relies on the subtraction of various noise contributions of the micro-resonator comb. Perfect noise compensation occurs when no relative delay is introduced between  $f_{\rm CEO}/N$  and  $f_{\rm rep}$  at the time of their final mixing. If a significant delay occurs between the signals, the noise compensation may be incomplete as the signals become imperfectly correlated [254] and the residual (uncompensated) noise scales according to

$$S_{\varphi}^{\text{signal}}(f) = \frac{1}{N^2} S_{\varphi}^{\text{USL}}(f) + 4\sin^2\left(\pi\tau f\right) S_{\varphi}^{\text{rep}}(f), \tag{5.8}$$

where  $\tau$  is the relative delay, f is the Fourier frequency and  $S_{\varphi}$  denotes the phase noise power spectral density. If  $\tau=0$  the repetition rate phase noise is properly cancelled. Some care is thus needed to minimise the delays, in order to maximise the cancellation bandwidth, but this factor is not critical. For example, a coarse 10 m length mismatch would correspond to  $\sim$  42 ns delay (assuming a velocity factor of 80 %) and the rejection effect would be null (0 dB) at a Fourier frequency of  $\sim$  4 MHz.

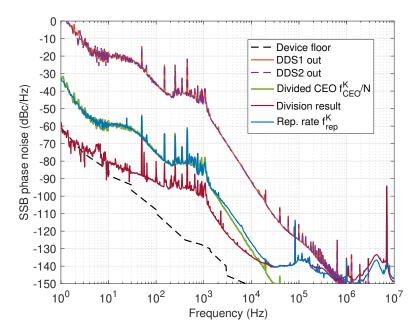


**Figure 5.16 – Noise division demonstration.** Demonstration of the noise division achieved by the 2-DDS scheme. The orange and dashed violet curves show the phase noise PSD separately measured at the output of each DDS at 101.095 MHz (DDS1) and 100 MHz (DDS2), respectively. The green curve displays the noise of the frequency-divided CEO signal of the Kerr comb, which overlaps the noise of the repetition rate (blue curve). Therefore, these two noise contributions compensate each other to a large extend in the final RF signal (red curve), which demonstrates the noise improvement brought by the transfer oscillator scheme, limited here by the Kerr comb injection locking bandwidth.

The high rejection of the Kerr comb phase noise offered by the transfer oscillator scheme

requires mixing signals with the proper sign combination, so that the frequency fluctuations of  $f_{\rm rep}^{\rm K}$  and  $f_{\rm CEO}^{\rm K}$  are indeed compensated in the final RF signal. The sign of  $f_{\rm CEO}^{\rm K}$  is determined by the heterodyne beat between the Kerr comb and the auxiliary comb, which can be controlled by the repetition rate of the auxiliary comb, and by the subtracted CEO signal of the auxiliary comb, whose sign can be changed using the frequency-shifting synthesizer as previously mentioned. The sign of the  $f_{\rm rep}^{\rm K}$  contribution to be removed can be adjusted by inverting the output frequencies of the two DDS, without changing any RF component. This is illustrated in fig. 5.17, which shows how the noise is correctly compensated with the proper sign and increases by a factor of 4 (in terms of PSD, or +6 dB) compared to the noise of  $f_{\rm rep}$  with the incorrect sign (as the resulting signal corresponds to  $v_{\rm USL}/N+2f_{\rm rep}$ ).

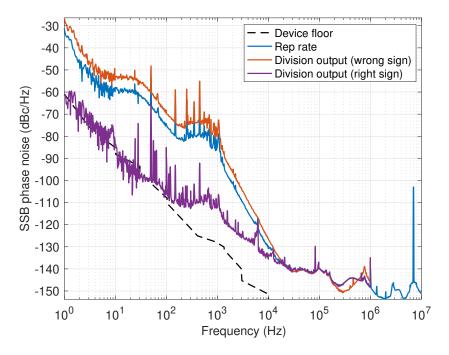


**Figure 5.17 – Sign effect.** Demonstration of the adjustment of the sign of the correction of the Kerr comb  $f_{\text{rep}}^{K}$  noise in the low-noise RF output signal generated by the transfer oscillator scheme. The blue curve displays the phase noise of the Kerr comb repetition rate. The purple curve shows the phase noise of the generated RF signal obtained with the correct sign where the  $f_{\text{rep}}^{K}$  noise is removed, whereas the orange curve corresponds to the other sign (obtained by inverting the frequency of the two DDS), which leads to a 6 dB noise increase (the output signal contains twice the frequency fluctuations of  $f_{\text{rep}}^{K}$ ).

#### 5.5.5 Outlook

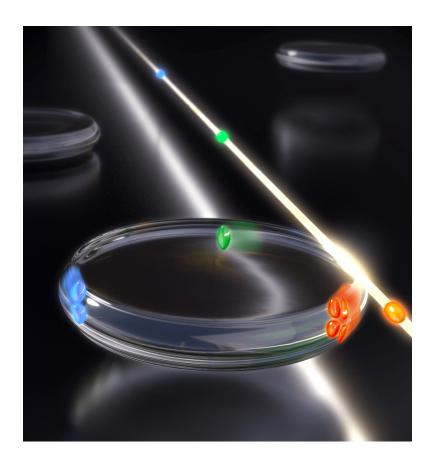
In summary, optical-to-microwave frequency division using a Kerr comb as transfer oscillator was achieved. This demonstrates the potential of this method in microwave photonics and enlarges its previously reported implementation with low repetition rate mode-locked lasers. The approach presented here can be further implemented with electro-optic combs, where self-referencing and feedback control were recently achieved [65, 66]. Although this

proof-of-principle experiment required an auxiliary comb to obtain the CEO frequency of the Kerr comb, directly self-referenced microcombs are technologically feasible in silicon nitride (Si<sub>3</sub>N<sub>4</sub>) photonic-chips [255]. While octave-spanning comb spectra have been achieved using dispersion control [70, 249], these implementations used THz repetition rates to cover such a large spectral range, which made photodetection of the repetition rate practically impossible. Nonetheless, the residual phase noise of these combs has been shown to be suitable for frequency division [256]. Recent improvements of integrated resonators have enabled soliton microcombs with K- and X-band (20 and 10 GHz) repetition rates in integrated resonators [150]. However, the achieved spectral spans, although wider than in the crystalline case, are far from covering one octave. Pulsed pumping [39, 257] appears as a promising approach to enable octave spanning microcombs with detectable microwave repetition rates. This approach uses synchronous pumping of the microresonator with picosecond pulses to generate a soliton with a much shorter duration and a spectrum that can cover an octave, similar to enhancement cavities [258]. It can be seen as a hybrid between an electro-optic (EO) comb and a microcomb, with the advantage that the spectral enlargement of the EO comb is performed in cavity and is therefore directly filtered. Crucially, even if the free-running phase noise of these integrated microcombs is typically higher than in the crystalline platform used in this work [150, 259, 260], the additional noise is cancelled over a broad frequency range via the transfer oscillator method that constitutes a powerful tool for low-noise frequency division without the need for a very low-noise comb. The free-running comb operation and the maturity of RF components, which can be suitably integrated, promise robust device operation. Furthermore, improvements in resonator actuation, using micro-heaters [187], piezoelectrical transducers [221, 261], or the electro-optic effect [262, 263], allow direct soliton generation with the stable laser via resonator tuning, alleviating the need for an optical phase-lock loop and greatly simplifying the detuning stabilisation. If a lower stability level is acceptable, simpler and more compact low-noise lasers can be employed [264–266] instead of the USL. We believe that the presented transfer oscillator method holds promising potential for ultralow-noise high-frequency generators with a new generation of compact photonic-based systems [267] for radar applications [268], high frequency telecommunications [269] and time–frequency metrology [42].

# 6 Multiplexing solitons in a microresonator

"The most exciting phrase to hear in science, the one that heralds new discoveries, is not 'Eureka' but 'That's funny...'"

ISAAC ASIMOV



The results in this chapter are partially adapted from the publication: E. Lucas et al., "Spatial multiplexing of soliton microcombs", *Nature Photonics* 12.11 (2018), pp. 699–705.

## 6.1 Introduction

Shortly after the inception of the optical frequency comb [271], it was realized that combining two combs with slightly different repetition rates on a photodetector produces an RF interferogram that samples the optical response [45, 46], without any moving parts, allowing improved speed and accuracy. Such dual-comb techniques have been demonstrated in both real-time [47, 48] and mid-infrared [49] spectroscopy, distance measurements [272], two-way time transfer [273], coherent anti-Stokes Raman spectro-imaging [50], as well as photonic analogue to digital conversion [274].

However, facing the complexity and cost associated with operating two laser frequency combs, novel methods are being actively explored with a view to reduce the system complexity and inherently improve the mutual coherence. For example, instead of phase locking two independent conventional mode-locked lasers, both combs can be generated in the same laser cavity [275], via repetition rate switching of a single comb [66], or spectrally broadened in the same fiber in opposite propagation directions [276]. As the noise sources are common mode, the relative coherence between the combs is significantly improved, allowing for longer coherent averaging [46].

Microcombs have followed the same kind of evolution. The initial demonstrations of dual-microcomb applications relied on pairs of physically distinct yet almost identical resonators [53, 122, 131, 277, 278]. The required FSR matching of the microcavities posed a significant challenge in their fabrication. Recent works [279, 280] demonstrated the generation of dual-DKS combs with counter-propagating solitons within the same spatial mode of a single microresonator, using the clockwise and counter-clockwise mode degeneracy, and showed a drastic improvement of the coherence. However, this technique is limited to counter-propagating pumps and as such requires nonreciprocal elements, i.e. circulators. Moreover, since the same mode family is used, only small relative combs offsets are possible, while the repetition rate difference is induced via the Kerr and Raman effects [281] and remains relatively moderate. As a result, the corresponding RF comb is not centered at sufficiently high frequencies, and RF lines near DC may overlap, which can lead to soliton-locking [280], but also implies that several pairs of lines beat at identical RF frequencies. Likewise, the small repetition rate difference restricts the acquisition speed. Finally, the scheme is inherently limited by the twofold degeneracy of WGM, only allowing dual-comb generation.

Like optical fibers, optical microresonators can also exhibit multiple spatial mode families, which provide additional degrees of freedom in which light can propagate. In fiber optical communication, space-division multiplexing utilizes different spatial modes of an optical fiber as additional parallel channels to transmit data [282, 283]. It remains an open question if dual-comb can be generated in an analogous way within different spatial modes of a cavity. Although pumping of two orthogonally polarized modes was investigated in preliminary works [284–286], generating independent soliton states in distinct spatial modes was not shown to date.

In this chapter, the spatial multiplexing of DKS states in a microresonator is demonstrated. Multiple DKS-based combs are simultaneously generated within distinct spatial modes of a single optical microresonator. Up to three different mode families of the same polarization are pumped using a laser and modulation sidebands (fig. 6.1c). This spatial multiplexing thereby allows not only dual but also triple frequency comb generation from one and the same device, which had so far not been achieved with any other laser frequency comb platform (e.g. Ti:Sa, semiconductor or fiber-based mode locked lasers). The technique introduced here also overcomes several of the previous shortcomings. The distinct free spectral ranges of the respective mode families enable the generation of independent soliton pulse streams with substantial repetition rate differences (100 kHz - 100 MHz). As a single laser and resonator are used, the resulting combs thus have excellent mutual coherence, and support dual-comb spectroscopy (with amplitude and phase retrieval) in spite of using a free running system. The larger offset between combs prevents soliton locking [280] and associated mapping ambiguity. The multiplexing can also be performed in co- or counter-propagating directions. Finally, scalability is demonstrated with the generation of three combs in a single resonator. Beyond established dual-comb techniques [45, 46], triple combs can be used for higher dimensional spectroscopy, with the potential to increase information content, accuracy or speed of acquisition, such as in 2D coherent spectroscopy [287, 288], as well as advanced comb-based distance measurements with increased ambiguity range [289]. The multiplexing approach could lead to significant simplifications in the implementation of these schemes.

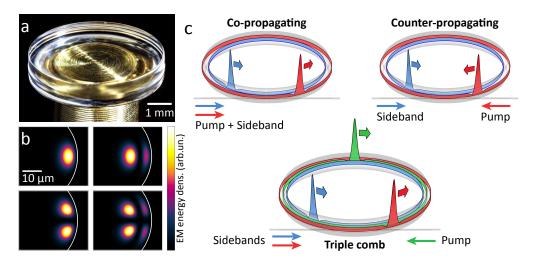


Figure 6.1 – Principle of spatial multiplexing of solitons in a single microresonator (a) Crystalline  $\mathrm{MgF}_2$  whispering gallery mode (WGM) resonator used in this work. (b) Simulation of several optical mode profiles supported by the WGM protrusion. (c) Schematic representation of the three multiplexing configurations applied.

We take advantage of the multi-mode nature of a crystalline  $\mathrm{MgF}_2$  WGM cavity (fig. 6.1a). The fabrication of  $\mathrm{MgF}_2$  crystalline cavities by diamond turning and subsequent polishing with diamond slurries typically produces multimode resonators with several mode families reaching ultrahigh quality factors (Q) exceeding  $10^9$ . In the present work, the resonator used has a

free spectral range (FSR) of 12.4 GHz, and features up to 5 mode families with the same polarization that sustain DKS formation ( $Q \ge 10^9$ ), as shown in fig. 6.3. The microresonator protrusion was fabricated via high-precision diamond turning of a mono-crystalline MgF<sub>2</sub> blank followed by hand polishing with diamond slurries and cleaning. The FSR of 12.4 GHz corresponds to a major radius of 2.8 mm. The resulting WGM protrusion can be approximated by an oblate spheroid with a width of 25 µm and a height of 80 µm (this very shallow protrusion appears almost flat in the picture fig. 6.1a). While single mode cavity protrusions have been demonstrated [290] using advanced micro-machining techniques, we target a wide protrusion instead, which supports a large number of WGM modes and makes the polishing less challenging. The obtained quality factors of the soliton-supporting resonances are above 10<sup>9</sup> at 1554 nm. The GVD of MgF<sub>2</sub> is naturally anomalous in the C-band ( $\beta_2 \sim -9.1 \text{ fs}^2/\text{mm}$ ), such that no geometric dispersion engineering is needed to reach this dispersion regime, which is necessary for soliton formation. Due to the loose confinement and the large main radius of the structure, higher order modes have a higher FSR without significantly changing the dispersion which is dominated by the material. Overall, 5 resonators were fabricated, featuring at least two soliton-supporting mode families (FSR 8, 12, 14, 17 and 26 GHz).

Evanescent coupling to the WGM is achieved with a tapered optical fiber. The mode of the tapered fiber and of the WGM resonator are not orthogonal to each other and one taper mode can excite several WGMs, although the mode overlap and phase matching condition are different for each WGM thus leading to variations of their respective coupling rate. However, shifting the optical fiber position out of the equatorial plane of the resonator, influences the coupling strength of the even and odd WGMs [291, p. 59] (in the polar direction). This degree of freedom is used in the experiment to adjust the coupled power in the modes producing the solitons.

# 6.2 Spatial multiplexing with co-propagating pump fields

# 6.2.1 Principle

We first study the use of co-propagating pumps. In this scheme (fig. 6.2), simultaneous pumping of two soliton-supporting resonances is achieved via electro-optical modulation. The light of an initial pump laser (external cavity diode laser, wavelength 1554 nm) passes through an IQ-modulator to generate a single sideband [292], without fully suppressing the carrier, such that both reach the same power level. This creates two mutually phase-coherent carriers with a tunable frequency offset. The modulation frequency is set to  $f_m = \omega_m/2\pi \sim 4.28$  GHz to match the separation of two soliton-supporting resonances, which belong to different spatial mode families but have the same polarization.

### 6.2.2 Identification of soliton resonances and tuning method

The identification of the modes supporting soliton was carried out by is scanning the high power pump laser over a full FSR of the cavity around 1554 nm, using the piezo-actuator of the

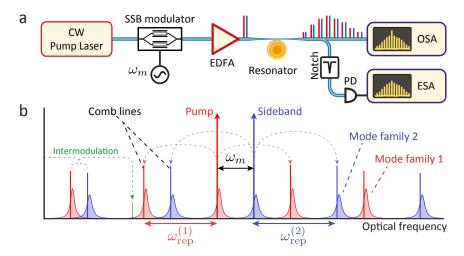


**Figure 6.2 – Principle of spatial multiplexing with co-propagating pumps (a)** Setup for dual DKS generation via spatial multiplexing in the co-propagating direction. The single-sideband (SSB) modulator creates an additional carrier to pump a second mode family. EDFA: erbium doped fiber amplifier. E/O-SA: electronic/optical spectrum analyser. **(b)** Principle of multiplexed comb generation. The main pump laser (red arrow) is modulated to generate one sideband (blue arrow). The laser and sideband pump one resonance of two different mode families (1 in red and 2 in blue) and generate a soliton comb in each of them through the Kerr effect (red and blue lines). Co-propagating pulses may experience intermodulation effects, as explained in section 6.2.5.

pump ECDL. The transmission and the generated comb light were recorded on an analogue to digital converter. Around 100 resonances were identified, five of which featuring the typical step transition in the generated light associated with the formation of solitons [9] (fig. 6.3a). Their relative frequency spacing was estimated using piezo voltage calibration.

In order to initiate the dual-comb formation, a pair of target mode families is first identified. The pump laser is tuned close to one resonance and the modulation frequency is set close to the frequeny spacing between the resonances, while the bias of the SSB modulator is adjusted to generate a blue or red sideband, depending on the sign of the frequency shift needed. After coarse adjustment, both resonances are visible when scanning the pump laser over a small frequency span (fig. 6.3b). The coupling can be optimized by changing the tapered fiber position in order to increase the soliton step length in both families.

The final adjustment consists of tuning the sideband frequency shift so that the large detuning end of both 'soliton steps' becomes aligned (fig. 6.3c). When scanning the laser, two soliton states can then be excited simultaneously more than 50 % of the time. Upon tuning the laser across resonance, the number of generated solitons in one state is typically stochastic, due to the chaotic modulation instability that seeds the solitons [9]. However, the single soliton state is the most attractive state due to its smooth envelope, but remains challenging to obtain in microresonators. We found that our procedure of matching the end of both 'soliton steps' also improves the success rate for dual single soliton generation. We believe this is because the

tuning to the 'high detuning end' makes it more favorable for solitons to collide or decay [113, 117]. Nonetheless dual single soliton production remains less probable, with an estimated success rate below 10 %. This rate could be improved by implementing an 'active capture feedback mechanism' [185].

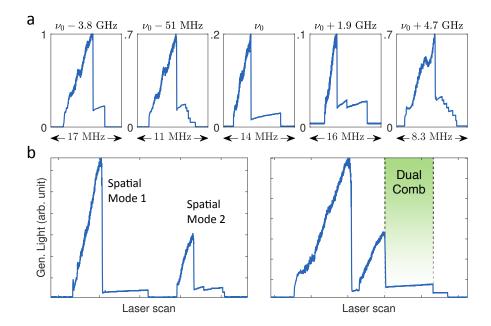


**Figure 6.3** – **(a)** Identification of the soliton-supporting resonance over one cavity FSR. The graphs display the generated comb light at the output of the resonator as the laser frequency is decreased. The step features correspond to the detuning region where solitons exist. **(b)** Sequential excitation of two soliton-supporting resonances (in the co-propagating scheme), when the offset frequency is detuned. The left resonance is excited with the pump laser light while the right is excited with the sideband. **(c)** Adjusting the sideband shift allows the overlap of the resonances. The region where the two steps coexist corresponds to the formation of the dual DKS comb.

The 'laser scanning technique' [9] is subsequently applied on the main pump laser to trigger DKS formation in both mode families simultaneously. Successful tuning is however challenging as each resonance induces a thermal shift. This is mitigated by tuning the laser across the resonances using the diode current, which allows tuning speeds faster than the thermal relaxation time of the cavity (typically ms timescale). After generation, the main laser is locked to the microresonator via the offset PDH method (see section 4.2.3) and the dual-DKS combs can be stably maintained for more than 12 hours.

#### 6.2.3 First demonstration

After successful tuning, two simultaneous streams of DKSs are produced. The optical spectrum of the microresonator output (fig. 6.4a) shows the two interleaved DKS combs offset by  $f_m$ . The repetition rates of the two combs differ by  $\Delta f_{\rm rep}$  = 655 kHz (around 12.4 GHz). This

corresponds to a relatively small spectral compression factor [46] of  $m = f_{\text{rep}}/\Delta f_{\text{rep}} = 1.8 \times 10^4$ , which is useful to increase the acquisition speed of a moderate optical span.

The beating of the dual-comb results here in an RF comb centered at  $f_m$  = 4.28 GHz. The individual lines of the RF comb are still resolution-limited at 100 Hz bandwidth, although the system is free running (neither the combs' repetition rates nor the pump wavelength are stabilized). In comparison, two combs generated in distinct microresonators pumped with the same laser have a linewidth broader than 1 kHz. Owing to the high center frequency  $f_m$ , the total ~ 200 MHz span of the RF comb can be mapped into the corresponding 3 THz of optical span without aliasing at baseband frequencies and no signs of inter-soliton locking [280] were observed consequently. Nevertheless, it may seem that a high center frequency is a drawback, as it requires the use of a very fast sampling rate to directly acquire the dual-comb interferogram, but since this frequency is set by the modulation  $f_m$ , it is possible to downmix the RF comb to baseband with an IQ demodulator and relax the requirement on the sampling rate.

Importantly, although the solitons circulate in distinct spatial modes, they can interact via four-wave mixing (FWM) when co-propagating and effectively become modulated at the rate at which the solitons  $\cos \Delta f_{\rm rep}$ , as detailed in section 6.2.5. The modulation products that arise around the comb lines will beat with adjacent comb lines at frequencies identical to the RF comb and may thus induce optical-to-RF mapping ambiguities. In the present case, the relative strength of the first intermodulation sideband is approximately  $-20~{\rm dBc}$  (see fig. 6.9c), in agreement with the effect of cavity filtering. We believe this effect is sufficiently weak to be neglected in most practical applications.

## **6.2.4** Repetition rate difference modification

## Larger repetition rate difference via selection of mode families

Several RF comb offset frequencies and repetition rate differences can be achieved in the same resonator, by changing the pair of modes supporting the solitons. In this way we could generate solitons in the co-propagating direction (fig. 6.5a) with an offset of 4.9 GHz and a repetition rate difference of  $\sim 9.3$  MHz. The corresponding compression factor  $m=1.4\times 10^3$  is more than one order of magnitude lower than the previous demonstrations with counterpropagating solitons  $(3.3\times 10^5$  in [280] and  $3.2\times 10^4$  in [279]), whilst typical mode-locked lasers are in the range [46]  $3\times 10^4-10^6$ . The resulting RF comb (fig. 6.5b) spans more than 4 GHz. However, this high offset frequency  $f_m$  combined with a broader comb implies that the RF comb extends beyond  $f_{\rm rep}/2$  and thus overlaps with the mirror comb [46] centered at  $f_{\rm rep}-f_m$ , leading to potential mapping ambiguities in the overlap region. Engineering the modes of the microresonator, enabled by better fabrication control, will allow an optimal bandwidth usage.

Note that increasing  $\Delta f_{\rm rep}$  enables even stronger intermodulation suppression ( $\sim$  -40 dBc here) as the sidebands are created well outside the cavity bandwidth section 6.2.5.

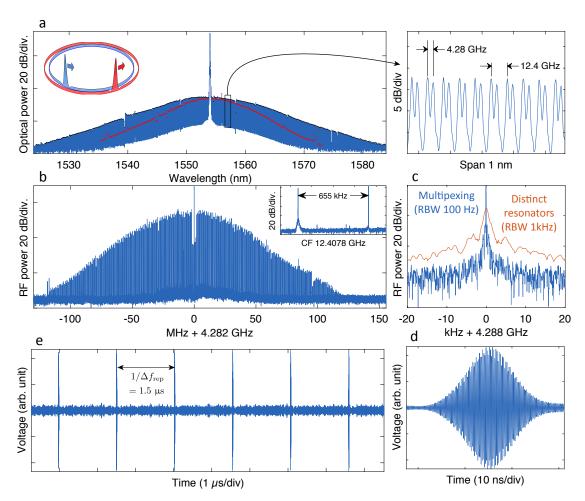


**Figure 6.4 – Dual-comb generation with spatially-multiplexed co-propagating solitons (a)** Generated dual-comb optical spectrum. The DKS-based combs are interleaved and spaced by ~ 4 GHz (see inset). The red markers delineate one comb from the other. **(b)** Resulting dual-comb RF heterodyne beatnotes. Resolution bandwidth (RBW): 3 kHz. The line spacing (repetition rate difference shown in inset) is 655 kHz. CF: center frequency. **(c)** Focus of one line of the RF comb. The blue trace denotes the multiplexed solitons in (b). Red represents the results from solitons generated in two distinct microresonators pumped with a single laser. **(d)** Detail of the temporal trace (e) when the two pulses overlap (~ 200× magnification). **(e)** Temporal interferogram of the dual-comb heterodyne shown in (b), recorded on a fast sampling oscilloscope, and after digital bandpass filtering to select the RF comb.

#### Pumping of orthogonally polarized modes

The microresonator not only supports higher order spatial modes but also fundamentally orthogonally polarized modes. Furthermore, as  $\mathrm{MgF}_2$  is birefringent ( $n_o \sim 1.37$  and  $n_e \sim 1.38$  at 1554 nm), and the axis of rotation of the WGM resonator is oriented along the optical c-axis, two orthogonally polarized modes feature a greater difference in their free-spectral range. Note that the material group velocity dispersion is anomalous in both direction. We demonstrate the generation of two co-propagating soliton states in orthogonally polarized modes (resonance

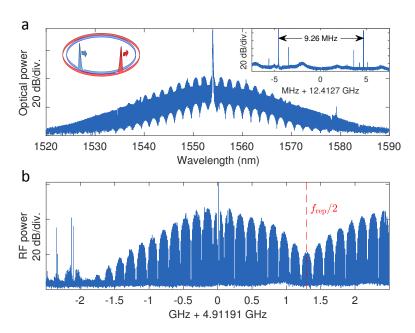


**Figure 6.5** – **(a)** Generated dual-comb optical spectrum in the co-propagating direction. One of the combs corresponds to a two-soliton state and hence has a distinct spectral interference pattern. The repetition rate difference is shown in the inset. **(b)** Corresponding RF heterodyne comb.

separation  $f_m=1.34$  GHz). The simultaneous pumping of both modes is achieved by aligning the polarization of the pumps at  $45^\circ$  with respect to the polarization of each respective mode. Note that half of the energy of each pump is unused in that case. The pumping efficiency could be improved by first splitting the laser light with a polarising beam splitter, modulating one path with the SSB, and combining both paths before coupling to the resonator. In this way, each pump can be aligned with the respective polarization mode, allowing for more efficient coupling and avoid energy loss. The resulting combs have a repetition rate difference of  $\sim 117$  MHz (fig. 6.6b), which is too high for the available bandwidth (very small compression factor m=106). As a result, the RF comb is heavily aliased at baseband frequency and with the image comb centered around  $f_{\rm rep}-f_m$ , which prevents any application without optical filtering to reduce the bandwidth. Pumping orthogonal mode can also be realized in counter propagation by selecting the proper pump polarization for each direction.

These experiments illustrate the flexibility of the technique and its potential to substantially increase the bandwidth of the dual-comb interferogram and acquisition speed, compared with prior schemes using counter-propagating solitons [280]. Although a collinear dual-comb is not suitable for some applications, co-propagating soliton generation simplifies the scheme considerably, as it lifts the requirement for nonreciprocal devices. Furthermore, two combs generated this way could be separated via de-multiplexing, if the offset  $f_m$  is high enough (e.g. beyond 25 GHz), which should be possible for integrated micro-resonators with larger FSR (> 100 GHz). Alternatively, if the pumped modes are orthogonally polarized, they could be demultiplexed with a simple polarization beam splitter.

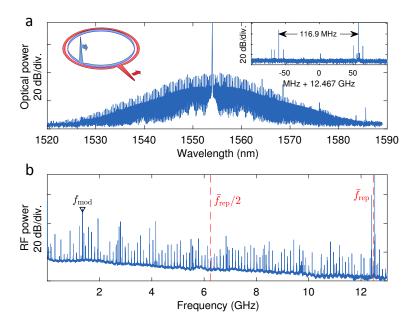


**Figure 6.6** – **(a)** Generated dual-comb optical spectrum in co-propagation, for mode families with orthogonal polarization. The repetition rate difference is shown in the inset. **(b)** Corresponding RF heterodyne comb. The modulation frequency is indicated. The RF comb is heavily aliased due to the insufficient bandwidth for such large repetition rate difference.

# **6.2.5** Intermodulation products

The two generated dissipative Kerr solitons, exhibiting different free spectral ranges, can in general interact and cause intermodulation products. Intermodulation of two co-propagating solitons can occur via four-wave mixing, and can lead to additional sidebands around the optical comb lines. We consider here the comb line frequencies in the case of two combs (1) and (2):

$$\omega_{\mu}^{(1)} = \omega_p + \mu \omega_{\text{rep}}^{(1)} \tag{6.1}$$

$$\omega_{\eta}^{(2)} = (\omega_p + \omega_m) + \eta \left(\omega_{\text{rep}}^{(1)} + \Delta \omega_{\text{rep}}\right) \tag{6.2}$$

where  $(\mu,\eta)$  are the azimuthal mode numbers (relative to the pumped mode, for which  $\mu=0$  and  $\eta=0$ ),  $\omega_p$  the pump laser frequency,  $\omega_{\rm rep}^{(1)}$  the repetition rate of the first comb,  $\omega_m$  the single sideband modulation frequency and  $\Delta\omega_{\rm rep}=2\pi\Delta f_{\rm rep}$  the difference in repetition rate. Inter-comb four-wave mixing can occur for lines fulfilling the phase matching condition (i.e. angular momentum conservation that is  $\int d\phi \cdot e^{i(\mu+\eta-\mu'-\eta')\cdot\phi} = 1$ ):  $\mu+\eta=\mu'+\eta'$ .

For counter-propagating solitons in distinct mode families, this momentum matching cannot be satisfied. However, for two co-propagating mode families for example,  $\mu+\eta=(\mu-1)+(\eta+1)$  is a possible path that conserves momentum, and the resulting frequencies are  $\omega_{\mu}^{(1)}+\omega_{\eta}^{(2)}=\omega_{\mu-1}^{(1)}+(\omega_{\eta+1}^{(2)}-\Delta\omega_{\rm rep})$ . As the last frequency does not coincide with an existing comb line, and falls outside the cavity resonance, the mixing is expected to be inefficient (and suppressed by the cavity lorentzian). Another series of FWM processes leading to the creation of the

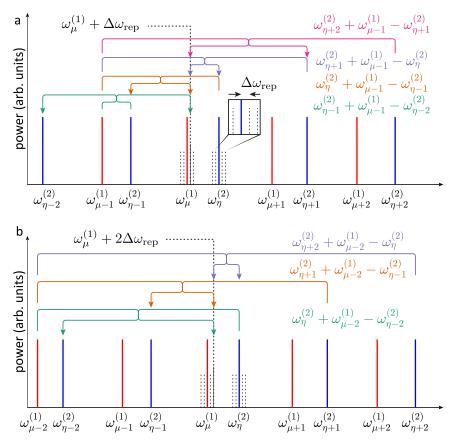


**Figure 6.7 – Intermodulation of co-propagating solitons (a)** Illustration of FWM processes leading to the formation of the  $+\Delta\omega_{\rm rep}$  sideband around the comb line  $\omega_{\mu}^{(1)}$  (five comb lines are considered here, the cavity filtering is not taken into account). **(b)** Processes leading to the formation of the  $+2\Delta\omega_{\rm rep}$  sideband around the comb line  $\omega_{\mu}^{(1)}$ 

intermodulation sideband at  $\omega_{\mu}^{(1)} + \Delta\omega_{\text{rep}}$  are represented in fig. 6.7a, when considering 5 comb lines (the cavity filtering is not accounted for).

The presence of sidebands spaced by  $\Delta\omega_{\rm rep}$  around each of the comb lines can induce optical-to-RF mapping ambiguities, as illustrated in fig. 6.8. The beat between lines  $\omega_{\mu}^{(1)}$  and  $\omega_{\mu}^{(2)}$  results in the frequency  $\omega_{\mu}^{(2)} - \omega_{\mu}^{(1)} = \omega_m + \mu \Delta\omega_{\rm rep}$ . However, the beat between the adjacent lines  $\pm\mu$  and their sidebands as well as a pair of sidebands around  $\mu\pm2$  will be at an identical frequency. Therefore, importantly, the presence of sidebands around the comb lines does not appear in the RF dual-comb spectrum, but can be evidenced by the appearance of several lines spaced by  $\Delta\omega_{\rm rep}$  around the repetition rates of the combs (or by a high resolution recording of the optical spectrum). Note that in the present experiments the cross products of a comb line and a sideband are attenuated by the relative amplitude of the sidebands i.e. at least 20 dB.

Experimentally, we evaluated the strength of the intermodulation sidebands by beating several lines of each soliton comb with another reference laser centered at 1556.5 nm (fig. 6.9a), having an optical linewidth of  $\sim$  30 kHz. If the solitons are co-propagating (fig. 6.9b-d), sidebands at  $\Delta\omega_{\rm rep}$  can be clearly identified. This measurement was repeated while pumping a different

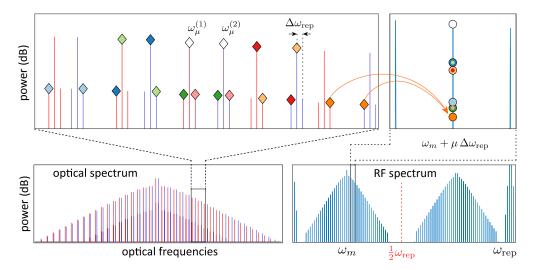
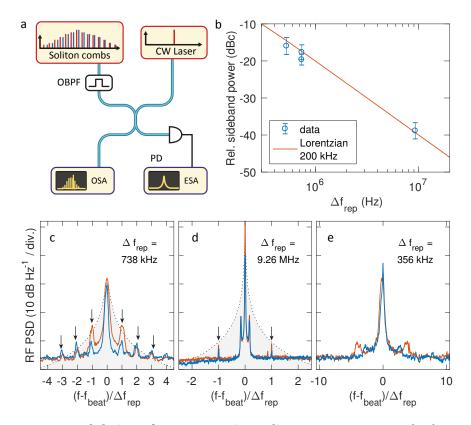


Figure 6.8 – Illustration of the mapping ambiguity induced by the intermodulation sidebands around the comb lines. The lines  $\omega_{\mu}^{(1)}$  and  $\omega_{\mu}^{(2)}$  beat at a frequency  $\omega_m + \mu \Delta \omega_{\text{rep}}$ , which is the same frequency as the beating between adjacent lines / sidebands. The pairs of optical lines / sidebands beating at the same frequencies are marked with identical color (top left, the spacing of the sidebands was expanded for visualization) and their corresponding mixing in the RF domain in indicated by a dot with the matching color (top right).

selection of mode families, such that the scaling of the sideband strength with  $\Delta \omega_{\rm rep}$  could be retrieved. The result shown in fig. 6.9b reveal that the mean power of the first sidebands (averaged over multiple comb lines) decreases for larger repetition rate difference, with a slope that matches a lorentzian profile with a typical linewidth of 170 kHz (full width half maximum) which is in line with the measured quality factors of the resonances.

Conversely, the measurement of the optical lineshape of counter-propagating comb lines, showed no detectable signs of intermodulation products in any of the  $\Delta\omega_{\rm rep}$  configurations (fig. 6.9e). In that case, the phase matching condition cannot be fulfilled at the same time as the energy conservation unless  $\Delta\omega_{\rm rep}=0$ .



**Figure 6.9 – Intermodulation of co-propagating solitons (a)** Experimental scheme for the characterization of the optical lineshape of individual comb lines via heterodyne with an independent laser. The beatnote is measured on an ESA. Lines are selected with an optical bandpass. (b) Scaling of the mean relative power in the first sidebands (at  $\pm \Delta \omega_{\rm rep}$ ) averaged over several comb lines, for different repetition rate difference  $\Delta f_{\rm rep} = \Delta \omega_{\rm rep}/2\pi$ . (c) Heterodyne beatnotes of the reference laser with a line of two co-propagating combs with a repetition rate difference of  $\Delta f_{\rm rep} = 738$  kHz (RBW 50 kHz). The black arrows show the intermodulation sidebands. (d) Same measurement in the case of  $\Delta f_{\rm rep} = 9.26$  MHz (RBW 100 kHz). (e) Lineshape of the lines of counter-propagating combs with  $\Delta f_{\rm rep} = 356$  kHz (RBW 50 kHz).

# 6.3 Spatial multiplexing in the counter-propagating configuration

# 6.3.1 Principle and demonstration

The two spatial mode families can also be excited in a counter-propagating way, analogous to previous implementations [279, 280]. First, the pump laser is split unevenly between two paths. A pair of circulators is then used to couple light into the resonator and to collect the transmitted combs on both sides (fig. 6.10a). 90% of the amplified pump power ( $\sim$  200 mW) is coupled directly into the counter-clockwise (CCW) direction. In the other path, the remaining 10% of the pump is sent through a single sideband modulator operated in carrier-suppressing mode to frequency-shift the light by the offset separating the two resonances. After amplification to a similar power level of  $\sim$  200 mW, the frequency-shifted light is coupled in the clockwise (CW) direction.

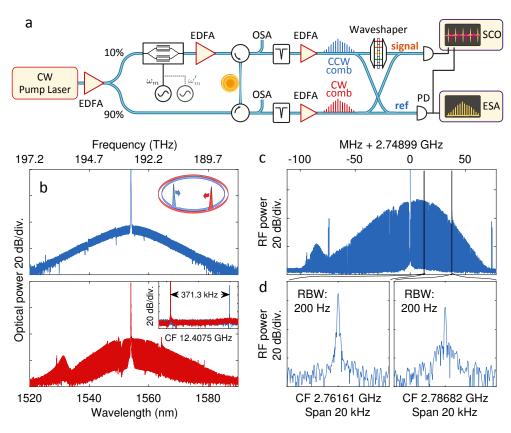


**Figure 6.10 – Dual-comb generation with spatially multiplexed counter-propagating solitons and proof-of-principle spectroscopy (a)** Setup for counter-propagating dual and triple DKS-comb generation and spectroscopy. **(b)** Optical spectra of the two counter-propagating combs. The inset shows the two repetition rate beats of the combs (CF: center frequency). **(c)** Resulting dual-comb beatnote (RBW 3 kHz). **(d)** High resolution spectra of two lines of the RF comb in (c).

We used another set of mode families which resonance offset is  $f_m$  = 2.75 GHz, and the repetition rate difference is  $\Delta f_{\rm rep}$  = 371 kHz to demonstrate the counter-clockwise spatial multiplex-

ing of DKSs. The soliton formation is triggered in the same way as in the co-propagating case. The two generated single-soliton combs are shown in fig. 6.10b. Each comb has an average power of  $\sim 400~\mu W$  at the output of the resonator (after excluding the pump). The corresponding RF comb (fig. 6.10c) features a similar degree of stability to the co-propagating scheme, with 200 Hz wide beatnotes throughout the RF comb (fig. 6.10d). A main advantage of the counter-propagating pump configuration is the absence of intermodulation products in the combs. This is to be expected, as in this case, the FWM process between two different combs is momentum-forbidden as mentioned in section 6.2.5. With this pumping configuration the combs can also be accessed individually, allowing the implementation of a wider range of dual-comb applications.

### 6.3.2 Dual-comb spectroscopy

A proof of concept dual-comb spectroscopy experiment was performed. The combs are first amplified to  $\sim 10$  mW average power. One comb is sent through a waveshaper before interfering with the second comb. The beating is recorded on a high sampling rate oscilloscope (1 ms acquisition time, corresponding to  $\sim 370$  averages). A reference signal without the waveshaper is recorded simultaneously. The amplitude and phase of the signal RF comb teeth are compared to the reference RF comb to retrieve the amplitude and phase modification experienced by the signal comb. Figure 6.11 shows that the retrieved amplitude and phase spectra closely match the programmed synthetic resonance profiles over a span of 4 THz.

# 6.3.3 Dual-comb imaging of the soliton dynamics

Rapid coherent linear optical sampling [52] was also realized to resolve the dynamics of a DKS pulse breathing [183, 184]. Indeed, the fast recording of the interferogram between a DKS comb and a reference comb offers the possibility to spectrally resolve the soliton dynamics in the microresonator, as recently demonstrated [114] where an electro-optic comb was used as reference. Here, the multiplexing scheme in counter-propagation is applied instead and the detuning in each direction is carefully set in order to generate a CCW breathing pulse and a stable DKS in the CW direction that serves as a reference (fig. 6.12a). The optical spectra of each pulse train can be viewed in panels b and c. The breathing soliton spectrum features a typical triangular profile on the optical spectrum analyzer due to the averaging of the periodic spectral broadening and compression.

First, resolving the spatiotemporal dynamics of the breathing soliton was carried out via direct sampling of the breathing pulse train, using a very fast photodiode ( $\sim 10$  ps impulse response) and real-time oscilloscope (120 GSa/s) in order to sample every roundtrip, as detailed in section 3.2.4. However, the temporal resolution of this method is limited by the photodiode impulse response ( $\sim 10$  ps) and closely-spaced solitons may not be distinguished (fig. 6.12e). Moreover, thanks to the long photon lifetime of microresonators, the oscillation period is much longer than the roundtrip time (the breathing rate is  $\sim 1$  MHz, for a 12.7 GHz repetition

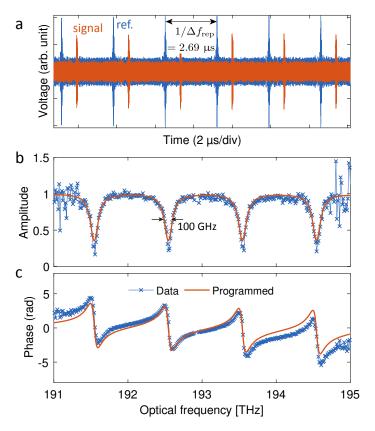


**Figure 6.11 – Proof-of-principle dual-combspectroscopy (a)** Temporal interferogram of the dual-comb heterodyne for the signal path (with waveshaper) and reference path. **(b)** Retrieved amplitude of the signal interferogram produced by coupling the dual-soliton pulse trains through a waveshaper programmed with synthetic absorption features (100 GHz FWHM). The orange lines display the programmed functions. **(c)** Retrieved phase of the same signal as in (b).

rate). With this approach, the slow breathing evolution is therefore heavily oversampled and can only be monitored for a short time span at such sampling rates.

The second method takes advantage of the dual-comb principle and is derived from coherent linear optical sampling [52, 293]. The envelope of a dual-comb interferogram between a breathing soliton and a reference pulse train with a slight difference in repetition rate  $\Delta f_{\rm rep}$  yields the convolution of the breathing pulse with the reference. The pulses overlap each  $1/\Delta f_{\rm rep}$ , which corresponds to the time for one pulse to sweep over one entire roundtrip of the other pulse train, and sets the imaging frame rate. Thus if  $\Delta f_{\rm rep}$  is faster than the breathing rate, the breathing dynamics can be monitored, while relaxing the requirement on the sampling rate (ultimately only to match RF comb bandwidth).

The dual-comb is generated via multiplexing two solitons in counter-propagation. The mode families are selected to reach  $\Delta f_{\rm rep} = 9.26$  MHz (one frame period is acquired over 1340 roundtrips), permitting the acquisition of  $\sim 9$  imaging frames over one roundtrip period. The real-time spectral evolution of the breathing soliton (multiplied by the reference pulse spectrum) can be retrieved by taking the Fourier transform of the dual-comb interferogram

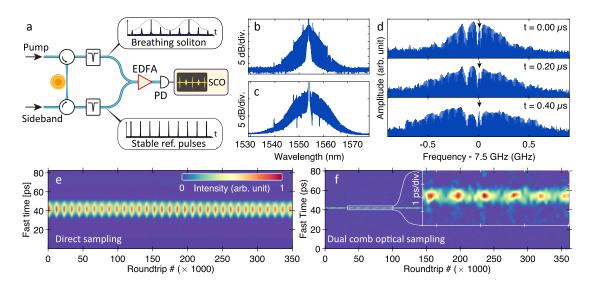


**Figure 6.12 – Resolving the breathing dynamics of a soliton (a)** Experimental setup for breathing DKS dual-comb imaging. **(b)** Optical spectrum of the breathing soliton pulse train and **(c)** of the stable reference pulse train. **(d)** RF spectrogram of the breathing soliton interferogram taken at maximum spectral contraction ( $t = 0 \mu s$ ) and expansion ( $t = 0.4 \mu s$ ). The arrow marks the pump position. **(e)** Spatiotemporal imaging of a breathing DKS via direct real-time sampling of the pulse train. **(f)** Same measurement realized with the multiplexed dual-comb. The fast time resolution is improved by an order of magnitude. The inset magnifies the white rectangular window.

(fig. 6.12d). In order to improve the signal to noise ratio, multiple interferogram frames at similar breathing phases were averaged together (after multiplication by a Gaussian window of width  $1/\Delta f_{\rm rep}$ ). The salient features of breathing DKS can be retrieved [184]: over half a breathing period, the spectrum contracts and expands. Furthermore, the comb lines located near the pump are oscillating out of phase from the wing.

To view the spatiotemporal dynamics of the breathing soliton, the interferogram envelope is retrieved via Hilbert transform and each frame is sliced and stacked (fig. 6.12f). The fast time axis can be rescaled to span  $1/f_{\rm rep}$  to account for the compression ratio of the dual-comb acquisition method. Panels e and f show the vast improvement in temporal resolution of the dual-comb method over the direct sampling method ( $\sim$  1 ps vs.  $\sim$  10 ps).

## 6.3.4 Stability

In our experiments, the detuning of the laser with respect to one of the pumped modes is actively stabilized via an offset PDH lock with feedback on the laser frequency as described in section 4.2.3. With regards to the relative stability of the produced dual-comb, this means that the main source of instability is the drift of the repetition rates difference  $\Delta f_{\rm rep}$ , since the frequency offset between the two pumps is set via electro-optic modulation. We counted the repetition rates of two counter-propagating combs and performed an Allan deviation analysis. for timescales up to 10 ms, the repetition rates are averaging down, meaning that

coherent averaging can be performed up to this duration. On longer timescales, thermal drifts dominate, but we believe that the stability can be easily improved via a thermal feedback stabilization scheme based on the measurement of  $\Delta f_{\rm rep}$ , as described in section 4.4.1.

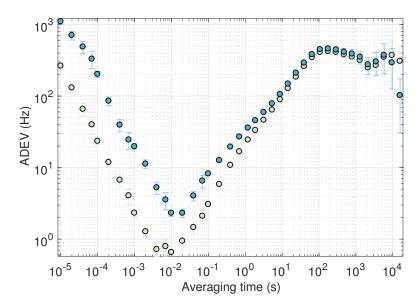


**Figure 6.13** – Overlapping Allan deviation of the repetition rates ( $\sim$  12 GHz) of two counterpropagating combs. The marker colors corresponds to each repetition rate.

# 6.4 Triple soliton comb generation via spatial multiplexing

# 6.4.1 Principle and demonstration

The multiplexing idea can be extended to produce three soliton combs by pumping three mode families simultaneously. This only requires a minor modification of the experimental setup. We employ the counter-propagating configuration, but combine two tones on the modulator (fig. 6.10a):  $f_m = \omega_m/2\pi = 2.17$  GHz and  $f'_m = \omega'_m/2\pi = 4.59$  GHz. This allows two mode families to be co-pumped, and thus the creation of two combs in the CW direction, while another comb is generated by pumping a third mode family in the CCW direction (fig. 6.1c). Remarkably, the excitation technique outlined earlier, was also applied successfully to generate all three single soliton state combs (fig. 6.14a,b).

Heterodyning the combs creates a set of three RF combs centered at  $f_m$ ,  $f'_m$  and  $|f'_m - f_m| = 2.42$  GHz and with a line spacing of 380 kHz, 355 kHz, and 735 kHz respectively. In the heterodyne RF combs between the CCW and each of the CW combs, we are able to observe weak additional lines resulting from the intermodulation products on each of the CW soliton combs (fig. 6.14b,d). The spikes around  $\pm 10$  MHz on these RF-combs are caused by the PDH phase modulation. Importantly, these additional beatnote products give rise to spectrally distinct frequencies and can thus be removed during signal processing (by only selecting the frequency components at e.g.  $f_m + n\Delta f_{\rm rep}$ ), and critically do not induce mapping ambiguities.

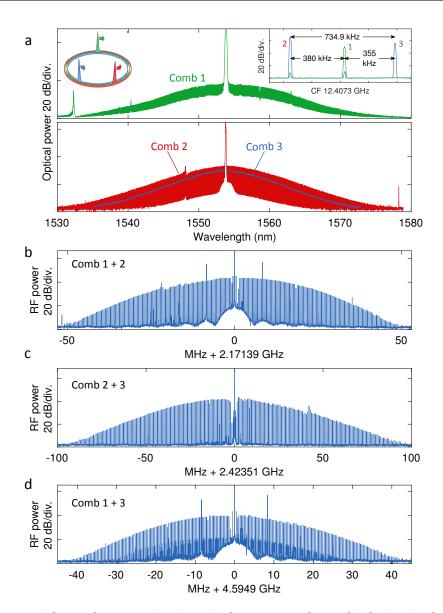


**Figure 6.14** – **Triple comb generation in a single resonator by multiplexing in three mode families (a)** Optical spectra. Comb 1 is generated in the CCW direction, while Comb 2 and 3 are generated in the CW direction. The inset shows the three distinct repetition rate beats. **(b-d)** Heterodyning the three pulse trains on the same photodiode leads to the formation of three RF combs (RBW 3 kHz).

The triple soliton comb configuration with two co-propagating combs could find applications in advanced spectroscopy schemes such as two-dimensional spectroscopy [288]. A recent demonstration [287, 294] employed three Ti:Sa lasers, two of which generated a pump and probe pulse trains to excite a photon echo in Rubidium vapor, which was heterodyned with the third local oscillator comb allowing the fast acquisition of 2D spectra with a single photodiode. The multiplexing approach would offer a major simplification and cost reduction of such schemes, as illustrated in fig. 6.15. Optical distance measurements can also benefit from this

triple comb scheme, as sending a pair of combs onto the target would provide two series of synthetic wavelength chains, allowing a great extension of the ambiguity range [272] without compromising the resolution. Such a scheme was recently demonstrated using three electro-optic combs [289] reaching an accuracy of 750 nm over an 80 m distance (instead of 15 mm with the dual-comb method).

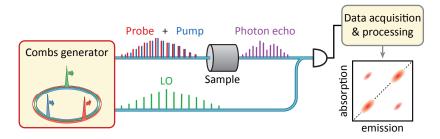


**Figure 6.15** – Envisioned application of the triple-comb generator for two-dimensional spectroscopy [287]

#### 6.4.2 Triple comb interferogram

We show here another triple comb state and a time-domain-based measurement of a triple comb interferogram. We employ the counter-propagating configuration, and set the modulation frequencies to  $f_m$  = 2.75 GHz and  $f'_m$  = 3.58 GHz on the modulator (fig. 6.10a). In this case, the CW combs (1 and 2) are in single-soliton states, while the CCW comb 3 has multiple solitons and features a complex modulation of the spectral envelope (fig. 6.16a,b). The soliton comb 1 is heavily impacted by a modal crossing on the short wavelength side, which decreases its bandwidth. Heterodyning the combs creates a set of three RF combs centered at  $f_m$ ,  $f'_m$ and  $|f'_m - f_m| = 828$  MHz and with a line spacing of 373 kHz, 761 kHz, and 1.13 MHz respectively (fig. 6.16d,g,j). The time domain interferogram was also acquired. The interferogram corresponding to heterodyning each pair of combs is retrieved after applying a bandpass filter to select the corresponding RF comb (fig. 6.16e,h,k). The envelope of each interferogram is also computed. One can note that the strong dispersive wave of comb 1 is clearly shown in the modulated background in fig. 6.16f. Since two of the soliton states (1 and 2) contain a single soliton, they can be used to image the number of solitons and their relative position  $\phi_i$  within a cavity roundtrip in the comb 3 (fig. 6.16f,i,j). In fig. 6.16i, it appears clearly that the comb 3 contains 8 solitons. To cross validate our position detection method, we compare the experimental optical spectrum of comb 3 with an analytical expression for N=8 solitons with the relative positions  $\phi_i/2\pi \in [0,0.071,0.110,0.169,0.291,0.416,0.487,0.567]$ , then the identical solitons circulating in the resonator produce a spectral interference on the single soliton spectrum [148] following:

$$S^{(N)}(\mu) = S^{(1)}(\mu) \left( N + 2 \sum_{j \neq l} \cos \left( \mu (\phi_j - \phi_l) \right) \right). \tag{6.3}$$

Here  $\phi_i \in [0,2\pi]$  is the position of the i-th pulse along the cavity roundtrip (assuming a roundtrip normalized to  $2\pi$ ),  $\mu$  is the comb mode index relative to the pump laser frequency and  $S^{(1)}(\mu)$  is the spectral envelope of a single soliton following an approximate secant hyperbolic squared:

$$S^{(1)} \approx A \operatorname{sech}^2\left(\frac{\mu}{\Delta\mu}\right),$$
 (6.4)

where A is the power of the comb lines near the pump and  $\Delta\mu$  is the spectral width of the comb (in unit of comb lines). The expression (6.3) is computed with the retrieved soliton positions and the parameter A and  $\Delta\mu$  are adjusted to fit the experimental comb amplitude and width. This analytical reconstruction is plotted on fig. 6.16b for comparison. The complex spectral interference pattern is faithfully reproduced, which validates the accuracy of our dual-comb imaging technique.

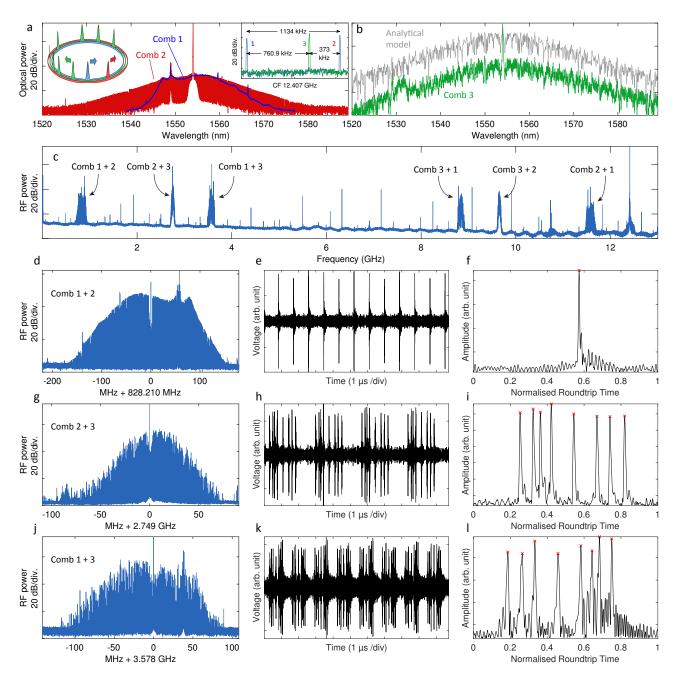


**Figure 6.16 – Triple comb interferograms (a)** Optical spectrum of the two CW co-propagating combs 1 and 2. The inset shows the three repetition rates of each comb. CF: center frequency. **(b)** Optical spectrum of the CCW comb 3 (green). The multi-soliton state spectrum is reconstructed after estimating the soliton number and position via dual-comb imaging and using the analytical expression (6.3) (grey, the trace is shifted by + 20 dB for visualization). **(c)** Broadband spectrum of the triple comb interferogram. The spurious peaks in-between the RF combs arise due to the presence of modulation harmonics in the SSB modulated light signal that beat with the comb lines. **(d,g,j)** Zoom in of each dual-comb RF spectrum **(e,h,k)** Time domain view of each interferogram (after selection with a bandpass filter). **(f,i,l)** Envelope of the interferogram over one period, showing the convolution between the two selected pulse trains.

### 6.5 Summary and outlook

In summary, spatial multiplexing of soliton combs in a single microresonator is demonstrated experimentally for the first time, both in co- and counter-propagating pump configuration. The multiple soliton pulse streams have excellent mutual coherence, and their frequency offset is a substantial fraction of the repetition rate, which prevents mapping to negative frequencies. The generated dual-combs are shown to be suitable for spectroscopy. Large relative differences in repetition rates can be obtained, enabling fast acquisition and improved bandwidth usage. Using the birefringence of MgF<sub>2</sub> even larger differences are possible, when pumping modes with orthogonal polarization. When combined with faster repetition rates, such configurations could find applications in RF signal processing and acquisition [295], or for ultra-rapid vibrational spectroscopy in condensed matter. The fast recording of a dual DKS-comb heterodyne also proves useful to investigate soliton dynamics with unprecedented resolution, such as measuring the line-by-line spectral dynamics of a breathing soliton. We also demonstrate that a high repetition rate difference is also beneficial to suppress the intermodulation products when the solitons are co-propagating.

The presented scheme is already within reach of microfabricated ring waveguide resonators [70, 139], as illustrated by the recent demonstration of a device supporting solitons in both the TE00 and TM00 mode families [149], for two closely spaced pump frequencies. In the future, this improved fabrication control will allow the control of the mode frequency separation and repetition rate difference, while mitigating the impact of modal crossings. Furthermore, waveguide geometric dispersion engineering will enable larger bandwidth coverage [70, 148] and central wavelength selectivity [133, 134]. The simplicity of the co-propagating scheme makes it compatible with full on-chip integration, as all the elements are readily available in photonic integrated circuits.

The method is flexible and easily scalable, as shown by the generation of three simultaneous soliton combs – so far out of reach for other frequency comb platforms. This multiple comb source has the potential to extend the capabilities of comb-based methods, for greater information content, accuracy or speed of acquisition.

# Conclusion and outlook

"The truth is, most of us discover where we are headed when we arrive"

BILL WATTERSON

Chapters 2 and 3 explored the nonlinear dynamics of DKS and aimed at providing an accurate verification of the LLE model. We showed remarkable agreements between experimental results and numerical simulations as well as analytic expressions. The results of these chapters are not only of relevance for the microcomb community, but could prove useful in other systems governed by LLE-like models, such as in plasma physics [190]. New observations were also made that open new questions about the properties of nonlinear systems. In particular, understanding the physical origin of the  $\mathcal{S}$ -resonance could bring insights about the energy transfer in dissipative solitons. The observation of soliton destabilization through modal crossing also necessitates additional investigations. Larger bandwidth coverage is indeed often achieved using dispersive wave emission [70, 148] and these instabilities may pose a limitation to the formation of DKSs.

Chapter 4 exposed the stabilization that were developed over the course of this work, which enabled a drastic improvement of the comb stability, allowing for the most precise investigation and optimization of the comb properties in this work. The soliton combs that lasted for a few minutes in the beginning of my thesis, can now be operated for over a week. We also revisited the injection-locking phenomenon, to allow the decoupling between the cavity FSR and the soliton repetition rate and thereby the full comb stabilization. Interestingly, we discovered that the soliton follows the injected signal with a bandwidth much smaller than the cavity cutoff. This opens interesting new prospects for noise rejection when pumping the soliton with optical pulses [39]. This topic is currently under investigation by my colleague M. Anderson and some preliminary results of pulse pumping a MgF<sub>2</sub> resonator are presented in appendix A.3

The limitations of the stabilization results in this work were mainly caused by the lack of appropriate cavity actuator. I am glad to observe the current developments of tunable microcavities using micro-heaters [187], piezoelectrical transducers [221, 261], or the electro-optic

effect [262, 263], which could open a new era of Kerr microcombs. Furthermore, these electro-optic cavities can be modulated at a rate that match their FSR, allowing for ultra-efficient EO-comb generation. Recent results [296–298] show impressive performances and suggest an exciting perspective toward the convergence between EO-combs and Kerr combs.

Chapter 5 presents an experimental analysis of the noise transduction in microcomb and identifies ways to mitigate it. The results described in this chapter represent the lowest absolute phase noise microwaves generated with an optical microresonator. This performance is allowed by the ultra-high quality factor and optical properties of the crystalline resonator (in particular the low nonlinearity of the structure). The transfer oscillator method developed in this chapter also constitutes an elegant way to suppress the comb noise for optical frequency division. In particular, it only requires to stabilize the DKS to the stable optical carrier and leave the repetition rate free running. The current proof of principle unfortunately needed an auxiliary comb to reference the DKS, which complicated this potentially simple scheme.

Finally, the spatial multiplexing of DKSs shown in Chapter 6 has the potential to greatly facilitate the generation of multiple frequency combs for dual or triple comb applications. The next logical step is to apply the method for e.g. distance measurement or optical coherence tomography. The low output power of the combs is probably the main limitation that will need to be addressed for applications such as spectroscopy. It also remains to be known if the intermodulation of the pulses when the solitons are co-propagating poses a significant issue.

Over the course of this thesis, the field of microresonator frequency comb has tremendously matured. Today, DKS combs can be reliably produced in a variety of microresonator platforms. Perhaps the most exciting advances have been made in integrated platforms, such as the  $\mathrm{Si_3N_4}$  waveguides, that are now commercially available. These allow the design of optical properties, especially dispersion, at a level rarely achieved. Thanks to the development of new fabrication processes, soliton generation has also become remarkably routine, even at lower repetition rates, as presented in appendix A.1. Nevertheless, a number of challenges remain to be solve to prove the true utility of microcombs:

Compact microcomb sources. With the maturation of the integrated microcomb technology, the question of the integration of these sources is becoming more and more topical. On the one hand, a straightforward method is to use more compact low noise lasers, fiber optic and electronic components from the telecommunications or sensing industry, to shrink the size of the setup presented in fig. 2.3. A major difficulty then lies in the low-loss optical packaging of the resonator, but demonstrations are beginning to emerge. [299, 300]. The field is gradually moving from research to engineering, where problems such as automatic and robust soliton generation need to be addressed.

Another approach relies on directly 'butt-coupling' a laser gain chip to a high-Q integrated microresonator. The laser diode is self-injection locked to the microresonator, which induces the narrowing of the laser linewidth, and the simultaneous formation of dissipative Kerr solitons [67, 68]. This architecture has been deployed by the company

OE-waves with discrete optical elements (crystalline resonator, prism). This approach offers potential for ultra-compact comb sources and opens up new perspectives and challenges on the interaction between self-injection locking and soliton generation control.

Generation of octave-spanning combs at detectable repetition rate. This goal remains a long-standing one for microcombs. The generation of coherent octave-spanning DKS combs has been realized, but with a repetition rate of 1 THz [70, 120, 157]. The generation of an octave at detectable repetition rate will simplify the current schemes of nested combs and unlock a number of applications, such as the optical frequency division. The difficulty is the associated high pump threshold (see eq. (1.60)). Here, driving the resonator with optical pulses [39, 258] seems a promising approach.

Conversion efficiency and output power. In the soliton state, the conversion efficiency from the pump laser to the frequency comb is very limited. For the presented experiments it is usually around one percent. This means that most of the pump power is wasted. Pulsed pumping, represent one possible way to enhance this conversion. Another solution is to operate the Kerr comb in the normal dispersion regime, where 'dark' pulses [301–303] (also called platicons [226]) are formed in the cavity. These comb states have a much higher conversion efficiency (reported > 30% [304]) as most of the cavity field stands on the upper branch instead of the lower one.

**Solitons interactions.** We have observed in this work that AMX can cause the destabilization of DKS. In general, the interaction of soliton with AMX allows for a rich panel of effects, such as symmetry breaking and further studies are needed to apprehend their complexity and diversity. Beyond AMX, the binding of solitons, such as the formation of soliton molecules [305] or the coexistence of states [306, 307] could help engineering new comb states.

**Tunable resonators.** As mentioned above, tunable resonators will greatly facilitate soliton generation and stabilization. A low-noise fixed frequency laser could be used as a pump and the cavity tuned to generate the soliton as shown in ref. [187]. Electro-optic tuning, which offers very high modulation bandwidth and potentially low modulation voltage, is particularly attractive. Lithium niobate LiNbO $_3$  is a well known choice and Kerr comb formation was recently achieved in this platform [262]. Another material, Barium Magnesium Fluoride BaMgF $_4$ , presents promising properties, featuring large Kerr and electro-optic coefficients and a wide transparency window [308–312]. Unfortunately the material is not commercially available. A collaboration with the laboratory of Prof. M. Tonelli at the University of Pisa has been initiated to grow this crystalline material. Such devices could be employed much beyond the scope of Kerr comb generation, for topological photonics or nonreciprocal devices.

# A Additional experimental results and contributions

# A.1 Microwave-rates solitons in integrated Si<sub>3</sub>N<sub>4</sub> microresonators<sup>1</sup>

#### A.1.1 Principle and sample description

Microwave synthesis based on soliton microcombs in monolithic crystalline resonators was presented in chapter 5. The principle is extended here to photonic integrated microresonators, as depicted in fig. A.1.



Figure A.1 – Principle of nanophotonic microwave synthesizers based on integrated soliton microcombs.

The soliton threshold power increases with decreasing FSR (see eq. (1.60)). The key challenge for microwave-rates soliton generation in integrated microresonators, is therefore to reach sufficiently high quality factors to allow operation at pump power levels, which are compatible with integrated laser sources [313, 314]. This is the reason why all photonic integrated microcombs so far operated at repetition rates significantly beyond what conventional electronics can detect and process. This challenge was overcome by using the latest advances of the photonic Damascene reflow process [151] developed in our lab. It enabled high-Q integrated microresonators based on ultralow-loss  ${\rm Si_3N_4}$  waveguides (linear propagation loss  $\alpha_{\rm loss} \sim 1$  dB/m). The fabrication details can be found in ref. [150]. Microresonators with FSRs in the K-and X-band of the microwave spectrum were fabricated. Importantly, single soliton states (see fig. A.2c-d) were generated using simple laser piezo frequency tuning in all tested samples.

#### A.1.2 Phase noise characterization

We performed a thorough analysis of the phase fluctuations of the photonically generated K-band microwave carrier. The measurement setup is shown in fig. A.2a: the soliton pulse stream

 $<sup>^1</sup>$ The results of this section are partially adapted from the publication: J. Liu et al., "Nanophotonic soliton-based microwave synthesizers" (Jan. 2019), arXiv: 1901.10372.  $\square$ 

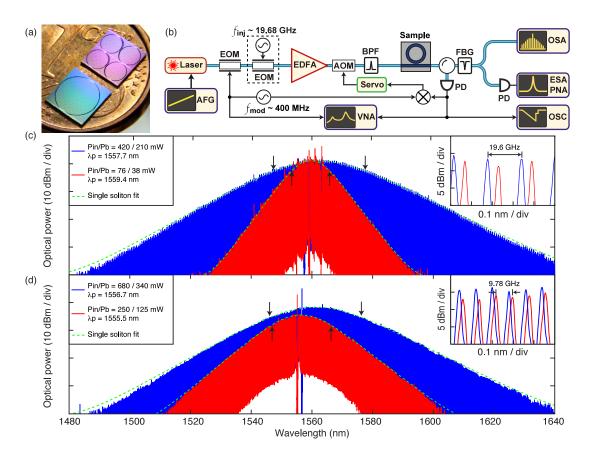
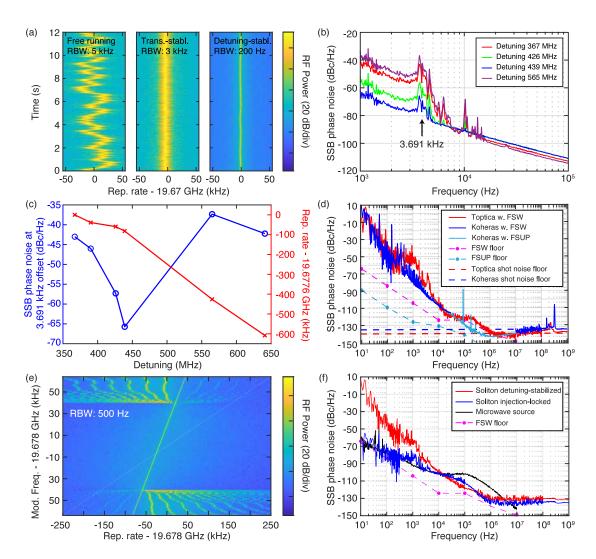


Figure A.2 - Single solitons of microwave K- and X-band repetition rates. (a) Photograph of  $Si_3N_4$  photonic chips which are  $5 \times 5$  mm<sup>2</sup> in size, in comparison with a 1-cent Euro coin. The chip color is due to the light interference caused by the SiO<sub>2</sub> cladding. Photographic credits: Jijun He and Junqiu Liu. (b) Experimental setup to generate single solitons and to characterize the soliton phase noise. EOM: electro-optic modulator. AOM: acousto-optic modulator. EDFA: erbium-doped fiber amplifier. AFG: arbitrary function generator. VNA: vector network analyzer. BPF: band-pass filter. FBG: fiber Bragg grating. OSA: optical spectrum analyzer. OSC: oscilloscope. PD: photodiode. ESA / PNA: electrical spectrum analyzer / phase noise analyzer. Dashed box marks the components for soliton injection-locking experiment, which are not used for transmitted power stabilization and cavity-pump detuning stabilization. (c) Single soliton spectra of 19.6 GHz repetition rate with 38 mW power in sample A (red, 3-dBbandwidth of 11.0 nm), and with 210 mW power in sample B (blue, 3-dB-bandwidth of 26.9 nm), and their spectrum fit (green). Arrows mark the 3-dB-bandwidths, which contain 69 (red) and 170 (blue) comb lines, respectively. Inset: Spectrum zoom-in showing the 19.6 GHz mode spacing. (d) Single soliton spectra of 9.78 GHz repetition rate with 125 mW power in sample C (red, 3-dB-bandwidth of 17.4 nm), and with 340 mW power in sample D (blue, 3dB-bandwidth of 25.8 nm), and their spectrum fit (green). Arrows mark the 3-dB-bandwidths, which contain 139 (red) and 327 (blue) comb lines, respectively. Inset: Spectrum zoom-in showing the 9.78 GHz mode spacing. Note: for soliton spectra in (b) and (c), a BPF is used to filter out the EDFA's amplified spontaneous emission (ASE) noise in the pump laser, and an FBG is used to filter out the pump laser in the soliton spectra.

is driven by a CW diode laser (Toptica CTL) and the soliton repetition rate is detected on a fast InGaAs photodetector whose output electrical signal is fed to a phase noise analyzer (PNA, Rohde & Schwarz FSW43). First, the drift of the photodetected soliton repetition rate around 19.67 GHz is characterized in the free-running state. An oscillation at low frequency ~ 5 Hz of the microwave carrier is observed, as shown in fig. A.3a, which is likely caused by the unstable chip coupling using suspended lensed fibers, susceptible to vibrations. To mitigate this effect, an acousto-optic modulator (AOM) with a power servo based on a proportional-integral-derivative (PID) controller is used to stabilize the transmitted power through the chip, and compensate for the coupling fluctuations. The previously observed low-frequency oscillation is significantly reduced with stabilized transmitted power, as shown in fig. A.3a middle, which demonstrates that a more robust device coupling scheme is required to improve the soliton stability and the phase noise performance of the soliton-based microwave synthesizer.

The phase noise measurements with different cavity-pump detunings are performed with stabilized transmitted power, as shown in fig. A.3b. The detuning is measured using a vector network analyzer (VNA) to probe the resonance frequency relative to the laser [159]. A "quiet point" [172], caused by mode crossings, is observed at the detuning of  $\delta\omega/2\pi\sim439$  MHz, and provides the best phase noise performance compared with other detuning values. To evidence the phase noise reduction at the quiet point, the repetition rate shift and the phase noise value at 3.691 kHz Fourier offset frequency, where the laser phase noise exhibits a characteristic feature, are measured with different detunings, as shown in fig. A.3c. Note that the quiet point may not be found in every (multi-)soliton state but that, in future works, its presence could be engineered via the dispersion. The rest of our measurements are performed out of the quiet point regime.

To further stabilize the soliton-based microwave carrier, we actively stabilize the cavity-pump detuning using an offset sideband Pound-Drever-Hall (PDH) lock [219] with feedback applied to the pump laser power, which can effectively compensate the cavity resonance jitter induced by coupling fluctuations. As shown in fig. A.3(a) (right), such detuning-stabilization also stabilizes the soliton repetition rate. Two cases are investigated: In case A, with the powerstabilization, the soliton is driven by a diode laser (Toptica) and the PNA used is the FSW43; In case B, with the detuning-stabilization, the soliton is driven by a fiber laser (Koheras AdjustiK), and, besides the FSW43, an additional PNA (Rohde & Schwarz FSUP, with cross-correlations) is used only for measuring the 10 kHz - 1 MHz offset frequency range. Figure A.3(d) shows the measured phase noise in both cases, as well as the PNA noise floors. In case A, the noise feature within 100 Hz - 10 kHz offset frequency is caused by the Toptica laser phase noise, while the step-like feature within 20 kHz - 1 MHz is caused by the FSW43 noise floor, which is the reason why the FSUP is needed to measure this frequency range in case B. Using Koheras with FSW43 and FSUP, case B shows a reduced phase noise, while the phase noise within 200 kHz -10 MHz is marginally below the shot noise floor, likely caused by parasitic anti-correlation effects in FSUP [315]. Our analysis shows that, in case B, the main phase noise limitation is the laser relative intensity noise (RIN) for offset frequencies < 1 MHz, with a contribution from the impact of the thermo-refractive noise (TRN) [259] in  $Si_3N_4$  on the detuning within 10 –



**Figure A.3 – Phase noise characterization of the soliton repetition rate and soliton injection-locking to an external microwave source.** (a) Spectrogram of the soliton repetition rate in the free-running state, with transmitted power stabilization, and with cavity-pump detuning stabilization. (b) SSB phase noise measured at different cavity-pump detunings with power stabilization. A quiet point is observed at the detuning of  $\sim 439$  MHz. (c) SSB phase noise at 3.691 kHz offset Fourier frequency and measured repetition rate shift with different cavity-pump detunings. (d) SSB phase noise measured with the stabilized cavity-pump detuning at  $\delta\omega/2\pi \sim 400$  MHz, using different lasers and PNAs, in comparison with PNA noise floors. The estimated shot noise floors are -140 dBc/Hz for case A with Toptica laser (red), and -135 dBc/Hz for case B with Koheras laser (blue). (e) Microwave spectrum evolution showing the synchronization of the soliton repetition rate  $f_{\rm rep}$  with the modulation frequency  $f_{\rm inj}$  on the CW pump, when  $|f_{\rm rep} - f_{\rm inj}| < 40$  kHz. (f) SSB phase noise spectrum comparison of the injection-locked soliton, the microwave source used to discipline the soliton, and the soliton with a stabilized cavity-pump detuning. The soliton spectral purification effect is revealed above 10 kHz offset Fourier frequency.

100 kHz offset frequencies (see appendix A.1.4). The absolute single-sideband (SSB) phase noise power spectral density of the microwave carrier shows  $\sim$  -80 dBc/Hz at 1 kHz offset Fourier frequency,  $\sim$  -110 dBc/Hz at 10 kHz and  $\sim$  -130 dBc/Hz at 100 kHz. Note that the phase noise is not measured precisely at a quiet point in case B, therefore further phase noise reduction is possible through quiet point operation and laser RIN reduction.

#### A.1.3 Soliton injection-locking

A variety of microwave photonic applications require long-term stability of microwave signals, represented as low phase noise at low offset frequency. In our work, the low soliton repetition rate achieved allows soliton injection-locking to an external microwave source [218], which can discipline the soliton repetition rate and reduce the low-frequency phase noise. A modulation frequency  $f_{\rm inj}$  swept around 19.678 GHz is applied on the CW pump laser, and the microwave spectrum evolution is shown in fig. A.3e. The soliton injection-locking, i.e. synchronization of the soliton repetition rate  $f_{rep}$  to the modulation frequency  $f_{inj}$ , is observed when  $|f_{\text{rep}} - f_{\text{ini}}| < 40 \text{ kHz}$ . This injection-locking range is more than a 100-fold increase compared to that measured in MgF<sub>2</sub> resonators ( $\sim 300$  Hz in Ref. [218]), likely caused by the larger resonance linewidth in  $Si_3N_4$ . The phase noise spectra of the injection-locked soliton (blue), the microwave source used (black), and the soliton with a stabilized cavity-pump detuning (red, as described previously), are compared in fig. A.3f. The phase noise of the injection-locked soliton closely follows the microwave source's phase noise at offset frequency below 10 kHz, apart from a residual bump at 1 kHz which originates from the pump laser. For Fourier offset frequencies above 10 kHz, the soliton-induced spectral purification effect is revealed, as the soliton phase noise departs from the injected microwave phase noise, and becomes similar to the case with only active cavity-pump detuning stabilization. This soliton injection-locking technique can provide extended coherence time for applications such as dual-comb spectroscopy, and allows for coherent combination of microcombs and further scaling of soliton pulse energy.

#### A.1.4 Noise transduction mechanisms

#### Laser phase noise transduction estimation

The comparison of the laser phase noise (obtained by beating it against an ultra-stable laser) and the phase noise of soliton repetition rate, enables the estimation of the optical to microwave phase transduction (PM2PM). In particular, the Toptica CTL diode laser features a typical noise bump around 3 kHz. Under usual condition, i.e. out of "quiet point" regime, we measured a PM2PM coefficient of -55 dB, as shown in fig. A.4.

#### Laser intensity noise transduction estimation

The conversion of laser relative intensity noise (RIN) to the phase noise of soliton repetition rate is experimentally measured. A calibrated pure power-modulation of the pump laser was applied using a  $0^{\rm th}$ -order AOM at frequencies ranging from  $10^3$  to  $10^5$  Hz. The resulting phase modulation strength of the soliton repetition rate is measured by integrating the corresponding

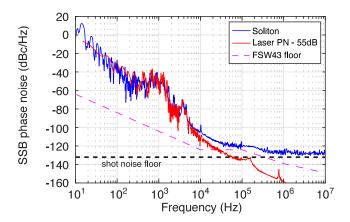


**Figure A.4 – Transduction of the laser phase noise to the microwave phase noise of soliton repetition rate**. The correlation between the optical phase noise of the Toptica laser (red) and the microwave phase noise of the soliton repetition rate (blue) yields an estimation for the PM2PM coefficient of -55 dB.

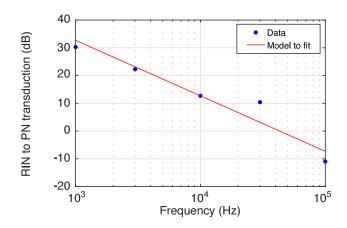


Figure A.5 – Transduction of the laser RIN into the phase noise of soliton repetition rate. Measured conversion of the pump relative intensity modulation to soliton phase modulation (dots). The red line shows the model  $(\alpha/f)^2$  where  $\alpha = 79$  Hz/mW.

peak of the phase noise power spectrum density (PSD). The result of the AM2PM transfer function measurement is shown in fig. A.5.

From this measurement, it appears that the AM2PM conversion mostly follows a  $1/f^2$  slope (red line in fig. A.5), meaning in fact that amplitude modulation leads to frequency modulation of the repetition rate as:

$$\delta f_{\rm rep} = \alpha \, \delta P_{\rm in} \tag{A.1}$$

We estimate a conversion coefficient of  $\alpha = 79$  Hz/mW to match our measurements (the power is defined as the input power in the lensed fiber, before coupled into the chip).

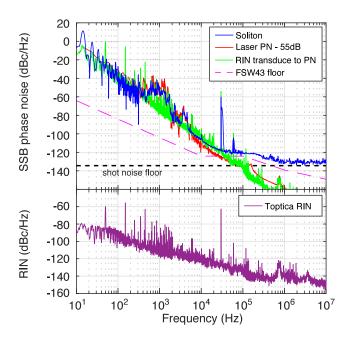


**Figure A.6 – Technical limitations of the soliton phase noise with Toptica diode laser.** The main source of phase noise limitation is the Toptica laser phase noise. The Toptica laser RIN is shown in the bottom panel and its transduction to soliton phase noise is plotted in the top panel (green). The Toptica RIN shows a modulation peak at 10 kHz, which is used to measure the transfer function in fig. A.5. The black dashed line shows the expected shot noise floor.

#### Sources of oscillator noise

From the previous conversion estimations, we can analyze the origins of the main sources of noise in our measurements of the soliton repetition rate. In the case with the Toptica diode laser, as shown in fig. A.6, the conversions of the laser phase noise and RIN, using the previously determined coefficients, show that the main limiting factor is the laser phase noise. Furthermore, the FSW43 without cross-correlations was used in this measurement, which limits the measurement within  $30~\rm kHz-1~MHz$  range. At high Fourier frequencies, the shot noise defines the white noise floor.

The same analysis with Koheras fiber laser shown in fig. A.7 reveals that the situation is reversed. Owing to the greater spectral purity of the fiber laser (compared to the ECDL), the RIN appears now as the main source of phase noise. Furthermore, in this measurement, the FSUP analyzer with cross-correlations was employed to measure the phase noise in the offset frequency range within  $30 \, \text{kHz} - 1 \, \text{MHz}$  ( $10^5 \, \text{cross-correlations}$  applied), which alleviates the limitation of the PNA floor. However, this cross-correlation measurement also shows a noise floor that is below the expected shot noise level. We attribute this artifact to a potential correlation between amplitude and phase quadrature of the microwave noise which are known to produce artificially low results [315]. At high offset frequency with FSW43, our measurement verifies that the signal follows the white shot noise floor.

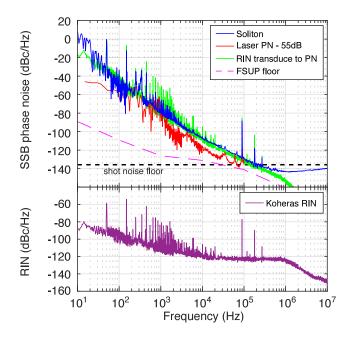


**Figure A.7 – Technical limitations of the soliton phase noise with Koheras fiber laser.** The main source of phase noise limitation is the Koheras laser RIN, as shown in the bottom panel. Its transduction to soliton phase noise is also plotted in the top panel (green), in comparison with the Koheras laser phase noise (red). The black dashed line shows the expected shot noise floor.

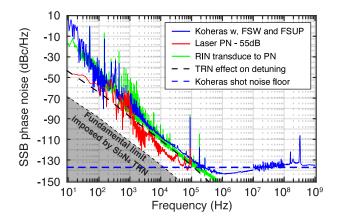


**Figure A.8 – Estimation of the resonator thermal noise impact.** This figure complements to Fig A.7, with the estimated TRN levels on the FSR (fundamental limit) and dutuning (with –55 dB transduction) added. The TRN simulation method is presented in Ref. [259].

#### Resonator thermal noise

The fundamental thermal fluctuations within the optical mode volume of the microresonators lead to thermo-refractive fluctuations of the resonator FSR [259, 260, 316], and thereby of the cavity resonance (magnified by the mode index  $m \approx 10^4$ ). While the thermal-induced FSR fluctuations directly affect the soliton repetition rate jitter (which matches the resonator FSR to a first-order approximation), the thermo-refractive noise (TRN) contributes to the phase noise

via a second channel. As mentioned in Sec. A.1.4, there is a transduction of  $\sim$  –55 dB from optical detuning phase noise to the microwave phase noise of soliton repetition rate. Not only the laser contributes to the detuning fluctuations, but also the cavity resonance jitter induced by TRN. This noise can be approximated by multiplying the FSR by the mode number to yield the resonance TRN and subtracting 55 dB to account for the PM2PM conversion. Note that the impact of this optical noise can be mitigated by operating at a quiet point (reduction of the PM2PM coefficient), but the FSR fluctuations set a fundamental limit to the phase noise of the microwave oscillator. Numerical simulations to investigate the TRN in  $\rm Si_3N_4$  microresonators were recently performed and validated experimentally [259]. Based on the estimated noise for a 20-GHz-FSR microresonator, the impact of TRN is shown in fig. A.8. The fundamental fluctuation are much lower than the currently measured phase noise level that appear to be limited by the laser RIN at low frequencies and by the optical short noise at higher frequencies.

# A.2 Self referencing of an on chip comb<sup>2</sup>

#### A.2.1 Broadband spectrum generation via soliton dispersive wave emission

Dissipative Kerr solitons in integrated optical microresonators also provide a route to synthesize spectra that are sufficiently broad for self-referencing without the need of external broadening similar to Ti:sapphire lasers [317, 318] and in contrast to previous demonstrations of self-referenced Kerr frequency combs that relied on both external amplification and broadening stages [247, 248].

The required optical bandwidth for self-referencing is achieved here via dispersion engineering [319] in photonic chip-based silicon nitride ( $\mathrm{Si_3N_4}$ ) microresonators. With careful geometric dispersion control, the amount of anomalous GVD can be reduced, such that higher order dispersion effects become relevant. This allows the generation of solitons featuring Cherenkov radiation [169, 320], a process related to third order dispersion and also known as dispersive wave emission. The soliton microcomb used here specifically relies on dispersive wave emission to generate a coherent spectrum spanning two-thirds of an octave [255]. It is based on a silicon nitride microresonator with a diameter of ~240  $\mu\mathrm{m}$ , resulting in a free spectral range of ~190 GHz. It is pumped with an amplified external cavity diode laser (ECDL) operating at  $v_{\mathrm{pump}} \approx 192.2$  THz (1560 nm) that is coupled into the chip (~2 W of cw power in the waveguide). Using the "power-kicking" method [255], the microresonator is brought into a soliton state that gives us directly from the chip the required bandwidth of two-thirds of an octave (fig. A.9a) [255].

#### A.2.2 2f - 3f interferometry and CEO detection

Since the spectral span of our soliton frequency comb is two-thirds of an octave the 2f-3f scheme (fig. A.9b) can be applied. As with similar (n-1)f-nf schemes [17, 321], the 2f-3f approach is a trade-off between optical bandwidth and the requirement of more complex nonlinear conversion. While for the common f-2f scheme a full octave of optical bandwidth but only one frequency doubling is required, the 2f-3f scheme requires only two-thirds of an octave but one frequency doubling and one frequency tripling. The resulting beat note after the nonlinear conversion is given by  $3(m f_{\rm rep} + f_{\rm CEO}) - 2(n f_{\rm rep} + f_{\rm CEO}) = f_{\rm CEO}$  if 2n = 3m (here n denotes the line number of the doubled frequency comb line and m the line number of the tripled line) and therefore enabling the measurement of the carrier envelope offset frequency. In order to achieve a sufficient signal-to-noise ratio we implement the doubling and tripling stages using two transfer lasers that are phase locked to the Kerr frequency comb.

The two transfer lasers at ~150 and ~225 THz (2000 and 1330 nm respectively) are phase locked independently with frequency offsets of  $f_{150}$  and  $f_{225}$  to their nearest comb line (fig. A.9b). The one transfer laser is then tripled in frequency (via second harmonic generation followed by sum frequency generation) while the other is doubled in frequency such that both have a frequency of around 450 THz (666 nm) where they generate the desired 2f-3f heterodyne beat note ( $f_{2f3f}$ , fig. A.9d).

<sup>&</sup>lt;sup>2</sup>The results of this section are partially adapted from the publication: V. Brasch et al., "Self-referenced photonic chip soliton Kerr frequency comb", *Light: Science & Applications* 6.1 (Jan. 2017), e16202. □

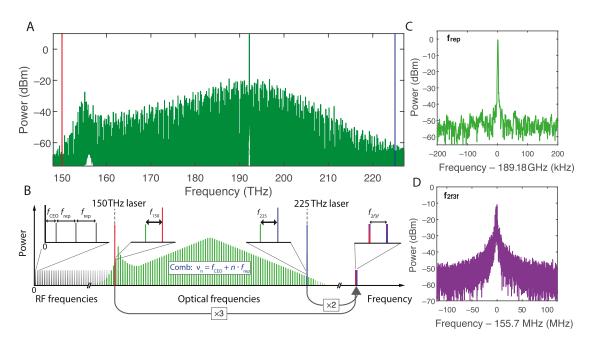


**Figure A.9 – Self-referencing Scheme (a)** Optical spectrum of the four-soliton state that was self-referenced in this work. **(b)** Schematic of the 2f-3f self-referencing with two transfer lasers as it was used in this work including the two stabilized frequency offsets  $f_{150}$  and  $f_{225}$  of the transfer lasers. **(c)** In-loop beat note of the stabilized repetition rate centered at 189.2 GHz. **(d)** Measurement of the free-running  $f_{2f3f}$  beat note which allows the computation of the offset frequency of the Kerr frequency comb.

### A.2.3 Experimental setup for self-referencing

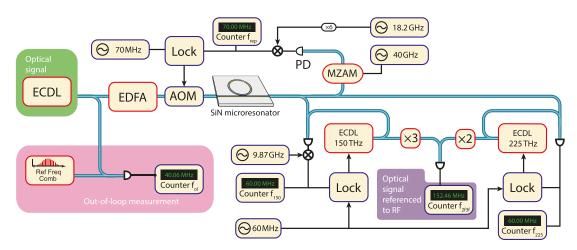


**Figure A.10 – Setup for self-referencing of a soliton Kerr frequency comb** AOM: acousto-optic modulator; ECDL: external cavity diode laser; EDFA: erbium-doped fiber amplifier; LOCK: combined phase comparator and proportional-integral-derivative (PID) servo controller for the phase locks; MZAM: Mach-Zehnder amplitude modulator; PD: photodiode. All RF frequencies are derived from one RF reference that is also used to reference the measurements and the fiber comb.

Although the large line spacing of our frequency comb of  $f_{\rm rep}=189.184$  GHz has the advantage that it can be easily resolved on an optical spectrometer, one challenge of the large mode spacing is that the measurement of the repetition rate as well as of the offset frequency requires the use of high frequency photodiodes and RF components. In our experiment the repetition rate is measured via optical amplitude modulation down-mixing [322] and RF down-mixing as shown in fig. A.10.

We also take advantage of special properties of the 2f-3f scheme with transfer lasers to decrease the measured frequency  $f_{2f3f}$ . First, it is important to note that with the 2f-3f scheme not all pairs of lines that are doubled and tripled respectively produce the same  $f_{2f3f}$  frequency. There are two relevant scenarios. The first one is if the condition 2n = 3m is fulfilled as described above, then the heterodyne beat note  $f_{2f3f}$  is equal to  $f_{CEO}$ . The second scenario is if 2n = 3m + 1 is fulfilled, then  $f_{2f3f} = f_{CEO} - f_{rep}$  is measured. Therefore, a pair of lines is chosen to minimize the value of the measured frequency, which in our case is the second scenario with 2n = 3m + 1. Second, taking into account the two frequency offsets of the transfer lasers in our setup, the measured  $f_{2f3f}$  can be expressed as  $f_{2f3f} = f_{rep} - f_{CEO} + 2f_{225} - 3f_{150}$  [247]. Therefore we use  $f_{150} \approx 9.87$  GHz to reduce the measured 2f-3f beat to a frequency of the order of 100 MHz (fig. A.9d). All frequencies (the repetition rate, the frequency offsets of the two transfer lasers as well as the 2f-3f beat note) are simultaneously monitored on RF frequency counters. These counters as well as all other RF equipment and in particular the RF synthesizers for the required local oscillators are referenced to a common 10 MHz reference derived from a commercial atomic clock (fig. A.10).

While this is in principle sufficient for self-referencing as the offset frequency and repetition rate of the frequency comb can be computed from the counter measurements [247], the repetition rate was also stabilized. For this we compare the repetition rate of the Kerr frequency comb to the RF reference and feedback onto the pump power [212, 255]. We record the overlapping Allan deviations of the three locked frequencies as shown in fig. A.11c. This is implemented using two gapless  $\Pi$ -type counters for the frequencies  $f_{rep}$  and  $f_{225}$  as well as one  $\Lambda$ -type counter with dead time for  $f_{150}$ . All overlapping Allan deviations average down for longer timescales (gate times  $\tau > 0.1$  s). The flat behavior of the Allan deviation of  $f_{\rm rep}$  for shorter timescales is due to the limited bandwidth of the actuation of its phase lock. However, the slope of -1.10 for longer time scales matches well the expected value of -1 [215, 216] showing that the phase lock compensates deviations on these timescales. The slope of -0.54 instead of -1 for the overlapping Allan deviation plot of the 225 THz transfer laser is due to some transient excursions of the laser frequency. The similar slope of the overlapping Allan deviation of the 150 THz laser lock however is mainly due to the different type of counter, which results in a slope close to the expected -0.5 for this Allan deviation [215, 216]. Having phase-locked all frequencies but the offset frequency of the Kerr frequency comb, we can determine the value of the offset frequency as  $f_{\text{CEO}} = f_{\text{rep}} - 3 f_{150} + 2 f_{225} - f_{2f3f} \approx 159.71 \text{ GHz}$ and measure its drift by monitoring  $f_{2f3f}$ .

#### A.2.4 Counting the continuous-wave pump laser frequency

One unique property of Kerr frequency combs is that the pump laser constitutes one of the lines of the frequency comb. Because the repetition rate of our comb is locked, the drift of the pump laser frequency is directly mapped to the excursion of the offset frequency of the comb. Therefore the self-referenced Kerr frequency comb can be used to derive the exact optical frequency of the cw pump laser and to track it over time. This is confirmed by taking an out-of-loop measurement. For this experiment a fraction of the pump laser is split off before the microresonator and the heterodyne beat note of the pump laser with a commercial self-referenced, fully stabilized frequency comb ( $f_{\text{CEO,ref}} = 20 \text{ MHz}$ ,  $f_{\text{rep,ref}} = 250.14 \text{ MHz}$ ) is counted (fig. A.10). At the same time, the measured  $f_{2f3f}$  is counted as well. The two frequency counters used are the same model of Π-type counters mentioned above and the reference frequency comb is stabilized to the same commercial atomic clock RF reference as all other RF equipment used in this experiment. By calculating the line number of the pump laser in the Kerr frequency comb (1015) and the line number of the line of the reference frequency comb that the pump laser beats with (768282) and using our knowledge of all frequencies ( $f_{rep}$ ,  $f_{\text{CEO}}$ ,  $f_{\text{rep,ref}}$ ,  $f_{\text{CEO,ref}}$  and  $f_{\text{ol}}$ ) we can calculate the optical frequency of the pump laser in two ways. Once using the Kerr frequency comb and its counted offset frequency and once using the out-of-loop measurement with the commercial self-referenced fiber frequency comb. The overlay of these two independent frequency measurements over time is shown in fig. A.11a. The correlation is very clear and no deviations are visible. In fig. A.11b a histogram of the differences between the two optical frequencies is shown. The data fits well to a Gaussian distribution with the center frequency of the distribution shifted by 172 Hz from 0 Hz for the 160-s-long measurement. This out-of-loop experiment validates our ability to precisely determine the offset frequency of our Kerr frequency comb using the 2f-3f scheme.

In summary, we demonstrate a self-referenced Kerr frequency comb without employing external broadening. Using dissipative Kerr soliton dynamics, we show that coupling a continuous wave laser into an integrated, on-chip microresonator is enough to coherently "broaden" its spectrum and to allow for self-referencing. Alleviating the need for additional external broadening in on-chip Kerr frequency comb devices shows that self-referenced, phase-stabilized integrated frequency comb sources are in principle possible. While transfer lasers are used in the current work, they do in principle constitute elements that are equally amenable to photonic integration [323]. Establishing devices that provide a microwave to optical link on a chip may catalyze a wide variety of applications such as integrated, microresonator-based atomic clocks [129] and on-chip, low-noise RF synthesis from optical references [40] and could contribute to making frequency metrology ubiquitous.

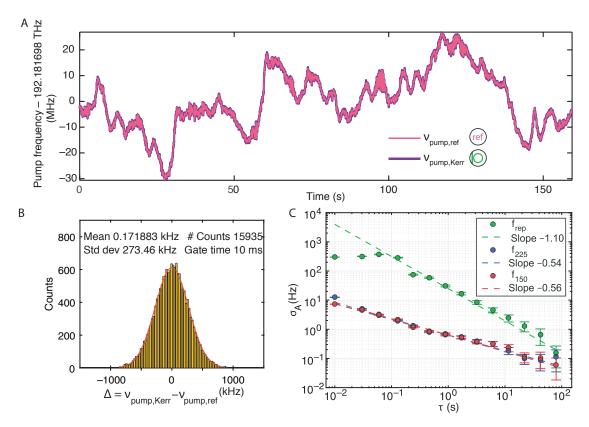
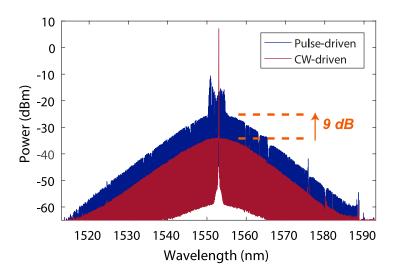


Figure A.11 – Tracking of the pump laser frequency with the self-referenced soliton Kerr frequency comb and an out-of-loop verification. a The drift of the frequency of the pump laser  $(v_{\text{pump}})$  over time as measured with the Kerr frequency comb (thick, dark violet line,  $v_{\text{pump,Kerr}} = f_{\text{CEO}} + 1015 f_{\text{rep}}$ ) and with a reference fiber frequency comb (thin, light pink line,  $v_{\text{pump,ref}} = f_{\text{CEO,ref}} + 768282 f_{\text{rep,ref}} - f_{\text{ol}}$ ). Gate time is 10 ms. As the repetition rate of the soliton Kerr frequency comb is locked and the pump laser itself is one line of the frequency comb, the drift of the pump laser is equivalent to the drift of the offset frequency of the Kerr frequency comb. The reference frequency comb is a fully self-referenced, stabilized fiber frequency comb. (b) The histogram of the difference of the two tracked pump laser frequencies  $\Delta = v_{\text{pump,Kerr}} - v_{\text{pump,ref}}$ . The Gaussian fit (red) shows a deviation of 172 Hz from the expected mean of 0 Hz. (c) Illustration that shows all the frequencies involved in this out-of-loop measurement. Solid, black horizontal bars indicate locked frequencies. The two pink and violet dashed bars are the two frequencies that are not stabilized but counted in order to derive the data shown in (a) and (b). (c) The overlapping Allan deviation  $\sigma_A$  of all locked frequencies (the repetition rate of the Kerr frequency comb  $f_{rep}$  and the offsets of the two transfer lasers  $f_{150}$  and  $f_{225}$ ) average down for longer gate times, showing all frequencies are indeed phase locked. The flat part of the Allan deviation for  $f_{\rm rep}$  is caused by the limited bandwidth of the actuation for this phase lock. The two transfer laser frequency offsets  $f_{225}$ and  $f_{150}$  are counted with different frequency counters. The beat  $f_{150}$  is counted on a counter with dead time resulting in a slope of only around -0.5 instead of -1. The beat  $f_{225}$  is counted on a gapless counter. The reason for the deviation from the ideal  $\tau^{-1}$  behavior for  $f_{225}$  are the occasional frequency excursions that the lock does not compensate perfectly.

# A.3 Pulsed driving of a crystalline microresonator

Recently, pulse-driving of nonlinear microresonators, as opposed to continuous-wave driving (CW), has been demonstrated as a powerful method for overcoming the fundamental inefficiency of single-state dissipative Kerr soliton (DKS) generation [39]. While DKS-based frequency combs have recently made compelling demonstrations in numerous applications such as spectroscopy and telecommunications, their total conversion efficiency between the CW pump and the frequency comb lines has been limited. The total number of lines successfully generated across a broad bandwidth has also been limited to several hundred, resulting in a trade-off between having a large bandwidth [70], and an electronically detectable repetition rate [167]. Using pulse-driving, near-unity conversion efficiency from an ultra-high-Q 14 GHz crystalline MgF<sub>2</sub> microresonator, was demonstrated.



**Figure A.12** – Comb spectra of the MgF<sub>2</sub> resonator overlaid for the two experimental cases, demonstrating the dramatic increase in conversion efficiency enabled by pulse-driving.

The pulsed source consists of a tunable CW laser which is intensity-modulated into pulses at the resonator repetition rate, or at a fraction of it [39]. The light is further modulated by two cascaded electro-optic modulators (EOM) driven at  $\sim 5V_\pi$  (RF power  $\sim 33$  dBm) between them. This strongly chirps the pulses and generates approximately 40 lines in the frequency domain. After the equivalent of  $\sim 300$  m of SMF acting as chirp-compensation, the pulses are compressed to approximately 1-2 picoseconds. An EDFA amplifies the low duty-cycle pulse-train to high peak powers before being coupled to the crystalline MgF $_2$  resonator via a tapered fiber. The microresonator is driven synchronously at its repetition rate of 14.09 GHz. We exploit the high attainable peak powers of the pulses to drive the microresonator in the strongly over-coupled regime, where  $\kappa_{ex}/2\pi\approx 2$  MHz and  $\kappa_0/2\pi\approx 100$  kHz, the external coupling linewidth and the internal loss linewidth respectively. In this regime, the total input-output conversion efficiency from pump to soliton is maximized, but high peak powers are required in order to reach the nonlinear threshold. The generated pulse-driven DKS comb is depicted in A.12

#### Appendix A. Additional experimental results and contributions

alongside a typical example of a CW-driven DKS comb with the same resonator in a close to critically coupled regime. In the pulse-driven case, the average ratio of pump-line to first soliton-line is 10 dB and the overall conversion efficiency achieved from pump to soliton is  $\sim$  40 %, in stark contrast to the CW-driven DKS with 41 dB and  $\sim$  1% respectively. Furthermore, the absolute comb power out is 9 dB higher in the pulse-driven case, despite the average pump power being less than that in the CW-driven case, with 50 mW required as opposed to 200 mW. This improvement comes thanks to the fact that much of the 2 ps driving pulse is directly converted into the 150 fs DKS, with only a little unconverted energy, demonstrating the capability in general for pulse-driving to dramatically improve conversion efficiency in Kerr resonators. Furthermore, the high Q of the crystalline resonator will help to study the noise conversion properties from the microwave drive to the optical comb lines in the microcavity.

## **B.1** Laser phase noise characterization

The spectral purity of several lasers in the lab was characterized by heterodyning with the ultrastable ORS system (at 1553 nm). The phase noise of the heterodyne beatnote was characterized on the FSW43 in IQ analysis mode [324] (sampling rate 160 MHz). The results are displayed in fig. B.1.

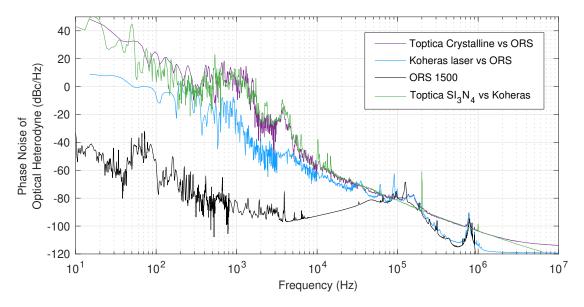


**Figure B.1 – Comparison of the laser noise.** Laser noise of free-running laser in the LPQM BM lab. The ORS system was characterized in ref. [228].

# B.2 Frequency counter benchmark for Allan deviation measurement

Depending on the way a frequency counter is designed and operated the resulting computed Allan deviation can significantly differ. The present note tries to benchmark different counters models and methods of measuring the Allan deviation by comparing with a phase noise measurement.

#### **B.2.1** Allan variance

#### **Definition**

The Allan variance characterize the frequency fluctuations of a signal. Considering the following signal

$$s(t) = A\sin(2\pi f(t) t) = A\sin(2\pi f_0 t + \varphi(t))$$
(B.1)

The absolute<sup>1</sup> Allan variance (or its square root, the Allan frequency deviation) is defined as

$$\sigma_A^2 \equiv \left\langle \frac{1}{2} \left( \bar{f}_{k+1} - \bar{f}_k \right)^2 \right\rangle \tag{B.2}$$

where we define the k-th sample of the frequency, averaged over some measurement time  $\tau$  (sometimes called the integration time), as

$$\bar{f}_k = \frac{1}{\tau} \int_{k\tau}^{(k+1)\tau} f(t) dt$$
 (B.3)

Under the ergodic assumption, the ensemble average in (B.2) is usually replaced by a summation of m consecutive measurements:

$$\sigma_A^2 \approx \frac{1}{m} \sum_{k=1}^m \frac{(\bar{f}_{k+1} - \bar{f}_k)^2}{2}$$
 (B.4)

Thus if  $f_k$  can be measured, computing the Allan variance is fairly straightforward. The integral in (B.3) corresponds to a single measurement of an ideal frequency counter (called  $\Pi$  type) for a selected measurement time,  $\tau$ , usually referred to as the gate time. There also shouldn't be any dead time between consecutive measurements.

#### **Frequency counters**

Known issues The real frequency counters do not implement the frequency measurement as described above. First most counters have dead time when the gating electronic rearms between each measurement. High resolution counters implement an internal averaging algorithm, which alters the effective temporal windowing function (they are referred to as  $\Lambda$  counters), as described by Dawkink et al. [216]. Moreover the counters are sensitive to amplitude noise which can cause so called cycles slips. All these effects can alter the measured Allan deviation.

**Measuring the Allan variance with counters** There are essentially two ways of measuring the Allan variance plot  $\sigma_A^2(\tau)$  with a frequency counter

<sup>&</sup>lt;sup>1</sup>Another common definition of the Allan variance considers the normalized frequency  $y(t) = f(t)/f_0$  instead of f(t) where  $f_0$  is the average frequency. It is usually noted  $\sigma_{\gamma}^2$  [325] and called the fractional variance.

**Numerical integration** With this method the gate time is fixed at a value  $\tau_s$  during the measurement and provides a measurement of the frequency series  $(f_k)_k$  with a regular sampling. The Allan variance for n-multiples of  $\tau_s$  can be numerically computed by averaging over n adjacent frequency measurements and then applying eq. (B.4). If the frequency is measured for a time T the accessible  $\tau$  values range from  $\tau_s$  to  $\lfloor T/\tau_s \rfloor \tau_s$  yet with a reduced number of points for the longer timescales. The statistical analysis is performed over the same dataset over different time scales. This measurement method also offers the possibility to track the frequency behavior over time, to track frequency drifts and to perform an overlapping Allan variance. One drawback of the method is that the gate time is fixed and so is the resolution of the counter. The counter resolution is usually reduced for smaller gate time and the numerical averaging may not compensate properly for it. Also the shorter the gate time, the larger ratio of the dead time.

**Gate time sweep** Another possibility is to measure with different gate times and to calculate the Allan variance for each gate time, separately. This is less flexible than the previous method as the values for  $\tau$  have to be defined in advance. Besides, the values of  $\sigma_A^2(\tau)$  are not measured over the same time interval and the properties of the system may change in between. Changing the gate time however means varying the counter resolution and the proportion of the dead time in the data.

#### Relationship between phase noise and Allan variance

The most frequently used tool for describing oscillator phase noise is  $S_{\varphi}(f)$ , defined as the onesided power spectral density of the random phase fluctuation  $\varphi(t)$ . The physical dimension of  $S_{\varphi}$  is rad<sup>2</sup>/Hz. The single sideband (SSB) phase noise  $\mathcal{L}(f)$  is related to  $S_{\varphi}$  via

$$\mathcal{L}(f) = 10 \log_{10} \left( \frac{1}{2} S_{\varphi}(f) \right) \tag{B.5}$$

and is expressed in dBc/Hz. In the frequency domain, the Allan variance can be seen as a lowpass filter with bandwidth  $\propto 1/\tau$  (See Rubiola [325] for more details). The phase noise can be related to the Allan deviation via

$$\sigma_A^2(\tau) = \int_{-\infty}^{+\infty} S_{\varphi}(f) \frac{2\sin^4(\pi\tau f)}{(\pi\tau)^2} df \tag{B.6}$$

#### **B.2.2** Experimental results

#### **Hewlett Packard 51130A**

Our lab was equipped with several counters of reference HP 51130A, that were used in section 4.3. As mentioned in this section, they are a  $\Lambda$ -type counter. Also, this counter cannot be read without dead time between consecutive measurements. All in all, it is not possible with these counters to perform true Allan deviation measurements, especially to assess the phase locking of a system, which necessitates to characterize white phase noise.

#### Agilent 53230A

This counter is specified to be dead time free and supposed to be able to operate both in true  $\Pi$  mode or in  $\Lambda$  mode.

In order to compare the different ways of measuring the Allan deviation, the signal of a R&S SMC100 synthesizer (frequency  $f_0 = 25$  MHz) is sent to the Agilent 53230A counter. All devices are referenced to the same common clock.

First, the counter is setup in 'CONT' mode that is supposed to provide dead time free and reciprocal mode ( $\Pi$  window) counting. Several series f(t) are acquired with different gate time and the numerical integration is applied on each series to compute the overlapping Allan deviation. The series are also processed to get the gate sweep approach. The gate is varied between  $10^{-5}$  s to 100 s, each time 50 points are acquired. Finally, the SSB phase noise is measured on the R&S FSUP (see fig. B.3) and converted to Allan deviation using (B.6).

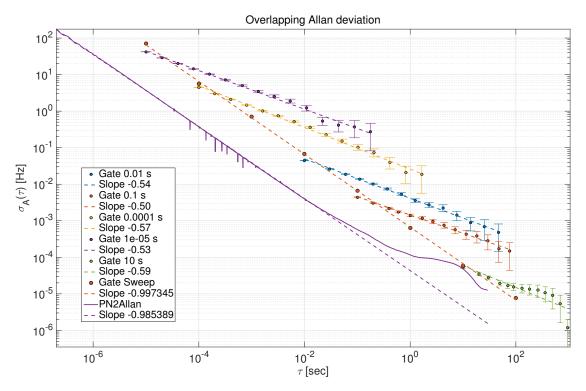


**Figure B.2** – Comparison of the Allan deviation of the R&S SMC100 25 MHz synthesizer obtained with the Agilent 53230A counter. The overlapping Allan deviation method is compared to the gate sweep method. A conversion of the phase noise to Allan deviation is also shown as a reference.

The results are presented on fig. B.2. There is a strong deviation between the averaged time series and the gate sweep method. The numerical method yields a slope around -0.5 for all gate time while the gate sweep method gives a slope of  $\sim -1$  in better agreement with the phase noise measurement yielding a slope of  $\sim -0.99$  for gate time smaller than  $10^{-2}$  s. This effect is reported by Bernhardt et al. [215]. An insight for this behavior is provided by Dolgovskiy [326]:

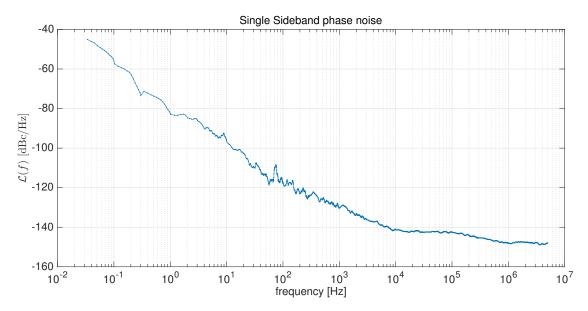


**Figure B.3** – Phase noise of the R&S SMC100 synthesizer measured with the PLL PN measurement unit of the R&S FSUP. Both devices were referenced to the same clock.

in the presence of white or flicker phase noise, the frequency fluctuations are correlated. The correlations between successive frequency measurements is lost in presence of a dead time. The data can thus not be juxtaposed to calculate an Allan deviation for an integration time longer than the gate time without distorting the result. For white phase noise, this leads to a  $\tau^{-1/2}$  dependence of the Allan deviation instead of  $\tau^{-1}$  dependence obtained with a dead time-free counter.

In any case in the presence of white / flicker phase noise the gate sweep approach should be privileged as it yields a more accurate slope. Yet the offset between the curve derived from phase noise measurement and the gate sweep at small gate time as well as the difference in behavior at longer gate time is not yet understood.

To further investigate the effect of  $\Lambda$  counter the gate sweep measurement was repeated with the counter in high-resolution ( $\Lambda$ ) mode ('HIRES'). The results are shown on fig. B.4. The slope in the reciprocal mode yield a correct  $\tau^{-1}$  dependence while it is steeper in the HIRES mode ( $\sim -1.17$ ). For  $\Lambda$  counters, Dawkins *et al.* [216] predict an evolution of the Allan deviation as  $\tau^{-3/2}$ , which may explain the deviation.

This observation indicates that despite its specification of dead time free counter, the Agilent 53230A counter doesn't meet the requirements for metrology applications . This has been further reported during discussions with the team of David Howe at NIST who mentioned having issues with the HP / Agilent counters. However, thanks to the indications of Scott Papp, I have been made aware that this counter can be used in true dead time free and reciprocal mode ( $\Pi$  window). For this, the *undocumented* mode 'RCON' must be used<sup>2</sup>. This feature has not been tested in the lab.

<sup>&</sup>lt;sup>2</sup>http://www.anderswallin.net/2015/06/cont-vs-rcon-mode-on-the-53230a-frequency-counter/

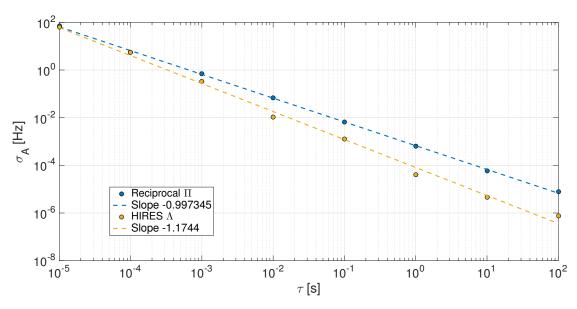


**Figure B.4** – Allan deviation comparison of the gate sweep method when the counter Agilent 53230A is operated in reciprocal ( $\Pi$ ) and in high-resolution ( $\Lambda$ ) modes. The signal is the R&S SMC100 25 MHz synthesizer.

#### **Tektronix FCA3100**

This counter was tested in similar conditions as the Agilent 53230A, and provided the expected 1/f slope expected for a phase locked oscillator. These tests motivated the purchase of these counter for replacing the former ones in our lab.

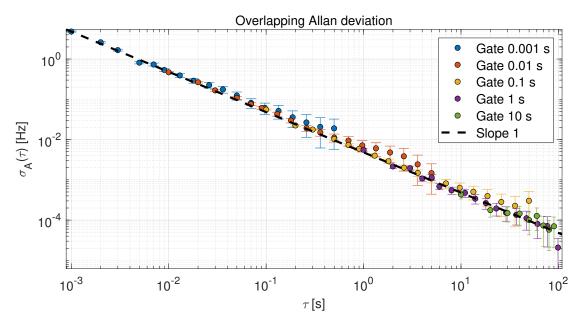


**Figure B.5** – Comparison of the Allan deviation of the R&S SMC100 synthesizer obtained with the Tektronix FCA3100. The correct slope and consistent measurements are obtained with the gate sweep method and the overlapping method.

#### The 'smart Allan' procedure

Using the counter Tektronix FCA3100, it is possible to combine the 'gate sweep' approach and the numerical integration. The 'smart Allan' procedure performs a gate sweep for the decades of gate times that are shorter than a target averaging time. Once this target gate is reached, the data is binned continuously for later numerical processing. For example, we want to count for 1000 s with a gate time of 1 s but would like to have some idea of the stability on shorter timescales. The smart Allan procedure starts by counting 100 bins for each of the gates [10  $\mu s$ , 100  $\mu s$ , 1 ms, 10 ms, 100 ms] and then initiates the counting for 1000 s with 1 s gate. With this approach, the stability of the signal on short time scales can be assessed, however, it only characterizes the stability of the signal at the beginning of the measurement.

# C Derivation of the coupled mode equations model

The FWM dynamics in a microresonator can be described as a nonlinear coupling of the modes [327]. We consider a single mode family of the resonator. We consider one continuous pump coupled to one mode, which is taken as reference (relative mode number  $\mu = 0$ ). The electric field in the cavity can be expanded into a sum of these eigenmodes

$$E(\mathbf{r}, y) = \frac{1}{2} \sum_{\mu} \sqrt{\frac{2\hbar\omega_{\mu}}{n_0^2 \varepsilon_0 V_{\text{eff}}}} \tilde{A}_{\mu}(t) e^{-i\omega_{\mu}t} \mathbf{u}_{\mu}(\mathbf{r}) + \text{c.c.}$$
(C.1)

We have chosen here a normalization such that  $|\tilde{A}_{\mu}(t)|^2$  corresponds to the photon number in mode  $\mu$ . The resonance frequency of the mode  $\mu$  in the presence of dispersion writes

$$\omega_{\mu} = \omega_0 + D_1 \mu + \frac{D_2}{2} \mu^2 + \dots$$
 (C.2)

where  $D_1$  is the FSR of the mode family and  $D_2$  the dispersion parameter.

Inserting (C.1) into the nonlinear wave equation eq. (1.10), and recalling that the eigenmodes  $u_{\mu}(\mathbf{r})$  are solution of the Helmholtz equation yields

$$\mu_0 \frac{\partial^2}{\partial t^2} \boldsymbol{P}_{NL} = \frac{1}{2} \left[ \sum_{\mu} \sqrt{\frac{2\hbar\omega_{\mu}}{n_0^2 \epsilon_0 V_{\text{eff}}}} \frac{n_0^2}{c^2} \left( \frac{\partial^2 \tilde{A}_{\mu}}{\partial t^2} + 2i\omega_{\mu} \frac{\partial \tilde{A}_{\mu}}{\partial t} \right) e^{-i\omega_{\mu}t} \boldsymbol{u}_{\mu}(\boldsymbol{r}) + \text{c.c.} \right]$$
(C.3)

In (C.3), we neglect the phenomenons of third harmonic generation and triple component sum frequency generation in  $\boldsymbol{P}_{\rm NL}$  to keep only the terms of the form  $\omega_u + \omega_v + \omega_w$  (where u,v,w can be equal) that account for SPM, XPM and FWM. We can write

$$\boldsymbol{P}_{\rm NL} = \frac{3\varepsilon_0}{8} \chi^{(3)} \sum_{\mu', \mu'', \mu'''} \tilde{A}_{\mu'} \tilde{A}_{\mu''} \tilde{A}_{\mu'''}^* e^{-i(\omega_{\mu'} + \omega_{\mu''} - \omega_{\mu'''})t} \boldsymbol{u}_{\mu'} \cdot \boldsymbol{u}_{\mu''} \boldsymbol{u}_{\mu'''}^* + \text{c.c.}$$
(C.4)

The factor of three accounts for the possible permutations. Using the slowly varying envelope approximation on A(t) and projecting (C.3) onto the particular mode  $\mu$  (i.e. projection on

 $oldsymbol{u}_{\mu}(oldsymbol{r})^*$  and integration over the volume of the resonator), results in

$$\frac{\partial \tilde{A}_{\mu}}{\partial t} = i g \sum_{\substack{\mu', \mu'', \mu''' \\ \mu' + \mu'' + \mu''' = \mu}} \Lambda^{\mu}_{\mu', \mu'', \mu'''} \, \tilde{A}_{\mu'} \, \tilde{A}^{*}_{\mu'''} \, e^{-i(\omega_{\mu'} + \omega_{\mu''} - \omega_{\mu'''} - \omega_{\mu})t}$$
(C.5)

with the nonlinear coupling coefficient

$$g = \frac{c n_2 \hbar \omega_0^2}{n_0^2 V_{\text{eff}}} \tag{C.6}$$

and the coupling strength between the four interacting modes  $\mu, \mu', \mu''$ , and  $\mu'''$ 

$$\Lambda^{\mu}_{\mu',\mu'',\mu'''} = \left(\frac{\omega_{\mu'} + \omega_{\mu''} - \omega_{\mu'''}}{\omega_0}\right)^2 \sqrt{\frac{\omega_{\mu'}\omega_{\mu''}\omega_{\mu'''}}{\omega_{\mu}^3}} \frac{\int_{V_{\text{res}}} [\mathbf{u}_{\mu'} \cdot \mathbf{u}_{\mu''}] [\mathbf{u}_{\mu''}^* \cdot \mathbf{u}_{\mu}^*] dV}{\int_{V_{\text{res}}} \|\mathbf{u}_{\mu}\|^2 dV}$$
(C.7)

The coupling strength essentially depends on the power density overlap of the modes. For relatively narrow-span comb, the modes overlap almost perfectly (the mode profiles for close longitudinal mode number  $\mu$  are almost the same) and the frequencies of the modes are close, such that we can assume  $\Lambda^{\mu}_{u',u''',u'''} \approx 1$  with a good approximation.

Physically, the coupling factor g can be interpreted as the per photon frequency shift of the resonance frequency due to the Kerr-nonlinearity (via SPM). The summation in (C.5) is done for all  $\mu', \mu'', \mu'''$  respecting the relation  $\mu' + \mu'' + \mu''' = \mu$  (phase matching).

The full nonlinear coupled mode equations are obtained by including the pump term and the cavity loss rate  $\kappa$  (assumed to be constant for the mode family):

$$\frac{\partial \tilde{A}_{\mu}}{\partial t} = -\frac{\kappa}{2} \tilde{A}_{\mu} + \delta_{\mu,0} \sqrt{\kappa_{\text{ex}}} s_{\text{in}} e^{-i(\omega_{p} - \omega_{0})t} 
+ i g \sum_{\substack{\mu',\mu'',\mu''' \\ \mu' + \mu''' = \mu}} \Lambda^{\mu}_{\mu',\mu'',\mu'''} \tilde{A}_{\mu'} \tilde{A}_{\mu''} \tilde{A}^{*}_{\mu'''} e^{-i(\omega_{\mu'} + \omega_{\mu''} - \omega_{\mu'''} - \omega_{\mu})t}$$
(C.8)

Without loss of generality, the reference phase of the pump is set to zero while  $s_{\rm in} = \sqrt{P_{\rm in}/\hbar\omega_0}$  denotes the amplitude of the pump power  $P_{\rm in}$  coupled to the cavity and  $\delta_{\mu,0}$  is the Kronecker delta.

Equation (C.8) can be rescaled with respect to the loss rate  $\kappa = \kappa_0 + \kappa_{ex}$ . The following normalization [95] is applied

$$\tau = \frac{\kappa}{2}t \quad ; \quad \eta = \frac{\kappa_{\text{ex}}}{\kappa} \quad ; \quad d_2 = \frac{D_2}{\kappa} \quad ; \quad f = \sqrt{\frac{8\eta g}{\kappa^2}} \, s_{\text{in}} \quad ; \quad \zeta_{\mu} = \frac{2}{\kappa} (\omega_{\mu} - \omega_p - \mu D_1) = \zeta_0 + d_2 \mu^2$$

$$a_{\mu} = \tilde{A}_{\mu} \sqrt{\frac{2g}{\kappa}} \, e^{-i(\omega_{\mu} - \omega_p - \mu D_1)t} \tag{C.9}$$

to get the dimensionless expression

$$\frac{\partial a_{\mu}}{\partial \tau} = -[1 + i\zeta_{\mu}] a_{\mu} + i \sum_{\mu' \le \mu''} (2 - \delta_{\mu', \mu''}) a_{\mu'} a_{\mu''}^* a_{\mu' + \mu'' - \mu}^* + \delta_{\mu, 0} f$$
 (C.10)

where we assumed  $\Lambda^{\mu}_{\mu',\mu'',\mu'''}=1.$ 

# **Bibliography**

- [1] BIPM, *Resolutions of the 26th CGPM*, tech. rep. **C** (cit. on p. 1)
- [2] V. Gerginov, N. Nemitz, S. Weyers, R. Schröder, D. Griebsch, and R. Wynands, "Uncertainty evaluation of the caesium fountain clock PTB-CSF2", *Metrologia* 47.1 (2010), pp. 65–79. 

  ☑ (cit. on p. 1)
- [3] H. Schnatz, B. Lipphardt, J. Helmcke, F. Riehle, and G. Zinner, "First Phase-Coherent Frequency Measurement of Visible Radiation", *Physical Review Letters* 76.1 (1996), pp. 18–21. 🗹 (cit. on pp. 1, 4)
- [4] S. T. Cundiff, "Phase stabilization of ultrashort optical pulses", *Journal of Physics D: Applied Physics* 35.8 (2002), R43–R59. (cit. on pp. 2, 4–6)
- U. Keller, "Recent developments in compact ultrafast lasers", *Nature* 424.6950 (2003), pp. 831–838. ☑ (cit. on pp. 2, 4, 6)
- [6] B. J. Bloom, T. L. Nicholson, J. R. Williams, S. L. Campbell, M. Bishof, X. Zhang, W. Zhang, S. L. Bromley, and J. Ye, "An optical lattice clock with accuracy and stability at the 10<sup>-18</sup> level", *Nature* 506.7486 (2014), pp. 71–75. ☑ (cit. on pp. 2, 6)
- [7] N. Hinkley, J. A. Sherman, N. B. Phillips, M. Schioppo, N. D. Lemke, K. Beloy, M. Pizzocaro, C. W. Oates, and A. D. Ludlow, "An atomic clock with 10<sup>-18</sup> instability.", *Science* 341 (2013), pp. 1215–1218. (cit. on p. 2)
- [8] P. Del'Haye, A. Schliesser, O. Arcizet, T. Wilken, R. Holzwarth, and T. J. Kippenberg, "Optical frequency comb generation from a monolithic microresonator", *Nature* 450.7173 (2007), pp. 1214–7. [2] (cit. on pp. 2, 8, 31, 97)
- [9] T. Herr, V. Brasch, J. D. Jost, C. Y. Wang, N. M. Kondratiev, M. L. Gorodetsky, and T. J. Kippenberg, "Temporal solitons in optical microresonators", *Nature Photonics* 8.2 (2013), pp. 145–152. (cit. on pp. 2, 31, 32, 35, 36, 43, 68, 92, 107, 130, 147, 148)
- [10] L. Essen and J. V. L. Parry, "An atomic standard of frequency and time interval: A cæsium resonator", *Nature* 176.4476 (1955), pp. 280–282. 🗷 (cit. on p. 3)
- [11] H. A. Haus, "Mode-locking of lasers", *IEEE J. Quantum Electron*. 6.6 (2000), pp. 1173–1185. 🗷 (cit. on p. 4)
- [12] G. Steinmeyer, "Frontiers in Ultrashort Pulse Generation: Pushing the Limits in Linear and Nonlinear Optics", *Science* 286.5444 (1999), pp. 1507–1512. (cit. on pp. 4, 6)

- [13] J. Rauschenberger, T. Fortier, D. Jones, J. Ye, and S. Cundiff, "Control of the frequency comb from a modelocked Erbium-doped fiber laser", *Optics Express* 10.24 (2002), p. 1404. (cit. on p. 5)
- [14] B. R. Washburn, R. W. Fox, N. R. Newbury, J. W. Nicholson, K. Feder, P. S. Westbrook, and C. G. Jørgensen, "Fiber-laser-based frequency comb with a tunable repetition rate", *Optics Express* 12.20 (2004), p. 4999. (cit. on pp. 5, 8)
- [15] B. R. Washburn, S. a. Diddams, N. R. Newbury, J. W. Nicholson, M. F. Yan, and C. G. Jørgensen, "Phase-locked, erbium-fiber-laser-based frequency comb in the near infrared", *Optics Letters* 29.3 (2004), p. 250. (cit. on p. 5)
- [16] T. R. Schibli, K. Minoshima, F.-L. Hong, H. Inaba, A. Onae, H. Matsumoto, I. Hartl, and M. E. Fermann, "Frequency metrology with a turnkey all-fiber system", *Optics Letters* 29.21 (2004), p. 2467. (cit. on p. 5)
- [17] H. Telle, G. Steinmeyer, A. Dunlop, J. Stenger, D. Sutter, and U. Keller, "Carrier-envelope offset phase control: A novel concept for absolute optical frequency measurement and ultrashort pulse generation", *Applied Physics B* 69.4 (1999), pp. 327–332. (cit. on pp. 5, 6, 131, 180)
- [18] D. J. Jones, S. A. Diddams, J. K. Ranka, A. Stentz, R. S. Windeler, J. L. Hall, and S. T. Cundiff, "Carrier-Envelope Phase Control of Femtosecond Mode-Locked Lasers and Direct Optical Frequency Synthesis", *Science* 288.5466 (2000), pp. 635–639. (cit. on pp. 5, 6, 131)
- [19] R. Holzwarth, T. Udem, T. W. Hänsch, J. C. Knight, W. J. Wadsworth, and P. S. J. Russell, "Optical Frequency Synthesizer for Precision Spectroscopy", *Physical Review Letters* 85.11 (2000), pp. 2264–2267. [7] (cit. on pp. 5, 6)
- [20] S. Cundiff and J. Ye, "Colloquium: Femtosecond optical frequency combs", *Reviews of Modern Physics* 75.1 (2003), pp. 325–342. (cit. on pp. 5, 6)
- [21] J. Ye and S. T. Cundiff, Femtosecond Optical Frequency Comb: Principle, Operation and Applications, Springer, 2005 (cit. on pp. 5, 6).
- [22] J. K. Ranka, R. S. Windeler, and A. J. Stentz, "Visible continuum generation in air–silica microstructure optical fibers with anomalous dispersion at 800 nm", *Optics Letters* 25.1 (2000), p. 25. (cit. on p. 5)
- [23] S. A. Diddams, D. J. Jones, J. Ye, S. T. Cundiff, J. L. Hall, J. K. Ranka, R. S. Windeler, R. Holzwarth, T. Udem, and T. W. Hänsch, "Direct Link between Microwave and Optical Frequencies with a 300 THz Femtosecond Laser Comb", *Physical Review Letters* 84.22 (2000), pp. 5102–5105. (cit. on p. 5)
- [24] J. M. Dudley and S. Coen, "Supercontinuum generation in photonic crystal fiber", *Reviews of Modern Physics* 78 (2006), pp. 1135–1184. C (cit. on p. 5)
- [25] J. M. Dudley and J. R. Taylor, "Ten years of nonlinear optics in photonic crystal fibre", *Nature Photonics* 3.2 (2009), pp. 85–90. (cit. on p. 5)

- [26] A. Klenner, F. Emaury, C. Schriber, A. Diebold, C. J. Saraceno, S. Schilt, U. Keller, and T. Südmeyer, "Phase-stabilization of the carrier-envelope-offset frequency of a SESAM modelocked thin disk laser", *Optics Express* 21.21 (2013), pp. 24770–24780. (cit. on p. 5)
- [27] N. Torcheboeuf, G. Buchs, S. Kundermann, E. Portuondo-Campa, J. Bennès, and S. Lecomte, "Repetition rate stabilization of an optical frequency comb based on solid-state laser technology with an intra-cavity electro-optic modulator", *Optics Express* 25.3 (2017), pp. 2215–2220. (cit. on p. 5)
- [28] T. Udem, J. Reichert, R. Holzwarth, and T. W. Hänsch, "Accurate measurement of large optical frequency differences with a mode-locked laser", *Optics Letters* 24.13 (1999), p. 881. (cit. on pp. 6, 7)
- [29] J. L. Hall, M. S. Taubman, and J. Ye, "LASER STABILIZATION Quantifying Frequency Stability", *Handbook of Optics: Volume II Design, Fabrication, and Testing; Sources and Detectors; Radiometry and Photometry* (2010), pp. 27.1–27.24. (cit. on p. 6)
- [30] J. Bechhoefer, "Feedback for physicists: A tutorial essay on control", *Reviews of Modern Physics* 77.3 (2005), pp. 783–836. (cit. on p. 6)
- [31] R. van Rooij, J. S. Borbely, J. Simonet, M. D. Hoogerland, K. S. E. Eikema, R. a. Rozendaal, and W. Vassen, "Frequency metrology in quantum degenerate helium: direct measurement of the  $2^3S_1 \rightarrow 2^1S_0$  transition.", *Science* 333.6039 (2011), pp. 196–198.  $\checkmark$  (cit. on p. 6)
- T. Udem, R. Holzwarth, and T.W. Hänsch, "Optical frequency metrology", *Nature* 416.6877 (2002), pp. 233–237. C (cit. on p. 6)
- [33] S. A. Diddams, J. C. Bergquist, S. R. Jefferts, and C. W. Oates, "Standards of time and frequency at the outset of the 21st century.", *Science* 306.5700 (2004), pp. 1318–24. C. (cit. on p. 6)
- [34] A. H. Zewail, "Laser femtochemistry.", *Science* 242.4886 (1988), pp. 1645–53. (cit. on p. 6)
- [35] A. M. Weiner, "Ultrafast optical pulse shaping: A tutorial review", *Optics Communications* 284.15 (2011), pp. 3669–3692. (cit. on pp. 6, 37)
- [36] F. Krausz and M. Ivanov, "Attosecond physics", *Reviews of Modern Physics* 81.1 (2009), pp. 163–234. (cit. on p. 6)
- [37] A. Jallageas, J. Nürnberg, C. G. E. Alfieri, D. Waldburger, S. M. Link, F. Emaury, J. Morel, and U. Keller, "Wavelength calibration of high-performance spectrometers with a stabilized optical comb from an ultrafast semiconductor disk laser", *Conference on Lasers and Electro-Optics*, OSA Technical Digest (online), Optical Society of America, 2018, ATh3O.6. (cit. on p. 6)
- T. Steinmetz et al., "Laser frequency combs for astronomical observations.", *Science* 321.5894 (2008), pp. 1335–7. ✓ (cit. on p. 6)

- [39] E. Obrzud, S. Lecomte, and T. Herr, "Temporal solitons in microresonators driven by optical pulses", *Nature Photonics* 11.9 (2017), pp. 600–607. (cit. on pp. 6, 141, 167, 169, 185)
- [40] T. M. Fortier et al., "Generation of ultrastable microwaves via optical frequency division", *Nature Photonics* 5.7 (2011), pp. 425–429. C (cit. on pp. 6, 119, 130, 183)
- [41] X. Xie et al., "Photonic microwave signals with zeptosecond-level absolute timing noise", *Nature Photonics* 11.1 (2017), pp. 44–47. [27] (cit. on pp. 6, 119, 130)
- [42] J. Millo et al., "Ultralow noise microwave generation with fiber-based optical frequency comb and application to atomic fountain clock", *Applied Physics Letters* 94.14 (2009), p. 141105. (cit. on pp. 6, 130, 141)
- [43] E. Portuondo-campa, G. Buchs, S. Kundermann, L. Balet, and S. Lecomte, "Ultra-low phase-noise microwave generation using a diode-pumped solid-state laser based frequency comb and a polarization-maintaining pulse interleaver", *Optics Express* 23.25 (2015), pp. 32441–32451. (cit. on pp. 6, 130)
- [44] E. Temprana, E. Myslivets, L. Liu, V. Ataie, A. Wiberg, B. P. P. Kuo, N. Alic, and S. Radic, "Two-fold transmission reach enhancement enabled by transmitter-side digital back-propagation and optical frequency comb-derived information carriers", *Optics Express* 23.16 (2015), pp. 20774–20783. (cit. on p. 7)
- [45] F. Keilmann, C. Gohle, and R. Holzwarth, "Time-domain mid-infrared frequency-comb spectrometer", *Optics Letters* 29.13 (2004), p. 1542. (cit. on pp. 7, 144, 145)
- [46] I. Coddington, N. Newbury, and W. Swann, "Dual-comb spectroscopy", *Optica* 3.4 (2016), p. 414. (2016) (cit. on pp. 7, 117, 144, 145, 149)
- [47] A. Schliesser, M. Brehm, F. Keilmann, and D. W. D. van der Weide, "Frequency-comb infrared spectrometer for rapid, remote chemical sensing", *Optics Express* 13.22 (2005), pp. 9029–9038. (cit. on pp. 7, 144)
- [48] T. Ideguchi, A. Poisson, G. Guelachvili, N. Picqué, and T. W. Hänsch, "Adaptive real-time dual-comb spectroscopy", *Nature Communications* 5.23 (2014), p. 3375. (cit. on pp. 7, 144)
- [49] G. Villares, A. Hugi, S. Blaser, and J. Faist, "Dual-comb spectroscopy based on quantum-cascade-laser frequency combs", *Nature Communications* 5.1 (2014), p. 5192. (cit. on pp. 7, 144)
- [50] T. Ideguchi, S. Holzner, B. Bernhardt, G. Guelachvili, N. Picqué, T. W. Hänsch, N. Picque, and T. W. Hansch, "Coherent Raman spectro-imaging with laser frequency combs.", *Nature* 502.7471 (2013), pp. 355–8. (cit. on pp. 7, 144)
- [51] J. Lee, Y.-J. Kim, K. Lee, S. Lee, and S.-W. Kim, "Time-of-flight measurement with femtosecond light pulses", *Nature Photonics* 4.10 (2010), pp. 716–720. ✓ (cit. on p. 7)
- I. Coddington, W. C. Swann, and N. R. Newbury, "Coherent linear optical sampling at 15 bits of resolution", *Optics Letters* 34.14 (2009), p. 2153. (cit. on pp. 7, 157, 158)

- P. Trocha et al., "Ultrafast optical ranging using microresonator soliton frequency combs.", *Science* 359.6378 (2018), pp. 887–891. (cit. on pp. 7, 37, 144)
- [54] M.-G. Suh and K. J. Vahala, "Soliton microcomb range measurement", *Science* 359.6378 (2018), 884 LP –887. (cit. on p. 7)
- [55] T. Brabec, C. Spielmann, P. F. Curley, and F. Krausz, "Kerr lens mode locking", *Optics Letters* 17.18 (1992), p. 1292. (cit. on p. 7)
- U. Keller, "Ultrafast solid-state laser oscillators: a success story for the last 20 years with no end in sight", *Applied Physics B* 100.1 (2010), pp. 15–28. (cit. on p. 7)
- U. Keller, K. Weingarten, F. Kartner, D. Kopf, B. Braun, I. Jung, R. Fluck, C. Honninger, N. Matuschek, and J. Aus der Au, "Semiconductor saturable absorber mirrors (SESAM's) for femtosecond to nanosecond pulse generation in solid-state lasers", *IEEE Journal of Selected Topics in Quantum Electronics* 2.3 (1996), pp. 435–453. ☑ (cit. on p. 8)
- U. Keller and A. C. Tropper, "Passively modelocked surface-emitting semiconductor lasers", *Physics Reports* 429.2 (2006), pp. 67–120. (cit. on p. 8)
- [59] S. Droste, Y. Gabriel, W. B. R, C. Ian, and N. N. R, "Optical Frequency Comb Generation based on Erbium Fiber Lasers", *Nanophotonics* 5 (2016), p. 196. (cit. on p. 8)
- [60] P. Manurkar et al., "Fully self-referenced frequency comb consuming 5 watts of electrical power", *OSA Continuum* 1.1 (2018), pp. 274–282. 🗗 (cit. on p. 8)
- [61] W. Hänsel et al., "All polarization-maintaining fiber laser architecture for robust femtosecond pulse generation", *Applied Physics B* 123.1 (2017), p. 41. ☑ (cit. on p. 8)
- [62] M. E. Fermann, F. Haberl, M. Hofer, and H. Hochreiter, "Nonlinear amplifying loop mirror", *Optics Letters* 15.13 (1990), pp. 752–754. 🗹 (cit. on p. 8)
- [63] J. Faist, G. Villares, G. Scalari, M. Rösch, C. Bonzon, A. Hugi, and M. Beck, "Quantum Cascade Laser Frequency Combs", *Nanophotonics* 5.2 (2016), p. 272. (cit. on p. 8)
- [64] H. Murata, A. Morimoto, T. Kobayashi, and S. Yamamoto, "Optical pulse generation by electrooptic-modulation method and its application to integrated ultrashort pulse generators", *IEEE Journal of Selected Topics in Quantum Electronics* 6.6 (2000), pp. 1325–1331. (cit. on p. 8)
- [65] K. Beha, D. C. Cole, P. Del'Haye, A. Coillet, S. A. Diddams, and S. B. Papp, "Electronic synthesis of light", *Optica* 4.4 (2017), pp. 406–411. 🗗 (cit. on pp. 8, 131, 140)
- [66] D. R. Carlson, D. D. Hickstein, W. Zhang, A. J. Metcalf, F. Quinlan, S. A. Diddams, and S. B. Papp, "Ultrafast electro-optic light with subcycle control", *Science* 361.6409 (2018), 1358 LP –1363. (cit. on pp. 8, 140, 144)
- [67] A. S. Raja et al., "Electrically pumped photonic integrated soliton microcomb", *Nature Communications* 10.1 (2019), p. 680. (cit. on pp. 8, 37, 168)
- B. Stern, X. Ji, Y. Okawachi, A. L. Gaeta, and M. Lipson, "Battery-operated integrated frequency comb generator", *Nature* 562.7727 (2018), pp. 401–405. (cit. on pp. 8, 37, 168)

- [69] T. J. Kippenberg, R. Holzwarth, and S. A. Diddams, "Microresonator-based optical frequency combs.", *Science* 332.6029 (2011), pp. 555–9. (cit. on pp. 8, 37)
- [71] R. W. Boyd, *Nonlinear Optics*, 2nd ed., Elsevier, 2003. C (cit. on pp. 11, 12)
- D. Gindre, H. Maillotte, J. Monneret, E. Lantz, and C. Froehly, "Coherent picosecond parametric amplification through a Kerr-induced index grating in a single-mode fiber", *Optics Communications* 112.1-2 (1994), pp. 75–79. (cit. on p. 13)
- [73] Y. Pochi and G. Claire, *Landmark Papers On Photorefractive Nonlinear Optics*, World Scientific, 1995, p. 619. (cit. on p. 13)
- [74] L. Thévenaz and F. Berghmans, *Advanced fiber optics : concepts and technology*, Lausanne : EPFL Press, 2011 (cit. on p. 13).
- [75] L. Wang, L. Chang, N. Volet, M. H. P. Pfeiffer, M. Zervas, H. Guo, T. J. Kippenberg, and J. E. Bowers, "Frequency comb generation in the green using silicon nitride microresonators", *Laser & Photonics Reviews* 10.4 (2016), pp. 631–638. (cit. on p. 13)
- [76] P. Del'Haye et al., "Octave Spanning Tunable Frequency Comb from a Microresonator", *Physical Review Letters* 107.6 (2011), p. 063901. (cit. on pp. 13, 31, 108)
- [77] G. P. Agrawal, *Nonlinear Fiber Optics*, 3rd, Academic Press, 2001 (cit. on pp. 14, 28).
- [78] M. Heiblum and J. Harris, "Analysis of curved optical waveguides by conformal transformation", *IEEE Journal of Quantum Electronics* 11.2 (1975), pp. 75–83. (cit. on p. 14)
- [79] H. M. Nussenzveig, *Diffraction Effects in Semiclassical Scattering*, Cambridge University Press, 1992. (cit. on p. 14)
- [80] D. Rowland and J. Love, "Evanescent wave coupling of whispering gallery modes of a dielectric cylinder", *IEE Proceedings J Optoelectronics* 140.3 (1993), p. 177. (cit. on p. 15)
- [81] R. Chang, "Highly efficient prism coupling to whispering gallery modes of a square  $\mu$ -cavity", *Summaries of Papers Presented at the Quantum Electronics and Laser Science Conference*, Opt. Soc. America, 2002, pp. 27–28.  $\square$  (cit. on p. 16)
- [82] T. J. Kippenberg, S. M. Spillane, and K. J. Vahala, "Demonstration of ultra-high-Q small mode volume toroid microcavities on a chip", *Applied Physics Letters* 85.25 (2004), pp. 6113–6115. (cit. on p. 17)
- [83] S. M. Spillane, T. J. Kippenberg, O. J. Painter, and K. J. Vahala, "Ideality in a fiber-taper-coupled microresonator system for application to cavity quantum electrodynamics.", *Physical review letters* 91.4 (2003), p. 043902. (cit. on p. 17)
- [84] H. A. Haus, *Waves and fields in optoelectronics*, Prentice Hall, Incorporated, 1984 (cit. on p. 19).

- S. Schiller, "Asymptotic expansion of morphological resonance frequencies in Mie scattering.", *Applied optics* 32.12 (1993), pp. 2181–5. 🔀 (cit. on p. 22)
- [86] L. Zhang, Y. Yue, R. G. Beausoleil, and A. E. Willner, "Analysis and engineering of chromatic dispersion in silicon waveguide bends and ring resonators", *Optics Express* 19.9 (2011), pp. 8102−8107. (cit. on p. 22)
- [87] H. Haus and W. Huang, "Coupled-mode theory", *Proceedings of the IEEE* 79.10 (1991), pp. 1505–1518. (cit. on p. 24)
- [88] T. Carmon, L. Yang, and K. J. Vahala, "Dynamical thermal behavior and thermal self-stability of microcavities", *Optics Express* 12.20 (2004), p. 4742. [27] (cit. on pp. 25, 68, 121)
- [89] J. Hofer, "Crystalline resonators for optomechanics and frequency comb generation", PhD thesis, Ludwig-Maximilians-Universität München, 2009 (cit. on p. 25).
- [90] T. Hansson and S. Wabnitz, "Dynamics of microresonator frequency comb generation: models and stability", *Nanophotonics* 5.2 (2016), pp. 231–243. 🗹 (cit. on pp. 26, 32)
- [91] K. Ikeda, "Multiple-valued stationary state and its instability of the transmitted light by a ring cavity system", *Optics Communications* 30.2 (1979), pp. 257–261. [27] (cit. on p. 26)
- [92] M. Haelterman, S. Trillo, and S. Wabnitz, "Dissipative Modulation Instability In A Nonlinear Dispersive Ring Cavity", *Optics Communications* 91.5-6 (1992), pp. 401–407. 🗹 (cit. on pp. 27, 29, 30, 32)
- [93] L. A. Lugiato and R. Lefever, "Spatial Dissipative Structures in Passive Optical Systems", *Physical review letters* 58.21 (1987), pp. 2209–2211. (cit. on pp. 27, 116)
- [94] I. V. Barashenkov and Y. S. Smirnov, "Existence and stability chart for the ac-driven, damped nonlinear Schrödinger solitons", *Physical Review E* 54.5 (1996), pp. 5707–5725. (cit. on pp. 27, 32, 63)
- [95] A. B. Matsko, A. A. Savchenkov, D. Strekalov, V. S. Ilchenko, and L. Maleki, "Optical hyperparametric oscillations in a whispering-gallery-mode resonator: Threshold and phase diffusion", *Physical Review A* 71.3 (2005), p. 033804. (cit. on pp. 28, 32, 196)
- [96] S. Coen, H. G. Randle, T. Sylvestre, and M. Erkintalo, "Modeling of octave-spanning Kerr frequency combs using a generalized mean-field Lugiato-Lefever model.", *Optics letters* 38.1 (2013), pp. 37–9. (cit. on pp. 28, 32)
- [97] S. Coen and M. Erkintalo, "Universal scaling laws of Kerr frequency combs.", *Optics letters* 38.11 (2013), pp. 1790–2. 🖸 (cit. on pp. 29, 30)
- [98] C. Godey, I. V. Balakireva, A. Coillet, and Y. K. Chembo, "Stability analysis of the spatiotemporal Lugiato-Lefever model for Kerr optical frequency combs in the anomalous and normal dispersion regimes", *Physical Review A* 89.6 (2014), p. 063814. (cit. on pp. 29, 30, 35, 36, 63, 75)
- [99] T. Herr, K. Hartinger, J. Riemensberger, C. Y. Wang, E. Gavartin, R. Holzwarth, M. L. Gorodetsky, and T. J. Kippenberg, "Universal formation dynamics and noise of Kerrfrequency combs in microresonators", *Nature Photonics* 6.7 (2012), pp. 480–487. Cott. on p. 31)

- [100] J. Pfeifle et al., "Microresonator-Based Optical Frequency Combs for High-Bitrate WDM Data Transmission", *Opt. Fiber Commun. Conf.* Optical Society of America, 2012, OW1C.4 (cit. on p. 31).
- [101] A. a. Savchenkov, E. Rubiola, A. B. Matsko, V. S. Ilchenko, and L. Maleki, "Phase noise of whispering gallery photonic hyper-parametric microwave oscillators", *Optics Express* 16.6 (2008), p. 4130. (cit. on p. 31)
- [102] W. Liang, A. B. Matsko, A. A. Savchenkov, V. S. Ilchenko, D. Seidel, and L. Maleki, "Generation of Kerr combs in MgF<sub>2</sub> and CaF<sub>2</sub> microresonators", *2011 Joint Conference of the IEEE International Frequency Control and the European Frequency and Time Forum (FCS) Proceedings*, IEEE, 2011, pp. 1–6. (cit. on p. 31)
- [103] K. E. Webb, J. K. Jang, J. Anthony, S. Coen, M. Erkintalo, and S. G. Murdoch, "Measurement of microresonator frequency comb coherence by spectral interferometry", *Optics Letters* 41.2 (2016), p. 277. (cit. on p. 31)
- [104] Y. Okawachi, K. Saha, J. S. Levy, Y. H. Wen, M. Lipson, and A. L. Gaeta, "Octave-spanning frequency comb generation in a silicon nitride chip.", *Optics Letters* 36.17 (2011), pp. 3398–3400. (cit. on p. 31)
- [105] M. Erkintalo and S. Coen, "Coherence properties of Kerr frequency combs.", *Optics letters* 39.2 (2014), pp. 283–6. [7] (cit. on p. 31)
- [106] F. Leo, S. Coen, P. Kockaert, S.-P. Gorza, P. Emplit, and M. Haelterman, "Temporal cavity solitons in one-dimensional Kerr media as bits in an all-optical buffer", *Nature Photonics* 4.7 (2010), pp. 471–476. (cit. on pp. 31, 32, 35, 75)
- [107] T. Ackemann, W. J. Firth, and G. L. Oppo, "Fundamentals and Applications of Spatial Dissipative Solitons in Photonic Devices", *Advances in Atomic, Molecular and Optical Physics* 57.March 2009 (2009), pp. 323–421 (cit. on p. 31).
- [108] N. Akhmediev and A. Ankiewicz, eds., *Dissipative Solitons*, Lecture Notes in Physics, Springer Berlin Heidelberg, 2005. [27] (cit. on p. 31)
- [109] N. Akhmediev, A. Ankiewicz, and A. A. Nail Akhmediev, *Dissipative Solitons: From Optics to Biology and Medicine*, Springer, 2008. [7] (cit. on p. 31)
- [110] J. K. Jang, M. Erkintalo, S. G. Murdoch, and S. Coen, "Writing and erasing of temporal cavity solitons by direct phase modulation of the cavity driving field", *Optics Letters* 40.20 (2015), pp. 4755–4758. C (cit. on pp. 31, 35, 113)
- [111] D. Anderson, "High transmission rate communication systems using lossy optical solitons", *Optics Communications* 48.2 (1983), pp. 107–112. (cit. on p. 32)
- [112] Y. Wang, B. Garbin, F. Leo, S. Coen, M. Erkintalo, and S. G. Murdoch, "Addressing temporal Kerr cavity solitons with a single pulse of intensity modulation", *Optics Letters* 43.13 (2018), pp. 3192–3195. (cit. on p. 35)
- [113] K. Luo, J. K. Jang, S. Coen, S. G. Murdoch, and M. Erkintalo, "Spontaneous creation and annihilation of temporal cavity solitons in a coherently-driven passive fiber resonator", *Optics letters* 40.Mi (2015), pp. 2–5. (cit. on pp. 35, 80, 148)

- [114] X. Yi, Q.-F. Yang, K. Y. Yang, and K. Vahala, "Imaging soliton dynamics in optical microcavities", *Nature Communications* 9.1 (2018), p. 3565. [27] (cit. on pp. 35, 80, 157)
- P. Parra-Rivas, D. Gomila, M. A. Matías, S. Coen, and L. Gelens, "Dynamics of localized and patterned structures in the Lugiato-Lefever equation determine the stability and shape of optical frequency combs", *Physical Review A* 89.4 (2014), p. 43813. (cit. on pp. 35, 51, 63, 65)
- [116] P. Coullet, C. Riera, and C. Tresser, "Stable Static Localized Structures in One Dimension", *Physical Review Letters* 84.14 (2000), pp. 3069–3072. (cit. on p. 35)
- [117] H. Zhou, S. W. Huang, Y. Dong, M. Liao, K. Qiu, and C. W. Wong, "Stability and Intrinsic Fluctuations of Dissipative Cavity Solitons in Kerr Frequency Microcombs", *IEEE Photonics Journal* 7.3 (2015), pp. 1–13. (cit. on pp. 35, 45, 54, 58, 92, 148)
- [118] T. M. Fortier, A. Bartels, and S. A. Diddams, "Octave-spanning Ti:sapphire laser with a repetition rate >1 GHz for optical frequency measurements and comparisons", *Optics Letters* 31.7 (2006), p. 1011. (cit. on p. 37)
- [119] A. Bartels, D. Heinecke, and S. A. Diddams, "10-GHz Self-Referenced Optical Frequency Comb", *Science* 326.5953 (2009), pp. 681–681. (cit. on p. 37)
- D. T. Spencer et al., "An optical-frequency synthesizer using integrated photonics", *Nature* 557.7703 (2018), pp. 81–85. (cit. on pp. 37, 169)
- [121] N. R. Newbury, "Searching for applications with a fine-tooth comb", *Nature Photonics* 5.4 (2011), pp. 186–188. C (cit. on pp. 37, 119)
- P. Marin-Palomo et al., "Microresonator-based solitons for massively parallel coherent optical communications", *Nature* 546.7657 (2017), pp. 274–279. (cit. on pp. 37, 117, 144)
- [123] Z. Jiang, C.-B. Huang, D.E. Leaird, and A.M. Weiner, "Optical arbitrary waveform processing of more than 100 spectral comb lines", *Nature Photonics* 1.8 (2007), pp. 463–467. C (cit. on p. 37)
- [124] F. Ferdous, H. Miao, D. E. Leaird, K. Srinivasan, J. Wang, L. Chen, L. T. Varghese, and A. M. Weiner, "Spectral line-by-line pulse shaping of on-chip microresonator frequency combs", *Nature Photonics* 5.12 (2011), pp. 770–776. (cit. on p. 37)
- [125] E. Obrzud et al., "A microphotonic astrocomb", *Nature Photonics* 13.1 (2019), pp. 31–35. (cit. on p. 37)
- [126] M.-G. Suh et al., "Searching for exoplanets using a microresonator astrocomb", *Nature Photonics* 13.1 (2019), pp. 25–30. (cit. on p. 37)
- W. Liang, D. Eliyahu, V. S. Ilchenko, A. A. Savchenkov, A. B. Matsko, D. Seidel, and L. Maleki, "High spectral purity Kerr frequency comb radio frequency photonic oscillator.", *Nature Communications* 6 (2015), p. 7957. (cit. on pp. 37, 98, 111, 128, 130, 134, 135)

- [128] W. Liang, A.A. Savchenkov, V.S. Ilchenko, D. Eliyahu, A.B. Matsko, and L. Maleki, "Stabilized *C*-Band Kerr Frequency Comb", *IEEE Photonics Journal* 9.3 (2017), pp. 1–11. [7] (cit. on pp. 37, 135)
- [129] S. B. Papp et al., "Microresonator frequency comb optical clock", *Optica* 1.1 (2014), pp. 10–14. (cit. on pp. 37, 96, 111, 183)
- [130] S. Schiller et al., "The space optical clocks project: Development of high-performance transportable and breadboard optical clocks and advanced subsystems", *2012 European Frequency and Time Forum*, IEEE, 2012, pp. 412–418. (cit. on p. 37)
- [131] M. G. Suh, Q. F. Yang, K. Y. Yang, X. Yi, and K. J. Vahala, "Microresonator soliton dual-comb spectroscopy", *Science* 354.6312 (2016), pp. 600–603. (cit. on pp. 37, 144)
- [132] M.-G. Suh and K. J. Vahala, "Soliton Microcomb Range Measurement", *Science* 359.6378 (2018), pp. 884–887. (cit. on p. 37)
- [133] M. Karpov, M. H. P. Pfeiffer, J. Liu, A. Lukashchuk, and T. J. Kippenberg, "Photonic chip-based soliton frequency combs covering the biological imaging window", *Nature Communications* 9.1 (2018), p. 1146. (cit. on pp. 37, 165)
- [134] S. H. Lee, D. Y. Oh, Q.-F. Yang, B. Shen, H. Wang, K. Y. Yang, Y.-H. Lai, X. Yi, X. Li, and K. Vahala, "Towards visible soliton microcomb generation", *Nature Communications* 8.1 (2017), p. 1295. (cit. on pp. 37, 165)
- [135] C. Y. Wang, T. Herr, P. Del'Haye, A. Schliesser, J. Hofer, R. Holzwarth, T. W. Hänsch, N. Picqué, and T. J. Kippenberg, "Mid-infrared optical frequency combs at 2.5  $\mu$ m based on crystalline microresonators", *Nature Communications* 4 (2013), p. 1345.  $\Box$  (cit. on pp. 37, 39)
- [136] A. G. Griffith et al., "Silicon-chip mid-infrared frequency comb generation", *Nature Communications* 6 (2015), p. 6299. (cit. on p. 37)
- [137] M. Yu, Y. Okawachi, A. G. Griffith, N. Picqué, M. Lipson, and A. L. Gaeta, "Silicon-chip-based mid-infrared dual-comb spectroscopy", *Nature Communications* 9.1 (2018), p. 1869. (cit. on p. 37)
- [138] C. Bao et al., "High-order dispersion in Kerr comb oscillators", *Journal of the Optical Society of America B* 34.4 (2017), pp. 715–725. (cit. on p. 37)
- [139] S. Kim, K. Han, C. Wang, J. A. Jaramillo-Villegas, X. Xue, C. Bao, Y. Xuan, D. E. Leaird, A. M. Weiner, and M. Qi, "Dispersion engineering and frequency comb generation in thin silicon nitride concentric microresonators", *Nature Communications* 8.1 (2017). (cit. on pp. 37, 165)
- [140] M. Soltani, A. Matsko, and L. Maleki, "Enabling arbitrary wavelength frequency combs on chip", *Laser & Photonics Reviews* 10.1 (2016), pp. 158–162. C (cit. on p. 37)
- [141] A. Savchenkov, V. Ilchenko, A. Matsko, and L. Maleki, "Kilohertz optical resonances in dielectric crystal cavities", *Physical Review A* 70.5 (2004), p. 051804. (cit. on p. 39)

- [142] A. A. Savchenkov, A. B. Matsko, D. Strekalov, M. Mohageg, V. S. Ilchenko, and L. Maleki, "Low Threshold Optical Oscillations in a Whispering Gallery Mode CaF<sub>2</sub> Resonator", *Physical Review Letters* 93.24 (2004), p. 243905. (cit. on p. 39)
- [143] A. A. Savchenkov, A. B. Matsko, V. S. Ilchenko, and L. Maleki, "Optical resonators with ten million finesse", *Optics Express* 15.11 (2007), p. 6768. [7] (cit. on p. 39)
- T. Herr, C. Wang, P. Del'Haye, A. Schliesser, K. Hartinger, R. Holzwarth, and T. Kippenberg, "Frequency Comb Generation in Crystalline MgF<sub>2</sub> Whispering-Gallery Mode Resonators", *CLEO:2011 Laser Applications to Photonic Applications*, OSA, 2011, QTuF1. (cit. on p. 39)
- [145] W. Liang, A. A. Savchenkov, A. B. Matsko, V. S. Ilchenko, D. Seidel, and L. Maleki, "Generation of near-infrared frequency combs from a MgF<sub>2</sub> whispering gallery mode resonator", *Optics Letters* 36.12 (2011), p. 2290. (cit. on p. 39)
- [146] D. J. Moss, R. Morandotti, A. L. Gaeta, and M. Lipson, "New CMOS-compatible platforms based on silicon nitride and Hydex for nonlinear optics", *Nature Photonics* 7.8 (2013), pp. 597–607. (cit. on p. 40)
- [147] M. H. P. Pfeiffer, A. Kordts, V. Brasch, M. Zervas, M. Geiselmann, J. D. Jost, and T. J. Kippenberg, "Photonic Damascene process for integrated high-Q microresonator based nonlinear photonics", *Optica* 3.1 (2016), p. 20. (cit. on p. 40)
- V. Brasch, M. Geiselmann, T. Herr, G. Lihachev, M. H. P. Pfeiffer, M. L. Gorodetsky, and T. J. Kippenberg, "Photonic chip-based optical frequency comb using soliton Cherenkov radiation.", *Science* 351.6271 (2015), pp. 357–360. 

  (cit. on pp. 40, 68, 108, 109, 130, 162, 165, 167)
- [149] J. Liu, A. S. Raja, M. Karpov, B. Ghadiani, M. H. P. Pfeiffer, B. Du, N. J. Engelsen, H. Guo, M. Zervas, and T. J. Kippenberg, "Ultralow-power chip-based soliton microcombs for photonic integration", *Optica* 5.10 (2018), pp. 1347–1353. (cit. on pp. 40, 165)
- [150] J. Liu, E. Lucas, A. S. Raja, J. He, J. Riemensberger, R. N. Wang, M. Karpov, H. Guo, R. Bouchand, and T. J. Kippenberg, "Nanophotonic soliton-based microwave synthesizers" (2019), arXiv: 1901.10372. (cit. on pp. 40, 141, 171)
- [151] M. H. P. Pfeiffer, J. Liu, A. S. Raja, T. Morais, B. Ghadiani, and T. J. Kippenberg, "Ultrasmooth silicon nitride waveguides based on the Damascene reflow process: fabrication and loss origins", *Optica* 5.7 (2018), pp. 884–892. (cit. on pp. 40, 171)
- [152] P. Del'Haye, O. Arcizet, M. L. Gorodetsky, R. Holzwarth, and T. J. Kippenberg, "Frequency comb assisted diode laser spectroscopy for measurement of microcavity dispersion", *Nature Photonics* 3.9 (2009), pp. 529–533. 🗹 (cit. on pp. 41, 56)
- [153] J. Liu, V. Brasch, M. H. P. Pfeiffer, A. Kordts, A. N. Kamel, H. Guo, M. Geiselmann, and T. J. Kippenberg, "Frequency-comb-assisted broadband precision spectroscopy with cascaded diode lasers", *Optics Letters* 41.13 (2016), pp. 3134–3137. (cit. on p. 41)
- [154] G. C. Bjorklund, "Frequency-modulation spectroscopy: a new method for measuring weak absorptions and dispersions", *Optics Letters* 5.1 (1980), p. 15. [C. (cit. on p. 41)]

- [155] Q. Li, T. C. Briles, D. A. Westly, T. E. Drake, J. R. Stone, B. R. Ilic, S. A. Diddams, S. B. Papp, and K. Srinivasan, "Stably accessing octave-spanning microresonator frequency combs in the soliton regime", *Optica* 4.2 (2017), pp. 193–203. (cit. on p. 43)
- T. C. Briles et al., "Interlocking Kerr-microresonator frequency combs for microwave to optical synthesis", *Optics Letters* 43.12 (2018), pp. 2933–2936. (cit. on pp. 43, 169)
- [158] S. Zhang, J. M. Silver, L. Del Bino, F. Copie, M. T. M. Woodley, G. N. Ghalanos, A. Ø. Svela, N. Moroney, and P. Del'Haye, "Sub-milliwatt-level microresonator solitons with extended access range using an auxiliary laser", *Optica* 6.2 (2019), pp. 206–212. (cit. on p. 43)
- [159] H. Guo, M. Karpov, E. Lucas, A. Kordts, M. H. Pfeiffer, V. Brasch, G. Lihachev, V. E. Lobanov, M. L. Gorodetsky, and T. J. Kippenberg, "Universal dynamics and deterministic switching of dissipative Kerr solitons in optical microresonators", *Nature Physics* 13.1 (2017), pp. 94–102. [7] (cit. on pp. 45, 49, 51, 68, 78, 80, 81, 83, 128, 173)
- [160] M. Karpov, M. H. P. Pfeiffer, H. Guo, W. Weng, J. Liu, and T. J. Kippenberg, "Dynamics of soliton crystals in optical microresonators" (2019), arXiv: 1903.07122. (cit. on p. 49)
- [161] J. K. Wahlstrand, J. T. Willits, T. R. Schibli, C. R. Menyuk, and S. T. Cundiff, "Quantitative measurement of timing and phase dynamics in a mode-locked laser", *Optics Letters* 32.23 (2007), p. 3426. (cit. on p. 49)
- [162] C. Bao, A. C. Funk, C. Yang, and S. T. Cundiff, "Pulse dynamics in a mode-locked fiber laser and its quantum limited comb frequency uncertainty", *Optics Letters* 39.11 (2014), pp. 3266–3269. (cit. on p. 49)
- [163] C.-C. Lee and T. R. Schibli, "Intrinsic Power Oscillations Generated by the Backaction of Continuum on Solitons and its Implications on the Transfer Functions of a Mode-Locked Laser", *Physical Review Letters* 112.22 (2014), p. 223903. (cit. on p. 49)
- [164] A. B. Matsko and L. Maleki, "Feshbach resonances in Kerr frequency combs", *Physical Review A* 91.1 (2015), p. 013831. (Ctit. on pp. 49, 116)
- [165] E. Lucas, H. Guo, J. D. Jost, M. Karpov, and T. J. Kippenberg, "Detuning-dependent properties and dispersion-induced instabilities of temporal dissipative Kerr solitons in optical microresonators", *Physical Review A* 95.4 (2017), p. 43822. (cit. on pp. 53, 75, 110, 122, 124)
- [166] T. Herr, V. Brasch, J. D. Jost, I. Mirgorodskiy, G. Lihachev, M. L. Gorodetsky, and T. J. Kippenberg, "Mode spectrum and temporal soliton formation in optical microresonators", *Physical Review Letters* 113.12 (2014), p. 123901. (cit. on pp. 54, 56, 58, 62, 86)
- [167] X. Yi, Q.-F. Yang, K. Y. Yang, M.-G. Suh, and K. Vahala, "Soliton frequency comb at microwave rates in a high-Q silica microresonator", *Optica* 2.12 (2015), p. 1078. (cit. on pp. 54, 62, 98, 99, 130, 185)

- [168] I. S. Grudinin, L. Baumgartel, and N. Yu, "Impact of cavity spectrum on span in microresonator frequency combs.", *Optics express* 21.22 (2013), pp. 26929–35. (cit. on p. 58)
- [169] N. Akhmediev and M. Karlsson, "Cherenkov radiation emitted by solitons in optical fibers", *Physical Review A* 51.3 (1995), pp. 2602–2607. (cit. on pp. 58, 180)
- [170] A. B. Matsko, W. Liang, A. A. Savchenkov, D. Eliyahu, and L. Maleki, "Optical Cherenkov radiation in overmoded microresonators", *Optics Letters* 41.13 (2016), p. 2907. (cit. on p. 58)
- [171] C. Milián and D. V. Skryabin, "Soliton families and resonant radiation in a micro-ring resonator near zero group-velocity dispersion", *Optics Express* 22.3 (2014), p. 3732. (cit. on p. 58)
- [172] X. Yi, Q.-F. Yang, X. Zhang, K.Y. Yang, X. Li, and K. Vahala, "Single-mode dispersive waves and soliton microcomb dynamics", *Nature Communications* 8 (2017), p. 14869. [27] (cit. on pp. 58, 59, 88, 122–124, 135, 173)
- [173] Y. Wang, F. Leo, J. Fatome, M. Erkintalo, S. G. Murdoch, and S. Coen, "Universal mechanism for the binding of temporal cavity solitons", *Optica* 4.8 (2017), pp. 855–863. (cit. on p. 58)
- [174] X. Yi, Q.-F. Yang, K. Y. Yang, and K. Vahala, "Theory and measurement of the soliton self-frequency shift and efficiency in optical microcavities", *Optics Letters* 41.15 (2016), p. 3419. (cit. on pp. 60, 110, 122)
- [175] M. Karpov, H. Guo, A. Kordts, V. Brasch, M. H. P. Pfeiffer, M. Zervas, M. Geiselmann, and T. J. Kippenberg, "Raman Self-Frequency Shift of Dissipative Kerr Solitons in an Optical Microresonator", *Physical Review Letters* 116.10 (2016), p. 103902. (cit. on pp. 60, 122)
- [176] S. P. S. Porto, P. A. Fleury, and T. C. Damen, "Raman spectra of  $TiO_2$ ,  $MgF_2$ ,  $ZnF_2$ ,  $FeF_2$ , and  $MnF_2$ ", *Physical Review* 154.2 (1967), pp. 522–526.  $\Box$  (cit. on p. 60)
- [177] Q.-F. Yang, X. Yi, K. Y. Yang, and K. Vahala, "Spatial-mode-interaction-induced dispersive waves and their active tuning in microresonators", *Optica* 3.10 (2016), p. 1132. Cart. (cit. on pp. 60, 122, 124)
- [178] R. Paschotta, "Noise of mode-locked lasers (Part II): timing jitter and other fluctuations", *Applied Physics B* 79.2 (2004), pp. 163–173. (cit. on p. 60)
- [179] H. Haus and A. Mecozzi, "Noise of mode-locked lasers", *IEEE Journal of Quantum Electronics* 29.3 (1993), pp. 983–996. (cit. on p. 60)
- [180] A. B. Matsko, Wei Liang, V. S. Ilchenko, A. A. Savchenkov, J. Byrd, D. Seidel, and L. Maleki, "Control of kerr optical frequency comb generation with temperature dependent group velocity dispersion", 2014 IEEE Photonics Conference, IEEE, 2014, pp. 108–109. (cit. on p. 61)
- [181] A. Matsko, A. Savchenko, L. Maleki, A. Savchenkov, and L. Maleki, "On Excitation of Breather Solitons in an Optical Microresonator", *Optics Letters* 37.23 (2012), pp. 4856–4858. (cit. on pp. 61, 64)

- [182] M. Yu, J. K. Jang, Y. Okawachi, A. G. Griffith, K. Luke, S. A. Miller, X. Ji, M. Lipson, and A. L. Gaeta, "Breather soliton dynamics in microresonators", *Nature Communications* 8 (2017), p. 14569. (cit. on pp. 61, 64, 68, 75)
- [183] E. Lucas, M. Karpov, H. Guo, M. L. Gorodetsky, and T. J. Kippenberg, "Breathing dissipative solitons in optical microresonators", *Nature Communications* 8.1 (2017), p. 736. (cit. on pp. 61, 68, 78, 157)
- [184] C. Bao, J. A. Jaramillo-Villegas, Y. Xuan, D. E. Leaird, M. Qi, and A. M. Weiner, "Observation of Fermi-Pasta-Ulam Recurrence Induced by Breather Solitons in an Optical Microresonator", *Physical Review Letters* 117.16 (2016), p. 163901. (cit. on pp. 61, 64, 68, 157, 159)
- [185] X. Yi, Q.-F. Yang, K. Youl, and K. Vahala, "Active capture and stabilization of temporal solitons in microresonators", *Optics Letters* 41.9 (2016), p. 2037. (cit. on pp. 62, 98, 148)
- [186] J. D. Jost, E. Lucas, T. Herr, C. Lecaplain, V. Brasch, M. H. P. Pfeiffer, and T. J. Kippenberg, "All-optical stabilization of a soliton frequency comb in a crystalline microresonator", *Optics Letters* 40.20 (2015), p. 4723. (cit. on pp. 62, 104)
- [187] C. Joshi, J. K. Jang, K. Luke, X. Ji, S. A. Miller, A. Klenner, Y. Okawachi, M. Lipson, and A. L. Gaeta, "Thermally controlled comb generation and soliton modelocking in microresonators", *Optics Letters* 41.11 (2016), p. 2565. (cit. on pp. 62, 130, 141, 167, 169)
- [188] S. B. Papp, P. Del'Haye, and S. A. Diddams, "Mechanical Control of a Microrod-Resonator Optical Frequency Comb", *Physical Review X* 3.3 (2013), p. 031003. (cit. on pp. 62, 105, 130)
- [189] F. Leo, L. Gelens, P. Emplit, M. Haelterman, and S. Coen, "Dynamics of one-dimensional Kerr cavity solitons.", *Optics express* 21.7 (2013), pp. 9180–91. (cit. on pp. 62–64, 68)
- [190] K. Nozaki and N. Bekki, "Solitons as attractors of a forced dissipative nonlinear Schrödinger equation", *Physics Letters A* 102.9 (1984), pp. 383–386. (cit. on pp. 63, 167)
- [191] K. Nozaki and N. Bekki, "Chaotic solitons in a plasma driven by an rf field", *Journal of the Physical Society of Japan* 54.7 (1985), pp. 2363–2366. (cit. on p. 63)
- [192] D. Turaev, A. G. Vladimirov, and S. Zelik, "Long-range interaction and synchronization of oscillating dissipative solitons", *Physical Review Letters* 108.26 (2012), pp. 1–5. (cit. on pp. 64, 78)
- [193] E. A. Kuznetsov, "Solitons in a parametrically unstable plasma", *Soviet physics Doklady* 22(9) (1977), pp. 507–508 (cit. on p. 65).
- [194] Y. C. Ma, "The perturbed plane-wave solutions of the cubic Schrödinger equation", *Studies in Applied Mathematics* 60.1 (1979), pp. 43–58 (cit. on p. 65).
- [195] M. Anderson, F. Leo, S. Coen, M. Erkintalo, and S. G. Murdoch, "Observations of spatiotemporal instabilities of temporal cavity solitons", *Optica* 3.10 (2016), pp. 1071–1074. (cit. on pp. 68, 74)

- [196] M. Scheffer, J. Bascompte, W. A. Brock, V. Brovkin, S. R. Carpenter, V. Dakos, H. Held, E. H. van Nes, M. Rietkerk, and G. Sugihara, "Early-warning signals for critical transitions.", *Nature* 461.7260 (2009), pp. 53–9.
- [197] J. R. Tredicce, G. L. Lippi, P. Mandel, B. Charasse, A. Chevalier, and B. Picqué, "Critical slowing down at a bifurcation", *American Journal of Physics* 72.6 (2004), pp. 799–809. Cont. on p. 74)
- [198] V. Dakos, M. Scheffer, E. H. van Nes, V. Brovkin, V. Petoukhov, and H. Held, "Slowing down as an early warning signal for abrupt climate change.", *Proceedings of the National Academy of Sciences of the United States of America* 105.38 (2008), pp. 14308–12. C. (cit. on p. 75)
- [199] S. R. Carpenter et al., "Early Warnings of Regime Shifts: A Whole-Ecosystem Experiment", *Science* 332.6033 (2011), pp. 1079–1082. (cit. on p. 75)
- [200] A. J. Veraart, E. J. Faassen, V. Dakos, E. H. van Nes, M. Lürling, and M. Scheffer, "Erratum: Corrigendum: Recovery rates reflect distance to a tipping point in a living system", *Nature* 484.7394 (2012), pp. 404–404. 🗷 (cit. on p. 75)
- [201] J. A. Jaramillo-Villegas, X. Xue, P.-H. Wang, D. E. Leaird, and A. M. Weiner, "Deterministic single soliton generation and compression in microring resonators avoiding the chaotic region", *Optics Express* 23.8 (2015), p. 9618. (cit. on p. 75)
- [202] A. E. Fomin, M. L. Gorodetsky, I. S. Grudinin, and V. S. Ilchenko, "Nonstationary nonlinear effects in optical microspheres", *Journal of the Optical Society of America B* 22.2 (2005), p. 459. (cit. on p. 80)
- [203] H. Guo, E. Lucas, M. H. P. Pfeiffer, M. Karpov, M. Anderson, J. Liu, M. Geiselmann, J. D. Jost, and T. J. Kippenberg, "Intermode Breather Solitons in Optical Microresonators", *Physical Review X* 7.4 (2017), p. 041055. (cit. on pp. 86, 88, 89)
- [204] R. W. P. Drever, J. L. Hall, F. V. Kowalski, J. Hough, G. M. Ford, A. J. Munley, and H. Ward, "Laser Phase and Frequency Stabilization Using an Optical Resonator", *Applied Physics B* 31.2 (1983), pp. 97–105. [7] (cit. on p. 99)
- [205] E. D. Black, "An introduction to Pound–Drever–Hall laser frequency stabilization", *American Journal of Physics* 69.1 (2001), pp. 79–87. [7] (cit. on pp. 99, 100)
- [206] J. I. Thorpe, K. Numata, and J. Livas, "Laser frequency stabilization and control through offset sideband locking to optical cavities", *Optics Express* 16.20 (2008), p. 15980. (cit. on p. 100)
- [207] N. G. Pavlov, S. Koptyaev, G. V. Lihachev, A. S. Voloshin, A. S. Gorodnitskiy, M. V. Ryabko, S. V. Polonsky, and M. L. Gorodetsky, "Narrow-linewidth lasing and soliton Kerr microcombs with ordinary laser diodes", *Nature Photonics* 12.11 (2018), pp. 694–698. (cit. on p. 101)
- [208] A.A. Savchenkov, A.B. Matsko, V.S. Ilchenko, N. Yu, L. Maleki, and V.S. Ilchenko, "Whispering-gallery-mode resonators as frequency references. II. Stabilization", *Journal of the Optical Society of America B* 24.12 (2007), pp. 2988–2997. (cit. on p. 102)

- [209] D. V. Strekalov, R. J. Thompson, L. M. Baumgartel, I. S. Grudinin, and N. Yu, "Temperature measurement and stabilization in a birefringent whispering gallery mode resonator", *Optics Express* 19.15 (2011), p. 14495. (cit. on pp. 102, 104)
- [210] I. Fescenko, J. Alnis, A. Schliesser, C. Y. Wang, T. J. Kippenberg, and T. W. Hänsch, "Dual-mode temperature compensation technique for laser stabilization to a crystalline whispering gallery mode resonator", *Optics Express* 20.17 (2012), p. 19185. (cit. on p. 102)
- [211] W. Weng, J. D. Anstie, T. M. Stace, G. Campbell, F. N. Baynes, and A. N. Luiten, "Nano-Kelvin Thermometry and Temperature Control: Beyond the Thermal Noise Limit", *Physical Review Letters* 112.16 (2014), p. 160801. (cit. on pp. 102, 111)
- [212] P. Del'Haye et al., "Full Stabilization of a Microresonator-Based Optical Frequency Comb", *Physical Review Letters* 101.5 (2008), p. 053903. (cit. on pp. 104, 105, 108, 182)
- [213] I. Grudinin, H. Lee, T. Chen, and K. Vahala, "Compensation of thermal nonlinearity effect in optical resonators", *Optics Express* 19.8 (2011), p. 7365. 🗹 (cit. on p. 104)
- [214] A. A. Savchenkov, D. Eliyahu, W. Liang, V. S. Ilchenko, J. Byrd, A. B. Matsko, D. Seidel, and L. Maleki, "Stabilization of a Kerr frequency comb oscillator", *Optics Letters* 38.15 (2013), p. 2636. (cit. on p. 105)
- [215] B. Bernhardt, T. W. Hänsch, and R. Holzwarth, "Implementation and characterization of a stable optical frequency distribution system", *Optics Express* 17.19 (2009), pp. 16849–16860. (cit. on pp. 107, 182, 190)
- [216] S. T. Dawkins, J. J. McFerran, and A. N. Luiten, "Considerations on the Measurement of the Stability of Oscillators with Frequency Counters", 2007 IEEE International Frequency Control Symposium Joint with the 21st European Frequency and Time Forum, vol. 54, 5, IEEE, 2007, pp. 759–764. [27] (cit. on pp. 107, 182, 188, 191)
- [217] P. Lesage, "Characterization of Frequency Stability: Bias Due to the Juxtaposition of Time-Interval Measurements", *IEEE Transactions on Instrumentation and Measurement* 32.1 (1983), pp. 204–207. C (cit. on p. 107)
- [218] W. Weng, E. Lucas, G. Lihachev, V. E. Lobanov, H. Guo, M. L. Gorodetsky, and T. J. Kippenberg, "Spectral Purification of Microwave Signals with Disciplined Dissipative Kerr Solitons", *Physical Review Letters* 122.1 (2019), p. 13902. (cit. on pp. 110, 132, 175)
- [219] J. R. Stone, T. C. Briles, T. E. Drake, D. T. Spencer, D. R. Carlson, S. A. Diddams, and S. B. Papp, "Thermal and Nonlinear Dissipative-Soliton Dynamics in Kerr-Microresonator Frequency Combs", *Physical Review Letters* 121.6 (2018), p. 063902. (cit. on pp. 110, 123, 128, 130, 173)
- [220] D. G. Matei et al., "1.5  $\mu$ m Lasers with Sub-10 mHz Linewidth", *Physical Review Letters* 118.26 (2017), p. 263202.  $\square$  (cit. on pp. 111, 119)

- [221] W. Liang, V. S. Ilchenko, A. A. Savchenkov, E. Dale, D. Eliyahu, A. B. Matsko, and L. Maleki, "Resonant microphotonic gyroscope", *Optica* 4.1 (2017), p. 114. (cit. on pp. 111, 141, 167)
- [222] S. B. Papp, P. Del'Haye, and S. A. Diddams, "Parametric seeding of a microresonator optical frequency comb", *Optics express* 21.15 (2013), pp. 17615–17624. (cit. on p. 111)
- B. Razavi, "A study of injection locking and pulling in oscillators", *IEEE Journal of Solid-State Circuits* 39.9 (2004), pp. 1415–1424. (cit. on p. 113)
- [224] H. Taheri, A. B. Matsko, and L. Maleki, "Optical lattice trap for Kerr solitons", *The European Physical Journal D* 71.6 (2017), p. 153. (cit. on p. 113)
- [225] H. Taheri, A. a. A. Eftekhar, K. Wiesenfeld, and A. Adibi, "Soliton formation in whispering-gallery-mode resonators via input phase modulation", *IEEE Photonics Journal* 7.2 (2015), pp. 1–9. 🗹 (cit. on p. 113)
- [226] V. E. Lobanov, G. Lihachev, T. J. Kippenberg, and M. Gorodetsky, "Frequency combs and platicons in optical microresonators with normal GVD", *Optics Express* 23.6 (2015), p. 7713. [7] (cit. on pp. 113, 169)
- [227] L.-S. Ma, Z. Bi, A. Bartels, L. Robertsson, M. Zucco, R. S. Windeler, G. Wilpers, C. Oates, L. Hollberg, and S. A. Diddams, "Optical Frequency Synthesis and Comparison with Uncertainty at the 10-19 Level", *Sci.* 303.5665 (2004), pp. 1843–1845. (cit. on p. 119)
- [228] M. Giunta et al., "Transportable Ultra-low Noise Photonic Microwave Synthesizer", Conference on Lasers and Electro-Optics, OSA Technical Digest (online), Optical Society of America, 2018, SM2L.5. (cit. on pp. 120, 187)
- [229] A. B. Matsko and L. Maleki, "On timing jitter of mode locked Kerr frequency combs.", *Optics express* 21.23 (2013), pp. 28862–76. (cit. on p. 122)
- [230] A. B. Matsko and L. Maleki, "Noise conversion in Kerr comb RF photonic oscillators", *Journal of the Optical Society of America B* 32.2 (2015), pp. 232–240. 🗹 (cit. on p. 124)
- [231] C. Bao, Y. Xuan, C. Wang, J. A. Jaramillo-Villegas, D. E. Leaird, M. Qi, and A. M. Weiner, "Soliton repetition rate in a silicon-nitride microresonator", *Optics Letters* 42.4 (2017), pp. 759–762. (cit. on p. 124)
- [232] D. J. Wilson, K. Schneider, S. Hoenl, M. Anderson, T. J. Kippenberg, and P. Seidler, "Integrated gallium phosphide nonlinear photonics", 2 (2018), pp. 1–13, arXiv: 1808. 03554. (cit. on p. 126)
- [233] M. L. Gorodetsky and I. S. Grudinin, "Fundamental thermal fluctuations in microspheres", *Journal of the Optical Society of America B* 21.4 (2004), p. 697. (cit. on p. 128)
- [234] W. Zhang, T. Li, M. Lours, S. Seidelin, G. Santarelli, and Y. Le Coq, "Amplitude to phase conversion of InGaAs pin photo-diodes for femtosecond lasers microwave signal generation", *Applied Physics B* 106.2 (2011), pp. 301–308. (cit. on p. 128)

- [235] R. Bouchand, D. Nicolodi, X. Xie, C. Alexandre, and Y. Le Coq, "Accurate control of optoelectronic amplitude to phase noise conversion in photodetection of ultra-fast optical pulses", *Optics Express* 25.11 (2017), pp. 12268–12281. (cit. on p. 128)
- [236] T. M. Niebauer, R. Schilling, K. Danzmann, A. Rüdiger, and W. Winkler, "Nonstationary shot noise and its effect on the sensitivity of interferometers", *Physical Review A* 43.9 (1991), pp. 5022–5029. (cit. on p. 128)
- [237] F. Quinlan, T. Fortier, H. Jiang, and S. Diddams, "Analysis of shot noise in the detection of ultrashort optical pulse trains", *Journal of the Optical Society of America B* 30.6 (2013), pp. 1775–1785. (cit. on p. 128)
- [238] F. Quinlan, T. M. Fortier, H. Jiang, A. Hati, C. Nelson, Y. Fu, J. C. Campbell, and S. A. Diddams, "Exploiting shot noise correlations in the photodetection of ultrashort optical pulse trains", *Nature Photonics* 7.4 (2013), pp. 290–293. (cit. on p. 128)
- [239] E. Lucas, P. Brochard, R. Bouchand, S. Schilt, T. Südmeyer, and T. J. Kippenberg, "Ultralow-Noise Photonic Microwave Synthesis using a Soliton Microcomb-based Transfer Oscillator" (2019), arXiv: 1903.01213. (cit. on p. 130)
- [240] G. Pillet, L. Morvan, M. Brunel, F. Bretenaker, D. Dolfi, M. Vallet, J.-P. Huignard, and A. Le Floch, "Dual-Frequency Laser at 1.5 μm for Optical Distribution and Generation of High-Purity Microwave Signals", *Journal of Lightwave Technology* 26.15 (2008), pp. 2764–2773. (cit. on p. 130)
- [241] L. Maleki, "The optoelectronic oscillator", *Nature Photonics* 5 (2011), p. 728. (cit. on p. 130)
- [242] J. Li, H. Lee, and K. J. Vahala, "Microwave synthesizer using an on-chip Brillouin oscillator.", *Nature Communications* 4 (2013), p. 2097. (cit. on pp. 130, 135)
- [243] J. Li, X. Yi, H. Lee, S. a. Diddams, and K. J. Vahala, "Electro-optical frequency division and stable microwave synthesis.", *Science* 345.6194 (2014), pp. 309–13. (cit. on pp. 130, 135)
- [244] D. D. Hudson, K. W. Holman, R. J. Jones, S. T. Cundiff, J. Ye, and D. J. Jones, "Modelocked fiber laser frequency-controlled with an intracavity electro-optic modulator", *Optics Letters* 30.21 (2005), pp. 2948–2950. (cit. on p. 130)
- [245] S. A. Diddams, M. Kirchner, T. Fortier, D. Braje, A. M. Weiner, and L. Hollberg, "Improved signal-to-noise ratio of 10 GHz microwave signals generated with a mode-filtered femtosecond laser frequency comb", *Optics Express* 17.5 (2009), pp. 3331–3340. (cit. on p. 130)
- [246] A. Haboucha, W. Zhang, T. Li, M. Lours, A. N. Luiten, Y. Le Coq, and G. Santarelli, "Optical-fiber pulse rate multiplier for ultralow phase-noise signal generation.", *Optics letters* 36.18 (2011), pp. 3654–6. [7] (cit. on p. 130)
- [247] J. D. Jost, T. Herr, C. Lecaplain, V. Brasch, M. H. P. Pfeiffer, and T. J. Kippenberg, "Counting the cycles of light using a self-referenced optical microresonator", *Optica* 2.8 (2015), pp. 706–711. (cit. on pp. 130, 180, 182)

- [248] P. Del'Haye, A. Coillet, T. Fortier, K. Beha, D. C. Cole, K. Y. Yang, H. Lee, K. J. Vahala, S. B. Papp, and S. A. Diddams, "Phase-coherent microwave-to-optical link with a self-referenced microcomb", *Nature Photonics* 10.8 (2016), pp. 516–520. (cit. on pp. 130, 132, 180)
- [249] Z. L. Newman et al., "Architecture for the photonic integration of an optical atomic clock", *Optica* 6.5 (2019), p. 680. (cit. on pp. 130, 141)
- [250] H. R. Telle, B. Lipphardt, and J. Stenger, "Kerr-lens, mode-locked lasers as transfer oscillators for optical frequency measurements", *Applied Physics B* 74.1 (2002), pp. 1–6. ☑ (cit. on p. 131)
- P. Brochard, S. Schilt, and T. Südmeyer, "Ultra-low noise microwave generation with a free-running optical frequency comb transfer oscillator", *Optics Letters* 43.19 (2018), pp. 4651–4654. (cit. on pp. 131, 133, 135)
- [252] E. S. Lamb, D. R. Carlson, D. D. Hickstein, J. R. Stone, S. A. Diddams, and S. B. Papp, "Optical-Frequency Measurements with a Kerr Microcomb and Photonic-Chip Supercontinuum", *Physical Review Applied* 9.2 (2018), p. 024030. (cit. on p. 132)
- [253] H. Tian, N. Raabe, Y. Song, G. Steinmeyer, and M. Hu, "High-detectivity optical heterodyne method for wideband carrier-envelope phase noise analysis of laser oscillators", *Optics Letters* 43.13 (2018), pp. 3108–3111. (cit. on p. 132)
- [254] E. Rubiola, E. Salik, S. Huang, N. Yu, and L. Maleki, "Photonic-delay technique for phase-noise measurement of microwave oscillators", *Journal of the Optical Society of America B* 22.5 (2005), p. 987. (cit. on p. 139)
- V. Brasch, E. Lucas, J. D. Jost, M. Geiselmann, and T. J. Kippenberg, "Self-referenced photonic chip soliton Kerr frequency comb", *Light: Science & Applications* 6.1 (2017), e16202. ☑ (cit. on pp. 141, 180, 182)
- [256] T. E. Drake et al., "A Kerr-microresonator optical clockwork" (2018), pp. 1–9, arXiv: 1811.00581. 🔀 (cit. on p. 141)
- [257] M. Anderson, N. G. Pavlov, J. D. Jost, G. Lihachev, J. Liu, T. Morais, M. Zervas, M. L. Gorodetsky, and T. J. Kippenberg, "Highly efficient coupling of crystalline microresonators to integrated photonic waveguides", *Optics Letters* 43.9 (2018), p. 2106. (cit. on p. 141)
- [258] N. Lilienfein et al., "Temporal solitons in free-space femtosecond enhancement cavities", *Nature Photonics* (2019). (cit. on pp. 141, 169)
- [259] G. Huang, E. Lucas, J. Liu, A. S. Raja, G. Lihachev, M. L. Gorodetsky, N. J. Engelsen, and T. J. Kippenberg, "Thermo-refractive noise in silicon nitride microresonators" (2019), arXiv: 1901.07112. [7] (cit. on pp. 141, 173, 178, 179)
- T. E. Drake, J. R. Stone, T. C. Briles, and S. B. Papp, "Thermal decoherence and laser cooling of Kerr microresonator solitons" (2019), pp. 1–16, arXiv: 1903.00431. 

  (cit. on pp. 141, 178)

- [261] H. Tian, B. Dong, M. Zervas, T. J. Kippenberg, and S. A. Bhave, "An unreleased MEMS actuated silicon nitride resonator with bidirectional tuning", *Conference on Lasers and Electro-Optics*, OSA Technical Digest (online), Optical Society of America, 2018, SW4B.3. [7] (cit. on pp. 141, 167)
- [262] Y. HE, Q.-F. Yang, J. Ling, R. Luo, H. Liang, M. Li, B. Shen, H. Wang, K. Vahala, and Q. Lin, "A self-starting bi-chromatic LiNbO3 soliton microcomb" (2018), arXiv: 1812.09610. (cit. on pp. 141, 168, 169)
- [263] K. Alexander, J. P. George, J. Verbist, K. Neyts, B. Kuyken, D. Van Thourhout, and J. Beeckman, "Nanophotonic Pockels modulators on a silicon nitride platform", *Nature Communications* 9.1 (2018), p. 3444. (cit. on pp. 141, 168)
- [264] F. Kéfélian, H. Jiang, P. Lemonde, and G. Santarelli, "Ultralow-frequency-noise stabilization of a laser by locking to an optical fiber-delay line", *Optics Letters* 34.7 (2009), p. 914. (cit. on p. 141)
- [265] W. Liang, V. S. Ilchenko, D. Eliyahu, a. a. Savchenkov, a. B. Matsko, D. Seidel, and L. Maleki, "Ultralow noise miniature external cavity semiconductor laser", *Nature Communications* 6 (2015), p. 7371. (cit. on p. 141)
- [266] S. Gundavarapu et al., "Sub-hertz fundamental linewidth photonic integrated Brillouin laser", *Nature Photonics* 13.1 (2019), pp. 60–67. C (cit. on p. 141)
- D. Marpaung, J. Yao, and J. Capmany, "Integrated microwave photonics", *Nature Photonics* 13.2 (2019), pp. 80–90. (cit. on p. 141)
- [268] P. Ghelfi et al., "A fully photonics-based coherent radar system.", *Nature* 507.7492 (2014), pp. 341–5. (cit. on p. 141)
- [269] S. Koenig et al., "Wireless sub-THz communication system with high data rate", *Nature Photonics* 7.12 (2013), pp. 977–981. (cit. on p. 141)
- [270] E. Lucas, G. Lihachev, R. Bouchand, N. G. Pavlov, A. S. Raja, M. Karpov, M. L. Gorodetsky, and T. J. Kippenberg, "Spatial multiplexing of soliton microcombs", *Nature Photonics* 12.11 (2018), pp. 699–705. [7] (cit. on p. 143)
- [271] T. Hänsch, "Einstein Lecture Passion for precision", *Annalen der Physik* 15.9 (2006), pp. 627–652. 🗹 (cit. on p. 144)
- [272] I. Coddington, W. C. Swann, L. Nenadovic, and N. R. Newbury, "Rapid and precise absolute distance measurements", *Nature Photonics* 3. June (2009), pp. 351–356. (cit. on pp. 144, 162)
- [273] L. C. Sinclair, H. Bergeron, W. C. Swann, E. Baumann, J.-D. Deschênes, and N. R. Newbury, "Comparing optical oscillators across the air to milliradians in phase and 10<sup>-17</sup> in frequency", *Physical Review Letters* 120.5 (2017), pp. 1–35. (cit. on p. 144)
- [274] V. Ataie, D. Esman, B. P.-. P. Kuo, N. Alic, and S. Radic, "Subnoise detection of a fast random event", *Science* 350.6266 (2015), pp. 1343–1346.

- [275] S. M. Link, D. J. H. C. Maas, D. Waldburger, and U. Keller, "Dual-comb spectroscopy of water vapor with a free-running semiconductor disk laser", *Science* 356.6343 (2017), pp. 1164–1168. (cit. on p. 144)
- [276] G. Millot, S. Pitois, M. Yan, T. Hovhannisyan, A. Bendahmane, T. W. Hänsch, and N. Picqué, "Frequency-agile dual-comb spectroscopy", *Nature Photonics* 10.1 (2015), pp. 27–30. (cit. on p. 144)
- A. Dutt, C. Joshi, X. Ji, J. Cardenas, Y. Okawachi, K. Luke, A. L. Gaeta, and M. Lipson, "On-chip dual-comb source for spectroscopy", *Science Advances* 4.3 (2018). (cit. on p. 144)
- [278] N. G. Pavlov, G. Lihachev, S. Koptyaev, E. Lucas, M. Karpov, N. M. Kondratiev, I. A. Bilenko, T. J. Kippenberg, and M. L. Gorodetsky, "Soliton dual frequency combs in crystalline microresonators", *Optics Letters* 42.3 (2017), pp. 514–517.
- [279] C. Joshi, A. Klenner, Y. Okawachi, M. Yu, K. Luke, X. Ji, M. Lipson, and A. L. Gaeta, "Counter-rotating cavity solitons in a silicon nitride microresonator", *Optics Letters* 43.3 (2018), p. 547. (cit. on pp. 144, 149, 156)
- [280] Q. F. Yang, X. Yi, K. Y. Yang, and K. Vahala, "Counter-propagating solitons in microresonators", *Nature Photonics* 11.9 (2017), pp. 560–564. (cit. on pp. 144, 145, 149, 151, 156)
- [281] X. Guo, C.-L. Zou, and H. X. Tang, "Second-harmonic generation in aluminum nitride microrings with 2500%/W conversion efficiency", *Optica* 3.10 (2016), p. 1126. (cit. on p. 144)
- [282] D. J. Richardson, J. M. Fini, and L. E. Nelson, "Space-division multiplexing in optical fibres", *Nature Photonics* 7.5 (2013), pp. 354–362. C (cit. on p. 144)
- [283] N. Bozinovic, Y. Yue, Y. Ren, M. Tur, P. Kristensen, H. Huang, A. E. Willner, and S. Ramachandran, "Terabit-Scale Orbital Angular Momentum Mode Division Multiplexing in Fibers", *Science* 340.June (2013), pp. 1545–1548. (cit. on p. 144)
- [284] C. Bao et al., "Orthogonally polarized frequency comb generation from a Kerr comb via cross-phase modulation", *Optics Letters* 44.6 (2019), pp. 1472–1475. C (cit. on p. 144)
- P. Donvalkar et al., "Broadband Frequency Comb Generation in the Near-Visible using Higher-Order Modes in Silicon Nitride Microresonators", *Conference on Lasers and Electro-Optics*, OSA, 2017, STu4J.5. (cit. on p. 144)
- [286] X. Zhao, J. M. Silver, L. Del Bino, P. Del'Haye, L. D. Bino, and P. Del'Haye, "Dual Comb Generation in a Single Microresonator", *Conference on Lasers and Electro-Optics*, OSA, 2017, STh3L.4. (cit. on p. 144)
- [287] B. Lomsadze, B. C. Smith, and S. T. Cundiff, "Tri-comb spectroscopy", *Nature Photonics* 12.11 (2018), pp. 676–680. (cit. on pp. 145, 161, 162)
- [288] S. T. Cundiff and S. Mukamel, "Optical multidimensional coherent spectroscopy", *Physics Today* 66.7 (2013), pp. 44–49 (cit. on pp. 145, 161).

- [289] X. Zhao, X. Qu, F. Zhang, Y. Zhao, and G. Tang, "Absolute distance measurement by multi-heterodyne interferometry using an electro-optic triple comb", *Optics Letters* 43.4 (2018), p. 807. (cit. on pp. 145, 162)
- [290] I. S. Grudinin and N. Yu, "Dispersion engineering of crystalline resonators via microstructuring", *Optica* 2.3 (2015), p. 221. (cit. on p. 146)
- [291] M. Joseph Humphrey and M. Humphrey, "Calculation of coupling between tapered fiber modes and whispering-gallery modes of a spherical microlaser", PhD thesis, Oklahoma State University, 2005 (cit. on p. 146).
- [292] M. Izutsu, S. Shikama, and T. Sueta, "Integrated optical SSB modulator/frequency shifter", *IEEE Journal of Quantum Electronics* 17.11 (1981), pp. 2225–2227. (cit. on p. 146)
- [293] V. Durán, S. Tainta, and V. Torres-Company, "Ultrafast electrooptic dual-comb interferometry", *Optics Express* 23.23 (2015), p. 30557. (cit. on p. 158)
- [294] B. Lomsadze and S. T. Cundiff, "Frequency combs enable rapid and high-resolution multidimensional coherent spectroscopy.", *Science* 357.6358 (2017), pp. 1389–1391. (cit. on p. 161)
- [295] D. Esman, V. Ataie, B. P.-P. Kuo, N. Alic, and S. Radic, "Subnoise Signal Detection and Communication", *Journal of Lightwave Technology* 34.22 (2016), pp. 5214–5219. Communication", *Journal of Lightwave Technology* 34.22 (2016), pp. 5214–5219.
- [296] M. Zhang, B. Buscaino, C. Wang, A. Shams-Ansari, C. Reimer, R. Zhu, J. M. Kahn, and M. Lončar, "Broadband electro-optic frequency comb generation in a lithium niobate microring resonator", *Nature* 568.7752 (2019), pp. 373–377. [7] (cit. on p. 168)
- [297] C. Wang, M. Zhang, M. Yu, R. Zhu, H. Hu, and M. Loncar, "Monolithic lithium niobate photonic circuits for Kerr frequency comb generation and modulation", *Nature Communications* 10.1 (2019), p. 978. (cit. on p. 168)
- [298] A. Rueda, F. Sedlmeir, M. Kumari, G. Leuchs, and H. G. L. Schwefel, "Resonant electrooptic frequency comb", *Nature* 568.7752 (2019), pp. 378–381. 🗷 (cit. on p. 168)
- [299] M.-G. Suh, C. Y. Wang, C. Johnson, and K. J. Vahala, "Directly pumped 10 GHz microcomb modules from low-power diode lasers", *Optics Letters* 44.7 (2019), p. 1841. (cit. on p. 168)
- [300] A. S. Raja, J. Liu, N. Volet, R. N. Wang, J. He, E. Lucas, R. Bouchand, P. Morton, J. Bowers, and T. J. Kippenberg, "Packaged photonic chip-based soliton microcomb using an ultralow-noise laser" (2019), pp. 3–7, arXiv: 1906.03194. (cit. on p. 168)
- [301] B. Garbin, Y. Wang, S. G. Murdoch, G.-L. Oppo, S. Coen, and M. Erkintalo, "Experimental and numerical investigations of switching wave dynamics in a normally dispersive fiber ring resonator", *European Physical Journal D* 193.1982 (2017), p. 2405. 🗹 (cit. on p. 169)
- [302] X. Xue, Y. Xuan, Y. Liu, P.-H. Wang, S. Chen, J. Wang, D. E. Leaird, M. Qi, and A. M. Weiner, "Mode-locked dark pulse Kerr combs in normal-dispersion microresonators", *Nature Photonics* 9.9 (2015), pp. 594–600. (cit. on p. 169)

- [303] P. Parra-Rivas, D. Gomila, E. Knobloch, S. Coen, and L. Gelens, "Origin and stability of dark pulse Kerr combs in normal dispersion resonators", *Optics Letters* 41.11 (2016), pp. 2402–2405. [7] (cit. on p. 169)
- [304] A. Fülöp et al., "High-order coherent communications using mode-locked dark-pulse Kerr combs from microresonators", *Nature Communications* 9.1 (2018), p. 1598. (cit. on p. 169)
- [305] W. Weng, R. Bouchand, E. Lucas, E. Obrzud, T. Herr, and T. Kippenberg, "Heteronuclear soliton molecules in optical microresonators" (2019), arXiv: 1901.04026. (cit. on p. 169)
- [306] M. Anderson, Y. Wang, F. Leo, S. Coen, M. Erkintalo, and S. G. Murdoch, "Coexistence of Multiple Nonlinear States in a Tristable Passive Kerr Resonator", *Physical Review X* 7.3 (2017), p. 031031. (cit. on p. 169)
- [307] A. U. Nielsen, B. Garbin, S. Coen, S. G. Murdoch, and M. Erkintalo, "Coexistence and interactions between nonlinear states with different polarizations in a monochromatically driven passive Kerr resonator" (2019), pp. 1–6, arXiv: 1902.05541. (cit. on p. 169)
- [308] Z. Wang, H. Dai, Y. Zheng, and X. Chen, "Measurement of the electro-optic coefficient of a BaMgF<sub>4</sub> single crystal", *Optical Materials Express* 7.2 (2017), p. 360. (cit. on p. 169)
- [309] J. Chen, X. Chen, A. Wu, H. Li, Y. Zheng, Y. Ma, L. Jiang, and J. Xu, "Femtosecond Z-scan measurement of third-order nonlinear refractive indices of BaMgF<sub>4</sub>", *Applied Physics Letters* 98.19 (2011), p. 191102. C (cit. on p. 169)
- [310] E. G. Víllora, K. Shimamura, K. Sumiya, and H. Ishibashi, "Birefringent- and quasi phase-matching with BaMgF<sub>4</sub> for vacuum-UV/UV and mid-IR all solid-state lasers", *Optics Express* 17.15 (2009), p. 12362. (cit. on p. 169)
- [311] L. Mateos, M. O. Ramírez, I. Carrasco, P. Molina, J. F. Galisteo-López, E. G. Víllora, C. de las Heras, K. Shimamura, C. Lopez, and L. E. Bausá, "BaMgF<sub>4</sub>: An Ultra-Transparent Two-Dimensional Nonlinear Photonic Crystal with Strong  $\chi^{(3)}$  Response in the UV Spectral Region", *Advanced Functional Materials* 24.11 (2014), pp. 1509–1518.  $\square$  (cit. on p. 169)
- [312] K. Shimamura, E. G. Víllora, H. Zeng, M. Nakamura, S. Takekawa, and K. Kitamura, "Ferroelectric properties and poling of BaMgF<sub>4</sub> for ultraviolet all solid-state lasers", *Applied Physics Letters* 89.23 (2006), p. 232911. (cit. on p. 169)
- [313] D. Liang and J. E. Bowers, "Recent progress in lasers on silicon", *Nature Photonics* 4 (2010), p. 511. (cit. on p. 171)
- [314] P.A. Morton and M. J. Morton, "High-Power, Ultra-Low Noise Hybrid Lasers for Microwave Photonics and Optical Sensing", *Journal of Lightwave Technology* 36.21 (2018), pp. 5048–5057. [7] (cit. on p. 171)
- [315] C. W. Nelson, A. Hati, and D. A. Howe, "A collapse of the cross-spectral function in phase noise metrology", *Review of Scientific Instruments* 85.2 (2014), p. 024705. (cit. on pp. 173, 177)

- [316] N. M. Kondratiev and M. L. Gorodetsky, "Thermorefractive noise in whispering gallery mode microresonators: Analytical results and numerical simulation", *Physics Letters, Section A: General, Atomic and Solid State Physics* 382.33 (2018), pp. 2265–2268. (cit. on p. 178)
- R. Ell et al., "Generation of 5-fs pulses and octave-spanning spectra directly from a Ti:sapphire laser", *Optics Letters* 26.6 (2001), pp. 373–375. 🔀 (cit. on p. 180)
- [318] T. M. Fortier, D. J. Jones, and S. T. Cundiff, "Phase stabilization of an octave-spanning Ti:sapphire laser", *Optics Letters* 28.22 (2003), pp. 2198–2200. (cit. on p. 180)
- [319] Y. Okawachi, M. R. E. Lamont, K. Luke, D. O. Carvalho, M. Yu, M. Lipson, and A. L. Gaeta, "Bandwidth shaping of microresonator-based frequency combs via dispersion engineering", *Optics Letters* 39.12 (2014), pp. 3535–3538. 🗷 (cit. on p. 180)
- [320] J. K. Jang, M. Erkintalo, S. G. Murdoch, and S. S. Coen, "Observation of dispersive wave emission by temporal cavity solitons", *Optics Letters* 39.19 (2014), p. 5503. (cit. on p. 180)
- [321] J. Reichert, R. Holzwarth, T. Udem, and T. Hänsch, "Measuring the frequency of light with mode-locked lasers", *Optics Communications* 172.1-6 (1999), pp. 59–68. [7] (cit. on p. 180)
- [322] P. Del'Haye, S. B. Papp, and S. a. Diddams, "Hybrid Electro-Optically Modulated Microcombs", *Physical Review Letters* 109.26 (2012), p. 263901. (cit. on p. 182)
- [323] S. Chen et al., "Electrically pumped continuous-wave III–V quantum dot lasers on silicon", *Nature Photonics* 10 (2016), p. 307. [7] (cit. on p. 183)
- [324] M. Schiemangk, S. Spießberger, A. Wicht, G. Erbert, G. Tränkle, and A. Peters, "Accurate frequency noise measurement of free-running lasers", *Applied Optics* 53.30 (2014), p. 7138. (cit. on p. 187)
- [325] E. Rubiola, *Phase Noise and Frequency Stability in Oscillators*, Cambridge University Press, 2008, p. 220. C (cit. on pp. 188, 189)
- V. Dolgovskiy, S. Schilt, N. Bucalovic, G. Di Domenico, S. Grop, B. Dubois, V. Giordano, and T. Südmeyer, "Ultra-stable microwave generation with a diode-pumped solid-state laser in the 1.5-μm range", *Applied Physics B* 116.3 (2014), pp. 593–601. ☑ (cit. on p. 190)
- [327] Y. K. Chembo and N. Yu, "Modal expansion approach to optical-frequency-comb generation with monolithic whispering-gallery-mode resonators", *Physical Review A* 82.3 (2010), p. 033801. (cit. on p. 195)

## The little art project

Parce qu'une thèse, au-delà d'un travail scientifique, constitue aussi une expérience personnelle, je place ici ce petit collage, témoin du temps passé à Lausanne. Certains y reconnaitront mes photos en couverture des calendriers successifs, qui tour à tour ont agrémenté mon bureau.













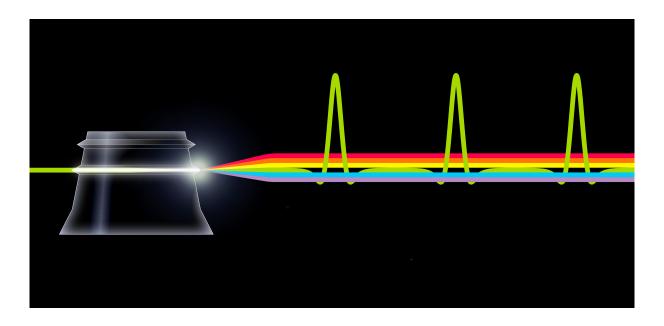


"Come in here, dear boy, have a cigar, You're gonna go far, You're gonna fly high, You're never gonna die, You're gonna make it if you try, They're gonna love you."

WISH YOU WERE HERE PINK FLOYD

Work and work for love and Ain't you hungry for success, success, success, success "

SOME GIRLS
THE ROLLING STONES



"Breathe, breathe in the air
Don't be afraid to care
Leave but don't leave me
Look around, choose your own ground
For long you live and high you fly
And smiles you'll give and tears you'll cry
And all your touch and all you see
Is all your life will ever be"

THE DARK SIDE OF THE MOON
PINK FLOYD

"The time is gone, the song is over,
Thought I'd something more to say..."

THE DARK SIDE OF THE MOON
PINK FLOYD

## **Erwan LUCAS**

Address: Citizenship: French

Chemin du Noirmont 13, Mail: erwan.lucas@polytechnique.edu

1004 Lausanne, Switzerland Mobile: +41 78 665 48 53

#### **EDUCATION**

2019: PhD in Photonics 🗹

† Laboratory of Photonic and Quantum Measurement (EPFL, Switzerland)

**EPFL** 

2014 Thesis Director: Tobias J. Kippenberg

2014 : Master in Electrical engineering 🗹

Ecole Polytechnique Fédérale de Lausanne (EPFL, Switzerland)

EPFL

2012 Specialization in advanced signal processing. GPA: 5.7/6

2013 : Diplôme d'ingénieur de l'Ecole Polytechnique 🗹,

† Ecole Polytechnique (Palaiseau, France)

2009 Multidisciplinary program with a focus in Electrical Engineering

(semiconductor physics and photonics).



#### ACADEMIC EXPERIENCE

**Cur.** : Teaching assistant (EPFL)

2014 : Research Project, LPQM (EPFL, Switzerland)

Six month Master thesis supervised by T. Kippenberg:

Toward mid-infrared Kerr frequency comb generation in crystalline microresonators.

**2012** : **Research Project, ONERA The French Aerospace Lab** (Palaiseau, France)

Four month research internship supervised by R. Haidar and E. Rosencher:

Two-photon absorption in the silicon: origin of linearity at low optical flux.

**2011** : **Student scientific project** "**EyeT<sub>E</sub>X**" (Polytechnique)

Development of a software for the recognition of handwritten mathematical formulas based on machine learning, with 6 other students. IBM interested in the results.

Other professional experiences

2013: Research Project, ABB Corporate Research Center (Baden-Dättwil, Switzerland)

Five month internship, in image processing, computer vision and machine learning for automatic detection and recognition of power poles in static images.

2012 : Treasurer of student association Binet photo of the École Polytechnique

Grant applications, budget management, purchase of equipment.

2011 : Webmaster, Regionales Rechenzentrum Erlangen (Nürnberg, Germany)

Update of the IT center's website of the Friedrich-Alexander University.

#### **Member of Association** *Tremplin*

Tutoring students in disadvantaged neighborhoods to help access higher education.

**2010** : **Officer cadet, Gendarmerie nationale** (French Military Police), Versailles

Leadership training, Operational missions (criminal investigations, patrols & interventions), Audit on email exchange procedures and on the reorganization of the police department.

#### **AWARDS**

2016 - 2019 : European Space Agency NPI Grant

2018 : Emil Wolf Outstanding Student Paper Competition at Frontiers in Optics

2017 : Nature Photonics Best Student Paper at ISPALD

2017 : Best Student Award CNLP Summer School (Como, Italy)

2013 – 2014 : EPFL excellence scholarship

2012 : Outstanding physics research internship award X2009

2010 : Médaille de la Défense Nationale, bronze grade

#### PROGRAMMING AND SOFTWARE

English: Fluent Languages: Matlab, Java, Python, Languages: Matlab, Languages:

**German**: Fluent (Goethe-Zertifikat C1) OpenGL, Web (php, html, css).

**Software** : Office, Adobe suite

### OTHER INTERESTS AND ACTIVITIES

Sport : Climbing, Skiing, Sailing

Other interests : Photography ⑤, Cinema, Piano, Space-related topics, Kerbal Space Program ☑

